University of Valladolid

Department of Electronic Technology

Ph.D. program in Industrial Engineering

A thesis submitted in fulfillment of the requirements of the degree of
Doctor of Philosophy

Ph.D. Thesis Dissertation

Study and Evaluation of Distributed Power Electronic Converters in Photovoltaic Generation Applications

ZAID AHMED AL-JAWARY

Supervisors:
Santiago de Pablo Gómez
Luis Carlos Herrero de Lucas

Valladolid, March 2022

Acknowledgment

Working at the School of Industrial Engineering with the DEEPER Research Group at the Department of Electronic Technology at the University of Valladolid (UVa) has been a great pleasure and a wonderful privilege.

First and foremost, I would like to express my sincere gratitude and appreciation to my supervisor, Professor Dr. Santiago de Pablo, for his guidance, encouragement, support, and confidence in me from the beginning to the final stage of my Ph.D. journey.

I would also like to express my deepest gratitude and appreciation to my co-supervisor, Professor Dr. Luis C. Herrero, and Professor Dr. Fernando Martínez in the same research group for their invaluable supervision, contribution, and encouragement towards the completion of my thesis. I express my gratefulness to my supervisors for their time and guidance to improve my skills in research and teaching that I believe I learned from the best. Special thanks to my mentor, Professor Dr. Daniel Moriñigo, for his endless support to overcome all difficulties during my studies.

I would like to express my gratitude to my parents, my lovely wife, and my kids, for their unending love and encouragement.

Dedicated to my beloved Family

Resumen

Entre las diversas tecnologías de energía renovable, la energía procedente de paneles fotovoltaicos es una de las más implementadas comercialmente y ampliamente utilizadas en los paradigmas energéticos actuales en todo el mundo, donde ocupa un lugar significativo entre otras fuentes de energía renovable, y de hecho tiene una tasa de crecimiento más rápida que cualquier otra fuente. Las fuentes de energía renovable, como la conversión de energía solar fotovoltaica, han recibido una mayor aceptación en los últimos años debido a la necesidad de una menor dependencia de los combustibles fósiles. En comparación con los combustibles fósiles, los paneles fotovoltaicos tienen beneficios significativos, como la producción de energía limpia y confiable y su idoneidad para la generación distribuida.

A medida que aumenta la importancia de la energía fotovoltaica, la eficiencia y el rendimiento de los convertidores de potencia utilizados para controlar la energía fotovoltaica serán cada vez más importantes. Como resultado, es fundamental analizar el rendimiento de las aplicaciones fotovoltaicas basadas en convertidores de potencia conectados a red para lograr una alta productividad y crear técnicas de control mejoradas que permitan logras una mayor rentabilidad de los sistemas fotovoltaicos.

Recientemente se ha propuesto una nueva topología para los sistemas fotovoltaicos conectados a red, utilizando convertidores multinivel modulares (MMC) y distribuyendo los paneles fotovoltaicos en todas las celdas del MMC. La topología MMC ofrece varias ventajas en comparación con otros convertidores multinivel, como la modularidad del convertidor que permite alcanzar en principio cualquier nivel de tensión, mientras que el equilibrado de tensión de los condensadores se puede lograr con relativa facilidad. Además, se generan formas de onda con baja distorsión armónica, se puede implementar una operación tolerante a fallos y el condensador de enlace de continua (CC) se puede reducir al mínimo o incluso eliminar en una situación equilibrada. Sin embargo, todavía existen desafíos asociados con el control y la modulación del MMC, como su comportamiento en cortocircuito en el lado de continua. Por otra parte, la distribución de los paneles fotovoltaicos sobre la topología MMC tiene dos ventajas principales: elimina las pérdidas y los costos relacionados con los convertidores CC/CC utilizados para seguir el punto de máxima potencia en los string converters y los central inverters, porque esa tarea se delega a las celdas del MMC, y reduce las pérdidas de potencia relacionadas con el traslado de la

energía a los condensadores MMC desde una fuente de CC externa. Sin embargo, las técnicas tradicionales de modulación por ancho de pulso (PWM) tienen muchos problemas cuando se trata de esta aplicación porque la distorsión en la salida aumenta a valores inaceptables cuando las celdas del MMC tienen como objetivo diferentes tensiones.

Este proyecto de investigación ha propuesto una nueva técnica de modulación denominada "Modulación de ancho de pulso con portadora local" (LC-PWM) para MMC con diferentes voltajes de celda, teniendo en cuenta los voltajes de celda medidos para generar secuencias de conmutación obteniendo una sincronización más precisa. También adapta el periodo de muestreo del modulador para mejorar las transiciones de nivel a nivel, un aspecto importante para reducir el ruido de las corrientes circulantes internas. Como resultado, la nueva técnica de modulación LC-PWM reduce la distorsión de salida en un rango más amplio de situaciones de voltaje. Además, elimina de manera efectiva los componentes innecesarios de alterna de las corrientes circulantes, lo que resulta en menores pérdidas de energía y una mayor eficiencia de la aplicación.

Finalmente, se ha utilizado un modelo de simulación del MMC conectado a la red para evaluar la modulación propuesta. El rendimiento de LC-PWM también se ha validado comparándolo con un PWM de cambio de fase tradicional en cargas aisladas para descartar cualquier interacción de la red o del controlador. Los resultados de la simulación revelaron una distorsión de salida más consistente en un amplio rango operativo, así como una reducción efectiva de las corrientes circulantes y de las pérdidas de potencia.

Abstract

Among the various renewable energy technologies, photovoltaic (PV) cell energy is one of the most commercially implemented and widely used in today's energy paradigms throughout the world, where it has a significant place among other renewable energy sources, and with a growth rate faster than any other source. Renewable energy sources, such as solar PV conversion, have received greater acceptance in recent years with reduced reliance on fossil fuels. In comparison to fossil fuels, PV panels have significant benefits such as clean and reliable energy production and suitability for distributed generation.

As the importance of PV energy increases, the efficiency and performance of power converters used to control PV energy become increasingly important. As a result, it is essential to analyze the influence of power-converter-based PV applications on the grid in order to achieve high productivity and to create improved control techniques that will allow for further penetration of cost-effective PV systems.

A new topology has recently been proposed for grid-connected PV systems, using modular multilevel converters (MMC) and distributed PV panels throughout the MMC cells. The MMC topology offers various advantages compared to the other multilevel converters, such as the modularity of the converter that conceptually enables any voltage level to be reached, while capacitor voltage balancing can be achieved relatively easily. Furthermore, waveforms with low harmonic distortion are generated, the fault-tolerant operation can be implemented, and the DC-link capacitor can be reduced to the minimum or even eliminated in a balanced situation. However, there are still challenges associated with the control and modulation of the MMC, such as the short circuit fault DC side. In contrast, distributing the PV panels over MMC topology has two main advantages: it removes the losses and costs related to the DC-to-DC converters used to track the maximum power point on string converters or central converters, because that task is delegated to MMC cells, and it reduces the power losses related to moving the energy into the MMC capacitors from an external DC source. However, traditional pulse width modulation (PWM) techniques have many problems when dealing with this application: the distortion at the output increases to unacceptable values when MMC cells target different voltages.

This research project has proposed a new modulation technique called “Local Carrier Pulse Width Modulation” (LC-PWM) for MMCs with different cell voltages, taking into account the measured cell voltages to generate switching sequences with more accurate timing. It also adapts the modulator sampling period to improve the transitions from level to level, an important issue to reduce noise at the internal circulating currents. As a result, the new modulation LC-PWM technique reduces the output distortion in a wider range of voltage situations. Furthermore, it effectively eliminates unnecessary AC components of circulating currents, resulting in lower power losses and higher MMC efficiency.

Finally, a grid connected MMC simulation module has been used to evaluate the proposed modulation. The performance of LC-PWM has also been validated by comparing it to a traditional Phase Shift PWM on isolated loads to rule out any grid or controller interaction. The simulation results revealed a more consistent output distortion throughout a wider operating range, as well as an effective reduction in circulating currents and power losses.

Dissertation's Structure

- **Chapter 1.** This chapter explains the study objective and motivation, as well as the most relevant points of the modular multilevel converter (MMC) as a power converter for photovoltaic (PV) applications linked to a grid or to a load. An introduction to the state of the art is presented and a new modulation is identified for the MMC to deliver the highest power conversion efficiency and the lowest overall device losses.

- **Chapter 2.** This chapter introduces the basic operational concepts of PV panels and explains how costs and installed power are shifting. The characteristics of current-voltage (*I*-*V*) and power-voltage (*P*-*V*) are described in detail to represent their effects on various algorithms for maximum power point tracking. It also highlights the most important PV applications.

- **Chapter 3.** In this chapter, multi-level converter types are discussed focusing on the main parts and topologies of each type, with an emphasis on the advantages of raising the level of conversion and the pros and cons of each type.

- **Chapter 4.** Introduction to the MMC topology description, basic operation**,** and mathematical modeling have been demonstrated in this chapter. The chapter includes the technical work of the main part of the converter represented by the submodule (SM) to construct the arm's converter with different topologies. It also identifies the most essential MMC applications.

- **Chapter 5.** Different modulation methods and power control related to the MMC have been demonstrated in this chapter. The circulating current effect and voltage ripple control are described indicating the performance over power conversion. In terms of the MMC scalability and modularity, the advantages and implementations are listed in depth to illustrate the converter work.

- **Chapter 6.** This chapter explains and studies the controller of a grid-connected PV generation application with distributed panels throughout an MMC, taking into consideration phase to phase and arm to arm power imbalances, as well as maximum power point tracking (MPPT) for each set of PV cells connected to an MMC submodule. It also explains in detail the proposed modulation methodology, named Local-Carrier PWM (LC-PWM), as well as the rationale for using a new modulation and the precise calculations used to validate the modulation concept. The framework of the simulation results developed as part of this research project is presented. The consequences of on-grid and off-grid connections are discussed.

- **Chapter 7.** This chapter concludes with the findings of this research project and offers an outline of the immediate areas for future research.

Table of Contents

List of Figures

List of Tables

List of Acronyms

Acronyms	Dentition
AC	Alternating current
APOD-PWM	Alternative phase opposition disposition pulse-width modulation
BIPV	Building Integrated Photovoltaics
CB-PWM	Carrier-based pulse-width modulation
CHB	Cascaded H-bridge
CSC	Current-source converter
DC	Direct current
FACTS	Flexible AC transmission system
FB	Full bridge
FBSM	Full bridge submodule
FLC	Flying capacitor
FIFO	First in first out memory
FOCV	Fractional open-circuit voltage
FSCC	Fractional short circuit current
FWD	Free-wheeling diode
HC	Hill climb method
HVDC	High voltage direct current
HB	Half-Bridge
HBSM	Half bridge submodule
IGBT	Insulated-gate bipolar transistor
InCond	Incremental conductance method

LCC	Line commutated converter
LC-PWM	Local carrier pulse-width modulation
LHD	Low order harmonic distortion
LPF	Low pass filter
LS-PWM	Level-shifted pulse-width modulation
LUT	Look-up table
MMC	Modular multilevel converter
MPP	Maximum power point
MPPT	Maximum power point trucking
MVDC	Medium voltage direct current
NLM	Nearest level modulation
NPC	Neutral-point-clamped converter
P	Proportional controller
PI	Proportional-integral
PR	Proportional-resonant
P&O	Perturb and observe
PWM	Pulse-width modulation
PD-PWM	Phase-disposition pulse-width modulation
POD-PWM	Phase-opposition disposition pulse-width modulation
PS-PWM	Phase-shifted pulse-width modulation
PV	Photovoltaic
RES	Renewable energy system
RMS	Root mean square
SHE-PWM	Selective harmonic elimination pulse-width modulation
STATCOM	Static synchronous compensator
SM	Sub-module
SVC	Space vector control
SVM	Space vector modulation
THD	Total harmonic distortion
VOC	Voltage oriented control
VSC	Voltage-source converter

List of Symbols

Symbol	Definition
a	Diode ideality constant
C_{dc}	DC-Link capacitor
C_{SM}	Submodule capacitor
C_o	Output capacitor
D	Diode
d_u	duty cycle for the upper arm
d_l	duty cycle for the lower arm
F_c	Carrier frequency
F_n	Resonant frequency
F_s	Switching frequency
f_{fund}	Fundamental frequency
h	Upper or lower arm
g	Neutral point
I_{pv}	PV panels current
I_{pv_cell}	Current at each PV cell
I_{mpp}	Current at maximum power point
I_{sc}	Short circuit current
I_d	Shockley diode current
i_h	Upper or lower arm current
i_o	Output current
i_{o_d}	Output current at direct axis

i_{o_q}	Output current at quadrature axis
i_z	Differential mode current (Circulating current)
i_{z_ac}	AC component in the differential current
i_{z_dc}	DC component in the differential current
i_{z_d}	Circulating current at direct axis
i_{z_q}	Circulating current at quadrature axis
i_L	Inductor current
i_l	Lower arm current
i_u	Upper arm current
K_i	Integral gain
K_p	Proportional gain
k	Boltzmann constant
L_{arm}	Arm inductor
L_o	Output inductor
L_{eq}	Equivalent inductor
m	Middle point
N_{sm}	Number of SMs per arm
n	negative point
n_{sm}	Inserted SM
P	Active power
P^*	Active power reference
P_{MMC_IN}	Power at the input of the MMC
P_{MMC_OUT}	Power at the output of the MMC
P_{losses}	Power loss
P_{pv}	PV panels power
p	Positive point
Q	Reactive power
Q^*	Reactive power reference
Q_C	Reactive power at the capacitor
q	Absolute value of electron charge
R_{arm}	Arm resistor

R_o	Output resistor
R_L	Load resistor
R_{eq}	Equivalent resistor
R_s	Series resistor
R_{sh}	Shunt resistor
S	Switch
Slj	Switching states for the lower arm
Suj	Switching states for the upper arm
T	Temperature
T_i	Time response coefficient
T_s	Sampling time
T_u	Sampling time to insert or bypass an SM from the upper arm
T_l	Sampling time to bypass or insert an SM from the lower arm
T_{ref}	Standard test condition temperature
T_{Kvoc}	Temperature coefficient at open circuit voltage
V_{ref}	Voltage reference
V_{mpp}	Voltage at maximum power point
V_{pv}	PV panels voltage
V_{oc}	Open circuit voltage
V^*_{abc}	Phase's voltage references
V_C	Average capacitor voltage in each SM
V_{Clj}	Individual capacitor voltage in the lower arm with j=1 until N
V_{Cuj}	Individual capacitor voltage in the upper arm with j=1 until N
V_{SM}	SM voltage
V_{dc}	DC-link voltage
v^*_u	A normalized sinusoidal reference voltage signal for the upper arm
v^*_l	A normalized sinusoidal reference voltage signal for the lower arm
v_{max}	Maximum voltage from the inserted SM voltages in the upper and lower arms
v_{max_up}	Maximum voltage from the inserted SM voltages in the upper arm
v_{min_up}	Minimum voltage from the inserted SM voltages in the upper arm
v_{min}	Minimum voltage from the inserted SM voltages in the upper and lower arms

v_{max_lw}	Maximum voltage from the inserted SM voltages in the lower arm
v_{min_lw}	Minimum voltage from the inserted SM voltages in the lower arm
$\hat{v}_{level}$	Estimated voltage level
v_l	Total voltages of the cascaded SMs in the lower arm
v_u	Total Voltages of the cascaded SMs in the upper arm
v_z	Differential voltage
v^*_{ac}	AC grid reference voltage
v_{ac}	AC grid voltage
$v^*_{ac\_d}$	AC grid reference voltage at direct axis
$v^*_{ac\_q}$	AC grid reference voltage at quadrature axis
v_{ac_d}	AC grid voltage at direct axis
v_{ac_q}	AC grid voltage at quadrature axis
x	Phases (a, b, or c)
ω	Angular frequency
ω_n	Angular resonant frequency
θ	Phase angle
θ_{grid}	Grid phase angle

Introduction

Contents of This Chapter

- **Section 1.1** introduces the aim and motivation of the research project, as well as the most effective use of a modular multilevel converter as a power converter in photovoltaic applications. New modulation for this converter based photovoltaic applications has been identified that give the highest power conversion efficiencies and the lowest overall device power losses.

- **Section 1.2** defines the scope of this research project and the key scientific objectives are presented.

- **Section 1.3** defines the tools used to verify the simulation and analyzing the functional effects.

- **Section 1.4** lists the most critical points of the study production to present the key scientific contributions.

- **Section 1.5** demonstrates the journal that confirmed the thesis work.

- **Section 1.6** shows the structure of the thesis work by defining the topics and main points of each chapter.

1.1 Introduction

The global energy situation is undergoing a significant transformation. Because of environmental issues, scarce energy, and the rising cost of traditional fossil fuels, reducing reliance on them has become a priority for developed countries. As a result of this situation, countries have allocated significant capital to the quest for safer and affordable energy supplies, as well as optimum productivity in all energy conversion processes [1]. Since a large portion of the installed capacity will be linked to delivery levels in the near future, the growing penetration of renewable energy, as well as more challenging criteria in terms of performance and stability in the electrical network, poses a significant challenge.

Among various renewable technologies, photovoltaic (PV) energy is one of the most commercially applied and broadly adopted green energies in today's energy paradigms around the world [2]. In fact, it has a relevant position among other renewable energies, its growth rate is faster than all other sources [3], and it may eventually surpass all other renewable energies in the near future. This is because PV cell installations are spreading around the world almost in step with Moore's Law, approximately doubling the cumulative installed PV capability every two years: in 2002, about 2 GWp were installed, 40 GWp were usable in 2010, and in 2018 and 2019, more than 480 to 593 GWp were operational globally [3][4][5]. The installed capacity reached 707.5 GWp in 2020 [3]; compared to 2010, PV installed power has grown rate at a sustained rate of +33% per year. Currently, according to the latest research [6][7], PV panel installations rose by 27% in the early start of 2021, reaching more than 950 GWp. Moreover, since 1980, photovoltaic modules have decreased regularly in cost at an average rate of about 10% per year [4]. As long as this trend continues, efficiency, performance, and cost are the most important features of power converters used to manage PV energy.

Grid connected PV systems usually consist of series or strings of PV panels. They are frequently made up of a couple of serially connected power converters, first a DC-DC converter that gets the maximum energy from the panels and then a DC/AC inverter transfers all the available power to the grid [8].

Central inverters are normally used in three-phase grid connected PV plants larger than tens of kWp [9][10]. This technology generally delivers great productivity at a lower cost due to the maximum power point tracking (MPPT) control applied across all linked panels; yet it requires high voltage DC connections [11] and uniform irradiance. Furthermore, due to its low immunity to hotspots and partial shading, the power mismatch issue is significant in this concept, leading to a lower PV utilization. In contrast, the MPPT control is achieved separately in each string of the string/multi-string PV inverters, leading to a better total energy yield [8]. However, this topology requires more power electronics converters and reactors, resulting in increasing costs and losses, and there are still mismatches in the PV panels in each string.

For low-power PV applications, module PV inverters are generally used, allowing module-level monitoring and diagnostics [1]. This topology also minimizes the effects of partial shadowing and power mismatch since the module converter acts on a single PV panel with an individual MPPT control. However, the low overall efficiency is the main disadvantage of this concept [1].

Considering the above issues, spreading the PV panels over the submodules (SM) of a modular multilevel converter (MMC) by integrating PV strings directly on converter cells has recently been proposed in [12][13]. This topology has nearly the same installation cost as central inverters while achieving better performance, as it gets mostly the same power optimization as string converters at a lower cost, and it may work in a wider power and voltage range with fewer losses than all previous topologies due to the removal of DC-DC converters.

MMC converters were introduced in 2003 [14] and they have attracted significant research interest in medium-voltage [15] and high-voltage applications [16]. Modular converters, such as the MMC, allow any number of voltage levels to be reached by increasing or decreasing the number of SMs. They also offer various advantages over other multilevel topologies, such as fault tolerant operation, easy to achieve capacitor voltage balance, low harmonic distortion, and the elimination of the bulky DC-link capacitor [16][17]. Therefore, they have seen fast growth in a broad field of applications, including DC transmission, solid-state transformers, and renewable energy integration.

When using MMC converters on renewable energies, specifically on PV applications as in [18][19], PV panels are connected to the grid or load by the MMC through a DC-link. In contrast, a new topology has recently been proposed in [12][20][21]. This thesis focuses on the latter due to important advantages: on the one hand, the optimization function of string converters is performed at no additional cost by the MMC cells, reducing the costs and losses related to the intermediate booster converters; on the other hand, with an appropriate control, placing the PV panels inside the MMC converter leads to smaller circulating currents that mean smaller power losses, increasing the converter efficiency. However, this topology has an important drawback: the voltage of each SM depends on the irradiance and temperature of its PV panels, and when MMC cells target different voltages and traditional PWM modulations are used, the output distortion increases, reducing the operation range. The new modulation proposed in this thesis will solve this problem and reduce the MMC internal circulation currents, while simultaneously reducing semiconductor power rating and conduction power losses.

In addition, a developed sorting method, used to sort all SM voltages in the MMC, means the SMs capacitor voltages must be balanced to keep the average cell voltage at the reference value [22]. This results in less SM switching and lower switching losses, as well as reducing the sorting complexity and cost.

In order to expand the application of MMCs to medium-voltage and high-voltage renewable energy applications, this thesis proposes a new modulation method, named Local Carrier Pulse Width Modulation (LC-PWM). The LC-PWM deals with different voltages in MMC cells, and the higher precision of this technique reduces the output distortion in a wider range of voltage situations. In addition, with appropriate control of the MMC arms in a balanced situation, it removes unwanted AC components of the circulating currents, which also means fewer power losses, thus increasing the MMC efficiency. As an important variable of the MMC, internal circulating currents affect the semiconductor rating because of the arm peak current and capacitor voltage ripple, and they also change the operating range of the MMC under balanced conditions [23][24].

In fact, using capacitor voltage information on duty cycle computation, switching sequences generated by the proposed LC-PWM modulation greatly reduce the root mean square (RMS) value of circulating currents. Circulating currents usually contain a DC component when energy is transferred from phase to phase or from an external energy source at the DC side to the MMC phases [25]. That energy is then sent to the AC side by means of the output AC current. In addition, circulating currents may have a 50 Hz component that can be used by the controller to transfer energy from the upper arm to the lower arm or back [20] and keep the arm in a balanced situation as much as possible. The main drawback of the MMC is that an additional 100 Hz negative-sequence component arises in the circulating current when using traditional modulators, and, under unbalanced AC grid conditions, they may also include a 100 Hz positive-sequence and even a zero-sequence component [26]. All of these undesired effects, which become more critical on unbalanced grids, usually have an important impact on the operating range of the MMC, so this issue has been analyzed for different circulating current control methods [27].

The implementation of LC-PWM is discussed and checked using simulations in diverse circumstances to verify the above concepts, first to show the feasibility of the proposed concept, while the performance and behavior of the LC-PWM is evaluated using a grid connected MMC simulation module. Later on, the performance of this new modulation technique is compared to a conventional PS-PWM on isolated loads to rule out any possible grid or controller interaction. Finally, the feasibility of the proposed LC-PWM modulation is evaluated through a study and analysis of the circulating currents, the corresponding converter power losses, input power accuracy, the performance and efficiency of the MMC converter on this application, and the total harmonic distortion (THD) under different scenarios is used to assess the viability of the proposed LC-PWM modulation.

1.2 Objectives of The Thesis

The main objectives of the thesis are to:

1. Study and analyze the recently suggested topology of directly connecting PV panels to the MMC cell by detecting the behavior of the circulating current and analyzing its generated components to further explain the power losses and reveal more details of the converter performance.

2. Evaluate the efficiency of various modulation techniques, such as level-shifted pulse-width modulation (LS-PWM), when applied to distributed PV panels over MMC. The total harmonic distortion (THD) of line-to-line voltage and the root mean square (RMS) value of the circulating current are used as a benchmark to evaluate the performance of the different modulations.

3. Propose, analyze, and test a new modulation system to handle instantaneous voltage level changes caused by the recently proposed topology, which will distribute the MMC cells over the PV panel string.

4. Study and analyze the controller of a grid-connected distributed PV application-based MMC to determine converter efficiency and application performance with an AC grid interaction.

5. Improve the cell selection algorithm to reduce the computational load implementation of the voltage balancing algorithm.

1.3 Tools Used

The findings of this study are based on extensive simulations of different scenarios in order to validate the proposed modulation technique. The main program used to model the power electronics converter is MATLAB/Simulink. The MATLAB function code is used to define the controller function and the variables in a highly flexible manner.

In addition, Microsoft Visio has been used to create the diagrams required for the descriptions of the topologies and schemes. Microsoft Excel has been used to draw the registered simulation results in order to provide precise figures for high-quality presentations.

1.4 Thesis Contributions

The main contributions of this thesis are:

- By integrating the PV panels directly in the cells of an MMC and injecting the energy directly in the converter phases, the DC component of the circulating currents has been eliminated, reducing conduction losses.

- Controlling the MPP of the PV panels with the MMC cells, power losses are further reduced by eliminating the requirement for a DC-DC booster converter, which is generally required to keep the PV voltage at its maximum when the PV is externally connected.

- Proposing a new modulation that is more appropriate for distributed PV applications that accommodates an instantaneous voltage level due to the PV panels being directly connected to the MMC cells.

- A secondary effect of the proposed modulation is that it removes the 100 Hz frequency component of the circulating current.

- The new proposed LC-PWM modulation helps to further reduce the power losses caused by the circulating current by applying a very hard synchronized level-to-level transition to remove transients in the circulating current.

- Implements a cluster distribution in the PV panel field by placing the MMC SM of each arm from each phase in the same location, so as to make the arms and legs of the converter as balanced as possible, lowering the DC and 50 Hz components of the circulating current, and further decreasing the power losses.

- Other modulation techniques help to balance the energy stored at the MMC arms when there are small imbalances, while LC-PWM does not. So a controller has been implemented to react to any unbalanced energy in the MMC arms and legs caused by circulating current while using the proposed modulation.

- A comparison of conventional PS-PWM and the proposed LC-PWM modulation, demonstrating the superior performance of the proposed modulation in MMC based PV applications with a low number of SMs per arm.

- The sorting method used to keep the capacitor voltages balanced has been improved with a reduction complexity from $O(n^2)$ to about $O(n)$.

1.5 Publication

- Aljawary, Z.A.; de Pablo, S.; Herrero-de Lucas, L.C.; Martinez-Rodrigo, F. Local Carrier PWM for Modular Multilevel Converters with Distributed PV Cells and Circulating Current Reduction. *Energies* **2020**, *13*, 5585. https://doi.org/ 10.3390/ en13215585.

  In this paper, a new modulation technique for MMC based PV application has been proposed. The proposed modulation shows more consistent behavior in the output distortion throughout the operating range; it also reduces the circulating currents and cuts the conduction losses by half. The behavior of the new modulation has been compared to a traditional modulation to validate the idea.

1.6 Thesis Outline

The thesis is organized as follows:

- Chapter 2 introduces the basic operational concepts of PV panels and explains how costs and installed power are shifting. The characteristics of current-voltage (*I*-*V*) and power-voltage (*P*-*V*) are described in detail to represent their effects on various algorithms for maximum power point tracking. It also highlights the most important PV applications.

- Chapter 3 discusses multi-level converter types, focusing on the main parts and topologies of each type, with an emphasis on the advantages of raising the level of conversion and the pros and cons of each type.

- Chapter 4 introduces the MMC topology description, basic operation**,** and mathematical modeling. The chapter includes the technical work of the main part of the converter represented by the submodule (SM) to construct the converter arms with different topologies. It also identifies the most essential MMC applications.

- Chapter 5 introduces different modulation methods and power controls related to the MMC. The circulating current effect and voltage ripple control are described, indicating the performance over power conversion. In terms of the MMC scalability and modularity, the advantages and implementations are listed in depth to illustrate the simplicity of the converter work.

- Chapter 6 explains and investigates the controller of a grid-connected PV generation application with distributed panels through an MMC, taking into consideration phase to phase and arm to arm power imbalances, as well as MPPT for each PV panel connection. It explains the methodology of the proposed LC-PWM in depth, including the reason for using a new modulation and the precise calculations used to validate the modulation concept. The framework of simulation results developed as part of this research project is presented. The consequences of on-grid and off-grid connections are discussed.

- Chapter 7 concludes, setting out the findings of this research project and offers an outline of the immediate areas for future research.

2

Photovoltaic System

Contents of This Chapter

- **Section 2.1** introduces the value of using PV panels as a renewable energy source. The statistic illustrates the rapid growth of PV energy usage around the world, especially as prices fall at an exponential rate.

- **Section 2.2** describes the characteristics of PV cells and defines the solar cell parameters required for extracting the maximum power generated by PV panels. The influence of limiting factors on the efficiency of PV cells is also revealed.

- **Section 2.3** analyzes the equivalent electric circuit of a PV cell to get a deeper understanding of how it operates. It also demonstrates how it performs under different circumstances.

- **Section 2.4** presents a general configuration of different PV module power converters by identifying the most common power converter technologies and their applications across a broad range of power ratings. In addition, a more efficient high-power converter is demonstrated.

- **Section 2.5** emphasizes the significance of tracking the PV panels' maximum power output and introduces several tracking strategies for the maximum power point.

- **Section 2.6** explores possible PV power applications for off-grid and on-grid connections.

2.1 Introduction

Photovoltaic (PV) cell energy, among various renewable technologies, is one of the most economically deployed and generally used in today's energy trends worldwide [2]. Solar PV conversion has achieved significant acceptance and popularity in recent years due to its ability to provide energy with reduced reliance on oil fuels and other renewable energy sources. Particularly opposed to oil derivatives such as gasoline, PV panels offer such significant advantages as sustainable and reliable energy production and distributed generation appropriateness.

A photovoltaic energy system is one of a simple, clean, inexpensive, and inexhaustible renewable energy source and can be considered an important alternative sustainable energy source for the next electricity generations. According to NASA research and calculations, the sun, as a bright star that provides light and heat to the earth, may still have around 6500 million years of life remaining, and it sends more energy to Earth per hour than is required to meet the global need for a year. The entire planet's surface could receive about 120,000 terawatts of sunlight irradiation, which is 20000 times more power than the planet requires, and it is estimated that in about 18 days of solar irradiation, the earth receives an amount of energy equivalent to all the world's reserves from such sources as coal, oil, and natural gas [28].

In the last few decades, the contribution of solar energy to the world total electricity generation has increased rapidly, and PV installations have grown throughout the world almost in line with Moore's Law, duplicating the cumulative installed PV capacity roughly every two years: about 2 GWp were installed in 2002, 40 GWp were available in 2010 and more than 593 GWp operate worldwide in 2019 [2][5]. In 2020, the installed capacity reached 707.5 GWp [3][29], see Figure 2.1, which represents a growth percentage of more than 33% each year. PV deployment will continue to grow as the global energy portfolio transitions more towards renewable energy to reach approximately 4800 to 8500 GWp of cumulative PV capacity by 2040 and 2050 respectively [30].

Recent reports clearly show a high rising trend in the use of solar energy, with many large and powerful countries setting ambitious goals and strategies for the next few decades to embrace highly penetrated PV systems as part of their renewable energy systems and deploying various projects across their territories to promote the use of clean energy. For example, the European Commission has set renewable energy regulations for 2020 and 2030 in countries with abundant solar resources, such as Germany, Spain, and Italy, with 13 percent of European electricity consumption predicted to be met by PV systems by 2021.

In Spain, with better sunshine than many other European countries, the installed capacity is currently at 5.6 GW and the coming years will see significant solar capacity additions because of the national target to reach a 100% renewable power sector by 2050 [31]. Denmark, on the other hand, which has a short summer season and a prolonged winter season, has begun to plan for increasing the use of renewable energy in order to reshape its associated renewable energy structure, with a goal of 100% renewable energy in power and heating by 2035 [32].

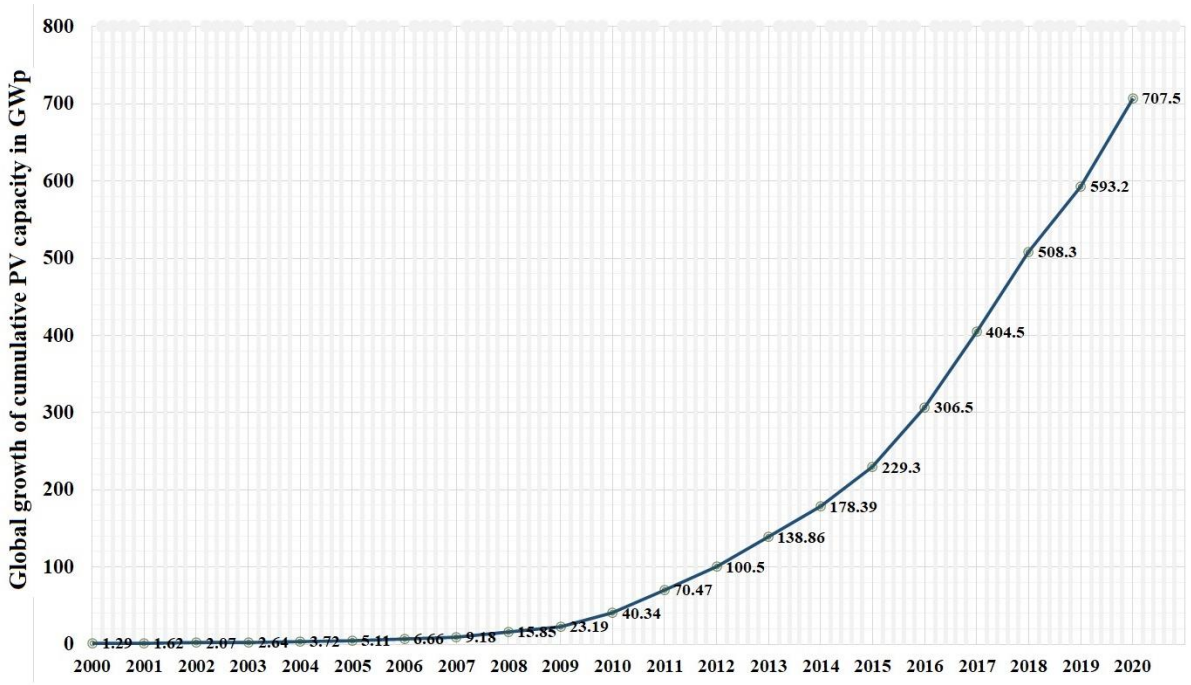

Figure 2.1: Cumulative PV capacity estimated growth worldwide.

On the other side of the world, notably in Asia, China and Japan are leading the solar energy market, even though Japan's solar PV industry is predicted to shrink by 9% in 2020 compared to 2019. However, China is predicted to build almost 33% more PV capacity in 2020 than it did in 2019. According to reports, China and Japan intend to build a total installed capacity of 200 GW by 2050 [1].

As a result, there are rising global expectations for energy production via PV panel energy systems, notwithstanding the challenges that come with this increased need for reliable and clean energy. Furthermore, due to the difficulty of reaching the mainline electricity connection, solar PV provides the possibility of increasing energy accessibility in poor regions or remote places by constructing off-grid systems, where a further cost reduction is a key focus with a high-power efficiency [34].

Moreover, over the last 40 years, PV panel prices have dropped exponentially at an average rate of about ten percent for per year [4]. Figure 2.2 shows a comparison of the increase in PV panel production with a notable decrease of the prices, where the solar module production increased from about 20 GW in 2010 to 140 GW in 2020. On the other hand, solar cell (multi-silicon module) prices dropped by 10% within ten years, from over $2 per watt to just over $0.20 per watt in 2020, according to Wood Mackenzie. One of the most important elements driving the global expansion of the use of PV cell energy is the 90 percent price decrease over the last few years. During this time period, no other electricity generation technology has been able to keep up with PV panel cost reductions.

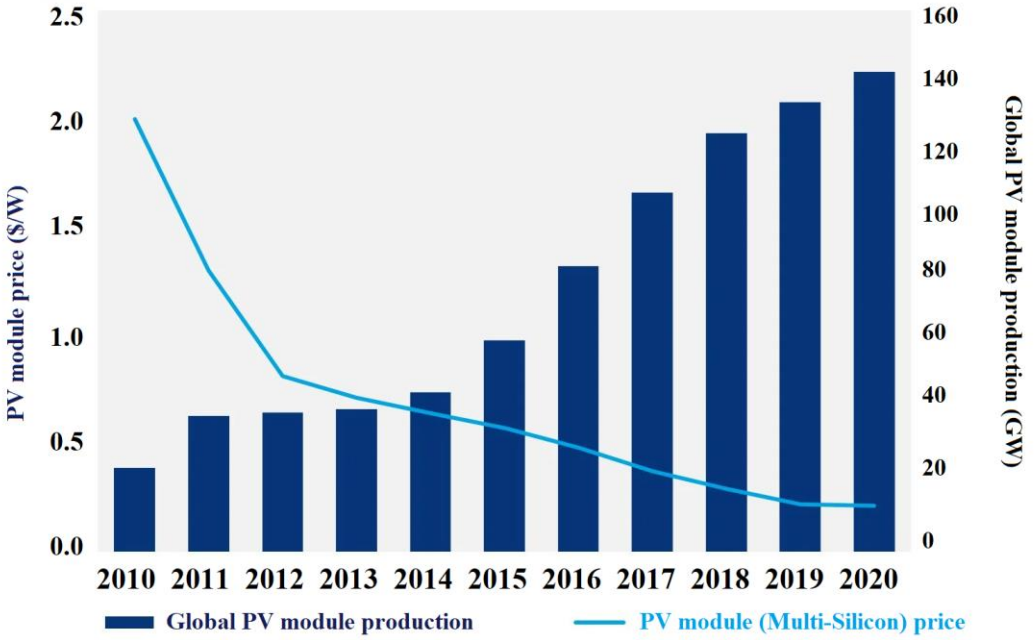

Figure 2.2: Global PV module manufacturing capacity versus module price for ten years between 2010-2020 [35].

As long as prices continue to fall, as Figure 2.2 shows, power converters that interact with PV panels must be developed in a highly efficient and cost-effective manner to properly manage PV energy. As a result, it is essential to examine the influence of power-converter-based grid connection PV applications in order to achieve high productivity and develop sophisticated control strategies that will help cost-effective PV systems become more widely used.

2.2 PV Cell Parameters

Photovoltaic cells are constructed in such a way as to take advantage of the photovoltaic effect, which means that when sunlight hits the PV panel's surface, the PV cells convert solar energy into electric energy. As of today, monocrystalline, polycrystalline, and amorphous silicon are the most commonly used materials for manufacturing solar cells [19]. Since one single cell power is limited, multiple cells are connected in series and parallel to build a higher-power PV array where modern panels modules typically included 72-96 cells connected in series with three to four bypass diodes connected over substrings of the panels [1]. When Solar-cells are connected in series and parallel; the output voltage and current flow increase correspondingly. Figure 2.3 depicts the behavior and characteristics of the current and voltage in an ideal PV module for a particular set of operating conditions, as specified by the current-voltage (*I-V*) characteristic curve [36]. A PV module *I-V* curve has a nonlinear behavior and is sensitive to such environmental influences as the temperature of the installed panels and the irradiation of light. To put it another way, this property fluctuates dramatically in response to changes in solar light and cell temperature

because the output current produced by each PV panel is mostly affected by solar radiation, whereas the terminal voltage is primarily affected by temperature.

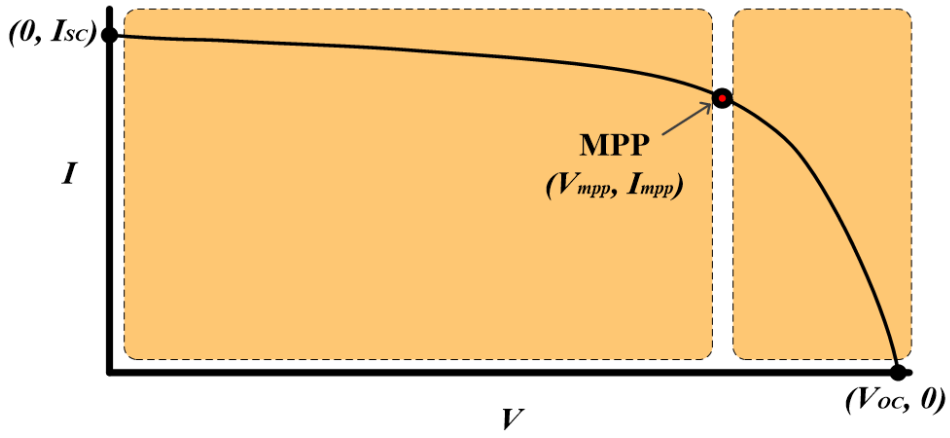

Figure 2.3: The *I-V* curve of a practical PV cell [36]**.**

The following parameters are used to describe a PV module:

1. Open-circuit voltage, V_{oc}: this voltage represents the maximum voltage produced from the cells in the PV module, which occurs when the net current through the device is zero.

2. Short-circuit current, I_{sc}: this current is the maximum current flow in a PV module cell and is measured when the voltage across the module terminals is zero.

3. Maximum power point, *MPP*: the maximum power point is the operating point on the *I* -*V* curve which yields the highest possible power output. The MPP can be measured by tracking the maximum value of the current and voltage produced through the PV module. The current and voltage at this point are referred to as the maximum current point I_{mpp} and the maximum voltage point V_{mpp}, respectively.

4. Mismatch losses: when the PV string connected the panels in series, the current in the string is restricted by the weakest cell in the string [37]. Thus, if the current of any single cell in the string is reduced by any cause as a hot-spot effect or partial shading, for example, the current is reduced for all the cells in the series connection. In addition, the weaker cell will dissipate some of the power, generating hot spots in the other cells, and this will cause heating and possible damage to the array if the error is not fixed [38]. Consequently, all the PV cells in a string should ideally be monitored and maintained periodically, also, if possible, to keep the work environment of the PV panels under the same conditions to prevent any possible damage between the cells in the same string and thus maximize efficiency. Mismatch losses can also occur due to physical imperfections in the cells. To limit the scope of the thesis, only mismatch losses caused by different irradiation will be considered. Furthermore, all cells in a string are considered to run at the same temperature.

5. Maximum power point tracking, MPPT: this represents a method to extract the maximum power from the PV module by tracking the produced voltage and current at their maximum values [39]. In fact, the PV cells should be controlled to continually operate on that point to extract all the available power in the module. From Figure 2.3, it is apparent that a PV module has a single maximum power point obtained from the multiplication of I_{mpp} by V_{mpp} for a given set of operating conditions.

2.3 PV Cell Modeling

Modeling the PV cell is important to better understand its functionality and the way it works under different conditions. The equivalent electric circuit model of the most commonly used model is the single-diode Rp-module PV cell, which is shown in Figure 2.4. There are many other models that have been proposed in [40], such as the Rs-module, and the two or three-diode modules, which include more parameters for their computation. Figure 2.4 also targets the ideal diode module, consisting of a current source and a diode. Thus, the presence of the shunt resistance, R_P, corresponds to the leakage from the diode *p-n* junction. The *I-V* curve is mathematically described by Equation (2.1), which leads to Equation (2.2):

$$I = I_{pv\_cell} - I_d - I_P \tag{2.1}$$

$$I = I_{pv\_cell} - I_O \left[exp\left(\frac{q\,(V + IR_S)}{a\,k\,T} \right) - 1 \right] - \frac{V + IR_S}{R_P} \tag{2.2}$$

where I_{pv_cell} is the current generated by the incident light (this value is proportional to the intensity of the radiation hitting the PV cell surface), I_d is the Shockley diode equation, I_o is the reverse saturation current of the diode, R_S represents the series resistor, T is the operating temperature of the PV cell, and a is the diode ideality constant or can represent the quality factor of the diode [36]; while k is the Boltzmann constant (1.380653×10^{-23} J/K), q is the absolute value of electron charge ($-1.60217646 \times 10^{-19}$ C), and R_S is the cell series resistance.

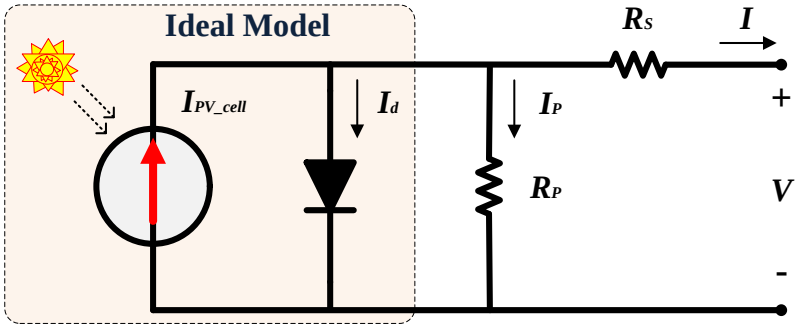

Figure 2.4: Equivalent electric structure of the single-diode Rp-model PV cell.

The two most important environmental factors that influence PV characteristics, and which also directly affect the produced voltage and current are solar irradiance incident on the PV surface, measured in (W/m^2), and cell temperature, measured in Celsius (°C).

Figure 2.5 describes the shape of the ideal PV cell output current I regarding the component (I_{pv_cell} - I_d), where I_{pv_cell} determines the vertical translation of the curve, while I_d defines the exponential shape.

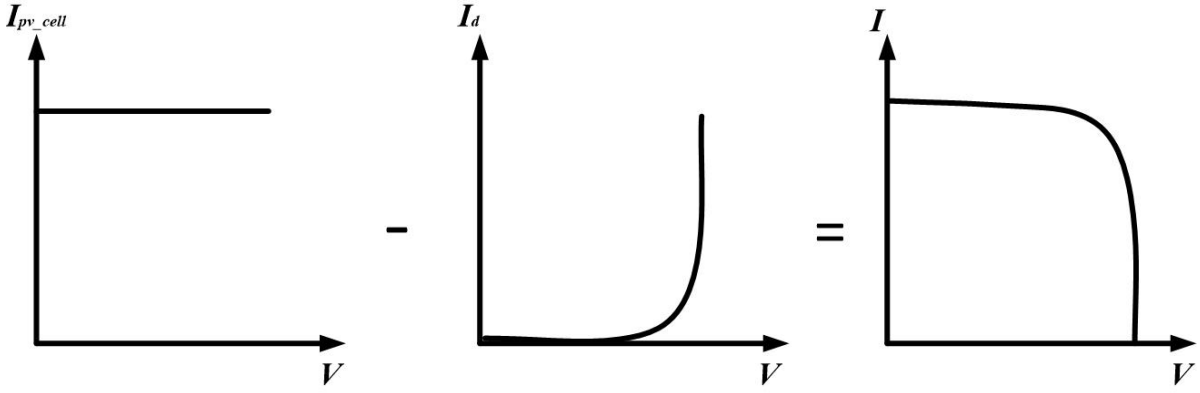

Figure 2.5: Decomposed characteristic *I-V* curve of PV cell. The net cell current (I) is composed of the light generated current (I_{pv}) and the diode current (I_d) [40].

2.4 PV Cell Converter Technology

Power converters for PV applications are power-dependent, with a maximum efficiency of 98.8% [8]. As a response, the design, control, and operation of the power electronic converters should be carefully considered in order to ensure a safe, stable, and effective energy conversion from PV panel systems. When it comes to the cost of PV energy, performance, efficiency, and reliability are the most essential factors to consider. PV systems usually consist of a set of PV panels connected to the load or grid system, as can be seen in Figure 2.6.

They are often made up of a pair of serially coupled power converters; first a DC-DC converter-based power optimizer that extracts the most energy from the panels, and then a DC/AC inverter that converts all the accessible power to an AC grid or AC load [8].

The DC voltage produced by the DC-DC converter is affected by the irradiance and temperature of the PV panels, but the DC voltage at the second inverter, measured at the capacitor in the middle of the two converters, is independent of the irradiance and temperature of the PV panels. The capacitor in the middle is often used at the DC-link to buffer the power imbalance between the DC and AC sides. It is positioned between the DC-DC converter and the DC/AC inverter, as can be seen in Figure 2.6.

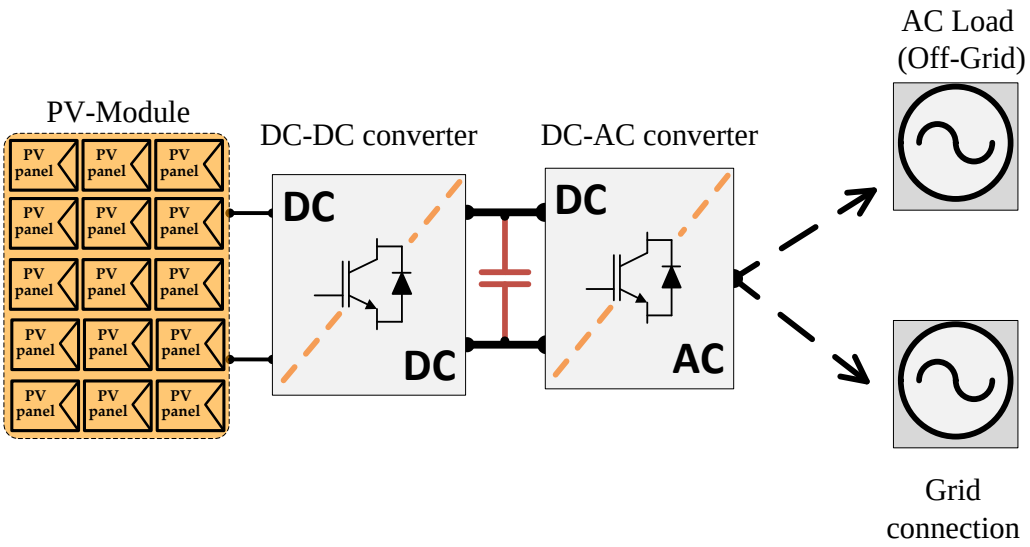

Figure 2.6: General structure of a PV module power converter.

Different types of DC-DC converters can be used for PV panels, including buck, boost, buck-boost, flyback, Cuk, and other converters. These converters have different connection topologies used for different voltage applications, some include a transformer for improved fault isolation, while others do not [41]. This thesis will concentrate on DC/AC inverter forms (as described in Chapter 3), primarily MMC converters.

The main power converters, represented by module inverters, string/multi-string inverters, and central inverters, are presented in the following section, covering a broad range of power ratings. In addition, a technology for a higher power converter is also presented.

2.4.1 Module Inverters

Each PV module is attached to a separate inverter in this configuration, and the maximum power is obtained from each PV panel as a result, since each inverter tracks the individual MPP, as can be seen in Figure 2.7. This configuration may be used when the operating points of the various modules vary significantly. However, it is more costly as each panel has its own DC-DC converter.

Module PV inverters are commonly used in low-power PV applications since they enable module-level monitoring and diagnostics [42]. As the module converter optimizes a single PV panel with an independent MPPT control, this topology minimizes the effects of partial shadowing and power mismatch. However, the average performance is lower and the efficiency is less when applied to central and string converters [1].

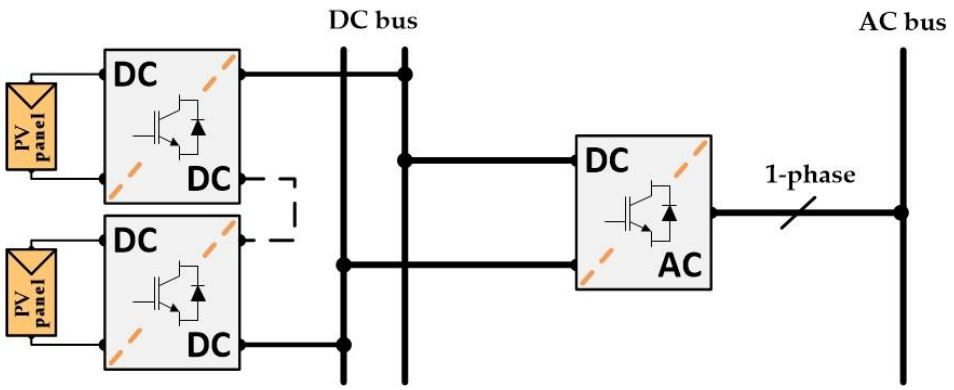

Figure 2.7: Module PV inverter configuration based on single-phase connection.

2.4.2 Multi-String Inverters

In this configuration, each string of PV panels connected in series is connected to a separate DC-DC converter before being connected to the central DC/AC inverter, as can be seen in Figure 2.8. Since MPPT is implemented independently on each string of the string/multi-string PV inverter, this individual DC-DC converter connection will potentially boost the MPPT power, resulting in better overall energy output [42]; nowadays, they represent a market share of 52% [3].

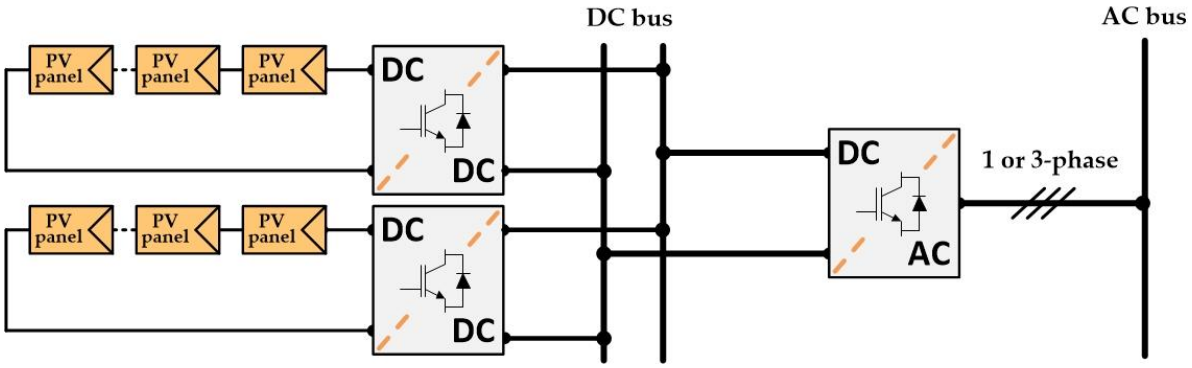

Figure 2.8: Multi-string PV inverter configuration based on single-phase or three-phase connection.

This topology, however, needs more power electronic converters and reactors, resulting in higher costs and losses, and there are still PV panel mismatches in each string.

2.4.3 Central Inverters

Central inverters represent a simple configuration connection as the PV panel strings, consisting of series of connected PV panels, are connected in parallel to obtain the desired output power as can be seen in Figure 2.9. This configuration is normally used in three-phase grid-connected PV plants larger than tens of kWp, with a market share of about 44% [3][10].

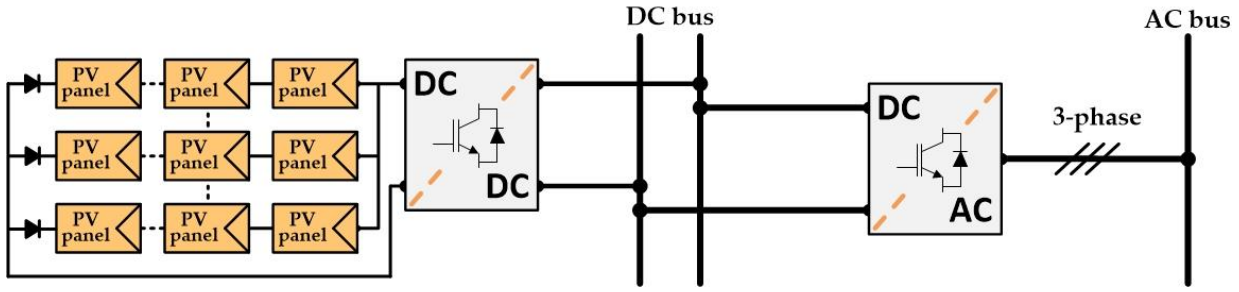

Figure 2.9: Central PV inverter configuration based on three-phase connection.

This technology generally achieves high productivity at a lower cost, yet it requires high-voltage DC cables [11] and uniform irradiance. Besides, the power mismatch issue is significant in this structure due to its low immunity to hotspots and partial shading, leading to a lower PV utilization.

2.4.4 High-Voltage Converters

On the one hand, there are problems with previous inverter technologies such as power mismatch, converter performance, power loss and increased cost. On the other hand, the problems reside in increasing the number of PV plants to meet high-power applications. Multilevel inverters, which run on more than three levels, should be improved to compensate for high voltage stress and efficiencies.

Modular converters, such as MMC, which were introduced in 2003 [14], can achieve any number of voltage levels due to the modularity of the converter topology. They also have a number of advantages over other multilevel topologies, including fault tolerance, capacitor voltage balance that is simple to achieve, low harmonic distortion, and the ability to remove the bulky DC capacitor [16][17]. Consequently, they have seen a rapid expansion in a variety of fields, including DC transmission, solid-state transformers, and renewable energy implementation.

The MMC are discussed in more depth in Chapters 4 and 5. Furthermore, a newly proposed topology, by integrating PV strings directly on the MMC converter cells, which has recently been proposed in [12][13], will be further investigated, analyzed, and simulated, with a new proposed modulation as part of the thesis developments.

2.5 Maximum Power Point Tracking Methods

Solar cells generate their MPP at a certain combination of voltage and current, depending on the cell temperature and solar irradiance that hits the cell surface, and even the irradiation angle affects the current generated by the PV cell [43][44]. The relationship between solar irradiance and temperature is proportional; as solar irradiance grows, the MPP current rises proportionally; as the cell temperature rises, the MPP voltage falls marginally, resulting in lower output power at the same input irradiance level [33]. It is thus considered that the effect of the changing solar irradiance is stronger and faster than the effect of the changing temperature.

Tracking the maximum power produced by the PV panels using MPPT algorithms is important for two reasons: first, to monitor the potential power generated by the PV panels in order to extract the maximum power; second, to monitor the power variation caused by the solar panel's power which is highly influenced by changes in the irradiation and temperature of the incident light.

Various strategies for tracking the MPP have been developed and suggested over the years. A total of 19 MPPT methods were investigated in [45][43]. The number of sensors needed, the complexity, cost, range of functionality, convergence speed, accurate monitoring under various mismatch losses, and the hardware associated with implementation, are just a few of the differences between these strategies. This information can be useful in determining the right method for a specific application.

MPPT techniques might be direct, indirect, or a combination of both [43][46]. This means that the MPPT can be monitored online or offline, depending on whether the PV panels are connected to a grid or supplying a load.

Hill Climbing (HC), Perturb and Observe (P&O), Incremental Conductance (InCond), Fractional Open-Circuit Voltage (FOCV), Fractional Short Circuit Current (FSCC), Curve Fitting, Look-up Table (LUT), Temperature, and Fuzzy Logic Control (FLC), are among the commonly used MPPT methods. Those methods are either direct and/or indirect in MPPT controllers, with some differences regarding the simplicity, efficiency, and execution time of each method.

The HC strategy introduces a perturbation in the duty ratio of the power converter and then observes the new power and compares it to the previous power level to determine the perturbation direction. Perturb and observe (P&O) and incremental conductance (InCond) are the most common HC methods. While the fuzzy logic control method, which is based on different work principles, is also common and does not need an accurate model, but it does require advanced user knowledge to set up the algorithm variables properly [45]. The FOCV, FSCC, Curve Fitting, LUT, and Temperature techniques are considered as indirect methods of tracking the MPP, as some PV features, such as material and/or electrical parameters at different irradiance and temperatures, are required before applying them.

In the next sub-section, these approaches are discussed further, including their benefits and drawbacks. Choosing those methods is comprehensible as they are the most generic algorithms capable of precisely detecting the MPPT under a variety of conditions [47]. The methods work

under uniform irradiance settings to describe the procedures clearly. It is assumed that all PV cells in the panel have the same cell temperature and irradiance.

2.5.1 Perturb and Observe Method

The Perturb and Observe (P&O) method, which is also called the hill-climb method based on how it is applied, is one of the most frequently used MMPT algorithms for the high-quality MPPT findings in practice. Figure 2.10 illustrates the procedure for determining the MPPT, in which the controller perturbs the system by marginally adjusting its operating point. It then observes the current power and compares it to the previous power level to decide the perturbation direction for the next step. More precisely, if the comparison indicates a power boost, as seen in Figure 2.10(a), the P&O algorithm keeps perturbing in the same direction, but if the power decreases, this means that the MPP has been exceeded and the P&O algorithm reverses the perturbation, as seen in Figure 2.10(b).

The P&O MPPT algorithm is illustrated in Figure 2.11 as a simple flow chart. The algorithm perturbation variables may be dependent on the duty ratio of the converter controlling the PV panel, or on a converter voltage reference value. If a reference value is used, that is either the PV input current or voltage, then this requires the use of a regulator to ensure that the converter retains a stable operation while providing the maximum amount of energy at the stated reference.

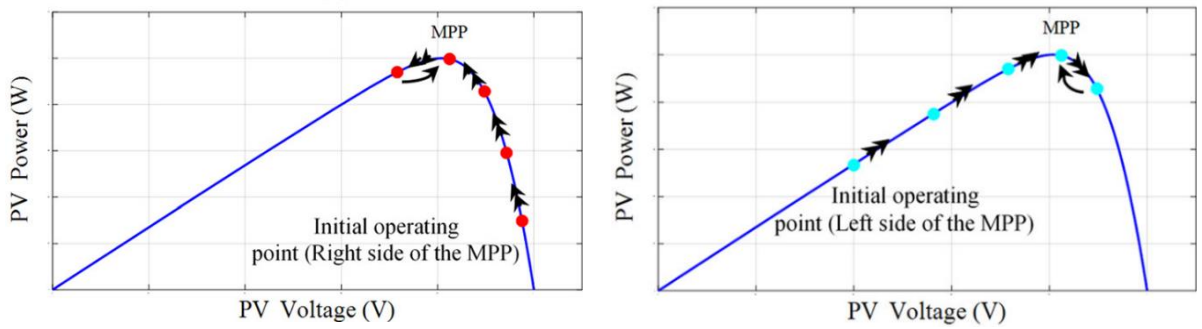

(a) (b)

Figure 2.10: The *P-V* characteristics of the PV operating points using the P&O algorithm. (a) The perturbation attempts to reach the MPP when the voltage reference is less than the voltage at the MPP point; (b) the perturbation attempts to reach the MPP when the voltage reference is higher than the voltage at the MPP point [48].

The operation point will still move toward the higher power point in a typical P&O MPPT, but if it hits the MPP, it will begin to oscillate at the MPP. This means that the procedure does not always operate at the exact MPP, resulting in power losses relative to the scale perturbation's movement. In fact, both the PV current and voltage must be measured since the PV power must be calibrated periodically in the P&O MPPT algorithm, and this requires both voltage and current sensor circuitry, which increases costs and takes up space on the hardware panel.

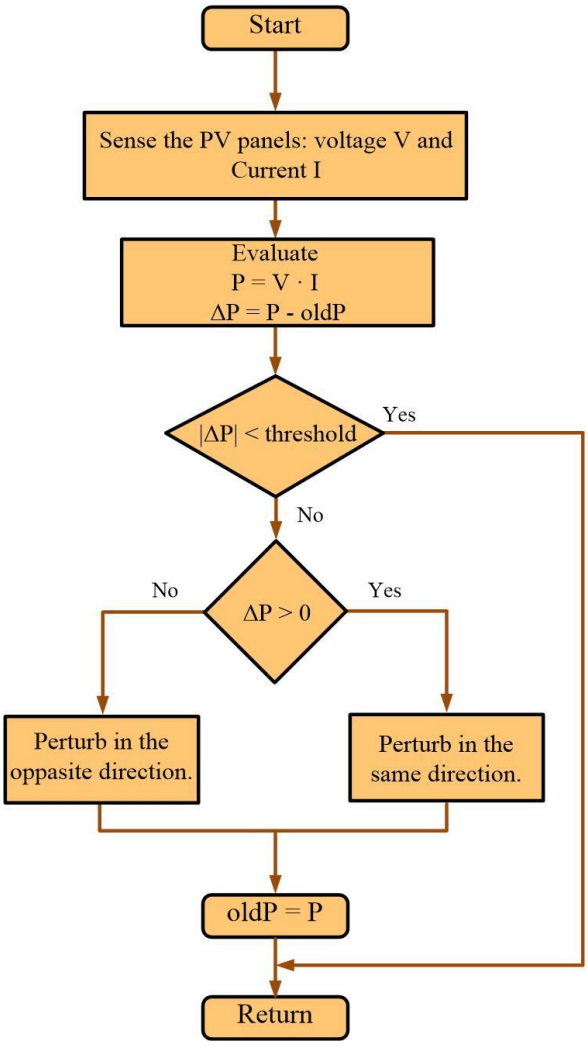

Figure 2.11: Flowchart of the P&O algorithm.

Lastly, the P&O algorithm will lose MPP monitoring in the case of rapidly changing irradiance conditions [49], depending on the perturbation steps. Even so, it is a simple and effective power optimization algorithm for PV systems in steady-state operation.

2.5.2 Incremental Conductance Method

The Incremental Conductance (InCond) process, the second well-known MPPT algorithm, claims to boost the P&O by contrasting the PV array's instantaneous (*I/V*) and incremental (*dI/dV*) conductance instead of the derivative of the power versus voltage *dP/dV* used by the P&O [49][50]. In Figure 2.12, the slope of the curve power versus voltage (current) of the PV module is zero at the MPP, positive (negative) on the left of the MPP, and negative (positive) on the right of the MPP as follows:

$dP/dV = 0$, or ($dP/dI = 0$) at the MPP.

dP/dV > 0, or ($dP/dI < 0$) on the left.

$dP/dV < 0$, or ($dP/dI > 0$) on the right.

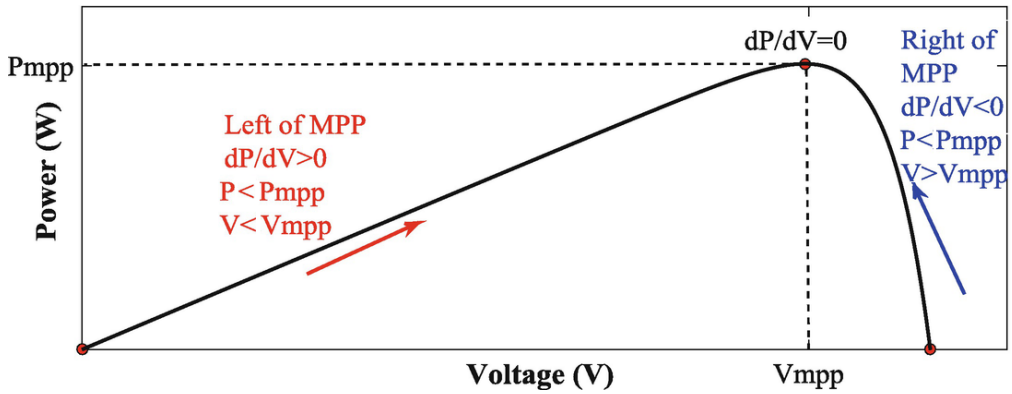

Figure 2.12: The *P-V* curve characteristics of the PV operating points using InCond algorithm [50].

The change in the MPP voltage can be determined using a method that compares the increase of power versus the increment of voltage between two successive intervals. Thus, the InCond method has better sensitivity than the P&O in terms of solar irradiance change, because the method can find how long far from the MPP depends on the ratio of the power derivative over the voltage derivative.

Both InCond and P&O have two major drawbacks. The first and most important is that if the irradiation varies quickly, they easily lose track of the MPP [51][52]; especially when the irradiance is not uniform, since the curve on which the algorithms are based changes continuously. As a result, the algorithms are unable to decide if the power shift is due to its own voltage increment or to a change in irradiation. The second drawback is the oscillations of the voltage and current around the MPP in the steady-state [53]. This is due to the control in the frequency domain while the voltage and current are changing in the time domain and there is no constant value at the MPP, so the controller oscillates back and forth. Therefore, the easiest solution to reduce the oscillation is to perturb in very small steps so that, the oscillations decrease. The MPP is then reached slowly, but accurately.

By adding an external calculation element, a modified P&O has been proposed in [51] and [52] to increase the process outcomes in terms of rapid change in irradiation conditions. In addition, a variable perturbation step for the P&O algorithm to solve the oscillation problem around MPP was introduced in [53].

2.5.3 Fractional Open-Circuit Voltage Method

The Fractional Open-Circuit Voltage (FOCV) algorithm, also known as the constant voltage method, is the most basic MPPT control method. It is considered an indirect or offline strategy, since it requires the PV electrical parameters to be known ahead of time in order to track the MPP [43].

The FOCV approach relies on a roughly proportionate relationship between the V_{oc} and the V_{mpp} [54][55]. It maintains that the most significant elements that might impact the PV solar cell are the irradiance level variation and the temperature. To keep the voltage at the MPP constant, Equation (2.3) is used to create a proportional controller:

$$V_{mpp} = k \cdot V_{OC} \tag{2.3}$$

where *k* is a proportionality constant. Since *k* depends on the solar cell technology and atmospheric conditions, it must be calculated beforehand determining both V_{oc} and V_{mpp} in different conditions of irradiance and temperature [43]. Approximately, *k* varies between 0.71 and 0.8 for polycrystalline PV panels. The common value used is 0.76; hence this algorithm is also called the "76% algorithm" [56]. Nevertheless, it can reach values of about 0.9, depending on the *I-V* curve characteristics of the PV panel module.

As a result, the voltage at MPP may be determined by measuring the V_{oc}, while disconnecting the PV system for a fraction of a second and applying Equation (2.3). According to [57], the V_{oc} is intended to remain generally constant throughout a wide range of irradiance and temperature levels. Finally, the MPPT controller changes the converter's duty ratio [58]. The FOCV method is shown in Figure 2.13 as a complete method for determining the MPPT [59].

Due to the fact that Equation (2.3) is only an estimate [43], this approach does not offer genuine MPP. Furthermore, according to [55][60], it is not accurate under partial shade. Finally, the V_{oc} is determined by making an open circuit when the load is disconnected for a fraction of a second. As a result of the power loss [55], modified open-circuit voltage methods have been advanced.

However, this technique has the benefit of being simple to implement while also requiring minimal costs, because no complex embedded systems like microcontrollers or fast processors, are required [43][55]. As a result, because it is not a precise method, it is used when accuracy is not a concern. It is also a quick technique that does not require a lot of sensors [58], which is means a low cost. Finally, [45] claims that the FOCV method is more successful in low-irradiance circumstances.

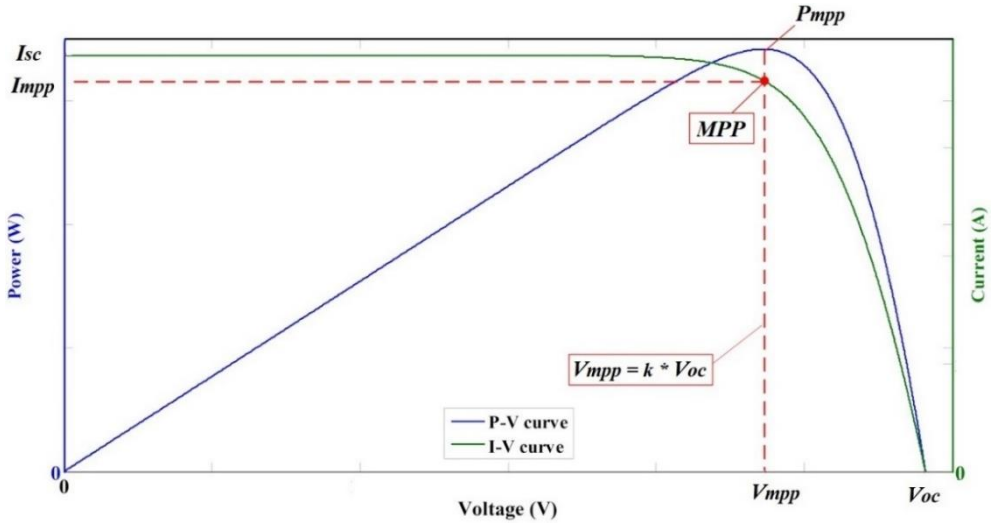

Figure 2.13: The *P-V* curve and *I-V* curve characteristics of the PV operating points using the FOCV method [59]**.**

2.5.4 Fractional Short-Circuit Current Method

The Fractional Short-Circuit Current (FSCC) algorithm uses the same technique as the FOCV, but instead of V_{oc} and V_{mpp}, it uses an approximate linear relationship between the short-circuit current (I_{sc}) and the current at the MPP (I_{mpp}). As shown in Equation (2.4), this is also implemented under different atmospheric circumstances [43][61].

$$I_{mpp} = k \cdot I_{SC} \tag{2.4}$$

The proportional constant *k* varies depending on the PV panel. The value of *k*, according to [62] [54], varies between 0.78 and 0.92, and it is difficult to determine the exact value for the best results. Other studies, however, suggest a broader range between 0.7 and 0.9 for accurate calculation, depending on the cell technology [58].

As a result, the current at MPP may be determined by measuring I_{sc} and using Equation (2.4), in the same manner as the V_{oc} can be determined using the FOCV method. If the duty ratio is controlled, then the pulses of the converter switch can be used to measure I_{sc} [62]. A current feedback loop is used to regulate the desired current until the I_{mpp} is reached [62]. The main advantage of the FSCC technique is that it is simple to use and is suitable for MPP tracking applications that do not require extreme precision [55]. Figure 2.14 shows a comprehensive explanation for calculating the MPPT with the fractional short-circuit current method.

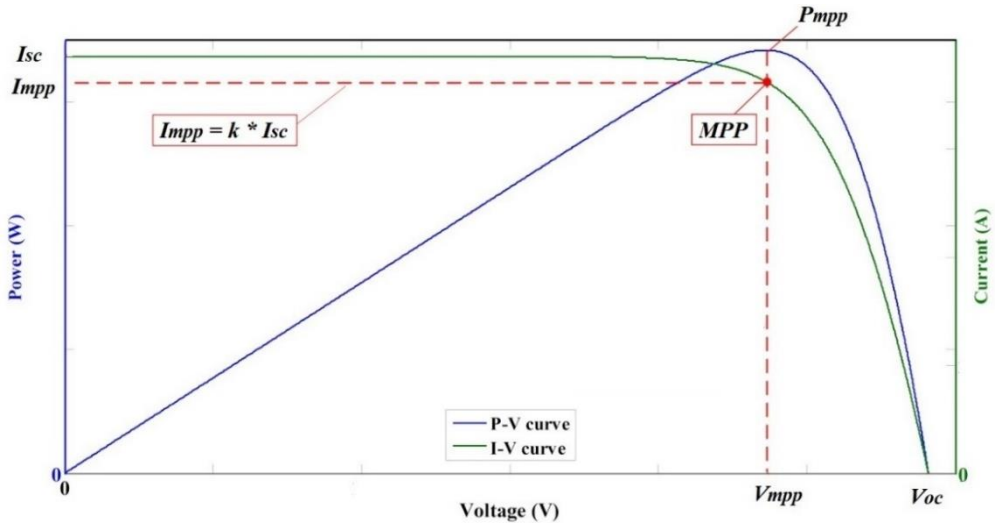

Figure 2.14: The *P-V* curve and *I-V* curve characteristics of the PV operating points using the FSCC method [59].

However, because Equation (2.4) is an estimation identical to that of the FOCV method in Equation (2.3), this methodology does not produce an exact MPP. Nonetheless, [57] claims that this method is more accurate than the FOCV technique because of practical issues with measuring the ISC. The fact that the current is more sensitive to changes in irradiance than the voltage is due to the fact that the latter is affected by temperature more than current, but the irradiance impact on the PV cell is typically quicker. To monitor the PV panel short-circuit current, a short-circuit switch and a high-sensitivity current sensor are required [55][63]. As a result, more units are required, resulting in higher prices and power losses.

Finally, partial shading can cause problems, since changes in the irradiance produce multiple local maximum power points. Therefore, the proportional gain k is updated periodically by sweeping the PV voltage from the open circuit to short-circuit for a better efficiency tracking the MPP and avoiding loss of power [62][63].

The FOCV and FSCC techniques fail to give maximum output power to the load for two reasons. The first is that the load interruption occurs during the I_{sc} or V_{oc} measurement, and the second is that the MPP can never be accurately tracked using these methods in the first place, as stated by Equations (2.3) or (2.4). In fact, these two approaches are just estimated MPPT methods; however, they are suitable for use in creative hybrid methods because of their simplicity and ease of implementation [57].

2.5.5 Curve Fitting Method

The Curve Fitting method represents an easy method with little complex mathematical calculation that can be considered an indirect technique, since it needs practical measurements for different situations of the *P-V* curve characteristics to build data for tracking the MPP accurately [55][58].

Essentially, this technique entails predicting the PV array characteristic curve and calculating the MPP as the maximum of that curve [55][54]. The nonlinear characteristic curve of the PV array is first modeled off-line using a polynomial function. The precision with which the curve can be estimated is determined by the degree of the selected polynomial function [43]. Generally, higher degree polynomials offer more exact calculations, but they also add complexity and make the process slower. A third-degree polynomial is employed in [61], as illustrated in Equation (2.5):

$$P_{pv}(V_{pv}) = a_1 \cdot V_{pv}^3 + a_2 \cdot V_{pv}^3 + a_3 \cdot V_{pv}^3 + a_4 \tag{2.5}$$

where a_1, a_2, a_3 and a_4 are the coefficients of this polynomial function, and V_{pv} is the voltage of the PV array. Thus, four equations must be constructed to obtain these coefficients, depending on the PV module current, voltage, and power changes regarding the experimental measurement under different solar irradiance and temperatures. The MPP is then determined using the polynomial coefficients in Equation (2.5) to obtain the maximum voltage, as illustrated in Equation (2.6) [61]. At the maximum voltage V_{mpp}, the dP_{pv} / dV_{pv} is equal to zero.

$$V_{mpp} = \frac{-a_2 \pm \sqrt{a_2^2 - 3 \cdot a_1 \cdot a_3}}{3 \cdot a_1} \tag{2.6}$$

One advantage of this method is its simplicity; even if the calculations are a little complicated, there will be no extra cost added to the process. However, there are certain drawbacks, such as the requirement for a prior understanding of PV electrical characteristics. Furthermore, fluctuations in atmospheric conditions are not taken into account in the simplified form, which might cause changes in the PV properties [58].

2.5.6 Look-up Table Method

The Look-up Table (LUT) method is considered an indirect MPPT method because a map of the PV cell module related to the *I-V* curve characteristic must be stored in the memory before starting to apply this method [64]. This means that, before it can be used, PV electrical properties at various temperatures and irradiances are required [58].

Essentially, the LUT method entails calculating multiple MPP at various irradiances and temperatures in the region where the PV panels are mounted and then storing all the data in the memory of the control system used to track the MPP [43]. Then, the V_{pv} and I_{pv} are measured in order to calculate the P_{pv}, which is then compared to the MPP corresponding to the current atmospheric irradiance and temperature circumstances [54][58].

Finally, because the PV panels are typically connected to a booster DC/DC converter, the duty ratio of the booster is adjusted by a PI controller to get the MPP [64]. Consequently, a benefit of the LUT approach is that it offers fast and accurate results under changing environmental conditions, but the accuracy is highly dependent on the information stored earlier under different environmental conditions [55].

However, because this tracking technology is applied to a specific PV system and requires prior knowledge of the datasheet of the PV module used in the system to be installed, a large memory is necessary for improved method efficiency [55][64]. This is not an important issue right now, because memory costs have decreased dramatically in recent decades, and increasing memory capacity will increase the prior information needed for calculating and tracking the MPP under various situations, thereby improving the accuracy of the LUT method [54].

2.5.7 Temperature Method

The Temperature method is one of the indirect simple methods for tracking the MPP, where, as previously said, the irradiance and temperature are the most essential conditions that affect the power produced by the solar cell. Whereas the short circuit current fluctuates with variations in irradiance, the temperature impact has a greater influence on the open circuit voltage [43].

As a result, because the V_{mpp} is directly proportional to the V_{oc}, as stated in the FOCV technique explanation, it is likewise affected by temperature. Consequently, the MPPT Temperature method is based on the temperature dependency that V_{mpp} exhibits [54]. As a result, the PV temperature is monitored, and Equation (2.7) is used to perform this procedure [65]:

$$V_{mpp}(t) = V_{mpp}(T_{ref}) + T_{Kvoc} \cdot (T - T_{ref}) \tag{2.7}$$

where T_{ref} is the standard test conditions temperature, T is the measured working PV temperature and T_{Kvoc} is the temperature coefficient computed from the PV cell data and the experiments [65]. Thus, the MPPT can be fulfilled regardless of temperature fluctuations, and a highly efficient temperature sensor is used to improve MPPT performance.

This method has the benefit of being simple to construct and inexpensive [54] due to the low cost of temperature sensors. However, because of the uneven temperature distribution of the PV cell and the sensor calibration error, the temperature reading may be inaccurate. In small PV converters, however, the inconsistency may be eliminated [43][65].

2.5.8 Fuzzy Logic Control Method

The Fuzzy Logic Control (FLC) method is one of the most used MPPT methods, according to [43][66]. The FLC method can be classified as an indirect or direct method, and it is also categorized as a soft computing technique [54].

The FLC controller, as shown in Figure 2.15, consists of three process blocks: Fuzzification, Fuzzy Inference Rules, and Defuzzification [62][66]. The following is an explanation of the FLC blocks, which have a direct impact on the controller's effectiveness:

- Fuzzification: this block represents the initial block, which takes input variables in realistic domain format and transforms them into linguistic variables. Typically, the input variables of the controller are the error (E) computed according to Equation (2.11), where P_{pv}, the instantaneous output power from a PV system, can be estimated using Equation (2.8), and the difference between every two consecutive powers and voltages may be calculated using Equations (2.9) and (2.10), respectively, where I_{pv} and V_{pv} are the PV system's current and voltage, respectively, and k denotes the sampling instant; while the error variation (ΔE) is given by Equation (2.12) [66][67]. The calculated error E shows the operating point of the PV system with respect to the MPP, where it would be zero ($\Delta P/\Delta V = 0$) at the MPP, because based on the fact that the MPP point is located at the top position of the power curve with respect to the PV voltage, and its variation shows how this point moves in the *P-V* curve [67], where the input linguistic variable of the instantaneous error *E(k)* is represented by the following five levels: NB (Negative Big), NS (Negative Small), ZE (Zero), PS (Positive Small), and PB (Positive Big). The input linguistic variable of the error change ΔE, however, is represented by three levels: NS (Negative Small), ZE (Zero), and PS (Positive Small). The output linguistic variable names are designed by five changes in the duty cycle level ΔD: NB (Negative Big), NS (Negative Small), ZE (Zero), PS (Positive Small), and PB (Positive Big) change [66].

$$\Delta P_{pv}(k) = P_{pv}(k) + P_{pv}(k-1) \tag{2.9}$$

$$\Delta V_{pv}(k) = V_{pv}(k) + V_{pv}(k-1) \tag{2.10}$$

$$E(k) = \frac{\Delta P_{pv}(k)}{\Delta V_{pv}(k)} \tag{2.11}$$

$$\Delta E(k) = E(k) + E(k-1) \tag{2.12}$$

- Fuzzy Inference Rules: this second block is designed using the Mamdani technique, which comprises the specified inference rules used to ensure a fast-tracking function of the proposed controller to the maximum power that the photovoltaic system can extract [66]. These block entries are the linguistic variables of the error, and their variation is responsible for implementing the rule-based table that defines the behavior of the controller [43]. The controller output is a linguistic variable that defines the duty ratio of the converter which iteratively makes the error tend to zero.

- Defuzzification: this block produces the realistic value of the change in the duty cycle *ΔD* based on the center of gravity method. The membership functions are applied to obtain a numerical output value. Based on the principle of the PWM strategy, controlling *D* controls the instantaneous value of the converter output voltage. Indeed, the FLC will decide the additional value change in the duty cycle *ΔD* to the initial constant duty cycle *D* by evaluating the instantaneous values and the trends of the input variables to the controller [68].

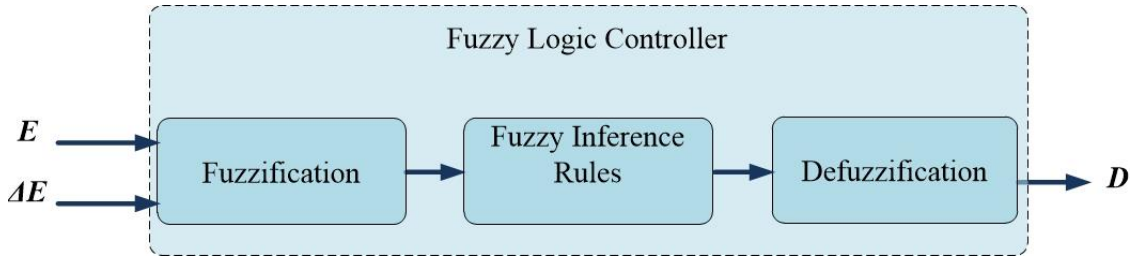

Figure 2.15: The main process blocks of the FLC method.

As a result, the FLC technique is useful for working with inaccurate entries, nonlinear systems, or systems without a precise mathematical model [43], and it is reasonably easy to develop [67]. It thus offers quick control and minimal oscillations once the MPP is attained, as well as a strong performance under changing irradiance [67][68]. However, it has the drawback of providing estimated outputs based on a trial-and-error method, which may be time-consuming when developing membership functions and inference rules [43][57].

2.6 Photovoltaic Applications

With the need for electricity growing in recent years, PV systems are being used in several applications, which can be classified into two categories: low-power applications, which are usually off-grid, and high-power applications, which are typically grid-connected, as can be seen in the PV panel connection shown in Figure 2.16.

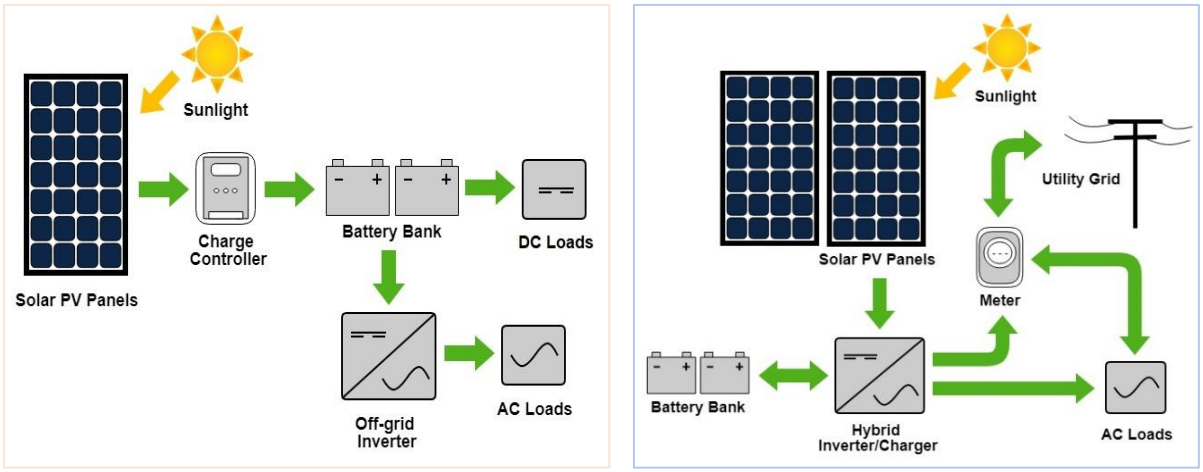

(a) (b)

Figure 2.16: PV power system connection. (a) Off-grid connection. (b) On-grid connection.

As shown in Figure 2.16(a), the off-grid application normally feeds a small system with energy, such as small rooftop PV units feeding remote houses or cottages and even some small DC appliances, such as toys, watches, calculators, radios, televisions, flashlights, and fans, can be directly connected to the DC power equipment. A battery storage system is used to store the energy and function as a backup power source when the need arises at night or when there is poor sunlight due to shadowing. In other cases, stand-alone systems rely on conventional generators for backup.

There are numerous applications of low-power PV systems, electricity for remote areas, disaster relief, water pumping and charging vehicle batteries, etc. On the other hand, in Figure 2.16(b), PV modules are connected to inverters that convert the DC power produced by the PV modules to the AC power in the grid-connected PV systems. Thus, connecting to the grid increases the system requirements in terms of connection synchronization, efficient power converters, high-performance MPPT as mentioned before and, a backup system is frequently required to ensure a continuous supply of electricity irrespective of the weather conditions by connecting batteries for saving power in the night, etc. Different applications are discussed in the following section for a better understanding of the importance of PV panels applications.

2.6.1 Disaster Relief and Remote Areas

Portable PV panel systems are easy to install, small, easy to move, and are commonly used to provide electricity in the aftermath of a disaster or provide services to remote areas in the absence of an electric grid.

Natural disasters frequently result in a power outage. As a result of natural catastrophes such as storms, floods, cyclones, and earthquakes, power generating, and distribution networks are destroyed. Portable PV systems can provide interim solutions for building light, and water systems in instances like these, where power will be off for a lengthy period, see Figure 2.17. Furthermore, because renewable energy eliminates the problems of fuel transportation and pollution, emergency health clinics prefer solar-powered electricity over traditional systems [69].

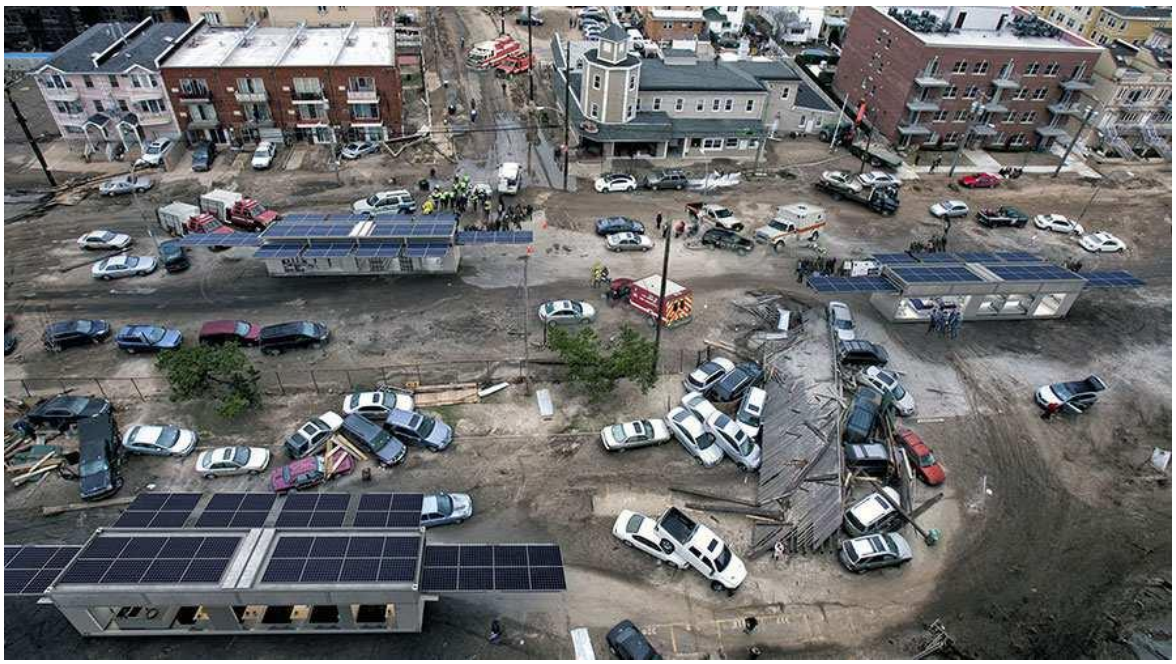

Figure 2.17: The power PV systems powering area struck by a natural disaster [70].

Moreover, some regions are too far away from the distribution network to connect to the grid. Before they may be linked, areas under development require a power source. PV systems are a viable choice in these situations. PV systems can also be backed up by conventional generators to ensure that power is available at all times.

2.6.2 Communication and Tele-Communication Power Backup System

Different communication systems require power 24/7 in many places, particularly in rural areas, and signals require amplification stations at intervals for long-distance connection for some communication systems. To improve radio, television, internet, and mobile phone transmissions, a number of relay towers have been erected. Repeater stations are most commonly located on high terrain. These locations are often located far away from grid-connection lines. PV systems with a backup battery are being deployed as a feasible alternative to generators to lessen the associated complexity and cost.

2.6.3 Scientific and Research Centers

Scientific experiments are set up in a variety of locations that are not connected to the electrical grid. PV systems may be used to provide electricity for scientific research in rural areas and remote locations. PV systems may power systems that monitor earthquake activity, roadway conditions, meteorological data, and other research operations. Nonetheless, navigational devices such as beacons, traffic warning signs, and airplane warning signals can be located far from the electric grid. PV systems can provide a stable power supply for these critical applications.

2.6.4 Water Pumping

PV panels are a fantastic option for agricultural and farm water demands, particularly during seasons of strong sunshine. These pumping systems may either give water directly to fields in times of need or store water in big tanks for later use. Additionally, it may offer water to isolated places and villages, as well as storing water in case of need [71].

Figure 2.18 depicts the ESSENSE company solar water pumping system, which is powered by a PV panel system [72].

Solar energy is converted into electricity by the photovoltaic array, which is used to power the motor pump set. Water is drawn from an open well, a bore well, a stream, a pond, or a canal via the pumping system. PV panels must be placed in an open location with sufficient irradiance to improve the energy system’s performance.

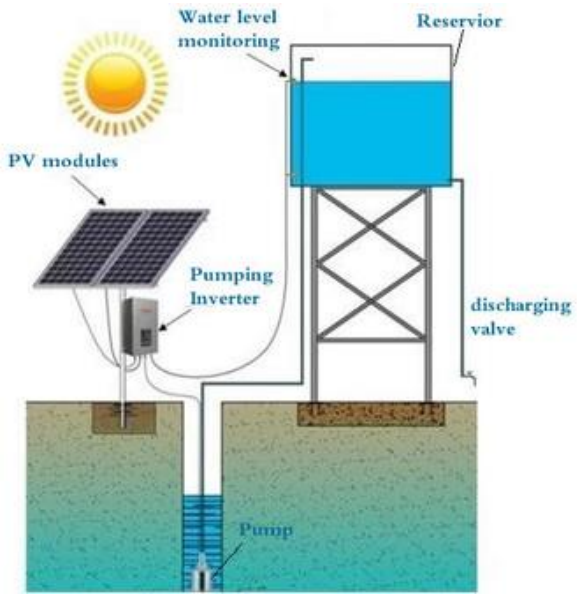

Figure 2.18: Solar-powered water pumps can be incredibly cost-effective for remote settlements [72]**.**

2.6.5 Charging Electric Automobiles

Vehicles that operate on electricity can be charged at solar-powered charging stations. These vehicles can also use PV-powered sources to maintain their key battery conditions. Electric vehicles are a wonderful way to enjoy your ride without the expensive cost or negative environmental effects associated with gas-powered engines.

Figure 2.19 shows a charging kit that enables users to increase their flexibility by installing a charging station in the works car park, or even in commercial lots, that is powered entirely by renewable energy [73]. PV systems can also be used to charge other types of transportation, such as boats and other recreational vehicles.

The massive amount of research that has been done over the last few decades has sparked a surge in interest in putting PV systems in place to meet energy demands. Instead of putting up separate support structures, PV systems can be installed directly on the building structure, saving space. PV systems come in a variety of sizes and may be installed on practically any surface, with different shapes to capture solar energy and provide clean and steady energy. The installation of PV panels on a building's exterior is known as Building Integrated Photovoltaics (BIPV) [74][75].

Figure 2.19: Solar charging stations for electric vehicles [73].

3

Multilevel Converters

Contents of This Chapter

- **Section 3.1** introduces the general multi-level converter of the different applications and explains the fundamental operating principles.
- **Section 3.2** presents the benefits of increasing the levels of voltage conversion.
- **Section 3.3** introduces the basic work of line commutated converters as two-level converters and highlights the drawbacks over high voltage applications.
- **Section 3.4** explains different topologies of voltage source converter to demonstrate the impact of increasing the voltage stages over high power transmission applications.

3.1 Introduction

The aim of this chapter is to clarify and bring into perspective the circuit topology and the function of different multilevel converters. For this reason, the chapter begins with an introduction to the evolution of different types of the two-level converter and multi-level converter. An analysis of the line commutated converter (LCC) and the various topologies for the voltage source converter (VSC) has also been presented. It acts as the basis for an MMC analysis and research which is discussed in depth in the next chapter.

Before the 1970s, the transfer of power relied heavily on current source converters (CSC) where the alternating current (AC) was converted to direct current (DC). Rectification, to provide direct voltage for DC motors and industrial processes, was the key application. High-voltage direct current (HVDC) transfer of electricity also initially made use of CSCs [76]. The valves then available, first mercury arc valves and later thyristors, lacked the capacity to turn off and were thus only suitable for naturally switched converters.

The beginning of power semiconductors that could be switched on and off (such as diodes) and full control switches (such as transistors), allowing for forced current commutation, paved the way for VSCs that would work independently off the AC grid. These converters provide enhanced controllability and enhanced harmonic efficiency, which have significantly extended the field of operation.

Several new problems in terms of energy conversion have arisen with various applications over the last few decades. The focus here is on green energies and questions about the harmful effects of conventional energy sources on the atmosphere, such as the burning of oil or fossil fuels, thus contributing to the use of cleaner sources such as wind and solar power as renewable energy sources (RES). None of these use the kind of large synchronous generators typically used for electricity generation that run at constant speed [77]. There is also a need for an electronic power interface, which is better introduced by VSC in most situations. Demands for energy conservation have also arisen from related issues. A transition to variable-speed control inside electrical drive systems would yield very considerable savings.

In earlier times, application work on motors, such as water pumps and fans, were typically run at a constant speed, with the fluid flow controlled by throttling, which caused performance at low flow rates to be very weak. If the electric machine's speed can be controlled, total power losses can be dramatically reduced. In addition, in many manufacturing processes, variable speed processing facilitates better control and accuracy, leading to increased automation and improved product quality. As it allows for easy torque and speed control of both synchronous and induction machines, the VSC suits these specifications very well. CSCs could control the speed of DC motors; however, because of the high maintenance expense of their brushes and commutators, such motors are less desirable [78].

Furthermore, due to the independently controlled active and reactive power, the VSC does not require reactive power adjustment, especially in the high voltage transmission grid applications such as HVDC and FACTS (flexible alternating current transmission systems). This allows the VSC to have greater overhead in comparison to the LCC converter [79][80]. As a result, the VSC

is more concise than an LCC station, since the harmonic filters at the output are smaller and no switch yards or transformers are required [79][81].

The two-level converter was the dominant VSC topology from the beginning but, due to the high losses, it is dedicated to applications of a few kilowatts. However, it is less effective for devices operating at voltages above a few kilovolts, since no power semiconductors are available that can block voltages beyond this amount. In order to build valves capable of resisting higher voltages, an alternative is to directly link semiconductor elements in a series. These principles have been developed, but they appear to be complicated because it is important to solve many problems to guarantee the operation and fault tolerance of such a valve [79]. Furthermore, this kind of valves cost more money and are more complex to control.

As an alternative, a move to multilevel converter topologies provides improved opportunities for higher voltages to provide cost-effective power transfer. To increase the operating voltage, such topologies do not need direct series connection. In addition, the overall total harmonic distortion (THD) is strongly improved, such that the voltage and current distortion requirements can be fulfilled without excessive switching losses and, of course, the filter can be minimal or it may even be eliminated at some stage [82].

The two and three stage neutral point clamped (NPC) converter was the first VSC multilevel topology to be used in a large-scale voltage application [83]. A flying capacitor converter (FLC) was then proposed to decrease the switching losses as well. For high-power engine drives, it is still in frequent use [84].

However, the voltage level cannot easily be expanded to additional levels due to the complexity of the converter design, which restricts the area of operation to the medium voltage range, at least if the semiconductor series link is not used to improve the voltage power. Using a cascaded half-bridge (CHB) converter, based on the serial connection of converter sub-modules rather than semiconductors for high-voltage operation, is a much more feasible solution and much simpler in terms of connection complexity to increase the voltage level [79][84].

This chapter aims to understand the development of multilevel VSC topologies for high and middle power conversion with a heavy emphasis on MMCs, as these are the key focus of the implementation of this thesis. First, as state-of-the-art, the LCC will be introduced to illustrate the benefits of the converter application, and then the multi-level VSC will be defined by demonstrating various forms of topologies.

3.2 Multilevel Converter Benefits

Two-level converters are generally the most cost-effective option for low power ratings, up to megawatts. They have a simple structure with a few elements that reduce the complexity of the controller. However, a variety of drawbacks are apparent for such applications as medium or large industrial drives, such as wind turbines and solar cell farms for grid connection, where a medium or high voltage needs to be highly regulated and stored. Due to the switching frequency, the converter output represented as AC-side voltages will include high major harmonic

components [83]. Any suggested alternatives, such as metal oxide semiconductor field effect transistors (MOSFETs), with high switching frequency low-voltage power semiconductors, can be used in converters to alleviate this problem, as low-order harmonics can dramatically decrease and only high-order harmonics can emerge in the spectrum. In contrast, for a converter in transmission line applications, such devices as insulated gate bipolar transistors (IGBTs) that work with kilovolts of blocking voltage are usually required. Due to switching and conduction losses, each switching of such devices usually results in high losses, which increase dramatically when the frequency increases, particularly when accessing 1 kHz or more [85].

On the other hand, the THD at the output would be increased with the use of a low switching frequency or fundamental frequency, leading to more expensive filters to prevent the harmonics from having harmful effects on the system or the grid connected to the converter.

The voltage drops for the switching devices, such as transistors and diodes, fall within the range of a few kilovolts for the high-power application, the key component of VSC converters. Consequently, a sequence of semiconductor contacts must be used to build a high-voltage converter for grid applications. This is linked to a few problems and there are no readily available technological solutions to accomplish such a relation in a sequence.

In addition, the step voltage is often transferred between the DC poles in a two-level converter. The switches must be fast, typically within a couple of kilohertz, in order to sustain switching losses at feasible speeds. This means that the voltage slope would be high at high direct voltages, which places very considerable stress on the insulation of any equipment attached to the AC terminal.

All these problems can be greatly modified by a transition to multilevel converter topologies. Since multilevel converters rely on the availability of many DC-link capacitors to manage several levels of voltages, those capacitors create distinct DC levels and generate additional levels inside the same converter. The various capacitor voltages, not only the highest DC connection voltage, are used to estimate the blocking capacity of any switch types utilized by that converter. The voltage level, and hence the converter's power rating can be increased without using direct series connections of semiconductor components [84].

On the other hand, the influence of the total harmonic distortion at the output voltage and the switching frequency losses of the semiconductor switch can be handled individually. First, the output voltage waveform has more than two different stages, and this is significant since it implies that the harmonics' amplitude can be reduced. Second, not every switching device is participating in every output voltage transition, which implies that the output voltage may be altered at a higher frequency without raising the switching frequency. As a result, the initial harmonics spectrum will emerge at a higher frequency, where they may be easily eliminated by using a filter.

The consequence of a change from the use of two-level to multilevel converter topologies is shown in Figure 3.1, which clearly displays the harmonics order being continuously decreased by increasing the voltage levels from two to seven. The switching frequency of the switching device is fixed at 15 times the fundamental, considering the switching losses will be the same in all cases. For any number of stages, both the phase voltage and the amplitude range of this signal are also shown [78].

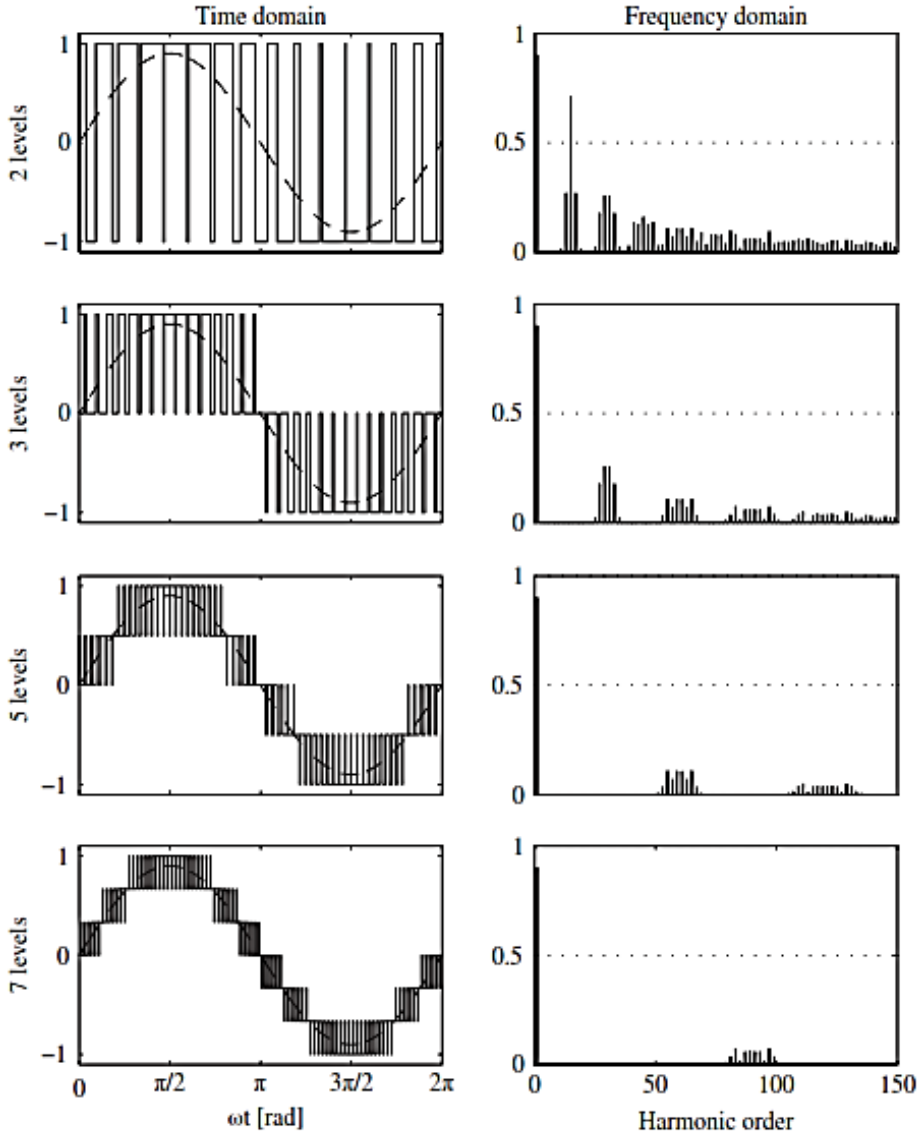

Figure 3.1: The consequence of the two-level to multi-level converter transition. (a) Shows the phase voltage of two, three, five, and seven-level converters in the time domain, respectively. (b) Shows the amplitude of the harmonics of all frequency domain converters [78].

The pulse frequency is often raised when a converter with a larger number of levels is used, as stated in the figure above. The two-level waveform does not resemble a sinusoid at all, the reason being that the use of PWM enables a distinction between the desired fundamental and the undesired harmonics in the frequency domain. However, the flipped waveform would gradually

imitate the reference with more levels. It is apparent in the frequency domain that more frequencies allow both the harmonics to appear at greater frequencies and to have a smaller magnitude. In order to achieve reasonable harmonic distortion, both effects lead to a reduction in the amount of filtering required [85].

3.3 Line Commutated Converters

Thyristor-based Load Commutated Converters (LCC) were originally presented in the 1970s [79]. The term "line-commutated" refers to a conversion method that uses the line voltage of the AC system to move from one switching unit to its neighbor.

LCC uses switching devices that can only be enabled by providing current by control operation, such as thyristors. While, in theory, HVDC converters can be made from diodes, they can only be used in the rectification mode and the lack of DC voltage controllability is a significant drawback [86]. Consequently, all LCC HVDC systems in practice used either grid-controlled mercury-arc rectifiers, at the beginning of the use of LCC, while the early installation had to be substituted by thyristors.

The LCC is still the highest power rating converter that can be constructed and is thus the best option for the transmission of high power. The low power losses, usually 0.7 percent per converter, are another advantage of LCC [76]. The main drawback is that a differing amount of reactive power from the grid is consumed by both the inverter and the rectifier, so flexible reactive compensation is required [80]. To be able to achieve performance with switching, the LCC would also require an AC voltage source at each terminal. These stations need a large AC network to be run due to the 'blocky' type of current arising from the low-frequency commutation process, as commutation draws large amounts of reactive power and produces a large number of low-order harmonics. Therefore, because of the harmonic filters and reactive power compensation needed, the station size is reasonably large [82][86].

3.4 Voltage Source Converters

Another technique has been available since the 1990's. This uses a capacitor as the feature of interface impedance and energy storage and occurs on the DC side as a constant voltage. It uses IGBTs that self-commutate. These techniques were called 'Voltage Source Converters (VSC)' [87]. They do not establish a strong AC grid since the systems are self-commuting, and they can turn at higher frequencies, removing low order harmonics and regulating the phase change on the AC side between the output voltage and current. This can substantially reduce or eliminate the need for DC filters, AC filters, and compensation for reactive power. The losses for VSC systems are significantly higher than for LCC due to the regular switching and use of IGBTs instead of thyristors [82].

Classical VSC-HVDC implementations were implemented by the HVDC Light definition of ABB in 1997 [82]. For HVDC applications, classical VSC is based on two-level or three-level

converters [88]. It is not possible to change the voltage magnitude at AC terminals with this definition, but the voltage will be either (*+V* or *-V*) with two levels, whereas the voltage would be (*+V, 0* or *-V*) with three levels of VSC [78]. To estimate the desired voltage waveform, PWM is used and the disparity between the desired and applied waveform is an unnecessary distortion that must be filtered. IGBTs are normally linked in series in various VSC topologies to increase the voltage blocking capability. Due to IGBTs, the power of the voltage blocking is limited. The use of the PWM technique has a great impact on reducing the voltage over each switching type, especially across the series of linked IGBTs that need to be switched simultaneously for better efficiency [82].

This entails complicated gate drive circuits to enforce voltage sharing under all conditions. The most important point in VSCs is that both active and reactive power flows can be controlled independently, and this lead compensation is needed to drive the reactive power [80]. As the harmonic filters are smaller and no switch yards or capacitor banks are required, VSC stations have more overhead than an LCC station. Other benefits of the VSC are that the converter can be connected to poor AC-grid networks [81], and it can use ordinary transformers as no phase shift is necessary. The primary downside of VCS is that it has higher power losses than LCC, which is usually 1.7% per converter [79].

In addition, power reversal in VSCs is accomplished by changing the current direction rather than the current direction being fixed, and power reversal is accomplished by changing the voltage polarity through LCC. As a result, the VSC technology is better suited to a DC grid application [3]. VSC power reversal can be achieved progressively so the maximum spectrum of active power is available, and a positive or negative reactive power can even be paired with zero active power. As positive and negative values can be obtained from both active and reactive power, the converter is said to work in all regions of the PQ plane [89]. LCCs usually have a minimum active power output of 5% below the rated power in [83]. This makes VSC more favorable for power transfer, as for electricity produced from a photovoltaic farm, with differing power. However, with LCC HVDC, one benefit is that in the converter station, DC pole to pole short circuit faults can be cleared. This is not the case for conventional VSC HVDC, where the fault currents have to be blocked in most situations by opening the AC breaker feeding the converter [90].

A few multilevel VSCs that were implemented and formed before the MMC and other cascaded topologies, namely the neutral point clamped (NPC) or diode clamped converter, flying capacitor converter (FLC) and cascaded half bridge (CHB) converter, are briefly defined in the following section. These types of multilevel converter have been used widely in the medium-voltage direct current (MVDC) systems, as well as high-voltage converters for power transmission applications in some circumstances. However, the number of levels cannot usually be easily expanded beyond a few due to the complexity of connecting and reconfiguring the converter, which means that, for handling transmission-level voltages, direct series communication of power semiconductors is necessary [91]. What all the types have in common, as is the case with the two-level converter, is that the maximum DC voltage supplied at the DC-side is taken up by a single DC-link capacitor, or a series connection of multiple capacitors.

3.4.1 Neutral Point Clamped Converter

Nabae, Takahashi and Akagi first invented the three-level Neutral Point Clamped (NPC) converters in 1981 [92]; the three-level and four-level converter topology is shown in Figure 3.2 and they clearly show how the design complexity increased through increasing levels. The DC connection is divided by series-connected capacitors which generate additional levels of DC. These topologies are often distinguished by the supply of diodes called clamping diodes; the main work of the diode is to provide additional current paths such that the AC terminal can be temporarily linked during operation to these DC stages.

Thus, it is possible to establish additional AC voltage levels. As the clamping diodes in this case will connect the AC terminal to the midpoint of the DC link, the three-level version is referred to as an NPC converter, as the diodes work as a clamped point to increase the voltage levels. This was also the name used in [92], which did not cover more than three levels in the definition because of the complexity of higher levels.

The only diode-clamped converter that has gained major market success is the NPC converter. While the principle can be generalized to four or more stages by increasing the diode clamped link, as seen in Figure 3.2, the losses were still not feasible in most cases in terms of costs. The number of clamping diodes increases as the number of levels increases and, more specifically, the number of interconnections between the various elements of the valve increases. This makes the converter's mechanical architecture more complicated. This is especially undesirable for a high-voltage converter because, due to the insulation specifications present, large mechanical clearances must be observed in this situation. On the other hand, the three-level NPC converter is widely used in medium-voltage applications, mainly industrial high-power motor drives [93]. They are also used in converters for tram train power and for the grid connection of renewable energy e.g., wind turbines.

In Figure 3.3, the various switching states of a single phase of the three-level NPC converter are clearly displayed. When the AC-side current is led out of the phase terminal, the states (a) to (c) are presented, whereas the states with the opposite current direction are (d) to (e) (f).

The states where the phase out, as seen in statuses (a), (c), (d) and (f), should be attached to each of the dc poles are the same as in the two-level converter. To reach these states, either all upper switches are ‘on’ to give the positive voltage output [$V_o = +V_{dc}/2$], or both lower switches are ‘on’ to produce the negative voltage output [$V_o = -V_{dc}/2$]. On the other hand, both internal transistors *S2* and *S3* are switched on in states (b) and (e), connecting the AC terminal of the phase leg to the DC connection midpoint to produce a zero voltage level [$V_o = 0$], while the outer switches are kept in the ‘off’ state.

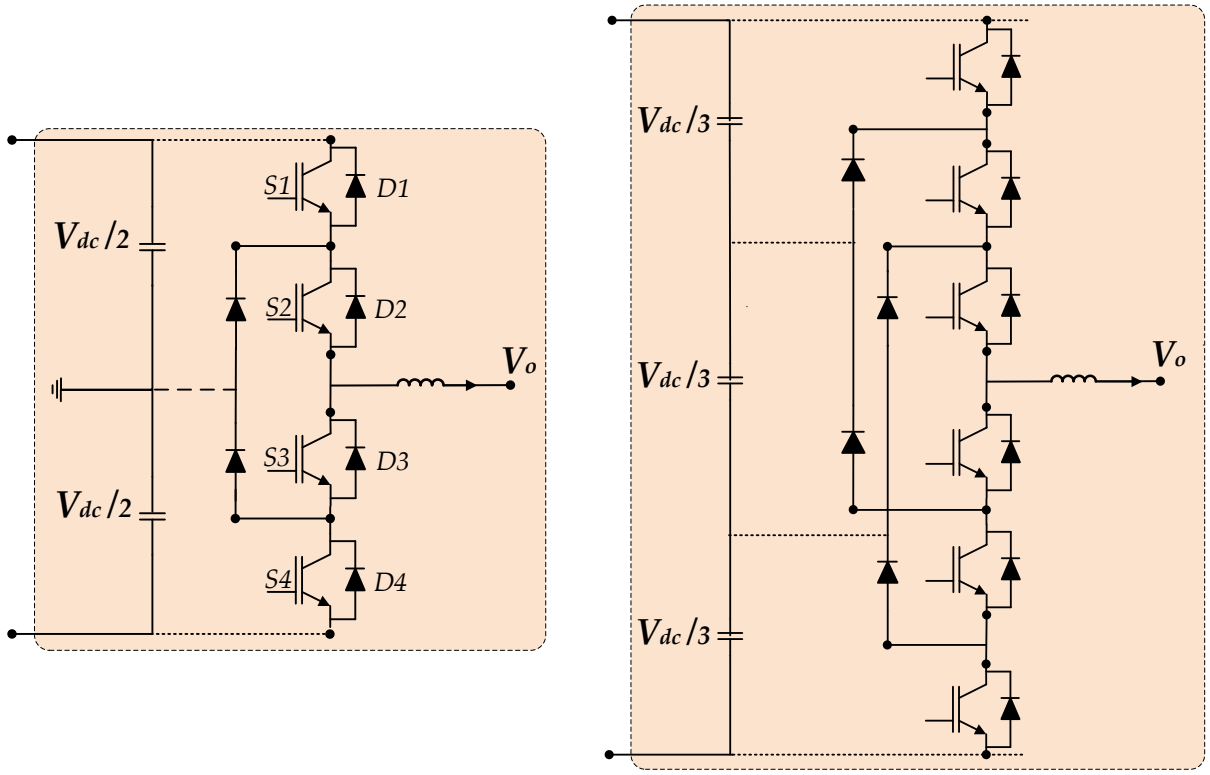

(a) (b)

Figure 3.2: NPC converter topologies for a single-phase connection. (a) Three-level connection to produce voltage output [$+V_{dc}/2$, *0, and* $-V_{dc}/2$]. (b) Four-level connection to produce [*0,* $+V_{dc}/3$, $+2V_{dc}/3$, *and* $+V_{dc}$] [3].

In fact, as long as the DC connection capacitors are well balanced, no switch needs to block more than ($V_{dc}/2$) in any of the switching states, as can be seen in Figure 3.2(a). Thus, the three-level NPC converter can accommodate two times the direct voltage and thus twice the power of a two-level converter using transistors and clamped diodes with a specified blocking voltage and current rating.

The key drawback of using the NPC converter in HVDC applications is that, when operating at high switching frequency and with mainly active power flow, the losses dissipated in the power semiconductors will be unevenly distributed. In the case of the three level NPC, the outer transistors represented in S1 and S4 will suffer both high switching losses and high conduction losses. On the other hand, the internal switches S2 and S3 will primarily have conduction losses, since they remain in the conducting mode while there are transitions between states (a) and (b) and between states (e) and (f) [78]. Therefore, the outer switches can see substantially greater losses than the inner switches at an operating point that is common for an HVDC converter. For this effect, it would be appropriate to use semiconductors with separate grades for the inner and outer switches, respectively; yet this kind of solution could increase the cost and complexity, especially for a higher level of conversion.

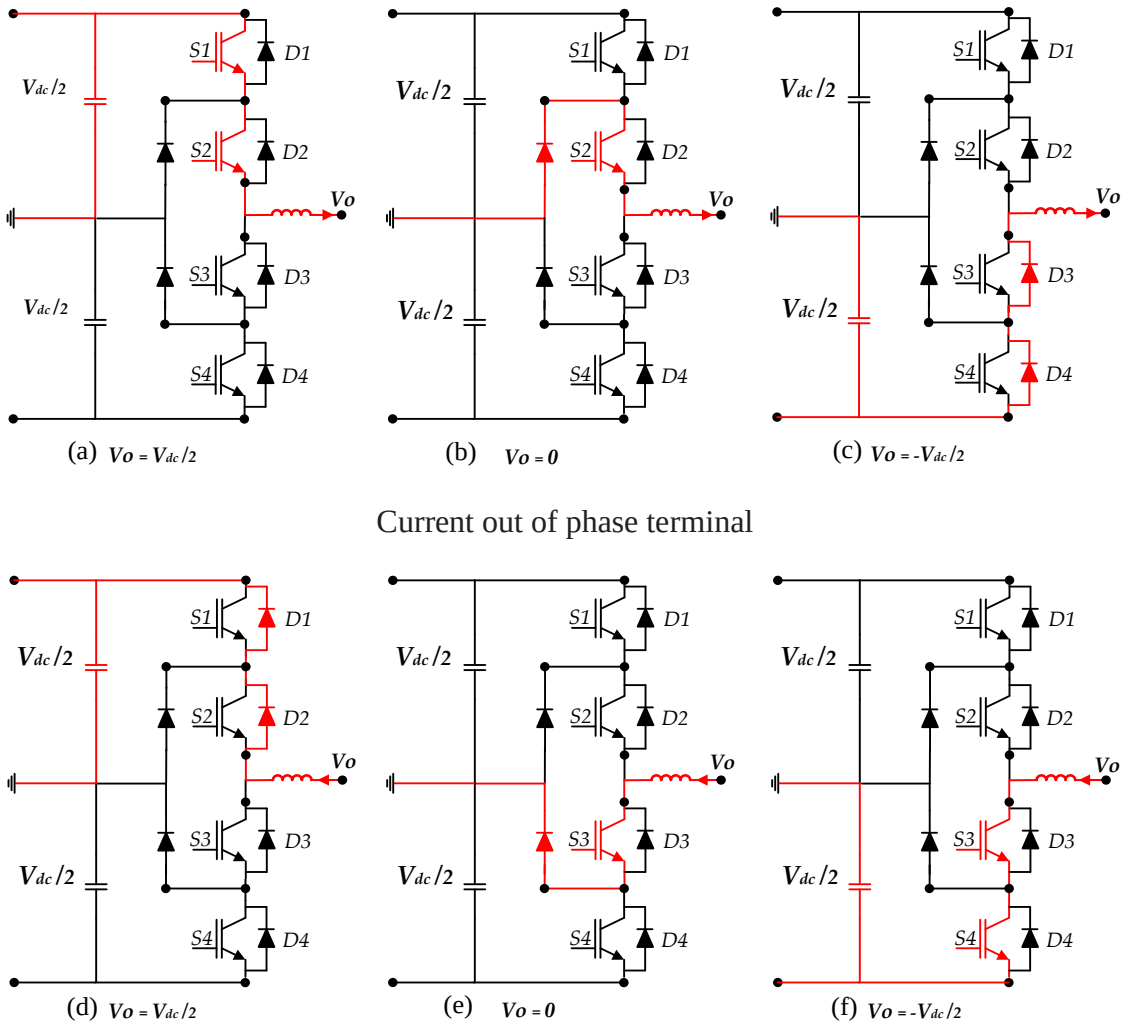

Figure 3.3: Switching states of a single phase three-level NPC converter.

The ANCP implemented a new NCP topology, proposed in [94] and called Active Neutral Point Clamped (ANPC), by removing the clamped diodes and exchanging them with the controlled transistors. This allows for a more even distribution of the losses among the semiconductors. The ANPC topology was successfully implemented in the framework for VSC HVDC [95].

3.4.2 Flying Capacitor Converter

The so-called Flying Capacitor converter (FLC), first introduced in 1992 by Meynard and Foch, is a further multilevel converter topology [96]. The structure of the FLC is like that of the NPC, except that a capacitor is used in the inverter instead of clamping diodes. The single-phase and three-phase topology can be seen in Figure 3.4, which demonstrates three-level single phase

leg schematics in Figure 3.4(a) and the three-level FLC topology for the three-phase connection in Figure 3.4(b). As with the diode clamping in the NPC, the capacitor clamping requires a large number of very big capacitors to clamp the voltage. For each of the capacitors, the voltage rating equals the main power transfer. The capacitors have no connection to a typical DC connection in this case and are thus referred to as flying capacitors.

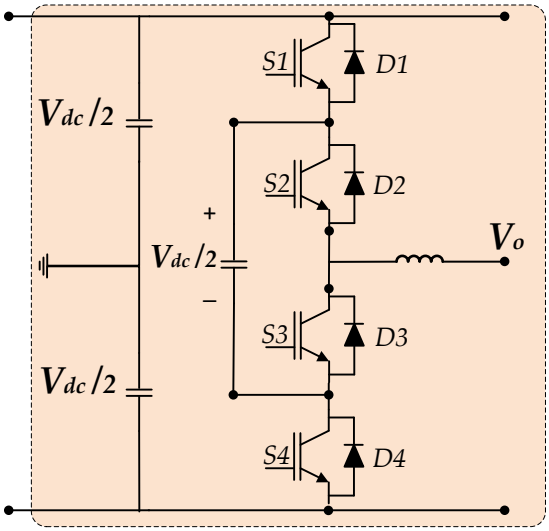

(a)

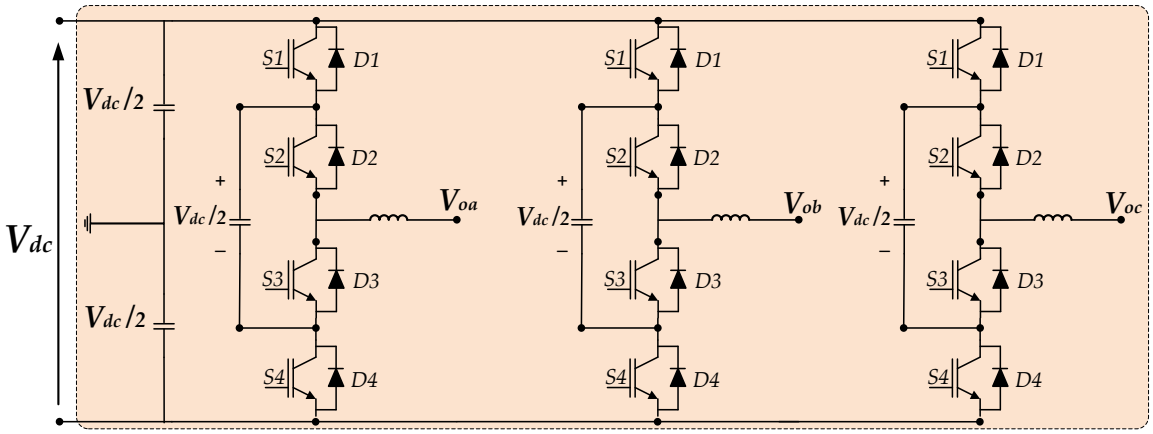

(b)

Figure 3.4: Three-level FLC converter topology (a) Single phase connection. (b) Three phase connections.

The multiple switching states of a three-level single phase leg are shown in Figure 3.5 for the scenario when the AC-side current is directed out of the AC terminal at the phase leg midpoint. The three-level voltages are approximately equal to [$+V_{dc}/2$, *0*, and $-V_{dc}/2$] as with the voltage out

as stated in (a) to (d). Here, the two upper switches need to be turned 'on' for the positive voltage level [$+V_{dc}/2$], as shown in (a); while, for the negative voltage level [$-V_{dc}/2$], the two lower switches need to be turned 'on' as shown in (d). For the zero-voltage level [0], however, we have the two situations as shown in (b) and (c), depending on the current direction. Thus, the flying capacitor will be charged in state (b), while it will be discharged in state (c). Therefore, the voltage ripple of the flying capacitor can be balanced through a proper selection of the zero-level switch combination.

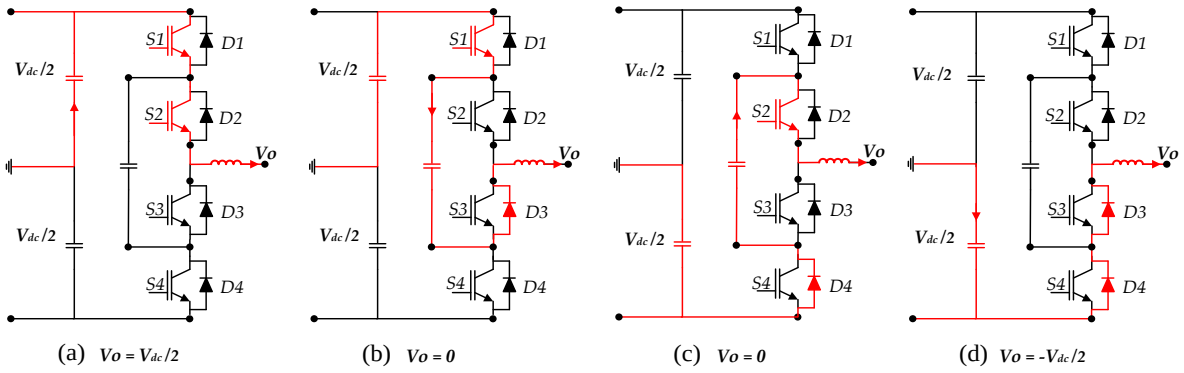

Figure 3.5: Switching states of a single phase three-level FLC converter.

As stated, when the AC-side current is driven out of the terminal, Figure 3.5 shows the current directions during the different possible switching states throughout the positive half-cycle. The current directions in the phase leg are the same for the reverse case, which means that the AC-side current is driven into the terminal, but the current flows through diodes in the valves whereas it flew through switches in this figure, and vice versa.

Each switch in the three-level flying capacitor converter has to block half of the DC-bus voltage in terms of voltage rating specifications. Therefore, the required voltage blocking capacity of each transistor device's is the same as that of a three-level NPC converter, and thus half that of a two-level converter with the same rating.

Increasing the level of conversion using FLC would be very complicated, referring to the many flying capacitors that would be bound to the switches at various locations, making many patterns. This would lead to problems in the technical design of the converter; not least because the necessary insulation standards, which involve the physical isolation of sections of separate electrical potential to prevent flashovers. In addition, a large number of capacitors rated for different voltages will also be needed, adding substantial costs and scale to the above.

Furthermore, using a voltage converter for a HVDC application means increasing the stored energy for the capacitors, and this will also increase the size and cost. On the other hand, the large-scale voltages needed to increase the number of levels of the converter will also result in an increase the number of capacitors needed to perform the conversion. Thus, a high-voltage

converter would most likely need to be installed using a relatively small number of levels and this would require switches capable of dealing with high voltages like IGBTs [97].

The key advantage of using a flying capacitor multilevel inverter is that it is capable of working at voltages greater than the blocking capability of each diode and switching element power cell [98]. The current coefficient of each arm in polarity is equal and opposite. That is why charging the capacitors does not have a negligible difference. Within a stable band, the cell and capacitor voltage differential are preserved and there is no risk of unbalancing the voltages of the capacitor either.

3.4.3 Cascaded Half-Bridge Converter

First introduced in 1990 to stabilize plasma, the Cascaded Half-Bridge (CHB) inverter is a well-known cascaded multilevel inverter topology. This was a fundamental principle for the sequence of connections between single-phase H-bridge inverters and multiple isolated DC supplies to produce multilevel waveforms [83]. In other words, the topology is established in separate DC sources and used by multiple full H-bridges to generate a staircase waveform for the output voltage, see Figure 3.6.

Each inverter level, or submodule, consists of four switch (like IGBTs with a freewheeling diode) H-bridge inverters, and can produce three output voltages [$+V_{dc}$, *0* or $-V_{dc}$], where transistor *S1* and *S3* are switched on to obtain the positive voltage $+V_{dc}$. By switching on *S2* and *S4*, the negative voltage $-V_{dc}$ can be obtained: while the zero voltage can be obtained either by turning on *S1* and *S2*, or *S3* and *S4*. Each H-bridge will be switched on and off with a specific period and at a specific moment using the multicarrier pulse width modulation (MCPWM).

The harmonics produced in this way will be the main harmonic, in addition to odd sine harmonics only. The AC outputs of each of the various full-bridge inverter levels are then related in a sequence to synthesize the staircase waveform for the multilevel inverter output voltage. The number of output phase voltage levels in a cascade inverter is equal to (2 m + 1) for the m number of the full-bridge inverter. A seven-level staircase waveform voltage output is presented in Figure 3.6(b).

The three-phase seven-level CHB inverter is shown in Figure 3.7. Each phase employs three H-bridge circuits to provide a seven-level output voltage. The voltage out for phases 'a', 'b', and 'c' is represented by v_{o_a}, v_{o_b}, and v_{o_c}, correspondingly. The independent DC voltage source, V_{dc}, is attached to each H-bridge module. Both upper and lower switches of the H-bridge leg cannot be turned on at the same time in a standard CHB inverter. The dead-time between upper and lower switches should be used carefully to avoid any switch collisions that would result in high voltage out in the H-bridge circuit [99].

Along with its easy modular design, ease of control, and lack of clamping diode or voltage balancing for flying capacitors, CHB is preferred over other VCS topologies such as NPC and FLC multilevel inverters. Most importantly, the number of potential output levels is double that of the DC source [85].

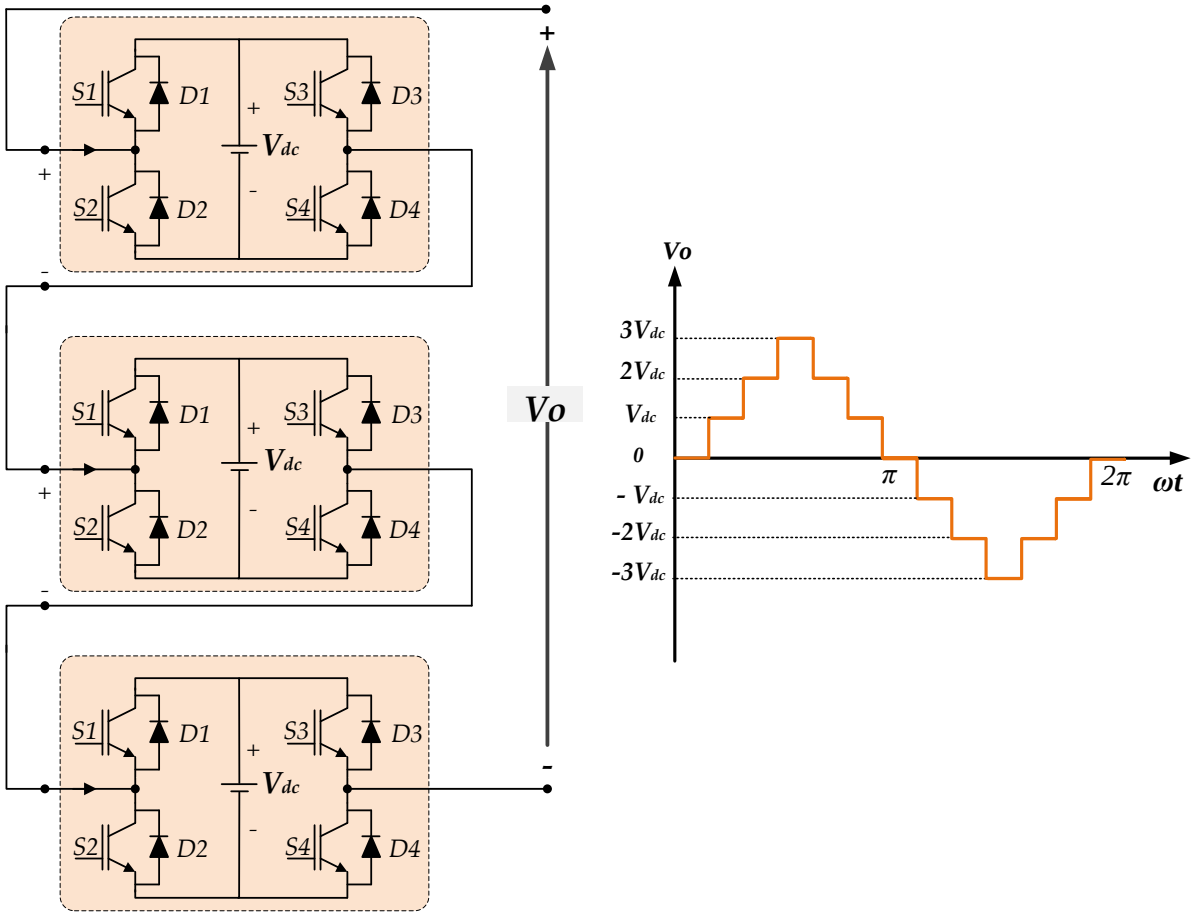

(a) (b)

Figure 3.6: Seven-level CHB converter (a) Single phase connection topology (b) Output voltage diagram.

The number of levels of a multilevel inverter must be chosen carefully, because higher levels create lower values of undesirable harmonics and need lower-rated power switches, but at the expense of increasing the number of components and management complexity. The sole flaw of the CHB is that each submodule will require its own DC supply, which limits the circuit's uses dependent on the available sources [85][100].

Furthermore, the most essential issue is to maintain phases balanced energy, since the way the three-phase CHB connects, as shown in Figure 3.7, demonstrates that there is no mechanism to transfer energy between phases and no DC component of circulating current to transfer power between phases as with the MMC converter.

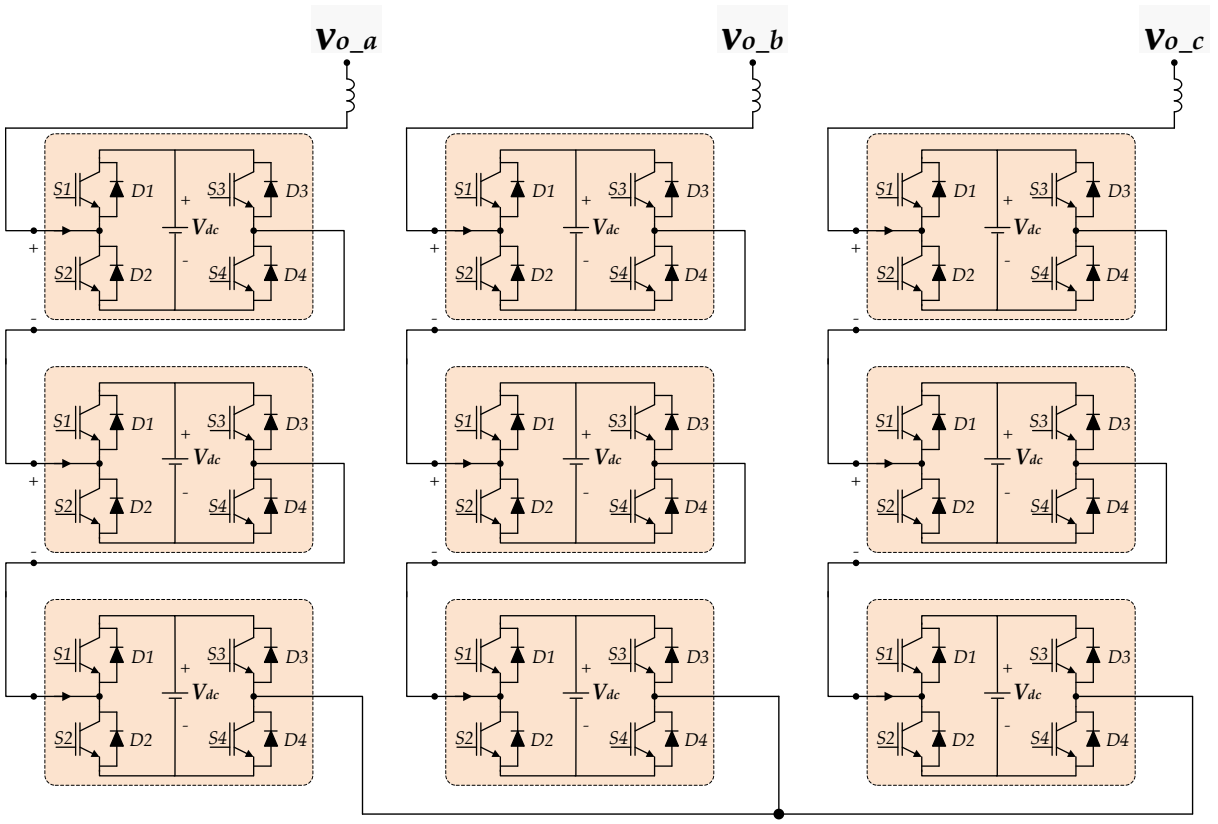

Figure 3.7: Three-phase seven-level CHB converter.

3.4.4 Modular Multilevel Converter

No pure cascaded converter topologies for power conversion have been available in recent decades. Wide scale voltage VSCs for HVDC applications have been introduced to sustain the voltage using direct series-connection of semiconductor devices. Reactive power compensation converters using full-bridge submodules have been used [101], but they lacked a DC terminal and were thus not suitable for DC/AC conversion. CHB converters existed, but these involved individual isolated transformers feeding the submodules and were not genuinely modular.

A breakthrough was made with the introduction, by Prof. Marquardt in 2002 of the MMC with half-bridge submodules [14]. It allows easy to use submodule strings to be created in an ingenious way in order to make DC/AC conversion possible, while retaining the major voltage scalability and harmonic efficiency advantages of cascaded converters [34].

Figure 3.8 depicts the MMC single-phase connection and the submodules string connection streamlining across each arm, where the MMC normally has an upper and lower arm in each phase leg. The two-transistor in series and the compact in parallel with capacitor architecture represents one submodule that may be adjusted in various topologies to satisfy the voltage scale required by the application when used with a converter [42]. Furthermore, the number of conversion levels is

determined by the submodules linked in each arm, with the number of level conversions equal to the number of submodules in each arm plus one in a non-interleaving situation.

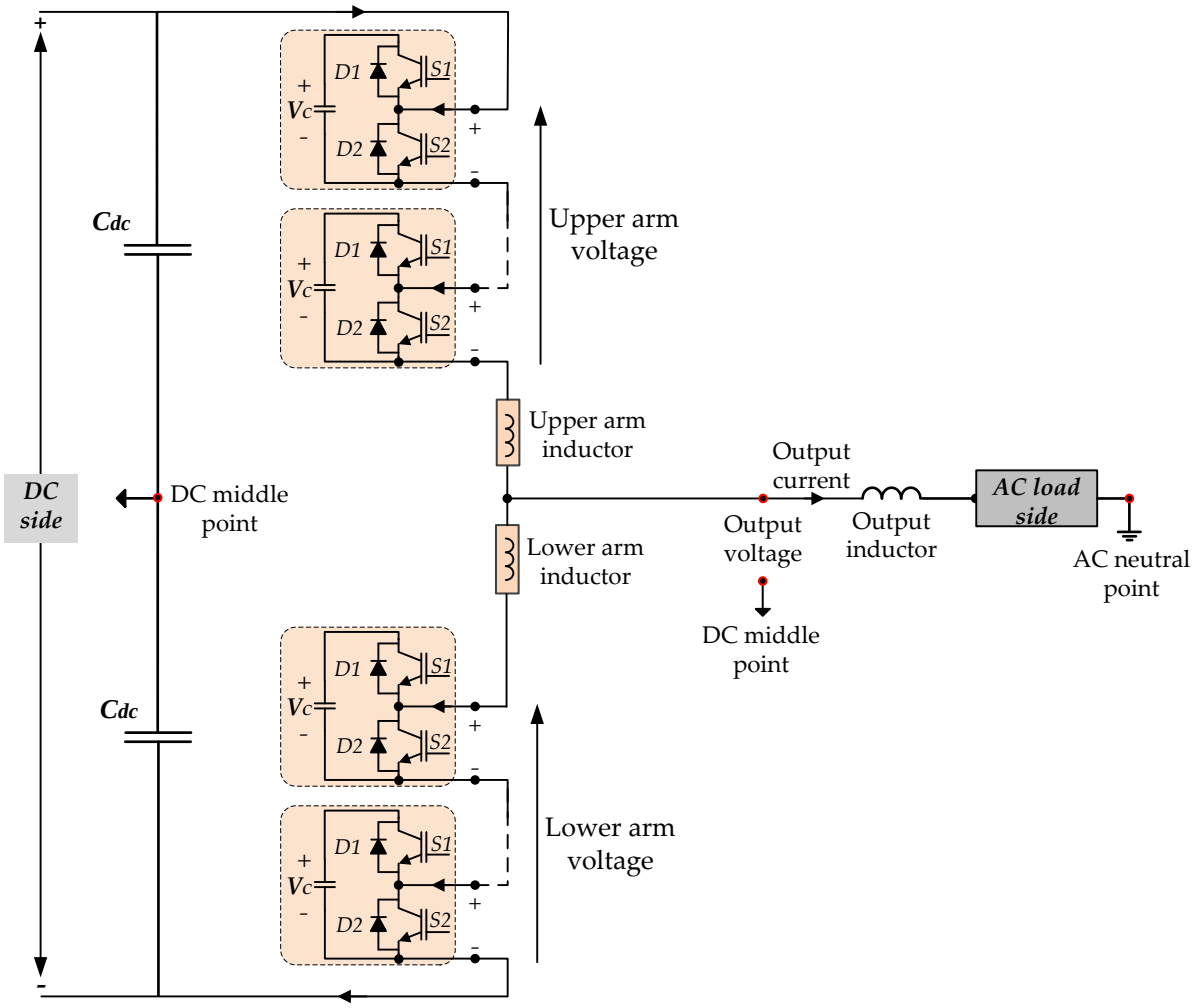

Figure 3.8: Single-phase of the MMC with an AC load connection.

This explains the MMC topology's simplicity and scalability, which helped it to outperform all other multilevel converters. When a submodule is selected, it will contribute to the voltage of its own capacitance, which implies that switch one, *S1*, will be on and switch two, *S2*, will be off. On the other hand, if the SM is not selected or it is bypassed, *S1* is turned off and *S2* is turned on.

Additionally, the MMC topology has a single connected arm inductor in both the upper and lower arms to control the arm current; in fact, it is used to reduce the phase circulating current weight and its impact on the output voltage. The MMC output voltage is determined by the voltage of the upper and lower arms, where the voltage of each arm is equal to the sum of the voltages of the chosen submodules in that arm. Thus, the output voltage scale can be expanded by having more

connected submodules in each arm. The output current, on the other hand, will be determined by the current flow on each arm, which is first provided through the DC side [102]. In this case, the DC side of the MMC, which represents the primary power provided to the converter, has been split by two capacitors, C_{dc}, with the initial voltage value equal to $V_{dc}/2$ to create the middle point, where the converter output voltage is referenced to that point and separated from the neutral point, which serves as the AC load side reference.

Due to the key subject constraints of this study, Chapters 4 and 5 would describe the topologies, mathematical modeling, modulation, control methods and organizational specifications of the three-phase MMC in depth.

4

Modular Multilevel Converter

Contents of This Chapter

- **Section 4.1** introduces the Modular Multilevel Converter (MMC) for the different applications and explains the fundamental operating principles.
- **Section 4.2** presents the different submodule topologies and highlights the advantages and disadvantages of the main two topologies, the half-bridge and the full-bridge.
- **Section 4.3** presents a general description of the MMC topology, summarizing the essential advantages and drawbacks.
- **Section 4.4** describes the general mathematical modeling to analyze the operation of the MMC. The converter equations are decoupled using a linear variable transformation that links the phase arm currents and voltages to values that make it easier to describe the process.
- **Section 4.5** identifies the most appropriate applications for the MMC, with emphasis on high-voltage direct current applications as the MMC has high power scalability.

4.1 Introduction

Modular Multilevel Converters (MMC) were first introduced in 2003 [14] and have attracted significant research interest in medium-voltage and high-voltage applications [15]. Modular converters, such as the MMC, reach any number of voltage levels by increasing or decreasing the number of connected submodules (SM). MMCs are built up by a series of connected SMs that are individually controllable. They offer various advantages over other multilevel topologies, such as fault-tolerant operation, easy to achieve capacitor voltage balance, low harmonic distortion, and elimination of the bulky DC-link capacitor [17]. They have therefore seen rapid growth in a broad field of applications, including DC transmission, solid-state transformers, and renewable energy integration [42].

SMs identify the most important part of the MMC platform and can be expressed in various topologies to generate the voltage level needed by the converter. The general topology used for each SM may be either a half-bridge converter, which is considered to be a two-level converter because each SM is capable of producing positive or zero voltage, or a full-bridge converter, which also produces two levels of voltage, positive or negative [90].

A two-level controllable voltage source reflects each SM in the MMC, and the voltage output levels can be conveniently increased by increasing the number of SM attached in series in the MMC. The independence of regulating the SM in the MMC provides the modularity properties of the converter. Increasing the voltage level, on the other hand, impedes the production of any significant harmonic material in the output [81].

The MMC not only has modularity features but is also a highly scalable technology. The voltage standard determines the number of available submodules and the technology can be used up to the highest transmitting voltages without the semiconductor transfer sequence relationship, so simultaneous switching issues are irrelevant [103].

In terms of power losses, compared to VCS, MMC has about one percent fewer losses, considering the two or three levels of the converter. This is due to the lower frequency used to switch each transistor and the fact that the SMs are selected at different times. In addition, the low losses are obtained by considering the voltage across each switch, which is slightly lower in the MMC [79].

On the other hand, by increasing the SMs, the MMC can increase the voltage level, which will then increase the connected switches in the converter, and this will certainly increase the power losses. However, the harmonic distortion is intensified by increases in the levels. In short, the additional voltage levels in the transistors of each SM boost the equilibrium between harmonic distortion and power loss. Depending on the application, whether this gain of increasing voltage level is significant enough to avoid the increased number of semiconductors may be further evaluated.

This chapter focuses on the basic operation and design constraints of the MMC, beginning with the SM general topologies and how, by increasing the voltage level, these devices can help to handle high voltages. In addition, to explain the theory of the converter operations, the

mathematical modeling of conventional MMC topology is described in detail, showing the current and voltage direction in each case.

4.2 Submodule Topologies and Theory Works

The typical configuration of the MMC consists of a series of SM connections. The most commonly used topologies of SM are based on a half-bridge or full-bridge circuit with a capacitor as a source of DC voltage to store energy in each SM. This represents the basic building blocks of all the multilevel cascading converters. The capacitor size is analyzed further in [104].

Different topologies of SMs have been studied and suggested for MMC over many years, such as the cascaded half-bridge SM, which can be done by joining two half-bridge SMs in series [105]. In terms of power loss and performance, this topology is close to that of the half-bridge. It is also easy to mount and monitor. This topology will generate three voltage levels (positive, negative, and zero) at the SM output terminal.

Another SM topology built with four series-connected transistors, two clamping diodes each connected to the middle point of two series transistors, and two capacitors is analyzed in [106]. This is called the three-level point-clamped neutral topology. Its benefits are the output of the bipolar voltage to control the ride through the DC fault; while the main issues are the loss distribution between the switches and the neutral point voltage balance. The replacement of the clamping diode with transistors would lead to an improved distribution of losses as well as improving the neutral point voltage balance power, as suggested in [107].

However, increasing the connected switches and the connection complexity leads to less reliability, lower efficiency, and greater losses of power. Different SM topologies are developed either to generate bipolar voltages to deal with the DC-side faults, or to improve the performance with less connected switches, as well as providing better controllability for capacitor voltage ripple [87][108].

In this chapter, two fundamental SM topologies are explained in detail. Figure 4.1 shows the half-bridge SM with unipolar output voltage and the full-bridge SM reflecting the bipolar output voltage with respect to the switching status.

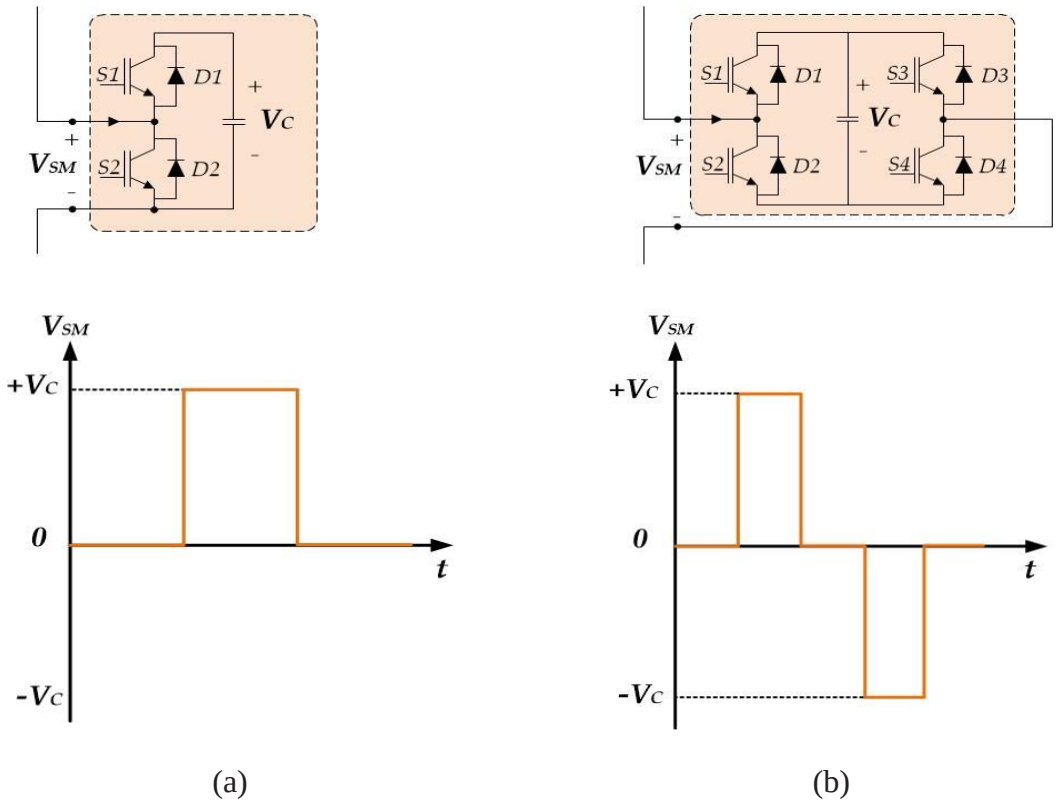

Figure 4.1: SM topologies with output voltage waveform. (a) Half-bridge SM (b) Full-bridge SM.

4.2.1 Half-Bridge Submodule

The Half-Bridge Submodule (HBSM) consists of a two-level phase leg represented by two IGBT transistors with a Freewheeling Diode (FWD) connected in parallel with a DC capacitor to maintain a direct voltage. The output terminals of the SM are formed by the phase leg midpoint on the one hand, and one of the DC capacitor terminals on the other. The output voltage has two possible switching states. The output voltage of the SM, V_{SM}, is described in Table 4.1.

Table 4.1. Switching states for HBSM.

SM states	*S1*	*S2*	V_{SM}
ON	*ON*	*OFF*	V_C
OFF	*OFF*	*ON*	*0*

When the SM is selected and its status is *ON*, the V_{SM} equals the voltage of the capacitor, V_C; otherwise, when the SM is not selected or bypassed, the V_{SM} equals zero. The dead time state can be considered when both switches (*S1* and *S2*) in the off status consider the SM that has not been selected. In this state, the V_{SM} value will be affected by the flow direction of the current, since only the FWD in each IGBT may conduct. When the current flows into the SM, the capacitor voltage will be present; however, in the other direction, the current flows out of the SM, so the voltage will be zero. This state is not used in normal operation, only during start-up and certain emergency conditions.

The HBSM connection can only provide a positive or zero voltage, unipolar voltage, and is therefore the produced voltage has an AC plus a DC component. Figure 4.2 clearly indicates the series of HBSM connections with the output voltage beginning from level zero to the complete voltage of all selected SMs.

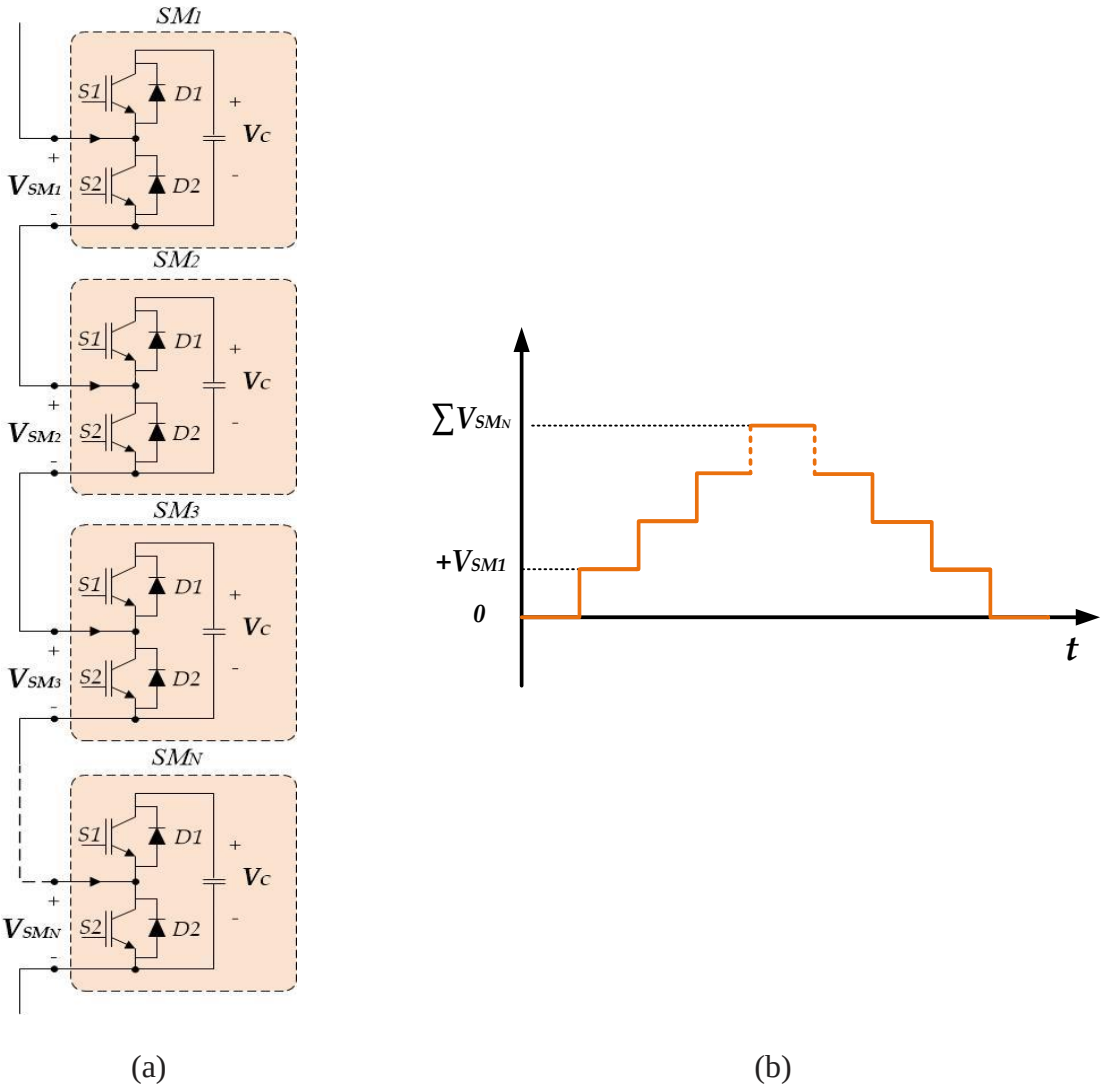

(a) (b)

Figure 4.2: (a) String connection of N_{sm} module of the HBSM (b) Possible output voltage levels.

The serial connection of the submodules helps to extend the voltage that can be managed. Figure 4.2(b), on the other hand, explicitly indicates that the amount of output voltage level rises when the number of submodules attached to the sequence increases. The N_{sm} series connection, the number of connected SM, will yield total levels equal to $N_{sm} + 1$, with values between zero and N_{sm} *Vc*.

4.2.1 Full-Bridge Submodule

The Full-Bridge Submodule (FBSM) has two series of IGBTs (*S1*and *S2*) connected in parallel to another two series of IGBTs (*S3* and *S4*), all connected in parallel with the capacitor, as can be seen in Figure 4.1(b). The output voltage of the SM is formed by the midpoints between the *S1* and *S2*, representing the positive pole, and the midpoint between *S3* and *S4*, representing the negative pole. As shown in Table 4.2, the standard switching states of these switches give rise to four separate switching states for the entire submodule.

Table 4.2. Switching states for FBSM.

SM states	*S1*	*S2*	*S3*	*S4*	V_{SM}
OFF	*ON*	*OFF*	*ON*	*OFF*	0
ON	*ON*	*OFF*	*OFF*	*ON*	$+V_C$
OFF	*OFF*	*ON*	*OFF*	*ON*	0
ON	*OFF*	*ON*	*ON*	*OFF*	$-V_C$

When *S1* = *S4* = 0 and *S1* = *S4* = 1, the two states both select the submodule, resulting in (-*Vc*) and (+*Vc*) output voltages for the same current flow path. Also, when all the IGBTs are switched off, the FBSM can be blocked. It will serve as a diode bridge in this situation, and the terminal voltage will match the capacitor voltage (+*Vc*), irrespective of the current path.

In conclusion, if the voltage of the submodule capacitor is held sufficiently stable, the said converter submodules will act as controllable voltage sources. In comparison, unlike the HBSM, the complete bridge is actually capable of supplying differential voltage, positive and negative voltage. In reality, the full-bridge would create the negative voltage just to eliminate the effect of the system DC-link fault [109].

The sequence of FBSM contacts with the output voltage starting from the positive voltage level and going to the negative voltage level can be clearly seen in Figure 4.3.

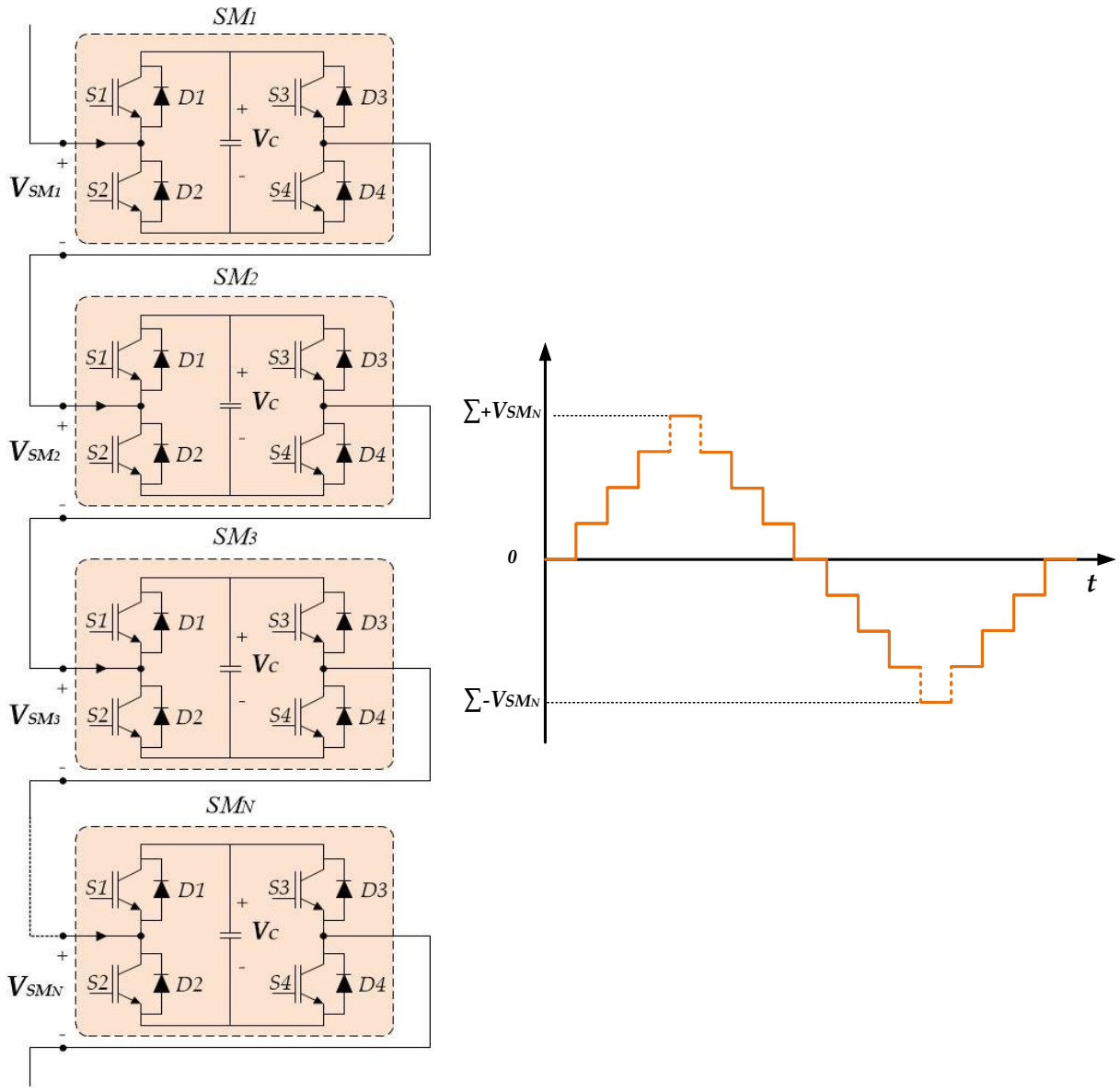

(a) (b)

Figure 4.3: (a) String connection of N_{sm} module of the FBSM (b) Possible output voltage levels.

Increasing the connected SM, as shown in Figure 4.2, would raise the voltage level and thus cause the voltage that can be managed to increase. Figure 4.3(b) indicates that the output voltage of the FBSM string connection will have all the voltage levels between - N_{sm} *Vc* and + N_{sm} *Vc*, including zero, since the voltage level produced is equal to $2N_{sm} + 1$ levels in total; this is due to the voltages produced.

Using the HBSM in an MMC requires twice the number of IGBTs of a three-level VSC type FLC or NPC at the same rating. While using FBSM in an MMC, the need for IGBTs is double

that when using HBSMs. In both SM topologies, the capacitor must be of a significant size, since it can retain an approximately constant direct voltage when holding significant currents. This makes the MMC special, since it has no DC-link capacitance, but rather an embedded capacitor in each SM; therefore, to maintain the voltage level and the energy stored on it, these capacitors need to be the correct size. A heavy and bulky circuit is the result of many high-rated semiconductor switches and capacitors, offering a converter that is less lightweight than the classic VSC, but much more compact than the LCC [79][110].

On the other hand, the MMC is intended for high voltage applications because the level of conversion can increase for many levels. Thus, series connections of a few hundred submodules may be required to handle the high voltage scale, like the HVDC transmission system needs about 200 to 400 SM in each arm to reach a few hundred of kilovolts to operate sufficiently [111][87]. This number could be less, between 15 to 200 SM per arm, if STATCOMs are used to reach the operating voltage of between (14 - 220) kV [87][112]. Under such circumstances, there is no need to connect a bulky filter at the output in this case, since the voltage given is almost continuous. This is because the size of one voltage level is extremely small in contrast to the overall voltage given by the submodule string, which is dependent on the capacitor size. Moreover, sing additional submodules significantly reduces the harmonic content.

To sum up, the primary difference between HBSM and FBSM, in terms of voltage output, is that the former can only give a unipolar output voltage and is thus only suitable for producing an AC voltage with a DC component. The latter, on the other hand, is bipolar and may supply either pure alternating voltage or a mix of AC and DC with negative polarity. The main advantage of the bipolar voltage produced by FBSM is that the MMC using HBSM cannot block fault currents during a DC-link fault because the voltage produced is just positive. The FBSM, however, can suppress the fault current as the opposing voltage produced in terms of the DC fault happens. This would thus, eliminate the need to use a fuse or AC breaker in the grid side connection [79][90]. Nevertheless, this duplicates the need for IGBTs due to the different topology. This can be discussed and analyzed further in order to decide whether this benefit is significant enough to justify the higher number of semiconductors.

4.3 Basic Operation and Design Constraints of MMC

The previous section described the basic work of individual SM and the SMs string relations, and the different topologies of SM, the main component of MMC, were discussed in detail. It was concluded that, because of the integrated capacitor, the string of SMs can act as controllable voltage sources within the range of the summation of the capacitor voltages. In addition, to consider the SM string as an optimal power supply, the power balance must be maintained: firstly, by regulating the capacitor voltage in each SM to the overall capacitor voltage in the arm; and secondly, by controlling the total energy exchange within the total capacitor voltages of each arm, thereby maintaining a constant total energy in it. This is equivalent to regulating the sum of the capacitor's voltages at the desired value. This control feature is, therefore, aimed at regulating the average voltage over a cycle, which will be discussed further in the section in Chapter 6 concerning the control of the MMC.

The schematic diagram of a three-phase MMC is illustrated in Figure 4.4. It consists of three legs, one leg per phase. Each phase leg is designed with two cascaded arms, called upper and lower arms. There are six arms in total, each assembled in sequence by a string of SMs. However, the switches (transistors and diodes) are incorporated internally in the SM strings instead of floating in the phase arms of each stage. Therefore, the method of operating the converter is radically different due to the flexibility of increasing the converter levels.

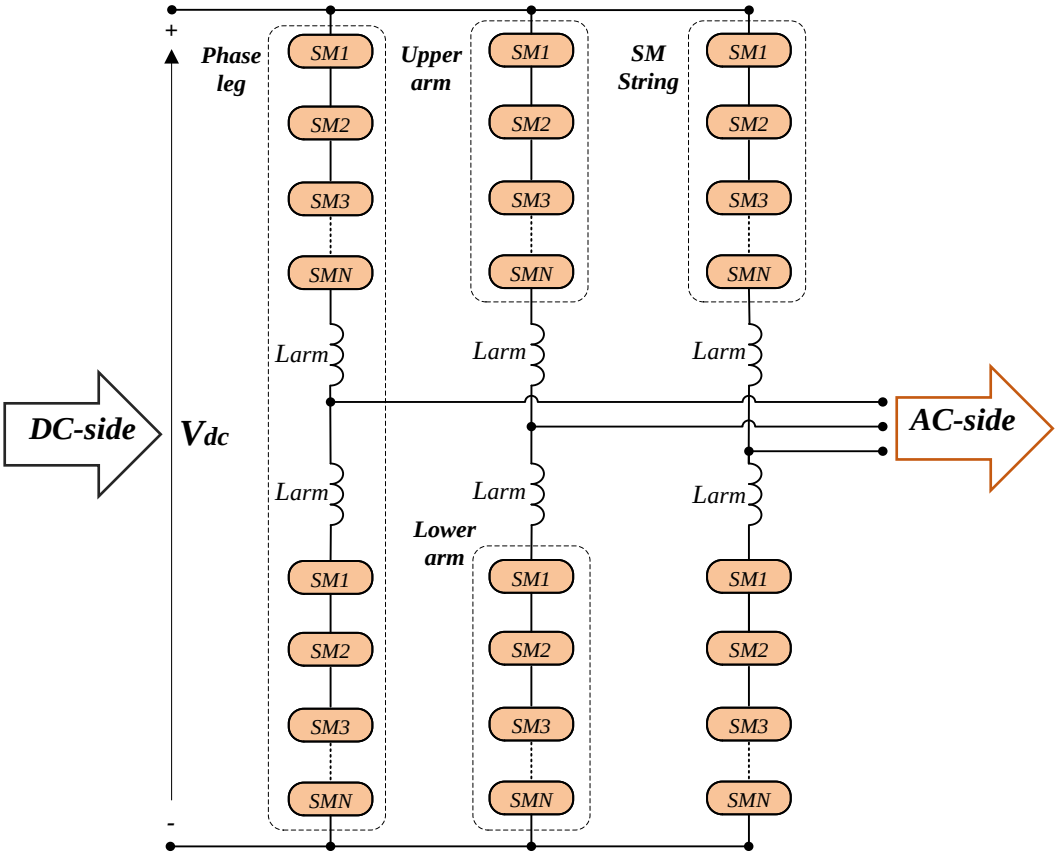

Figure 4.4: Schematic diagram of a three-phase MMC.

The MMC circuit diagram also reveals that each arm has small inductors connected to the SMs string in series, which is also a major difference from the previously described multilevel converters, where the inductance of the phase legs should be kept low to allow for a fast flow in the current during the phase leg transitions. This is not needed in the MMC because the commutations are internal to the SMs, and no such quick changes in the current flow in each phase arm could happen. Instead, reactors are needed in the phase arms to prevent the direct parallel connection of the voltage sources introduced by the SM strings. A DC fault current occurs between the legs of the phase without inductors. However, provided that the voltages of the SM strings can be regulated with great precision, these inductors normally do not need to be large, especially if the number of SMs is high [42][110].

In fact, each arm in the MMC can be represented as a voltage converter because they have the ability to generate a multilevel voltage, where the number of voltage levels depends on the number of connecting SM, with a DC offset of the DC-link voltage [79].

Furthermore, the MMC topology provides a solution with low power losses, low switching frequency, high system modularity, and voltage scalability. This is because the easy cascading of SMs will increase the voltage levels at the output, producing a pure sine voltage, which leads to the elimination of the filter on the AC side. By establishing a proper modulation technique, a sinusoidal multilevel waveform at the AC terminal is synthesized [113][114].

4.4 Mathematical Modeling for MMC

The conventional structure of a three-phase MMC is shown in Figure 4.5, which typically makes up a series of SMs. The basic SM topology is discussed in this section, based on the half-bridge circuit with a capacitor (C_{SM}) as a DC voltage source (V_C).

The switches are usually constructed with an IGBT and FWD. As stated in Table 4.1, the two switches (*S1* and *S2*) at each SM operate in a complementary fashion, so when *S1* is *ON*, *S2* must be *OFF*, and vice versa. Based on the state of the two switches, the SM is either inserted or bypassed, adding a voltage V_{SM} to the arm that is equal to either V_C or zero, respectively. This operation of the SM is illustrated in Figure 4.6. When an SM is bypassed (*OFF*), its capacitor voltage remains constant, but inserted capacitors will charge or discharge depending on the flow direction of the arm current, i_h, (*h* denotes the upper or lower arm).

The phase-leg consists of upper and lower arms with a number of SMs (N_{sm}) per arm connected in series with the arm inductor (L_{arm}). The function of the arm reactor is to limit the phase circulating current and the DC fault current within the phase-leg of the MMC. It also allows for the current flowing inside the converter to be controlled [42].

The voltage out for the upper and lower arms can also be seen in Figure 4.5, for the relationship to the converter voltage out, which reflects the average voltage difference of the lower and upper voltages over one cycle. So, the output voltage magnitude will not overtake the DC-link voltage, V_{dc}, average. This makes it possible to set the potential at the AC outlet to any point between the DC poles, neglecting the voltage drop across the relatively small arm inductors [110].

In Figure 4.5, as symmetry is being considered, the operation of the separate phases ('a', 'b', and 'c') will be equivalent, aside from a phase shift of 0°, -120° and -240° degree respectively, applicable to all the variables of the corresponding phase leg. So, all the analyses take phase 'a' as an example.

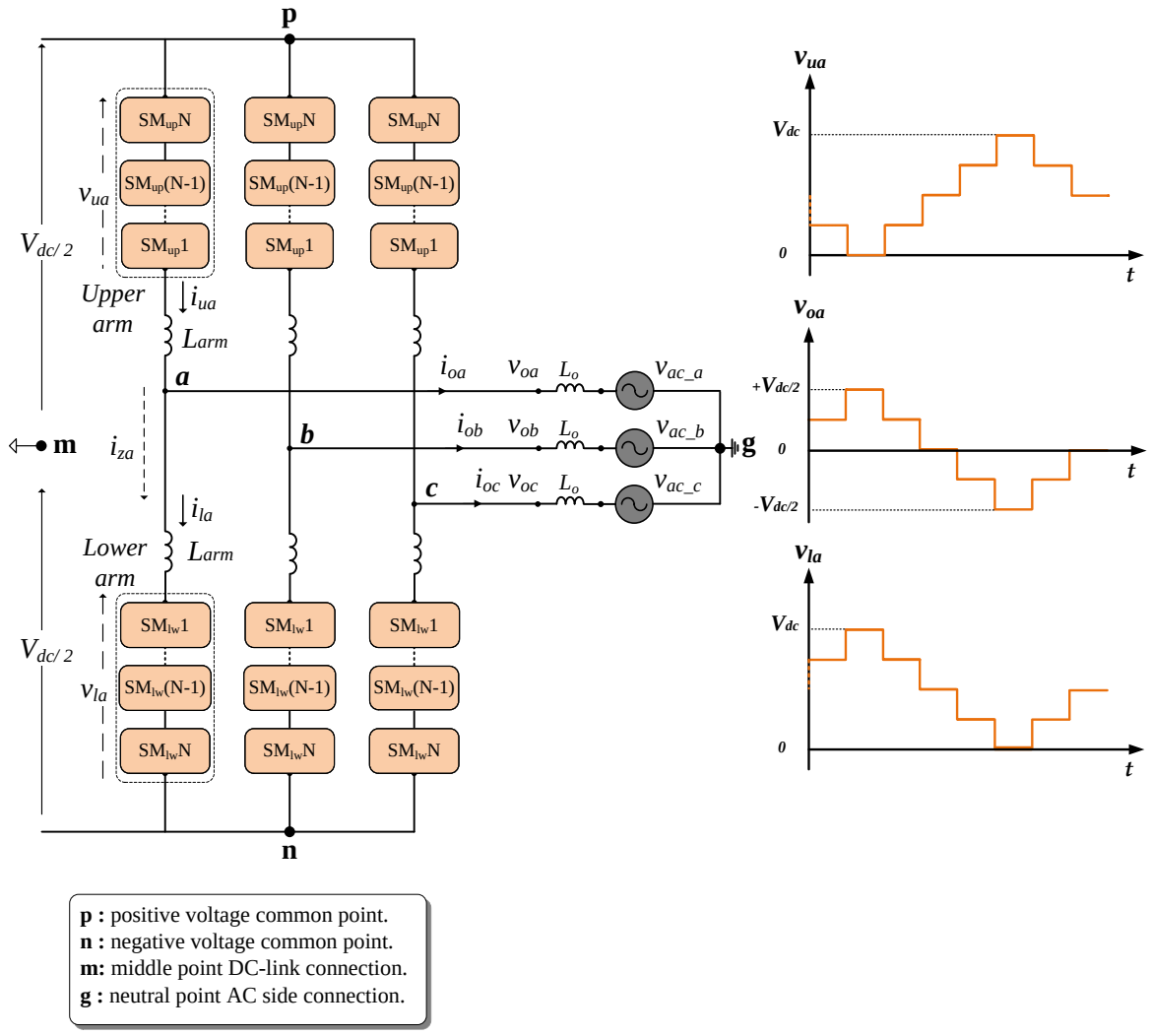

Figure 4.5: The conventional structure of a three-phase MMC with the upper arm voltage out, lower arm voltage out, and the converter voltage out based on phase 'a'.

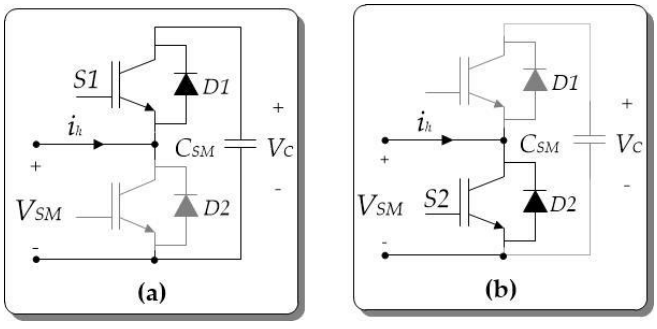

Figure 4.6: MMC based on a half-bridge switching operation when: (a) The SM is *ON* and (b) The SM is *OFF*.

The phase 'a' output current is denoted as i_{oa}; the upper arm current is i_{ua}; the lower arm current is i_{la}, and the DC current is defined as I_{dc}. The DC-link current is divided evenly between the three phase-legs in a balanced situation. The circulating current is made up of one-third DC-link current and an AC portion resulting from the voltage ripple on the phase leg capacitors and the voltage differences between the phase legs. The circulating current is denoted as i_{za}. As a result, the current in the upper and lower arms can be represented as Equations (4.1) and (4.2).

$$i_{ua} = \frac{i_{oa}}{2} + i_{za} \tag{4.1}$$

$$i_{la} = -\frac{i_{oa}}{2} + i_{za} \tag{4.2}$$

Equation (4.3) is obtained by subtracting Equation (4.2) from Equation (4.1), which represents the output current i_{oa}. This is obtained by using Kirchhoff's Current Law:

$$i_{oa} = i_{ua} - i_{la} \tag{4.3}$$

The circulating current is defined as the current that circulates through both the upper and lower arms, as described in Equation (4.4), after adding Equations (4.1) and (4.2).

$$i_{za} \equiv \frac{i_{ua} + i_{la}}{2} \tag{4.4}$$

The DC component of this current, represented by (⅓ I_{dc}), is responsible for the energy sent or received by this phase to or from other phases or from a common DC network [25]; its 50 Hz AC component can be used to move energy from the upper to the lower arm, and vice versa [20]. Other unregulated components, normally at 100 Hz, that cause losses with no contribution to the MMC control, can be present in the circulating current [26].

Furthermore, by applying Kirchhoff's Voltage Low on phase 'a', the voltages of the upper and lower arms of the MMC can be expressed as in Equations (4.5) and (4.6):

$$\tfrac{1}{2}V_{dc} - v_{ua} - L_{arm}\frac{di_{ua}}{dt} - v_{oa} = 0 \tag{4.5}$$

$$\frac{1}{2}V_{dc} - v_{la} - L_{arm}\frac{di_{la}}{dt} + v_{oa} = 0 \tag{4.6}$$

where v_{ua} and v_{la} are the total voltages of the cascaded SMs in the upper and lower arms for phase 'a', respectively. Meanwhile, v_{oa} is the output voltage from phase 'a' to the DC middle point 'm'.

Adding Equations (4.5) and (4.6) leads to Equation (4.7), expressed as Equation (4.8) using the circulating current defined in Equation (4.4):

$$V_{dc} = v_{ua} + v_{la} + L_{arm}\frac{di_{ua}}{dt} + L_{arm}\frac{di_{la}}{dt} \tag{4.7}$$

$$(V_{dc} - v_{ua}) - v_{la} = 2 \cdot L_{arm}\frac{di_{za}}{dt} \tag{4.8}$$

where v_{la} is the voltage of the inserted cells at the lower arm, and also the value of the converter voltage referred to point 'n' through the converter lower arm; while $(V_{dc} - v_{ua})$ reflects the converter voltage related to the negative point 'n' from the upper arm, which is normally required to be equal to v_{la} in order to keep the upper and lower arms in a balanced state.

The conduct of the circulating current is explained in Equation (4.8). In fact, later in Chapter 6, this equation will be used to design an effective controller.

At the same time, subtracting Equation (4.5) from Equation (4.6) leads to Equation (4.9), and applying Equation (4.3) leads to Equation (4.10):

$$v_{la} - v_{ua} = L_{arm}\frac{di_{ua}}{dt} - L_{arm}\frac{di_{la}}{dt} + 2v_{oa} \tag{4.9}$$

$$\frac{v_{la} - v_{ua}}{2} = v_{oa} + \frac{1}{2}L_{arm}\frac{di_{oa}}{dt} \tag{4.10}$$

where v_{oa} again represents the converter voltage in phase 'a' referred to point 'm'.

Connecting the converter to grids, the output voltage at each phase is related to the grid voltage by the output inductor L_o, as stated in Equation (4.11):

$$v_{oa} = L_o \frac{di_{oa}}{dt} + v_{ac\_a} + v_{gm} \tag{4.11}$$

where v_{ac_a} is the AC voltage at phase 'a' related to a neutral point named 'g', and v_{gm} is the voltage between that AC neutral point and the DC middle point 'm'. The latter voltage, v_{gm}, could be neglected for output current controllers as long as there is no path for the zero sequence components of those currents. Thus, an equivalent inductor L_{eq} can be defined in Equation (4.12) to get Equation (4.13), an equation usually applied to PI or deadbeat controllers to manage the active and reactive power transferred to the grid.

$$L_{eq} \equiv \frac{1}{2} L_{arm} + L_o \tag{4.12}$$

$$\frac{v_{la} - v_{ua}}{2} \cong v_{ac\_a} + L_{eq} \frac{di_{oa}}{dt} \tag{4.13}$$

As stated in Equation (4.13), output currents depend on the voltages generated by the upper and lower arms, which rely on the switching states of the SMs, and the modulation technique applied to the converter.

The above mathematical equations are developed for the MMC with DC-link connection and middle point connection, but these equations are also applicable to the newly proposed topology of the MMC without the DC-link [20], as described in Chapter 6, whose results are shown in the simulation section. There is no direction for the output current in the suggested MMC model. Hence, it is possible to neglect the proposed model corresponding to the common-mode current. So there is no change in the output current at the AC side, the AC component of the circulating current, or the DC current component models. In addition, Equation (4.11) shows that, underbalanced situation the zero-sequence voltage can be neglected, while it can be used to decrease the capacitor voltage ripple in the SM in an unbalanced situation [87].

4.5 Applications of MMC

For high-power applications, MMCs are commercialized as standard and personalized products. MMCs are mostly used in HVDC transmission systems because of their high voltage capacity and high-power efficiency. The MMC is used in a variety of industrial applications, including power transmission systems, motor drives, and power quality improvement. This section delves into the finer points of high-power applications, such as HVDC, which have a strong connection to the application of the thesis work.

HVDC transmission systems become more viable and economical for transmitting power over a long distance with low power losses. This is due to the high increase in building renewable energy projects, such as hundred acres farm of PV panels far from the cities. HVDC systems have several additional operational and environmental benefits, such as higher controllability and stability, improved power quality, low acoustic noise, and less expensive bus-bar structures on the AC-side in comparison with the high-voltage alternating current systems [115].

The HVDC system has been implemented before with a two-level converter represented by LCC and a three-level converter by using different VCS converter topologies. However, there were many consequences, represented through a high THD at the voltage output leading to the application of a bulky filter to improve the voltage out. Of course, the VCS has improved those issues, as it is improved the independent control of active and reactive power, the black-start capability, operation with passive and weak grid connections, and the possibility of implementing a multiterminal connection [116].

As a result, using a multilevel converter for HVDC, such as MMC, allows for a significant rise in output voltage levels and output switching frequency, allowing for a further decrease in filter size due to the high dynamics of increasing the conversion level. Despite the high-performance switching frequency, the switching frequency in each cell may be as low as a few hundred hertz or even operate at the fundamental frequency, minimizing switching losses even more. In comparison to LCC and three level VSC converters, where the voltage steps are the full or half DC-link voltage, the MMC's output voltage waveform has small voltage steps. Since the voltage time derivative is reduced, this function decreases the high-frequency emissions.

A typical back-to-back configuration of an MMC-based HVDC system is shown in Figure 4.7. The AC-side of MMC1 and MMC2 is connected to the grid through a transformer, and their DC systems are interconnected through a DC-link cable of several hundreds of kilometers in lingth. Since long-distance connections require a DC voltage to avoid attenuation and power losses, back-to-back converters operate in the following way: the first converter MMC1 converts AC to DC, while the second converter MMC2 converts DC to AC. The MMC generates high-quality output voltage and current waveforms, eliminating the need for harmonic filters on the DC and AC sides of the MMC-HVDC configuration.

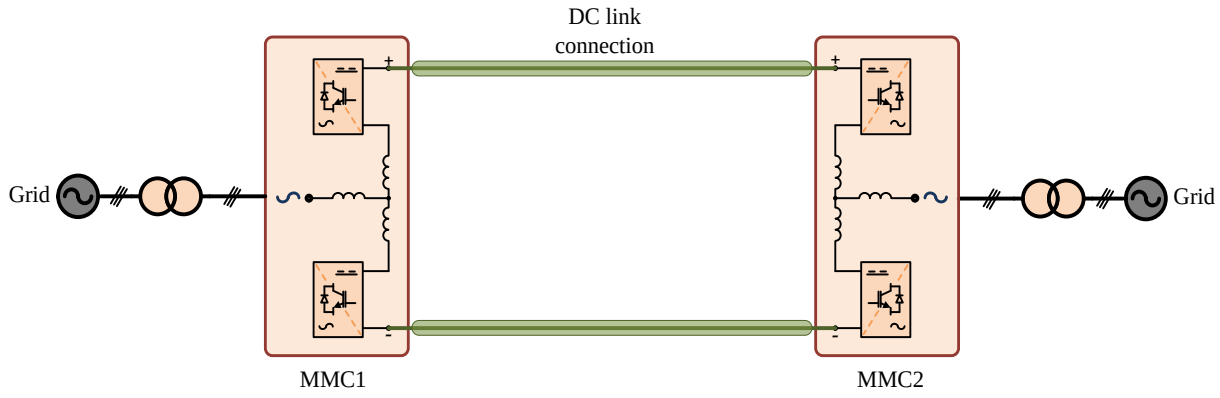

Figure 4.7: MMC based HVDC back-to-back system.

The MMC is equipped with a large number of SMs to achieve a high conversion ratio and lower THD. The SMs numbers could reach 200 - 400 SM/arm in HVDC applications. This high number is necessary for representing an operating voltage range of 320 kV to 500 kV. In the future, it is expected that the MMC- HVDC system could reach an operating voltage of more than ± 600 kV [117], which means increasing the SMs in each arm or using high voltage semiconductors to manage the high voltage scale . The Trans Bay project in San Francisco, which was Siemens' first MMC-based HVDC system project implemented in 2010, is one example of MMC-HVDC project connection systems. This project uses an 85-kilometer subsea cable to carry 400 MW of electricity at a voltage of 200 kV [104]. The MMC used in this project was constructed using cascade HBSMs [80]. In 2015, Siemens completed another HVDC project in Europe, the France-Spain Electrical Interconnection: This interconnection between Spain and France is made possible by a 65-kilometer-long underground cable. Two DC-links, each capable of transmitting 1000 MW and running at 320 kV, were considered for the project [118].

The implementation of the MMC can be applied with a different SM topology by using standard half-bridge, full-bridge or diode clamped cells [16].

The modularity and scalability of the converter topology are the key advantages of using MMC in high-power applications, where the MMC provides distributed energy storage and has a modular configuration that offers higher availability and fault tolerant operation. The MMC biggest disadvantage to the other alternative converters is that the controller is more complex, and the control hardware needs more computing power.

5

Modulation and Control Schemes for MMC

Contents of This Chapter

- **Section 5.1** presents the controlling aspects of the MMC by pointing out the important elements that need to be controlled to improve the quality of the converter.

- **Section 5.2** illustrates the classifications of MMC modulations regarding the implementation work that summarizes the vital positive and negative aspects of each method.

- **Section 5.3** explains in detail the output current control and identifies all the dynamics that the elements need in the controller in terms of grid connection.

- **Section 5.4** sets out the regulating process of the capacitor voltage balance in each SM and details their impact on the stability and controllability of the MMC.

- **Section 5.5** describes the voltage ripple problems on each SM capacitor and how they affect MMC performance.

- **Section 5.6** explains in detail the cause and effect of the existing circulating current flow in the MMC phases, and the controlling process for removing undesirable harmonic components.

5.1 Introduction

The control aspects of the MMC are considered in this chapter. The MMC has relatively complicated internal dynamics, unlike many other converter topologies. For this reason, the previous chapter started with a description of the converter topology for the purpose of clarifying the dynamic modeling and paving the path towards a better understanding of the MMC control.

The MMC control objectives can be divided into two main parts, as shown in Figure 5.1. The primary part consists of regulating voltages or currents at the input/output terminals of the converter. The first part includes controlling the voltage of the capacitor at each SM, as those capacitors have a great impact on the MMC work stability. It may be appropriate to regulate the DC and AC voltages or currents, depending on the specific application. In addition, the converter acts as an energy interface between input and output, using the SM capacitors as energy storage modules, which is why the average capacitor voltage must be regulated. The second part consists of reducing the capacitor voltage ripple and the circulating current. Meanwhile, the circulating current control is considered as an internal control to improve the performance of the converter.

Therefore, control of the MMC may be separated into many parts based on the control objectives by controlling all of the following: the output voltages using the output currents, the average (balancing) capacitor voltage, the capacitor voltage ripple, and the circulating (internal) current.

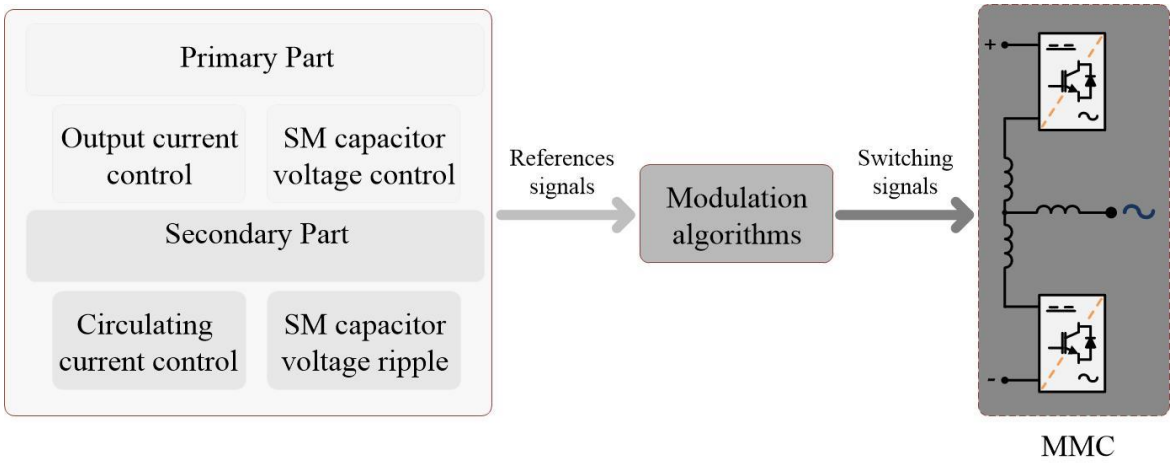

Figure 5.1: The block diagram of the MMC control system.

The modulation algorithms block appears in Figure 5.1. This is responsible for producing the switching signal for each SM to be inserted or bypassed, and plays an important role in balancing the SM capacitor voltage based on separate modulations of the upper and lower arms [119].

These objectives can be implemented using either classical control methods, such as the PI controller, or advanced control methods related to module predictive control. This chapter provides an outline of the classical regulation methods and their limits. Each control part is accomplished using an individual PI regulator. In addition, various modulation techniques are proposed to produce the control signal for the SMs.

5.2 Modulation Methods for MMC

The modulation technique is widely used to control the output voltage of the converter. The modulation work is based on generating specific signals to turn switching devices on or off to get the targeted AC voltage at the output. The modulation schemes are designed to reduce the total harmonic distortion of the output voltage and to increase the magnitude of the output voltage at a given switching frequency. In addition, the SM capacitor voltage balance can be regulated, power losses can be minimized by reducing the switching frequency of devices, and the minimization of the output current ripple can be achieved with different modulation methods [120], particularly if the modulation methods can pinpoint the exact time to switch levels.

The modulation schemes are graded based on the applications used with the MMC. As seen in Figure 5.2, the scalar methods are phase-voltage modulation techniques, i.e., they work to individually modulate each phase, and can be divided into two types: carrier-based methods that typically use high switching frequencies and carrier-less methods that correspond to simple switching frequencies [121].

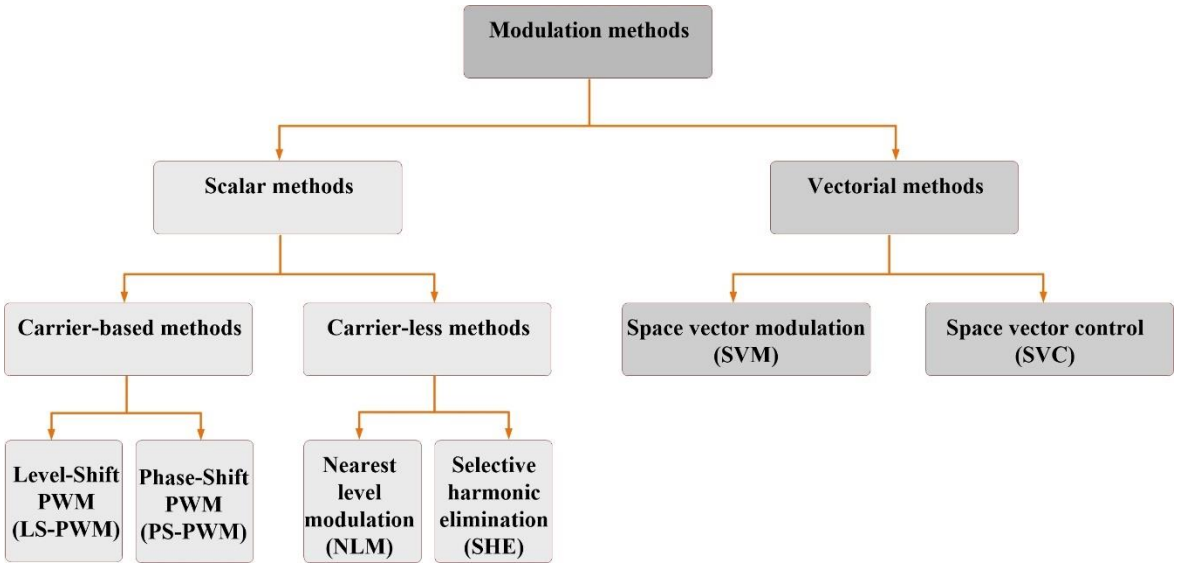

Figure 5.2: Different modulation schemes for controlling MMC.

While the vectorial methods work line to line voltage, i.e., they simultaneously work with all phases [122], selecting the right modulation method depends on the level, or the number of SM per arm, applied by the MMC. A low level of conversion would indicate choosing high-frequency modulation in order to reduce the harmonics distortion at the MMC output. Conversely, a low-frequency modulation would be chosen to reduce the switching losses when a high level of conversion is applied [123]. Low, medium, and high conversion levels define the low, medium, and high-power application used by MMC, respectively.

5.2.1 Carrier-Based Methods

Carrier-Based PWM (CB-PWM) methods are modulation techniques at high switching frequencies that are based on triangular-wave carrier signals with shifted phase or level, as shown in Figure 5.3. The technique works on the basis of comparing modulation signals with a single triangular carrier signal, in the case of the two-level converter, to generate the gating signals for the switching devices. While the comparison can be extended to the multiple triangular carrier signals, in the case of the multilevel converter, each carrier will present one level of conversions. This method is regarded as a multicarrier PWM scheme [87].

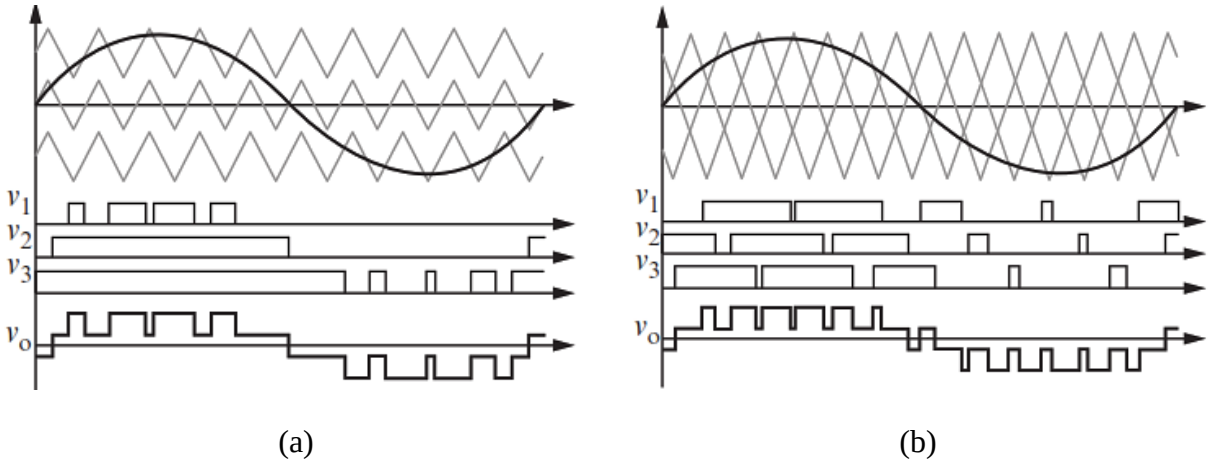

(a) (b)

Figure 5.3: CB-PWM techniques for MMC: (a) LS-PWM, (b) PS-PWM [124].

Overall, carrier-based modulation techniques are simple and straightforward to implement using the MMC control system. The disadvantages include the significant switching losses compared to simple frequency modulation, and the change in the number of SMs impacts the modulation scheme carrier structure, which means that adding or deleting one carrier completely changes the modulation framework. As a result, the carrier PWM modulator must be modified in accordance with the converter configuration, adding to the difficulty of expanding the present MMC system to a higher voltage scale [125].

Depending on the carrier arrangement, the CB-PWM is divided into two groups: level-shift PWM (LS-PWM) and phase-shift PWM (PS-PWM), as presented in Figure 5.3. The LS-PWM is detected by positioning multi-carriers at adjacent vertical heights; while the PS-PWM is characterized by having multi-carriers shifted in phase angles. The individual descriptions are presented in the next sections.

5.2.1.1 Level Shift PWM

The Level Shift-PWM (LS-PWM) strategies were mainly the carriers that have the same amplitude and frequency, but were positioned at a different height. Those strategies have been used with such early multilevel converter as NPC, FLC, and CHB [126]. For CHB converters, the LS-PWM is not an acceptable choice because they create an uneven distribution of power between the SMs, resulting in an increase in harmonic distortion on the output side [127]. In MMC, however, this problem was partly solved by combining it with selective control of the SMs in each arm [128].

As can be seen in Figure 5.4, the different LS-PWM strategies are listed briefly in the following sections:

Phase Disposition (PD): all the carriers in this type have the same phase angle with different offset levels, as seen in Figure 5.4(a). The configuration of the carrier produces considerably greater harmonic distortion at the frequency of the carrier.

Phase Opposition Disposition (POD): in this case, the carriers above the zero line of the reference wave were shifted to 180°degrees with respect to those carriers below the zero line of the reference wave, as seen in Figure 5.4(b). The arrangement of this carrier indicated a decrease in the harmonic distortion at the frequency of the carrier by increasing the symmetry between the upper and lower arm modulators; however, the result shows that the distortion at the frequency of the carrier is still high.

Alternative Phase Opposition Disposition (APOD): this approach uses zero and 180°-degree alternating phase changes between each neighboring carrier, as seen in Figure 5.4(c). This arrangement of carriers provides better results than the previous one due to the better symmetrical attitude of the carriers by moving the greater harmonic distortion to the sideband along the frequency of the carrier [110].

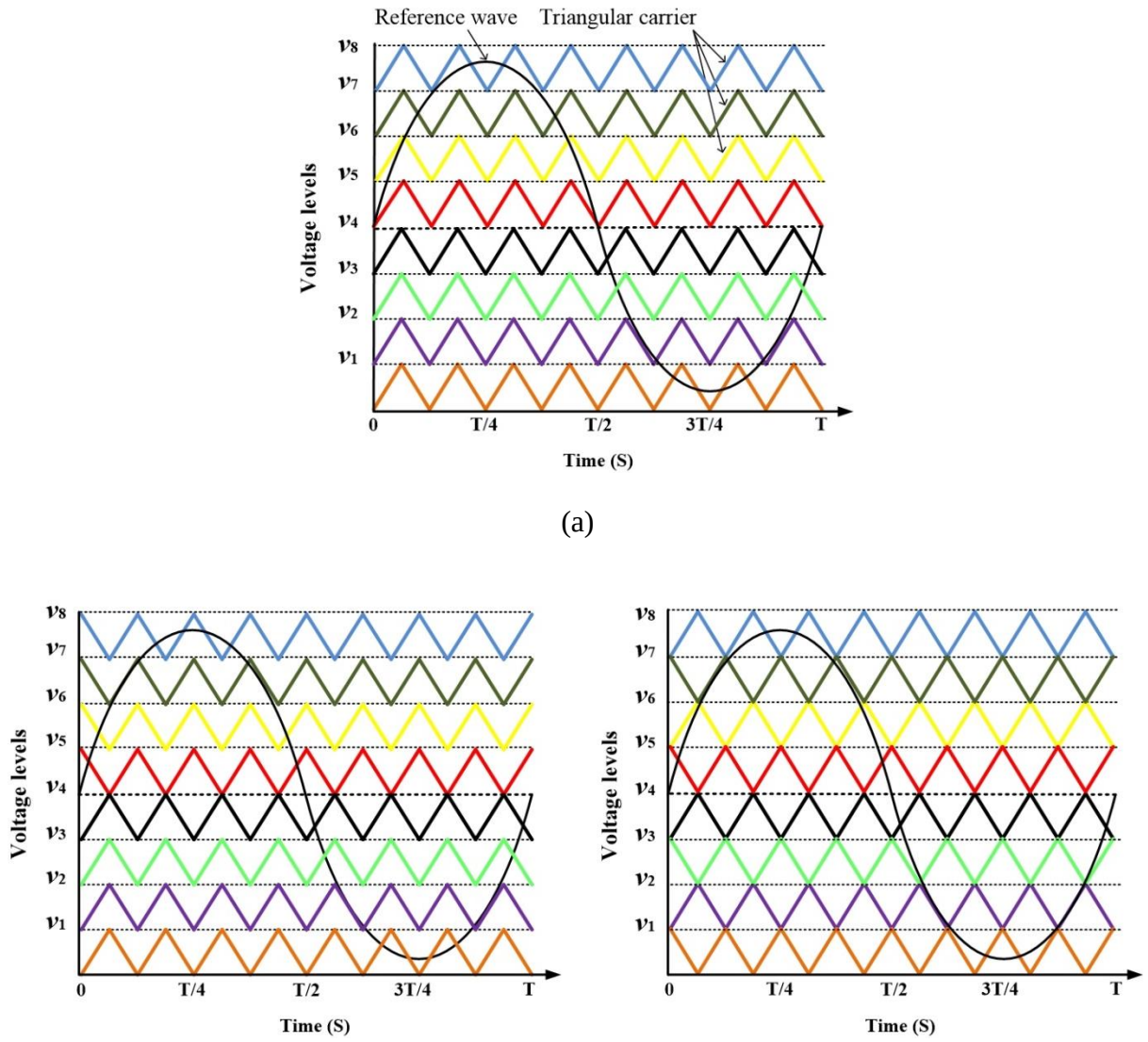

Figure 5.4: Level-shifted PWM strategies: (a) phase disposition (PD), (b) phase opposition disposition (POD), (c) alternate phase opposition disposition (APOD).

Other carriers and hybrid LS-PWM arrangements are presented in [128], such as carrier overlapping and variable frequency PWM, which show strong outcomes in certain situations based on a high modulation index and low/high frequency switching, respectively. However, no references found for these strategies were practically applicable to MMC.

5.2.1.2 Phase Shift PWM

This strategy has horizontal arrangement of carrier signals of identical triangles with the same frequency and amplitude, and an angle shift, ϕ, equal to ($360°/N_{sm}$) between the carriers, where N_{sm} is the number of SMs in each arm. The intersection of each carrier with the voltage reference wave, V_{ref}, produces the switching signals for each SM, see Figure 5.5. This method has advantages over other LS-PWM modulation techniques [129], as it provide a great balance between the SM capacitor voltage and the harmonic distortion reduction.

The highly symmetrical carriers in this modulation method lead to an equal distribution of the voltage stress on the semiconductors and the power handled by each SM. Furthermore, the practical results are better in the DC-bus current ripple [121].

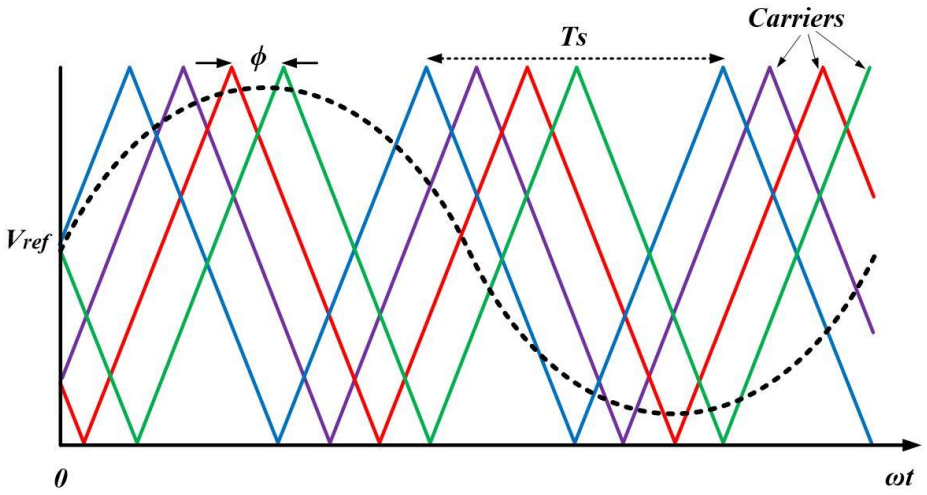

Figure 5.5: Phase-Shift PWM strategy.

These CB-PWM techniques, because of the high number of SMs, are not suitable for MMC-HVDC application [130]. Since one carrier is allocated to one SM in a similar manner, the SM string can create unequal switching patterns. The SM switching patterns will be somewhat different, allowing unequal loading and switching losses to be spread unevenly. More specifically, though, this method does not provide the potential for balancing the energy of the capacitors. This is because the DC and fundamental components of the output voltage of the SMs would differ considerably. Therefore, methods that decouple the waveform generation from the SM selection are used in [125], since the power balances cannot be fulfilled simultaneously. These strategies can also be implemented with an interleaving angle, i.e., the carriers used in the upper arm have opposite phase angles of 180°degrees, with the lower arm carriers, which improves the output voltage harmonic spectrum. This is because it duplicates the output voltage level, and naturally balances the SM capacitor voltages by decreasing the select time for each SM [121][131]. However, this process raises the ripple of the capacitor voltage in the SM, which also increases the

amplitude of the circulating currents. For these purposes, assigning carriers to SMs is not an attractive method [110].

5.2.2 Carrier-Less Methods

The carrier-less modulation strategy works at low/fundamental frequencies to reduce the semiconductor switching losses. The absence of the carriers makes this scheme very effective for such high-power converters as CHB and MMC [122]. This is because the increase in the conversion level enhances the effect of the harmonics at the output and makes no extra work for the configuration of the converter as compared to the carrier-based method. The Selective Harmonic Elimination (SHE) and staircase modulation, or nearest level modulation (NLM), schemes belong to this category [87][132]. The individual descriptions are presented in the next sections.

5.2.2.1 Selective Harmonic Elimination

The Selective Harmonics Elimination (SHE) is a carrier-less method working at fundamental frequency [133]. The method involves the calculation of switching angles, α, as seen in Figure 5.6 [134]. This calculation can greatly reduce the undesirable low frequency harmonics, but the mechanics are complicated and slow [135], since the calculation attitude for solving the equations to find the angles, α, is nonlinear and depends on iteration. The method shows a good behavior with a CHB converter [136].

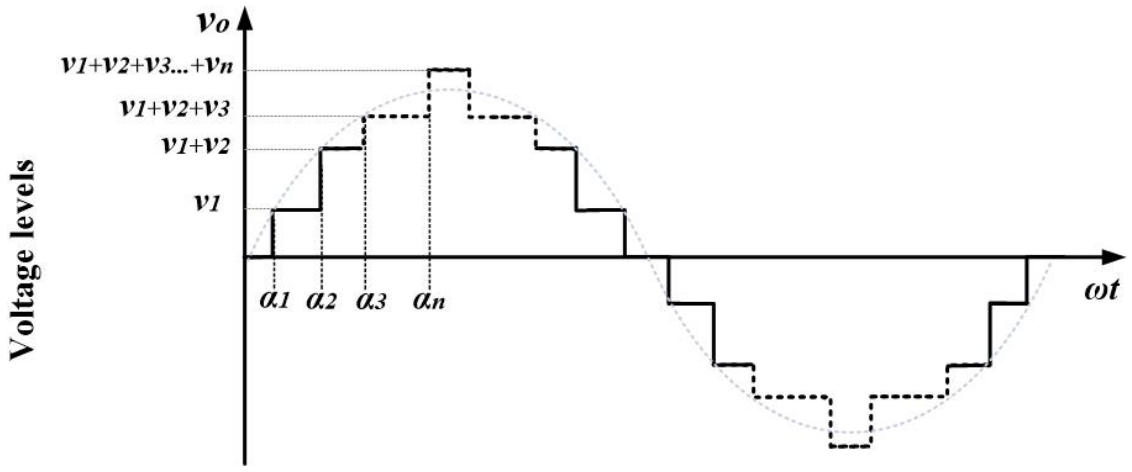

Figure 5.6: The SHE method creates a staircase sinusoidal output waveform for a multilevel converter by using switching angles (α) [134].

Applying this scheme with MMC [137] to a low and medium voltage scale application [138]would be preferable rather than being applied with HVDC. This is because the complex calculation of defining the switching angles, which in turn is due to the complex process with a huge number of voltage levels. In other words, the number of switching angles increases greatly with the increase in the number of voltage levels [138].

As a result, the SHE scheme is not an optimal solution for a high voltage MMC application, especially for PV panel applications, since the voltage levels change constantly, possibly resulting in incorrect angle calculations. The staircase modulation method, on the other hand, is simple to apply and does not need any complex calculations [87].

5.2.2.2 Nearest Level Modulation

The staircase modulation, or Nearest Level Modulation (NLM) as seen in Figure 5.7, is switching the power converters at a fundamental frequency to minimize switching losses [139]. The principal work of the NLM method is to generate the voltage level when switching at the closest point to the voltage reference (V_{ref}) over the whole switching time. As a result, this strategy relies on an estimate of finding the closest point to the voltage reference rather than on modulating the reference.

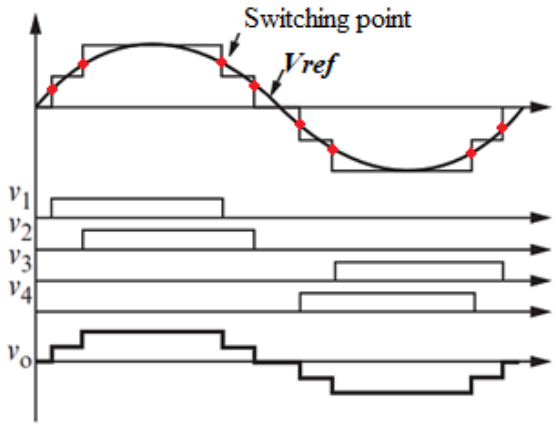

Figure 5.7: The NLM method generates a staircase sinusoidal output waveform for a multilevel converter by switching at the closest point to the voltage reference (V_{ref}).

However, the Total Harmonic Distortion (THD) of the output voltage and current waveforms is significantly high. Since the HVDC system needs a large number of SMs in each arm to achieve a high-power level, resulting in very low THD at the output voltage, the NLM scheme is commonly used in MMC-HVDC applications [140]. Otherwise, a large filter at the

converter output will be used. As can be seen in [141], the NLM technique has been applied to a 401-level MMC-HVDC system with THD less than 1.25%.

However, increasing the level to get more sinusoidal output can also be done by designing the NLM with an interleaving angle to improve the output voltage quality, which generates an output voltage with a double number of voltage levels in comparison to the non-interleaving angle [21]. At each switching cycle, the interleaving work is based on increasing the level by approximating two nearest levels instead of one, which introduces the PWM operation and leads to a reduction of the THD.

In addition, fundamental frequency modulation schemes need a higher sampling frequency to produce an output voltage equivalent to its target [142]. Thus, in this situation, the capacitor voltage ripple in the SM and the circulating current amplitude would both increase.

To sum up, different modulation schemes have been presented for MMC [143]. The fundamental switching frequency modulation regimes are the best alternative for the HVDC application. Furthermore, the NLM considers a suitable strategy, since these methods do not include average value calculations compared to SHE and no complexity of configuration.

As well as increasing the capacitor voltage balance, the low-frequency modulation schemes could be combined with the sorting methods for all the SM voltage capacitors, and the SM can be on or off depending on the current flow direction, as explained in [124]. The SM capacitor voltage balance control will be discussed further in section 5.4.

5.2.3 Space Vector Modulation

The Space Vector Modulation (SVM) works with line-to-line voltages and can represent another adapted carrier-based technique, which is applied at low-frequency switching compared to the carrier-based techniques. SVM eliminates the effect of common-mode voltages, used by phase-voltage modulation by directly regulating the line-to-line voltages relative to the above-mentioned modulation methods, as well as allowing more freedom to improve the output of the MMC [144][145].

However, the SVM reveals greater difficulties, in particular when considering a large number of SMs. In other words, because of the park transformation, in each calculation of the reference vector position, the new orientation axes of the *d-q* plane need to be rotated by a certain angle, so the procedure is not easily applied to higher-level inverters, see Figure 5.8.

The complexity created by the greatly increased number of switching states and sequences that surround the higher number of levels [145] is an obstacle to applying SVM to MMC- HVDC applications. However, new computing algorithms, described as fast and simple, and proposed in [146] to compute SVM duty cycle based on hexagon vectors close to the reference voltage rather than the normal three nearest vectors, simplify the selection of the central space vector and increase the possibility of using SVM with a high-level inverter.

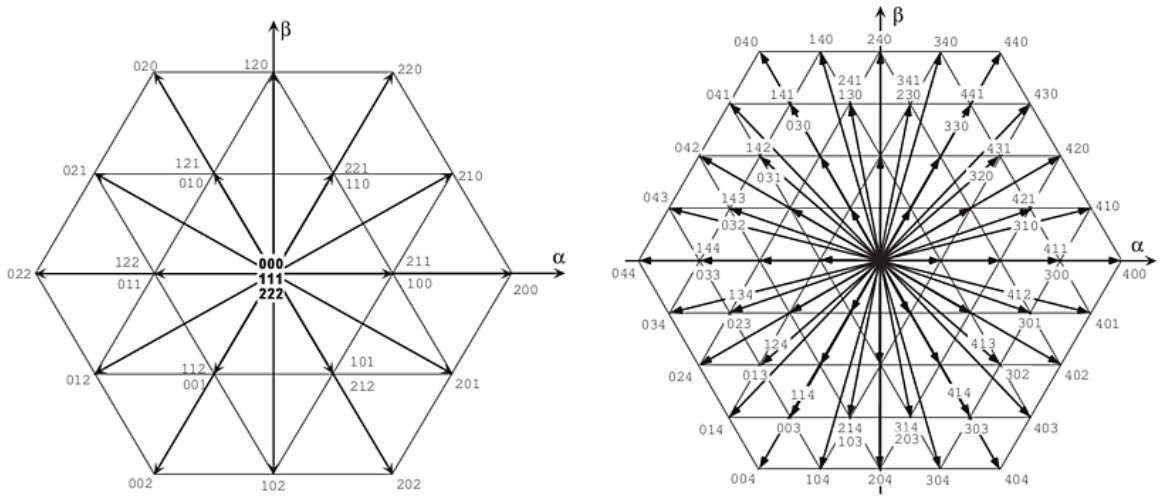

(a) (b)

Figure 5.8: Space vector modulation states for (a) Three-level inverters (b) Five-level inverters [147].

In addition, [144] presents a new SVM scheme that is suitable for any reference vector with any modulation index and can be easily generalized to satisfy particular specifications, such as symmetric switching sequences, and has been implemented with a 101-level inverter in a real-time scheme.

5.2.4 Space Vector Control

Space Vector Control (SVC) is a vectorial method, which deals with line-to-line voltages and can represent another adapted carrier-less technique. It is applied to fundamental frequency switching.

According to Figure 5.9, the function theory is based on estimates of the voltage related to the nearest accessible state vector. This vector strategy is explicitly defined for use with the large number of voltage vectors produced by multilevel converters. This principle enables the SVC to work under fundamental switching frequencies, so power losses will decrease further due to the lower losses from switching. The basic concept of the SVM operates in a similar way to the NLM methods, approximating the close voltage level instead of the vector that can be generated by the converter [143]. Indeed, the NLM represents the time domain version of SVC. At the same time, the switching sequence can be generated online, resulting in a comparatively simple implementation of SVC compared to SHE in closed-loop and high-bandwidth applications [148].

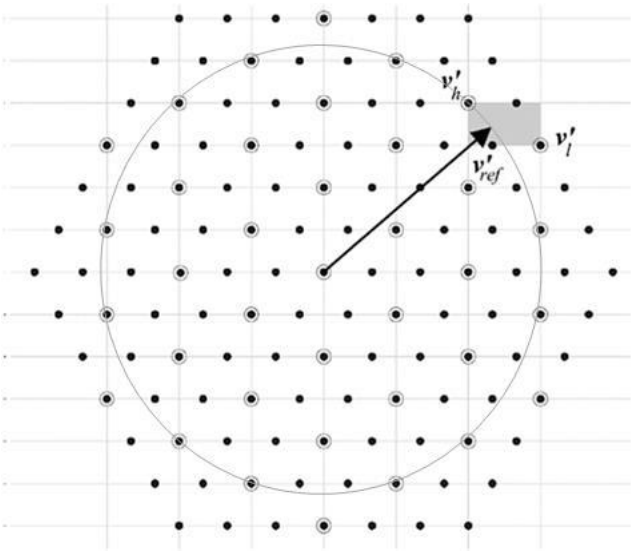

Figure 5.9: The SVC is based on estimates of the voltage related to the nearest accessible state vector; comparing the distances of each candidate vector v'_h and v'_l with respect to v'_{ref}, where the nearest vector is chosen [149]**.**

Both SVC and NLC are ideal for MMC with a high number of SM string connections on the basis of an approximation instead of a modulation. On the other hand, owing to the low and variable switching frequency, while the voltage levels and/or modulation indexes are low, these two strategies suffer from high THD. Therefore, to minimize THD by increasing voltage levels, it is advisable to work with the HVDC applications.

In general, depending on the converter parameters such as topologies and applications, each modulation scheme has its own set of advantages and disadvantages. In fact, due to lower switching loss and lower THD (in the case of high conversion levels), low switching frequency modulation techniques are preferred for high-power applications; whereas high switching frequency algorithms allow better output power quality and higher bandwidth and are therefore more suitable for applications of low or medium voltage scale.

5.3 Output Current Control

Depending on the application, the MMC has a separate strategy for current and voltage regulation. As in [22], the voltage-oriented control is used for the HVDC application; while in the STATCOM application, the current control is used to satisfy the requirements for reactive power [150]. Typically, the control strategies are established and implemented in the three-phase stationary-*abc*; by using the Clark and Park transformation, the reference frames are produced in the $\alpha\beta$-stationary, and the synchronous *dq*, respectively, for easy control [87].

Figure 5.10 indicates the key current control schemes that can be used in the modulation system to fire the switching signals for the generation of the three-phase voltage reference.

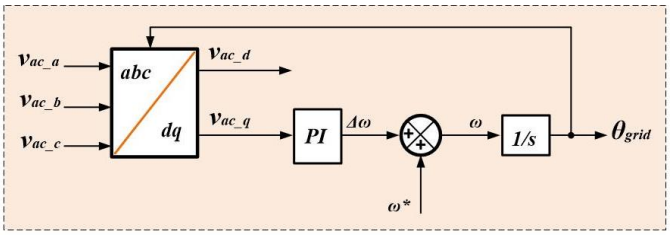

(a)

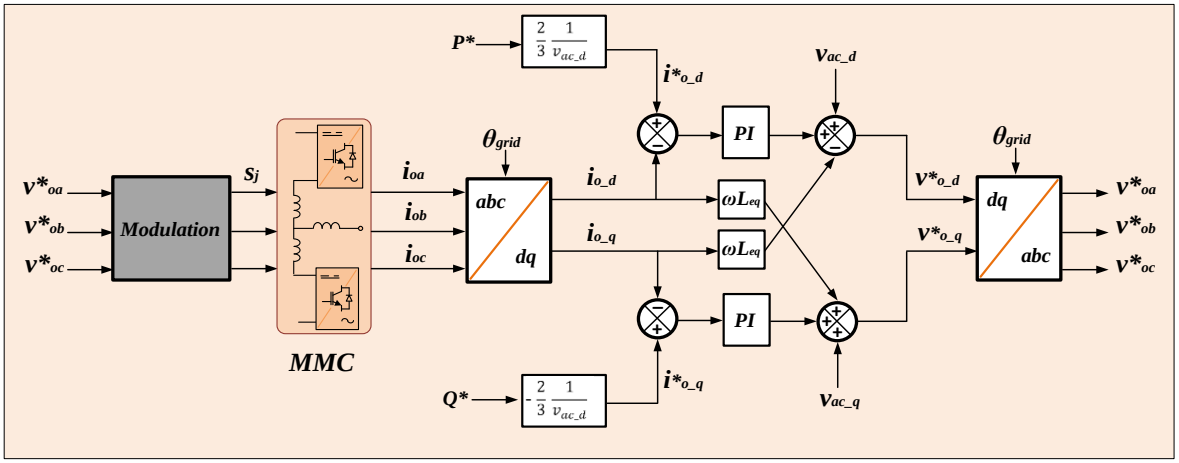

(b)

Figure 5.10: MMC control scheme (a) dq-PLL synchronization (b) Output current control.

Connecting the MMC with the grid must essentially be synchronized using a phase-locked loop (PLL); thus the phase angle, $\theta_{grid,}$ is needed to successfully transform the quantities from the *abc* frame to the *dq* synchronous reference frame, as shown in Figure 5.10(a) [151]. In the other words, PLL can be specified as a feedback system used to synchronize the MMC converter to the grid connection.

The PLL transforms the grid three-phase voltage values represented by the *abc*-frame into the *dq*-frame. Thus, the q-axis component is forced to be null, with the PI regulator to remove any reactive power. The PI controller in the PLL measures the rotation speed of the *dq*-axes by calculating the phase angle of the grid, as seen in Equation (5.1), such that the q-axis component of the grid voltage vector is preserved at zero.

$$\omega = \frac{d\theta_{grid}}{dt}$$
$$\omega = s \,.\, \theta_{grid} \tag{5.1}$$
$$\theta_{grid} = \frac{1}{s}\,\omega$$

In fact, the PLL does not measure the frequency, ω. However, it can regulate the frequency difference, $\Delta\omega$, through a PI controller, and this brings it back to the point where the PI controller is slow. Thus, the PI controller can rapidly find the difference and move the system into a steady state; otherwise, measuring the frequency could make the system unstable for a long time. The PI output value can thus be positive, which means the rotation of the d-axis needs to be speeded up in order to realign with the grid voltage; or it could be negative, which means the rotation of the d-axis needs to be slowed down in order to realign with the grid voltage. It is also necessary to know the grid frequency reference value ($\omega = 2\pi \cdot f$) to find the frequency and phase angle to apply to the MMC voltage references. This criterion is interpreted as a grid synchronization. That is, the d-axis information is aligned with the real grid voltage vector in the control algorithm. In this way, a reference point can be provided by independently monitoring the active and reactive current elements. For instance, to regulate the active power, the current part associated with the grid voltage vector is used.

The MMC voltage regulation needs to control the output current, which is calculated from the measurements of the current flow through each arm. The arm currents have two major components: the output and circulating currents, as can be seen in Equations (5.2) and (5.3).

$$i_{ux} = \frac{i_{ox}}{2} + i_{zx} \tag{5.2}$$

$$i_{lx} = -\frac{i_{ox}}{2} + i_{zx} \tag{5.3}$$

where i_{ux} and i_{lx} represent the upper and lower arm currents, respectively, and x refers to phase 'a', 'b', or 'c'.

If the arm currents are measured, then these components can be isolated and regulated. If the MMC is replaced by a regulated voltage source, such as v_{oa}, v_{ob}, and v_{oc}, as seen in Figure 4.5, an equivalent MMC topology can essentially be modeled, as in Figure 5.11, where the grid voltage is expressed by v_{ac_a}, v_{ac_b}, and v_{ac_c}. The MMC output voltages can be represented by Equations (5.4), (5.5), and (5.6), where the corresponding resistance, R_{eq}, describes a sum of half of the arm impedance and the output impedance.

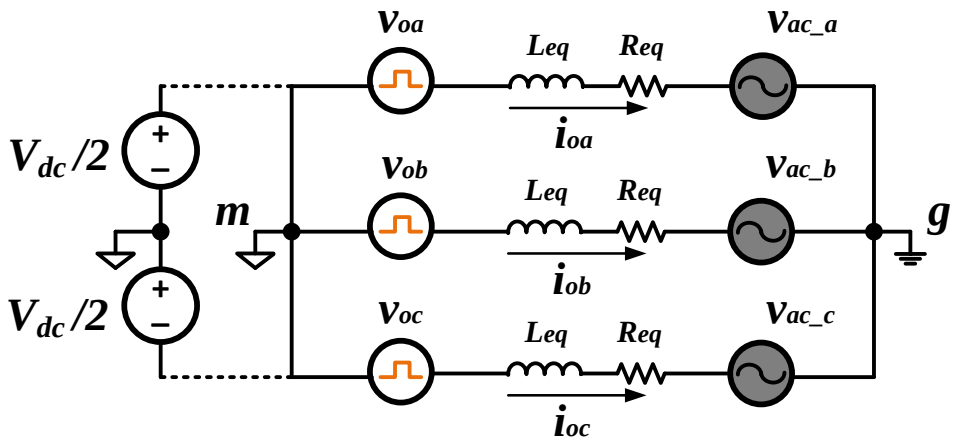

Figure 5.11: The basic three phase MMC equivalent circuit connected to an AC grid.

$$v_{oa} = R_{eq} i_{oa} + L_{eq} \frac{di_{oa}}{dt} + v_{ac\_a} \tag{5.4}$$

$$v_{ob} = R_{eq} i_{ob} + L_{eq} \frac{di_{ob}}{dt} + v_{ac\_b} \tag{5.5}$$

$$v_{oc} = R_{eq} i_{oc} + L_{eq} \frac{di_{oc}}{dt} + v_{ac\_c} \tag{5.6}$$

$$i_{oa} + i_{ob} + i_{oc} = 0 \tag{5.7}$$

Due to Equation (5.7), the sum of the three-phase currents is zero, which means that the three phases are not independent. Therefore, transforming to the *dq* frame representation is mainly used to test the entire system, while it also reduces the number of independent variables from three variables (*a*, *b*, and *c*) to two (*d* and *q*). The fundamental concept behind using the *dq* representation comes from electrical machine analysis, where the vectors represent the sum of the fluxes of the three phases and are expressed in a two-dimensional coordinate system.

The three-phase currents can be described in Equations (5.8), (5.9), and (5.10), considering that the currents are balanced and in a positive sequence.

$$i_{oa} = \widehat{I_o} \cos(\omega t + \theta) \tag{5.8}$$

$$i_{ob} = \widehat{I_o} \cos(\omega t + \theta - 2\pi/3) \tag{5.9}$$

$$i_{oc} = \widehat{I_o}\, cos(\omega t + \theta - 4\pi/3) \tag{5.10}$$

The three phase currents can also be represented in the space vector as magnitude and phase. Normally, transforming the three-phase current from the *abc* frame to the *dq*-synchronous frame means it will pass through the stationary *αβ*-frame axes, which is known as the Clark Transformation (*abc*–to–*αβ*) [151]. Whereas the *α* and *ß* axes are stationary representations, the *d* and *q* axes represent the synchronous reference frame rotating with the space vector. Generally, the *d*-axis is synchronized with a reference vector which may be a rotor grid voltage vector. Therefore, the projections of the space vector on the *d* and *q* axes become the DC quantity, which is easier to deal with. This transformation is also known as the Park Transformation (*αβ*–to–*dq*).

The direct transformation of the output currents from the *abc*-frame to the *dq*-frame (*abc*–to–*dq*) may be done as shown in Equation (5.12), using the transformation Equation (5.11), where *T* represents the matrix transformation from the *abc*–to–*dq* frame.

$$T = \frac{2}{3}\begin{bmatrix} cos(\theta) & cos(\theta - 2\pi/3) & cos(\theta - 4\pi/3) \\ sin(\theta) & -sin(\theta - 2\pi/3) & -sin(\theta - 4\pi/3) \end{bmatrix} \tag{5.11}$$

$$\begin{bmatrix} i_{o\_d} \\ i_{o\_q} \end{bmatrix} = T \begin{bmatrix} i_{oa} \\ i_{ob} \\ i_{oc} \end{bmatrix} \tag{5.12}$$

Similarly, applying the Park transformation over the three-phase voltages, by using the transforming matrix in Equation (5.13), it may be performed as in Equation (5.14).

$$T \begin{bmatrix} v_{oa} \\ v_{ob} \\ v_{oc} \end{bmatrix} = R_{eq} T \begin{bmatrix} i_{oa} \\ i_{ob} \\ i_{oc} \end{bmatrix} + L_{eq} \quad \frac{d}{dt}\left(T \begin{bmatrix} i_{oa} \\ i_{ob} \\ i_{oc} \end{bmatrix} \right) \qquad + T \begin{bmatrix} v_{ac\_a} \\ v_{ac\_b} \\ v_{ac\_c} \end{bmatrix} \tag{5.13}$$

$$\begin{bmatrix} v_{o\_d} \\ v_{o\_q} \end{bmatrix} = R_{eq} \begin{bmatrix} i_{o\_d} \\ i_{o\_q} \end{bmatrix} + L_{eq} \left(\frac{d}{dt} \begin{bmatrix} i_{o\_d} \\ i_{o\_q} \end{bmatrix} + \begin{bmatrix} -\omega\, i_{o\_q} \\ \omega\, i_{o\_d} \end{bmatrix} \right) \quad + \quad \begin{bmatrix} v_{ac\_d} \\ v_{ac\_q} \end{bmatrix} \tag{5.14}$$

Equation (5.14) describes the overall structure of the current controller in the *dq*-frame, as illustrated in Figure 5.10(b). However, Equation (5.14) indicates there are decoupling terms ($\omega L_{eq} i_{o\_d}$ and $\omega L_{eq} i_{o\_q}$) to compensate for the voltage drop in the reactors and the grid voltages (v_{ac_d} and v_{ac_d}) as disturbances. The decoupling can describe the effect of axes *d* and *q* on each other, due to the derivative which actually represents a rotation of 90° degrees. In addition, the output of the PI controller, Δv_{o_d} and Δv_{o_q}, becomes the only one that affects the voltages on i_{o_d}

and i_{o_q} after using the feed-forward terms. Here, the purpose of the PI is to compensate for the effect of the resistance, R_{eq}, which is due to the hard measurements of the temperature effect. Therefore, in the control part, the feed-forward terms are used to generate the reference voltage v_{o_d} and v_{o_q} terms. In the end, the v_{o_d} and v_{o_q} will transfer back to the *abc*-frame to generate the reference voltages v^*_{oa}, v^*_{ob}, and v^*_{oc}, which are produced by the current controller in Figure 5.10. This reference information will be combined with the circulating current controller outputs (presented in Section 5.6) to determine the arm voltage reference through the modulation block.

On the other hand, the reference current in the *dq*-frame ($i^*_{o\_d}$ and $i^*_{o\_q}$) used in Figure 5.10(b) can be generated using the references of active power, P^*, and reactive power, Q^*. Here, Equations (5.15) and (5.16) describe the active and reactive power in the *dq*-frame, respectively.

$$P = \frac{3}{2}\left(v_{ac\_d} \cdot i_{o\_d} + v_{ac\_q} \cdot i_{o\_q}\right) \tag{5.15}$$

$$Q = -\frac{3}{2}\left(v_{ac\_d} \cdot i_{o\_q} - v_{ac\_q} \cdot i_{o\_d}\right) \tag{5.16}$$

If power loss in the MMC is artificially neglected, the active power on the DC side should be equal to that on the AC side. Thus, the v_{ac_q} is forced to be zero by the dq-PLL, as it aligns the d-axis with the grid voltages, and the only vector to influence the power is the current at the d-axis, for active power, or current in the q-axis to regulate the reactive power. Therefore, the power terms in Equations (5.15) and (5.16) can be simplified to define the power references in the *dq*-frame as shown in Equations (5.17) and (5.18).

$$P^* = \frac{3}{2} v_{ac\_d} \cdot i^*_{o\_d} = V_{dc} \cdot i_{dc} \tag{5.17}$$

where, V_{dc} and I_{dc} are the DC-link voltage and current entering from the DC side, respectively.

$$Q^* = -\frac{3}{2} v_{ac_d} \cdot i^*_{o_q} \tag{5.18}$$

since the v_{ac_d} value is constant and known to the controller through the PLL, the active and reactive power can be controlled linearly by changing i_{o_d} or i_{o_q}, respectively.

5.4 SM Capacitor Voltage Control

The operating voltage of the MMC can easily be increased by connecting more SMs in each arm, which will also increase the level of conversion. These SMs have floating capacitors, and their voltages should be balanced with a controller at their nominal value. The SM capacitor voltage control is an essential requirement to achieve a high-performance current control, as they represent the most important part of the converter. The controller over all these capacitors will then improve output power quality and provide stability and controllability to the MMC efficiency.

The voltage balancing of each SM capacitor in the MMC arms depends in general on two stages; first, each SM capacitor voltage must be controlled and sustained at the reference value, usually equal to V_{dc}/N_{sm}; second, the selection methods to manage switching on or off for each SM. Based on the capacitor voltage balancing, the selection methods are divided into individual and centralized selection control approaches.

The individual selection method is dependent on the direct selection of individual SMs, so this method can only be applied with the PS-PWM schemes [152][153]. As the PS-PWM technique has a high symmetrical carrier for the upper and lower arms, this makes it possible for each of the carriers to directly associate with an individual SM in order to switch it on or off frequently.

Regulating the SM voltage with individual selection methods can be defined as the distributed control approach. This controller fast and has better controllability, given that the SM switching frequency should be high enough, due to the charge and discharge of the capacitor in the selection stage. On the other hand, a huge number of linking SMs raises the difficulty due to the increase in the number of carriers needed in the PS-PWM.

The centralized selection depends on the regulation and sorting of all the SM capacitor voltages within each arm in order to make the right selection. Figure 5.12 shows the flow-chart that describes the commonly used selection algorithm [148][154], where the selection, implemented after the modulation stage, is based on sorting the capacitor voltage values and the direction of the arm currents.

First of all, the selection or deselection of the SM to be inserted or bypassed depends on the voltage reference of the arm voltage compared to the carrier signal used in the modulation, since each intersection between those two signals produces a ‘select’ or ‘deselect’ order of the SM, depending on which one is greater. Then, the selection of the SM will be applied based on the current direction in each arm individually, choosing the greatest or smallest voltage among the sorted SMs, or deselecting, as follows:

- If the current is positive and the number of connected SMs in the arm increases/decreases to generate the required voltage level, the new connected ones will be those that have lower/higher voltages because the current will be charging/discharging the selection SMs.

- If the current is negative and the number of connected SMs in the arm increases/decreases, the new connected ones will be those that have higher/lower voltages because the current will be discharging /charging the selection SMs.

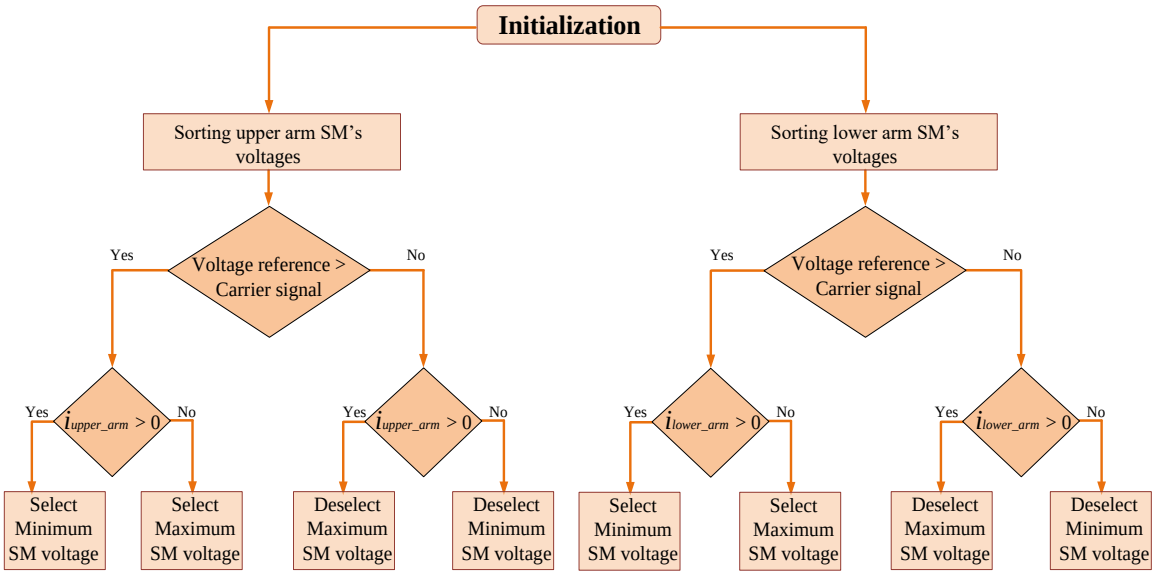

Figure 5.12: The centralized selection for balancing the SM capacitor voltages for both upper and lower arms separately.

The centralized control concept can be applied with the scalar and vectorial methods of modulation and still have a reliable outcome [87][155][156]. On the other hand, the sorting methods usually become overwhelming when the number of SMs increases.

5.5 SM Capacitor Voltage Ripple Control

One of the main issues related to power losses in the MMC is the SM capacitor voltage ripple [157]. Low-frequency operation of the MMC, specifically second and fourth-order harmonic components, can be observed to cause problems linked to the capacitor voltage ripples in the SM capacitor voltage.

Capacitors can be well regulated, as presented in the previous part, but the voltage peak value ripples become unacceptably high during charging, when the positive current flows within the arm, or discharging, when a negative current flows within the arm. The issue is that the arm current includes a circulating current with its low-frequency component, especially 100 Hz, which contributes to prolonged charging and discharging intervals in the capacitor voltage due to the increased period of output voltage and current. To overcome this problem, a sophisticated circulating current control method must be applied to limit the voltage ripple at the capacitors, as suggested in [158]. Here, the circulating current increases the peak value of the arm current, thus raising the voltage tension on the devices and introducing further conduction losses. So, the control approach uses circulating current to limit capacitor voltage ripple by forcing an artificial circulating current with a higher frequency than the output frequency, which eventually neutralizes the effects of the low output frequency operations and reduces the periods of capacitor charging and discharging. On the other hand, the SM capacitor voltage ripple can be minimized at the device

level by identifying the suitable size of the SM capacitor, which may lead to increases in the cost and size of the converter [87].

According to [154][159], an approximate value of the SM capacitor can be calculated using Equation (5.19), derived from the arm energy equation and depending on the energy deviation stored in each SM.

$$C_{SM} \geq \frac{|S|}{3\omega} \frac{1}{N_{sm} \cdot V_{SM}^2 \cdot \Delta V_{SM}} \tag{5.19}$$

where $|S|$ is the absolute apparent power of the MMC converter, V_{SM} represents the nominal SM capacitor voltage, and ΔV_{SM} is the desired voltage ripple in the SM capacitor.

5.6 Circulating Current Control

Another major issue in the MMC is the circulating currents among the converter legs as presented in the equivalent MMC circuit in Figure 5.13. These currents derive from the voltage differential at the arm inductors, between the upper and lower arms of the MMC legs.

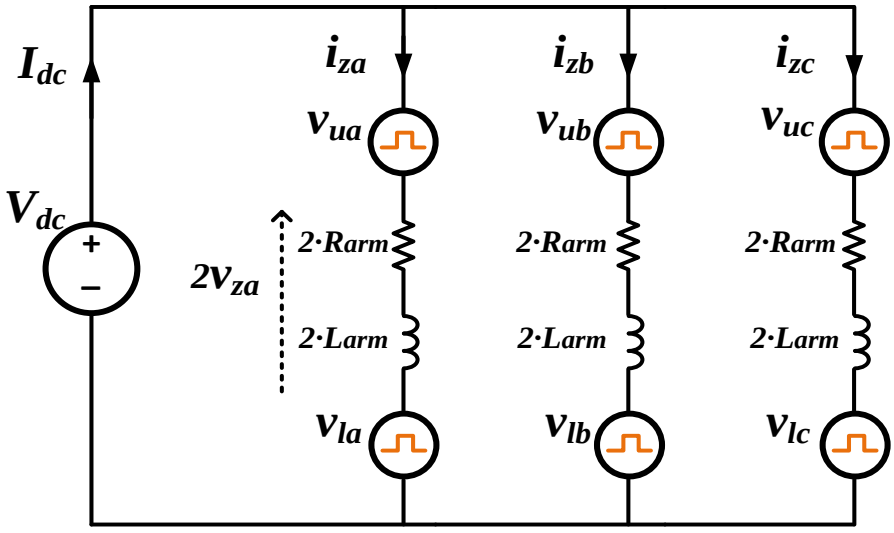

Figure 5.13: Equivalent MMC circuit for internal currents effect.

Regarding [42], the circulating currents typically have a DC component, representing the active power, when energy is transferred from phase to phase, or from an external energy source at the DC side to the MMC phases in order to exchange the energy with the AC side. In addition,

circulating currents may have an AC component at the fundamental frequency that can be used by the controller to transfer energy between the upper and lower arms to keep them balanced.

However, the most effective component over the MMC efficiency is the negative-sequence component, as some low-frequency fluctuations occur in the SM voltage at twice the fundamental frequency arise in the circulating current when using traditional modulators. Furthermore, under unbalanced AC grid conditions, they may also include a positive-sequence and even a zero-sequence component at twice the output frequency [26]. In fact, all components, other than the DC part, may well be classified as reactive power flow among the MMC phases.

Consequently, certain 100 Hz components in the circulating current with inadequate control contribute to raising the arm current magnitude value, which eventually increases the rating of the SM switches, the converter power losses, and the voltage ripple in the SM capacitor [160]. However, a closed-loop control technique is needed to eliminate, or at least minimize, the circulating currents entirely.

In [104], a different controller of the circulating current was established, where the circulating currents can be regulated in each arm, as they form a part of the input current of the upper or lower arms [161], or as a completely independent current controller scheme [162]. Both strategies have a similar performance, but the use of an individual controller simplifies the controller configuration. The popular way to monitor circulating currents is by using a series of proportional-resonant controls in the $\alpha\beta$-frame [163][164]. Besides, the circulating currents can be reduced in the modulation stage due to multilevel modulation [165]. On the other hand, the circulating current magnitude can be minimized to an extent by using arm inductors with a proper size [166].

Traditionally, the synchronous *dq*-frame based PI-regulator method is used for the complete elimination of the100 Hz component of the circulating currents, as can be seen in Figure 5.14.

These harmonic components are time-varying in nature, and difficult to control using PI regulators without any error or fault in the steady-state. Therefore, using the dq-frame, the time-varying signals are converted into DC signals, rotating at twice the fundamental frequency. The DC signals can be conveniently regulated using a simple PI-regulator [167].

The circulating current dynamics has been defined previously, in Chapter 4 Equation (4.8), and is based on the equivalent circuit in Figure 5.13. These dynamics can be modified as in Equation (5.20).

$$2 \cdot L_{arm} \frac{di_{zx}}{dt} + 2 \cdot R_{arm} \cdot i_{zx} = V_{dc} - v_{ux} - v_{lx} \tag{5.20}$$

where v_{ux} and v_{lx} are the total voltages of the cascaded SMs in the upper and lower arms for each phase, and they are the only components that will be used when applying the circulating current controller. Evidently, the circulating current regulation occurs in the summation expression of the

arm voltages and vanishes in the subtraction expression as the circulating current does not present any interaction with the output current.

Applying KVL in Figure 5.13, the sum of the arm voltages can be split into DC-link voltage and circulating current driving terms (referring to the circulating voltage), V_{dc} and v_{zx}, respectively. So the circulating current dynamics is again written as shown in Equation (5.21).

$$V_{dc} - (V_{dc} \; - \; 2v_{zx}) = 2 \cdot L_{arm} \frac{di_{zx}}{dt} \; 2 \cdot R_{arm} \cdot i_{zx} \tag{5.21}$$

Notice Equation (5.21) shows that $(V_{dc} - 2v_{zx})/2$ is common in the arm voltage reference of both arms, as can be seen in Figure 5.13. v_{zx} has been multiplied by coefficient 2 because it represents the control signal shared by the upper and lower arms. As a result, the current dynamics is reduced to Equation (5.22).

$$v_{zx} = L_{arm} \frac{di_{zx}}{dt} + R_{arm} \cdot i_{zx} \tag{5.22}$$

Through Equation (5.22), the three-phase circulating current model in the *abc*-stationary frame might be written as (5.23).

$$\begin{bmatrix} v_{za} \\ v_{zb} \\ v_{zc} \end{bmatrix} = L_{arm} \frac{d}{dt} \begin{bmatrix} i_{za} \\ i_{zb} \\ i_{zc} \end{bmatrix} + R_{arm} \begin{bmatrix} i_{za} \\ i_{zb} \\ i_{zc} \end{bmatrix} \tag{5.23}$$

Because the controlled part of the circulating current is based on the elimination of the second harmonic, the circulating currents for the phases 'a', 'b', and 'c' are separately formalized in Equations (5.24), (5.25), and (5.26).

$$i_{za} = \frac{1}{3} I_{dc} + \widehat{I_{za}} \; cos(2\omega t + \theta) \tag{5.24}$$

$$i_{zb} = \frac{1}{3} I_{dc} + \widehat{I_{zb}} \; cos(2\omega t + \theta + 2\pi/3) \tag{5.25}$$

$$i_{zc} = \frac{1}{3} I_{dc} + \widehat{I_{zc}} \cos(2\omega t + \theta + 4\pi/3) \tag{5.26}$$

The current phases are given according to the fact that the second harmonic is a negative sequence. The $\widehat{I_{zx}}$ is the peak value of the double line frequency circulating current. Note that the rotation is in a downward direction as the angle *(-2ωt + θ)* indicates. The control scheme, in Figure 5.14, indicates the circulating current regulated at *dq*-frame spinning at (*-2ωt*) speed, since the second harmonic is a negative series. The phase angle that dq-PLL produces is multiplied by negative two (*-2*), while being used in the park transformation (*abc*-to-*dq*), as well as in the inverse park transformation (*dq*-to-*abc*) at the control scheme to compensate for the values in the *abc*-frame.

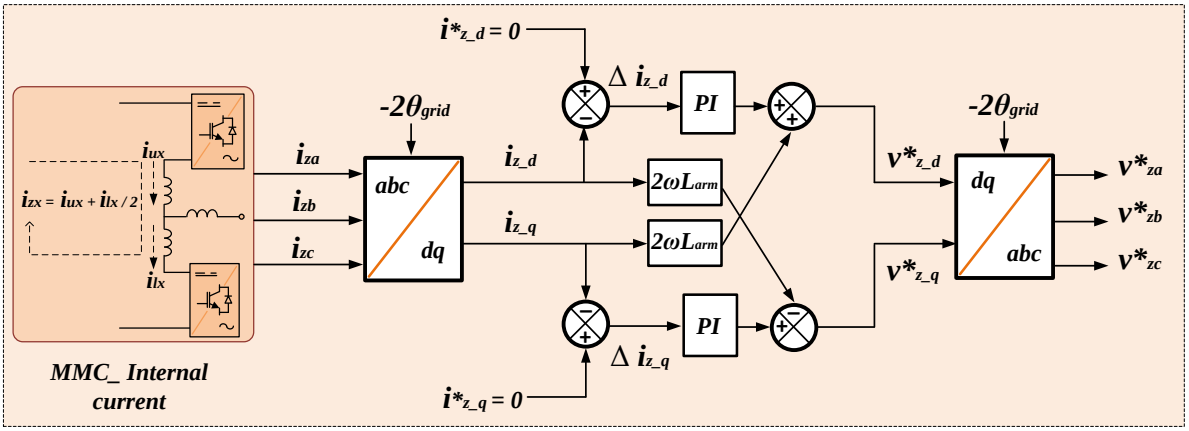

Figure 5.14: Closed loop circulating current control.

Notice that the DC components are disregarded in the analysis, since the controller targets the second harmonic portion in the circulating current. The phase angle *θ* used in this transform is equivalent to (*-2ωt*). In the end, applying the transfer function in Equation (5.11) over Equation (5.23) to represent the circulating dynamics in the *dq*-frame, can be seen in Equation (5.27).

$$\begin{bmatrix} v_{z\_d} \\ v_{z\_q} \end{bmatrix} = R_{arm} \begin{bmatrix} i_{z\_d} \\ i_{z\_q} \end{bmatrix} + 2L_{arm} \left(\frac{d}{dt} \begin{bmatrix} i_{z\_d} \\ i_{z\_q} \end{bmatrix} + \begin{bmatrix} \omega\, i_{z\_q} \\ -\omega\, i_{z\_d} \end{bmatrix} \right) \tag{5.27}$$

Obviously, the mathematical model in Equation (5.27) shows how the circulating current control scheme in Figure 5.14 has been configured [129][168]. This configuration indicates that the input circulating currents are derived from the measured upper and lower arm currents in each converter leg.

These currents are transformed to the synchronous *dq*-frame and give the i_{z_d} and i_{z_q} current components. The reference current components in the *dq*-frame, represented by $i^*_{z\_d}$ and $i^*_{z\_q}$, are set to zero, as the control target is to eliminate the circulating current. The error produced from the comparison between the reference and real currents, described as Δi_{z_d} and Δi_{z_q}, are reduced by applying PI-regulators. The *d* and *q* axes current control loops are decoupled by adding the induced speed voltages in the inductor to the current control loops. The PI regulator generates the reference voltage at the *dq* frame commands $v^*_{z\_d}$ and $v^*_{z\_q}$. The reference *dq* voltages are transformed back to the stationary-*abc* frame using the inverse Park transformation. The resultant reference voltages, v^*_{za}, v^*_{zb}, *and* v^*_{zc}, are used, along with the SM capacitor voltage balance controller and output current controller, to improve the efficiency and reliability of the MMC.

Proposed Local Carrier Modulation

Contents of This Chapter

- **Section 6.1** introduces the benefits of power conversion choices for processing PV energy by demonstrating the advantages of spreading MMC cells over PV energy; as well as the significance of using the proposed modulation in terms of increasing converter performance and efficiency with distributing PV panels.

- **Section 6.2** describes the MMC general controller in detail based on its application to PV panels, starting with the MPPT method, output current control, and voltage differences at the arm inductor by regulating the circulating current components. Its controller has been demonstrated in the module used with the proposed modulation.

- **Section 6.3** describes the proposed modulation technique in depth by describing the key method components for calculating the specific duty cycle, the needle eye passing to eliminate the circulating current glitches, and the sorting method development to reduce the capacitor voltage computation burden.

- **Section 6.4** implements different scenarios used to test the MMC performance in grid and load connections with the proposed modulation. These scenarios have also been used with PV applications in two ways: by connecting PV panels externally located outside of the MMC, and by distributing the MMC cell throughout the PV panel string.

6.1 Introduction

Grid connection requirements are the most important point for the configuration, control, and service of grid connected PV systems that must be achieved without exception. The THD level, for example, should usually be less than 5% [1]. Furthermore, under the rating condition with optimum MPPT, the power quality requirements demand that the efficiency and output power extraction must be kept at acceptable levels. The controllability of the power converters should be retained as the heart of the power conversion process, where reliability is essential [1].

The PV panel inverters connected to the grid systems typically consist of a pair of serially connected power converters, where the first represents a DC-DC converter that manages the PV panel to ensure that it works at its MPP; while the second represents a DC/AC inverter that converts all the available power to the grid system or isolated load [8], as described in Chapter 2. Synchronization is essential in terms of the grid connection, which means the inverter must synchronize its AC output with the grid in terms of phase, frequency, and amplitude to ensure that the collected solar power is efficiently transmitted, as described in Chapter 5, using a dq-PLL.

There are three main power conversion options to process PV energy: central, string, and module inverters, as described in detail in Chapter 2. Central inverters achieve a high efficiency at a lower cost, at the expense of high voltage DC cables [11], but they also need uniform irradiance. However, the power mismatch problem is important in this technology, due to its poor immunity to hotspots and partial shading, resulting in lower PV utilization. String inverter technology, on the other hand, achieves better MPPT control by applying the maximum power tracking separately to each string of PV connections, resulting in a higher total energy yield [8]. Conversely, this technology necessarily requires the use of more power electronics converters and reactors, resulting in higher costs and losses, and there are still PV panel mismatches at each string. Module inverter technology allows module-level monitoring and diagnostics. Since the module converter operates on a single PV panel with an independent MPPT control, the effects of partial shadowing and power mismatch are minimized in this technology. The biggest drawbacks of the module technology are poor overall efficiency [1] and the high cost due to replicating the structure of the converter for individual MPPT control.

Considering the above problems, a novel PV panel connection based on MMC has recently been proposed in [12][13] by distributing the MMC over the PV panels, integrating the PV strings directly on the converter cells. Integrating PV panels directly into the MMC topology has a lower installation cost than central inverters, which are based on two serially connected converters. Furthermore, central inverters usually require a DC-DC booster converter to regulate the PV voltage at its maximum before being connected to the MMC to generate a correct DC voltage for the inverter. This increases the cost, but delivers higher efficiency. In addition, the distributed topology achieves almost the same power optimization as string converters at a lower cost, and they can operate in a larger power and voltage range with fewer losses than all previous topologies, due to the removal of the DC-DC converters as mentioned before. In fact, the string and module technologies can be described as multiple DC-DC converters plus one DC to AC inverter; whereas MMC with distributed PV panels can be described as multiple DC to AC inverters that greatly increase converter efficiency by removing the need for multiple DC to DC converters in the latter technologies.

As described in Chapter 4, MMCs allow any number of voltage levels to be achieved by increasing or decreasing the number of SMs, and they have a number of advantages over other multilevel topologies, including fault tolerant operation, easy capacitor voltage balance, low harmonic distortion, and the removal of the bulky DC-link capacitor [16][17]. Therefore, they have seen fast growth in a broad field of applications, including DC transmission, solid-state transformers, and renewable energy integration.

When using MMC converters on renewable energies, specifically on PV applications, the mainstream is the topology shown in Figure 4.5, used in [18][19], where PV panels are separated from the converter and are connected to the grid or load by the MMC through a DC-link. In contrast, this thesis work focuses on distributing the PV panels over the MMC topology, as shown in Figure 6.1. This has important advantages: on the one hand, the optimization function of the string converters is performed at no additional cost by the MMC cells, reducing the costs and losses related to the intermediate booster converters; on the other hand, removing the DC-link by placing the PV panels inside the MMC converter makes the DC component of the circulating current unnecessary, so the power losses will be reduced.

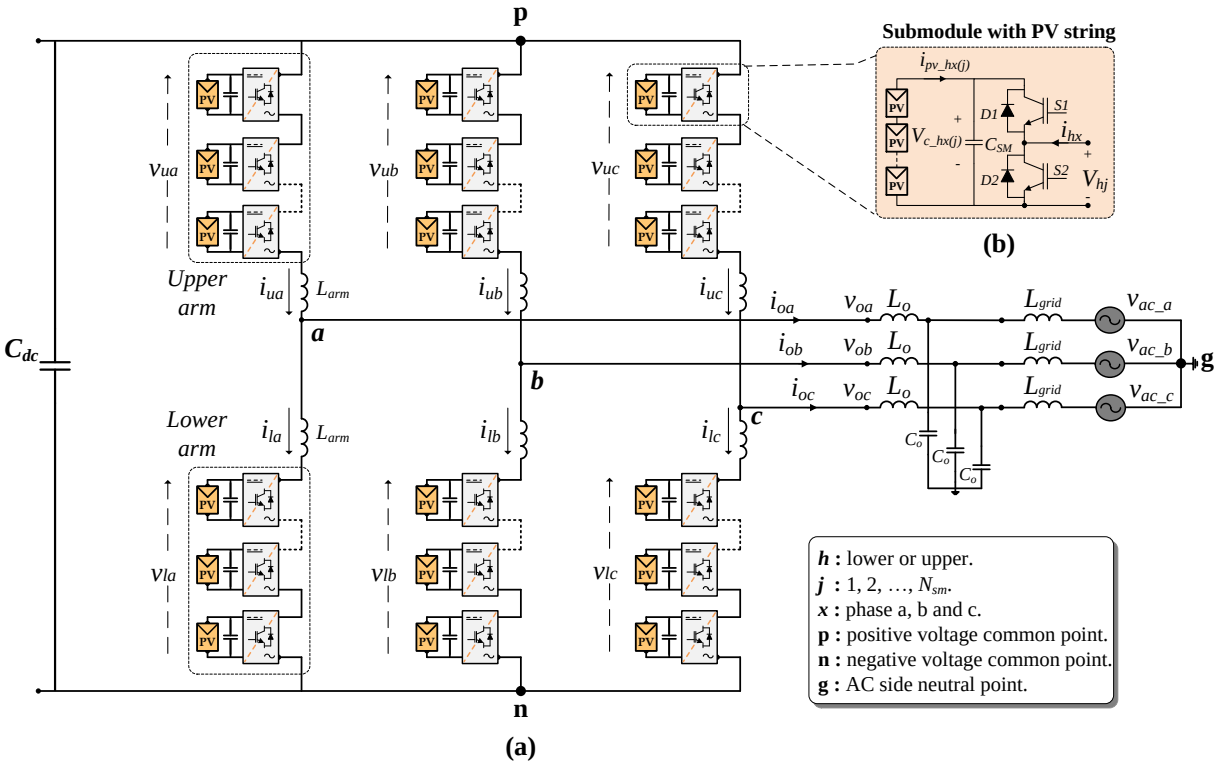

Figure 6.1: (a) Three phase MMC with integrated PV panels; (b) PV panel string integrated in SM.

In addition, using the MMC cells to track the maximum power in each PV string lowers the power accuracy. This is because the capacitor voltages, at each SM, have an AC component

that produces a voltage swing near the MPP. By increasing the capacitor size, the voltage swing can be reduced slightly, but the cost will also rise.

However, this topology has an important drawback: the voltage of each SM must follow the MPP, which depends on the irradiance and temperature of its PV panels; while the output distortion increases when traditional PWM modulations are used due to the MMC cells targeting different voltages, which also reduces the operational range.

The new modulation proposed in this thesis, named Local Carrier Pulse Width Modulation (LC-PWM), solves this problem and, at the same time, reduces the MMC internal circulating currents with important savings on the semiconductor power rating.

The LC-PWM deals with different voltages in the MMC cells, and the higher precision of this technique reduces the output distortion in a wider range of voltage situations. In addition, an appropriate control of the MMC arms to keep it in a balanced situation removes unwanted AC components of the circulating currents, which also means fewer power losses and increased MMC efficiency. In the subsequent simulation sections, the implementation of LC-PWM is discussed and checked using simulations in diverse circumstances to verify the above concepts; first to show the feasibility of the proposed concept, while the performance and behavior of the LC-PWM will be evaluated using a grid-connected MMC simulation module. Later on, the performance of this new modulation technique is compared to a conventional PS-PWM on isolated loads to rule out any possible grid or controller interaction. An analysis of the circulating currents, the resulting converter power losses, the performance of the MMC converter on this application, and the THD under various scenarios is used to assess the viability of the proposed LC-PWM modulation.

6.2 Control of MMC Based Distributed PV Panels

The fundamental objective of controllers and regulators in various sections of the MMC is to force the converter to obey the desired reference signals so as to improve the conversion performance and efficiency.

MMC switching and control difficulties are comparable to typical VSCs functioning on two or three levels, as discussed in earlier chapters. The methods for controlling the DC-link voltage, active and reactive power, and output current are substantially the same as for the other multilevel converters.

However, different multilevel converter connections and topologies have their own sets of characteristics. Extra control requirements must be added as the MMC includes floating capacitors in each SM. These floating capacitors store energy and that energy requires extra management to balance the energy of cells, arms, and phases. Moreover, attaching the PV panel string directly into the MMC SMs introduces energy sources inside the converter and increases the control needed to keep the converter arms and legs balanced, decrease the power losses, and maintain the converter stability. So the balancing of the arm and phase voltages is the most significant control difference. If they are not handled properly, the MMC may lose its stability and become unusable.

On the other hand, the existence of the circulating current implies the need for additional control, and the suppression of the circulating current's harmonic content. This approach would surely improve the converter efficiency. In addition, low-rated components may also be used to improve the converter efficiency.

In fact, the MMC has two major currents in each phase, as detailed in Chapter 4, one in the upper arm and another in the lower arm. These currents will be used to produce the phase output current and circulating current. The converter output current is responsible for delivering active power to the AC grid or loading through the MMC by determining the output voltage reference. The circulating current is in charge of moving energy between the converter phases via its DC component and moving energy between the upper and lower arms via its AC component. This is done to keep the converter legs and arms balanced by deciding the voltage reference in the arm inductors between the upper and lower arms.

A generic control diagram for a PV application is shown in Figure 6.2. It covers all aspects of MMC control, including DC-link voltage control and active/reactive power management, output current control, circulating current control, and the modulation scheme, which includes a sorting algorithm and PWM generators.

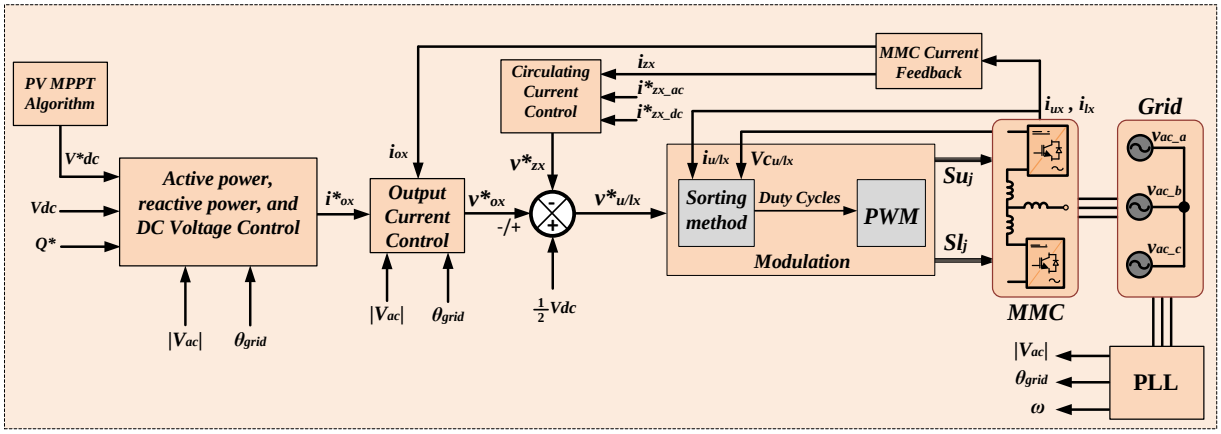

Figure 6.2: General controller scheme of MMC PV panels application-based grid connection.

The DC-link voltage reference and output power are the primary references for the whole controlling system of the MMC. Here, the DC-link voltage can decide the active power needed to be consumed at the load side in terms of the off-grid connection or the power to share with the grid in terms of the online connection. In fact, the active power controller generates the output current references, as Figure 5.10 in Chapter 5 shows, to regulate the output voltage produced by the MMC. Meanwhile, the MMC reactive power reference has been set to a value that reduces the grid's reactive power to be zero.

The DC-link voltage in our thesis work has been defined as the PV panels connected to the MMC under two considerations: first, the PV panels are connected externally to the MMC to provide the power required for the AC grid through the MMC; second, the MMC cells are

distributed throughout the PV panels, as shown in Figure 6.1, to provide the power produced inside the MMC to the grid. Therefore, an MPPT algorithm needs to track the maximum power to decide the voltage reference at the maximum power point.

6.2.1 MPPT Control System for Connected PV Panels

The MPPT control system is an essential component of any PV system. Indeed, its purpose is to decide the overall DC voltage, V^*_{dc}, at which the MMC should work, as well as the voltages of each PV module in order to get the maximum power under the given solar irradiation and temperature. Different methods for tracking the maximum power point of PV cells have been presented in the literature, see Chapter 2 section 2.5.

The LUT method is the MPPT technique used in this PV application because it provides a simple and efficient MPPT scheme where the required values are obtained directly from the data stored in a static memory.

The LUT method is applied in the simulation as follows: first, the temperature of the PV panels is measured to choose the correct lookup table; in the external PV panel connection, an average temperature is applied to all connected panels; whereas, in the internal PV panel connection, the average temperature of the PV panels for each SM is applied. For instance, several lookup tables registered for temperature values with 5°C intervals may be used. PV current and voltage measurements are used to find the PV panel irradiance using the proper LUT.

The measured current and voltage of the PV panel are used to look for the exact irradiance value for finding the maximum voltage from the defined irradiance LUT. To do so, different search methods may be used to find the irradiance value from the selected irradiance LUT. A binary search has been implemented to obtain the irradiance value, but other search methods, such as bottom-up or top-down searches, can also be implemented faster. Binary search method has been selected as it has a maximum search complexity of $O(\log_2(n))$; while other methods have a search complexity of $O(n)$, where n is the number of objects at the selected LUT. Thus, when compared to other search methods, the binary search method indicated a lower search cost with a little more complex implementation. In the end, these search techniques have no influence on the MPPT result or the stability of the simulation; the only consequence that can be considered is the search execution time.

The final stage of the LUT method procedure is to determine the voltage at the maximum power point V_{mpp} by using the irradiance value, where V_{mpp} is specified as a function of a two-dimensional matrix, V_{mpp} [Temperature][Irradiance], with varying temperatures and irradiances. Here, the irradiance data used in the lookup table range from 0 W/m^2 to 1000 W/m^2, with a continuous interval of 25 W/m^2. The intersection of the measured temperature in the matrix columns with the irradiance value determined in the previous step in the matrix rows corresponds to the specific V_{mpp} value.

To sum up, two lookup tables were used in the LUT method to obtain the MPPT: the first depended on the measured temperatures to select the right lookup table and with the observed

current and voltage of the PV panel to determine irradiance; while the second depended on the irradiance table to determine the voltage at the maximum power point.

The main advantage of the LUT is that it is stable and does not require perturbations as in the P&O or InCond methods. Indeed, the P&O MPPT algorithm may have a better tracking performance at constant temperature and irradiance, but it has a delayed reaction to changes in variable weather conditions, and oscillations around the MPP may also be noticed [54]. The LUT method has a faster and more robust response to sudden changes in irradiation or temperature, compared to other MPPT, since it requires less time to obtain the MPPT.

The DC-link voltage reference, indicated by V^*_{dc}, is computed using Equation (6.1) in the case of PV panels distributed throughout the MMC; while in the case of the external PV panel connection, V^*_{dc} is computed by applying a global MPPT over all the connected PV panels. The observed V_{dc} value can be determined using Equation (6.2), which gives the average value of the sum of the SM voltages in each arm.

$$V^*_{dc} = \frac{1}{6}\sum_{j=1}^{N_{sm}} \left(V_{mpp\_ua}(j) + V_{mpp\_la}(j) + V_{mpp\_ub}(j) + V_{mpp\_lb}(j) + V_{mpp\_uc}(j) + V_{mpp\_lc}(j)\right) \tag{6.1}$$

$$V_{dc} = \frac{1}{6}\sum_{j=1}^{N_{sm}} \left(V_{c\_ua}(j) + V_{c\_la}(j) + V_{c\_ub}(j) + V_{c\_lb}(j) + V_{c\_uc}(j) + V_{c\_lc}(j)\right) \tag{6.2}$$

where the V_{mpp_ux} and the V_{mpp_lx} in Equation (6.1) represent the upper and lower arm voltages in each phase of the MPP, and each cell voltage is obtained by applying the MPPT method for its connected PV cells. However, the V_{c_ux} and V_{c_lx} in Equation (6.2) indicate the voltage measurement of the upper and lower arms in each phase, respectively. Furthermore, the sum of all voltages has been divided by six, as the number of arms in a three-phase MMC is equal to six.

6.2.2 Active Power Control

Figure 6.3 shows a typical controller design employing a PI controller to regulate the output power in response to the voltage provided by PV panels connected (externally or distributed internally) with the MMC. The PI regulator, also known as a proportional-integral regulator, contains two tuning components that are independent of other regulators and are indicated by K_p for the proportional gain and K_i for the integral gain, as seen in Figure 6.3, where the integral gain represents the ratio of the proportional gain with the time response coefficient denoted by T_i.

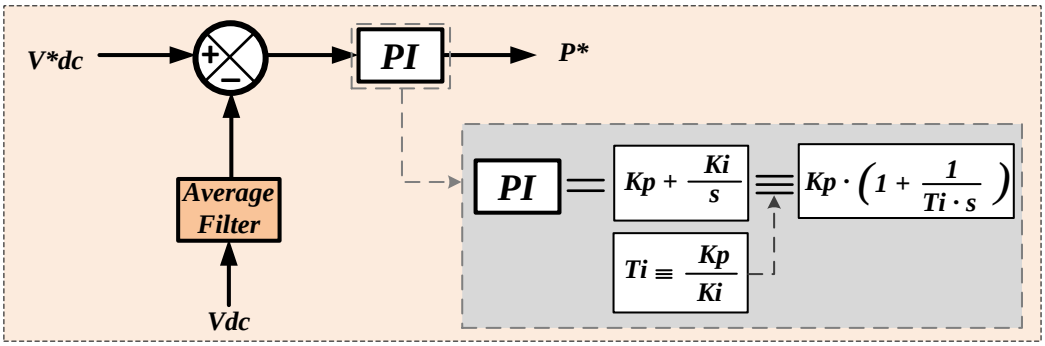

Figure 6.3: Active power regulation for connected DC side voltage, with a PI regulator block describing the proportional gain K_p, integral gain K_i, and time response coefficient T_i.

The PI controller can decide whether more or less power must be delivered to the grid, based on the measured DC voltage V_{dc} and the reference V^*_{dc}. When the V_{dc} is greater than the V^*_{dc} more power is delivered to the output to reduce the DC voltage and vice versa.

In addition, the V_{dc} measurement may be obtained directly through the DC-link capacitor, but the problem is that the DC capacitor, C_{dc}, was installed to provide a path for circulating currents to move between the upper and lower arms. Where, the power transfer between the upper and lower arms is required to keep the arm balanced, and the power transfer will be performed by using the circulating current AC component, the 50 Hz component, to move the power from the upper to the lower arm or vice versa. In fact, the DC capacitor can be eliminated or reduced if the upper and lower arms of each phase are kept in a fully balanced situation. So, as the AC components of the circulating current pass through, the C_{dc} produces an oscillation that will appear in the V_{dc} measurement, and this oscillation may propagate to the active power reference P^* through the PI regulator, leading to an imprecise measurement at the DC-link side. As a result, a moving average filter, used and adjusted to the grid frequency, works as a low pass filter to remove the oscillations generated by the unbalanced currents that pass through the DC capacitor C_{dc}. This averaging filter will attempt to reduce the voltage ripple at P^* by obtaining stable measurements of V_{dc}.

6.2.3 Output Current Control

The output current reference is produced after receiving the active power reference and the information supplied by the dq-PLL, which includes the voltage amplitude, phase angle, and frequency of the grid, as discussed in Chapter 5 and depicted in Figure 5.10. The output current controller produces the necessary output voltage reference that allows the active and reactive currents to flow as desired, see section 5.3 in Chapter 5. These voltage references are used to calculate the final voltage reference for the upper and lower arms in each phase, which will be used by the modulator, see Figure 6.4, after adding the effect of the circulating current control in the following section.

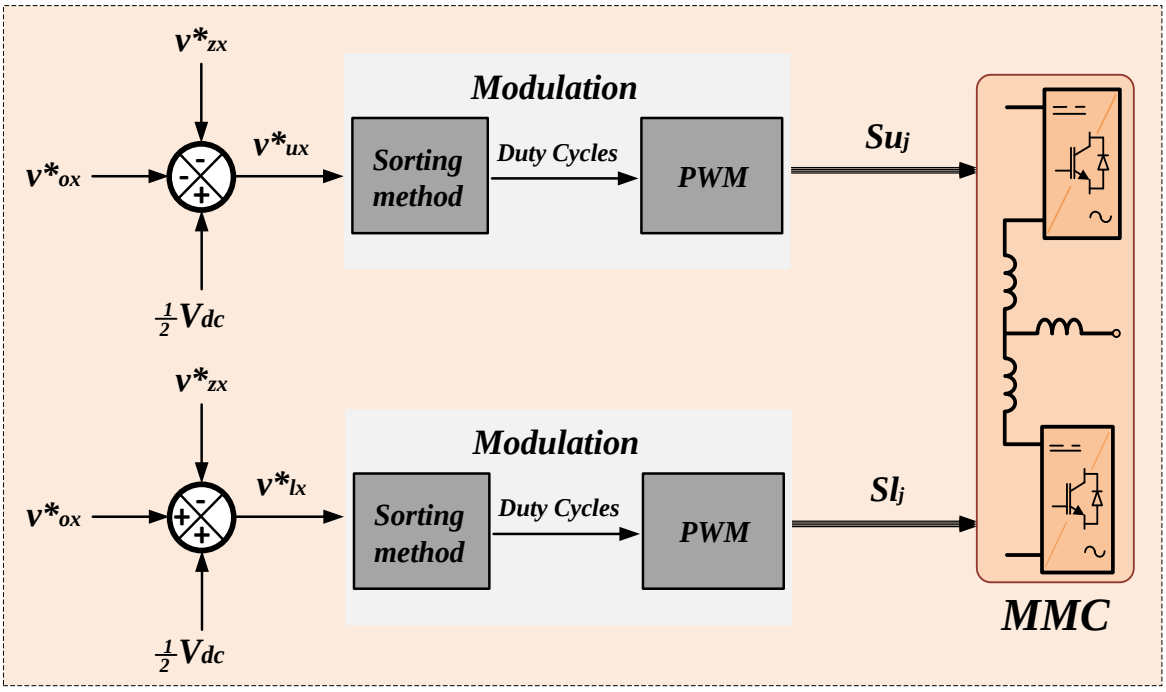

Figure 6.4: Upper and lower arms voltage references are generated to determine the correct number of chosen SM signals via modulation.

In Figure 6.4, v^*_{ux} and v^*_{lx}, are the upper and lower arm reference voltages, as specified in Equations (6.3) and (6.4), respectively.

$$v^*_{ux} = \frac{1}{2}V_{dc} - v^*_{ox} - v^*_{zx} \tag{6.3}$$

$$v^*_{lx} = \frac{1}{2}V_{dc} + v^*_{ox} - v^*_{zx} \tag{6.4}$$

where v^*_{ox} is the alternating reference for the output voltage in phase 'a', 'b', or 'c'. The references v^*_{zx} are used to control the evolution of the circulating current in each phase.

6.2.4 Circulating Current Control

At the MMC, the circulating currents have two major components that work together to provide a balancing power between phases using the DC component and to balance the energy between the upper and lower arms in each phase using the AC component at 50 Hz. On the one hand, these components must be regulated sufficiently to keep the energy of the MMC in a

balanced state; while on the other hand, suppressing those components to the minimum would increase the converter performance and efficiency.

Figure 6.5 depicts the MMC circulating current controller, which includes both the DC and AC circulating current component regulators.

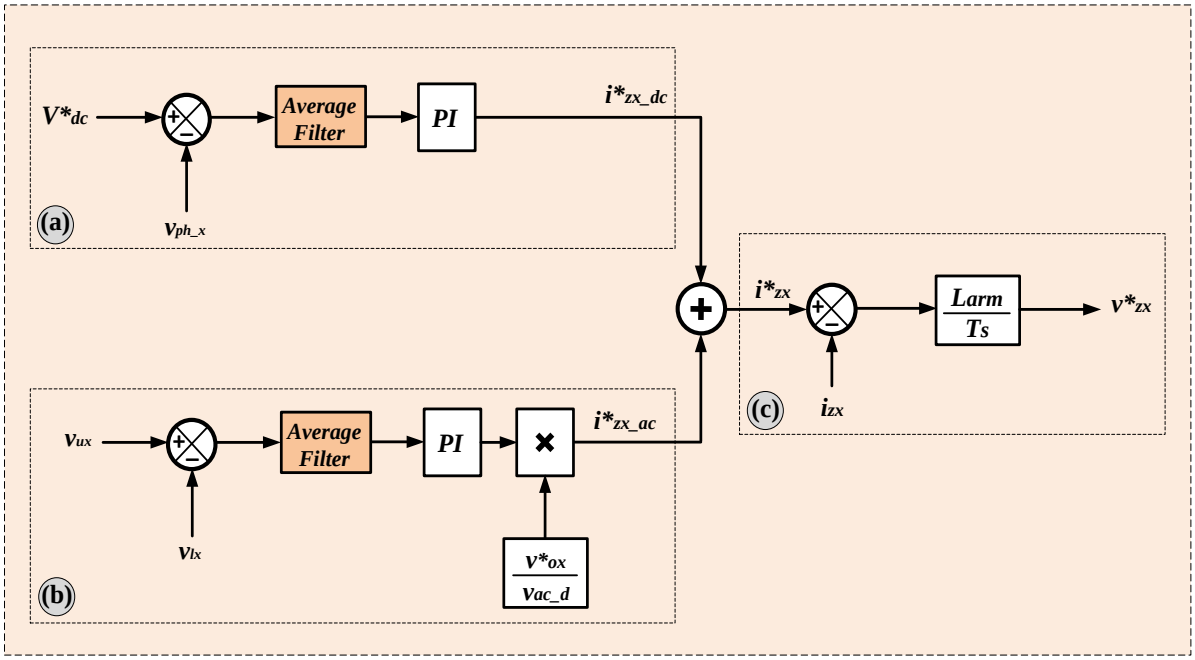

Figure 6.5: The circulating current controller regulates the internal flow of current: (a) the controller for the DC component for phase balancing; (b) the controller for the 50 Hz component for arms balancing; and (c) a fast controller to apply them using the proposed modulation.

Controlling the DC component of the circulating current has been sketched in Figure 6.5 (a). A PI regulator is applied to keep the energy of the three MMC phases in a balanced situation. This PI regulator deals with the value responsible for maintaining the phase voltage balance, while the PI inputs are determined by the DC voltage reference stated in Equation (6.1) and the phase voltage v_{ph_x} indicated in Equation (6.7), where v_{ph_x} represents the average voltage of the upper and lower arms calculated by using the measured voltage of each cell, as shown in Equations (6.5) and (6.6) for the upper arm and lower arm voltages, respectively. These regulators work with voltages, but their purpose is to balance the energy stored in the arm capacitors, which is proportional to the square of the voltages.

$$v_{ux} = \sum_{j=1}^{N_{sm}} V_{c\_ux}(j) \tag{6.5}$$

$$v_{lx} = \sum_{j=1}^{N_{sm}} V_{c\_lx}(j) \tag{6.6}$$

$$v_{ph\_x} = \frac{1}{2}\left[v_{ux} + v_{lx}\right] \tag{6.7}$$

Similarly, Figure 6.5(b) shows a controller that regulates the AC component of the circulating current using a PI regulator to balance the energy between the upper and lower arms, in which the PI regulator input value is based on the measured voltage of each cell, as shown in Equation (6.5) for the upper arm voltage and Equation (6.6) for the lower arm voltage. The PI results, which represent the amplitude of the AC component of the circulating current reference, are multiplied by the value of the output voltage reference, v^*_{ox}, divided by the amplitude of the voltage grid in the d-axis, v_{ac_d}. This is done to generate the circulating current reference with a sinusoidal shape in the same phase as the output voltage reference, so as to be able to transfer active power between the upper and lower arms in order to keep them balanced. If these currents were shifted 90° from their location, the reactive power will be transferred with no balancing effect.

The average filter used in the circulating current controller also has a very important role. Due to the AC components of the arm currents, the cell voltages are not constant. They have a 50 Hz component, and they may also have oscillations at 100 Hz, 150 Hz, and so forth. Thus, an average filter tuned at 50 Hz is very efficient for removing these variations in the cell voltages that do not contribute to the regulator's main task, which is to keep the energy of all SMs in the MMC balanced.

In order to be effective, the moving average filter must be adjusted to the grid frequency, which is measured using the PLL, as mentioned in Chapter 5. Therefore, the average filter works by calculating the average value between the instantaneous value and the previous value. The time separation between the two values is the sampling time, which is about 20 ms with regard to 50 Hz. To get the average, the number of samples regarding the switching frequency must be divided exactly at 800 samples, regarding the switching frequency equal to 2 kHz. Indeed, the length of samples can be implemented using a First In First Out (FIFO) memory; where the length of the FIFO represents the number of samples. The following steps can be used to determine the FIFO length for adjusting the average filter on the precise grid frequency: first, measure the grid frequency by using a PLL, then use an LPF in an extremely low pass frequency to eliminate variations in the frequency due to the phase change during the lock phase; and second, after the sampling division to get the average value between the instantaneous and previous values, this value has to be rounded up to determine the precise length of the FIFO. Eventually, the filtered frequency must be adjusted by using frequency detection, to find the proper frequency and thus exclude unnecessary frequencies.

Indeed, in the controller of the DC component, the average filter removes the 100 Hz component from the signal generated in the phase voltage, v_{ph_x}, due to the sum of the upper and lower arm voltages, as the simulation shows. However, in the AC component controller, the average filter is employed in the controller to eliminate the 50 Hz component that occurs when the upper and lower voltages of the same arm are subtracted.

Afterwards, the value of v^*_{zx} is used to regulate the evolution of the circulating current in the last section of the controller. Figure 6.5(c) shows that a fast deadbeat controller, based on Equation (5.20), has been used to keep the circulating current close to the required value, i^*_{zx}, as specified in Equation (6.8):

$$v^*_{zx} = \frac{L_{arm}}{T_{sx}} (i^*_{zx} - i_{zx}) \tag{6.8}$$

where the circulating current reference in each MMC leg is i^*_{zx}, a reference to its controller; while the i_{zx} is the measured circulating current in each phase, as stated before in Equations (5.24), (5.25), and (5.26) for phases 'a', 'b', and 'c', respectively. The deadbeat controller represents a proportional controller and is used for a quick response with a gain value, depending on the ratio of the arm inductor to the time sampling of the specific phase, as indicated in Equation (6.8).

The deadbeat controller plays an important role in the overall behavior of the MMC converter in terms of the circulating current control. The determination to use a deadbeat controller rather than a PI-controller to regulate the circulating current was taken for the following reasons:

- First and foremost, a different modulation is proposed in the following section that does not generate 100 Hz circulating current components, unlike other carrier-based modulations such as PS-PWM or LS-PWM, which can inject regular 100 Hz harmonic distortion due to the fixed frame of carriers used in those modulations that can be fixed with a regular PI-controller. The circulating current must follow both the DC and AC references, as shown in Figure 6.5; the DC references can be followed using a PI, but it would be too slow to follow the AC reference, but the deadbeat controller has a quick enough reaction to follow both.

- Second, the new modulation does not emit repetitive noise, which slows down the PI regulator by requiring it to constantly adapt for non-repetitive small glitches, preventing it from achieving the desired regulation on time. The deadbeat controller, on the other hand, can respond quickly to those glitches and keep the circulating current at its reference.

When using the proposed modulation care must be taken not to drive any energy to become unbalanced on the MMC converter. This requires a separate PI controller to control the AC and DC components before using the deadbeat controller to correct those components, bringing them close to the most reasonable value and suppressing the effect to the bare minimum. The following section describes in detail the work methodology and mathematical module of the newly proposed modulation.

6.3 Proposed Local Carrier-PWM

The Local Carrier PWM (LC-PWM) modulation approach has been proposed to control the MMC switching signals in a difficult circumstance, such as when the variable voltage power sources are inserted into the MMC, as is the case when the MMC is distributed over the PV panels by integrating the MMC SMs directly to the PV panel string.

In the proposed modulation, instead of using a fixed carrier frame where modulator waves locate their switching times, as in previous carrier-based modulations, the LC-PWM creates a private carrier for each modulator at each switching interval using the measured cell voltages, which results in more precise switching times. Consequently, the LC-PWM technique reduces the output distortion in a wider range of voltage situations. Furthermore, it effectively eliminates unnecessary AC components from circulating currents, resulting in lower power losses and higher MMC efficiency.

In contrast, a great challenge has been faced in the LC-PWM as the modulator introduces small changes in the switching periods to anticipate each change in the number of cells used to modulate the output in order to reduce distortion. Incorrect duty cycle computation leads to wrong decisions when crossing from one level to another, resulting in fast transients or glitches in the circulating currents that must be avoided. The main challenges and modifications of the proposed LC-PWM are explained in detail in the following sections.

6.3.1 Duty-Cycle Computation

The LC-PWM modulation produces a specific local carrier, for each MMC arm, to compute a precise duty cycle for each sampling period, as illustrated in Figure 6.6. Using the capacitor voltage information on modulation improves the timing of the switching sequence, produces more precise voltages at the converter output, and helps to eliminate the annoying 100 Hz component on circulating currents; in fact, it removes all unwanted components from the circulating currents, except the switching ripples. Since those voltages are measured and used in the sorting process to keep the cell capacitors balanced, using that information on MMC modulators has no extra overheads.

Figure 6.6, which refers to the lower arm of phase 'a', describes the proposed modulation in detail. When using four-SM per arm, the available voltages for each arm are the closest voltages [0, ¼V_{dc}, ½V_{dc}, ¾V_{dc}, V_{dc}]. However, the real arm voltages will be a few volts above or below those levels, not only because of voltage fluctuations on the MMC capacitors due to their charge and discharge processes, but also because the MPPT on PV panels may target different voltages for different cells due to the differences in irradiance and/or temperature. Despite these challenges, the LC-PWM method produces an effective output voltage by computing a local carrier for the lower arm, using the previous voltage and the target voltage of each arm at each sampling time, as described in Equations (6.9) and (6.11). A separate carrier is generated for the upper arm using Equations (6.10) and (6.12).

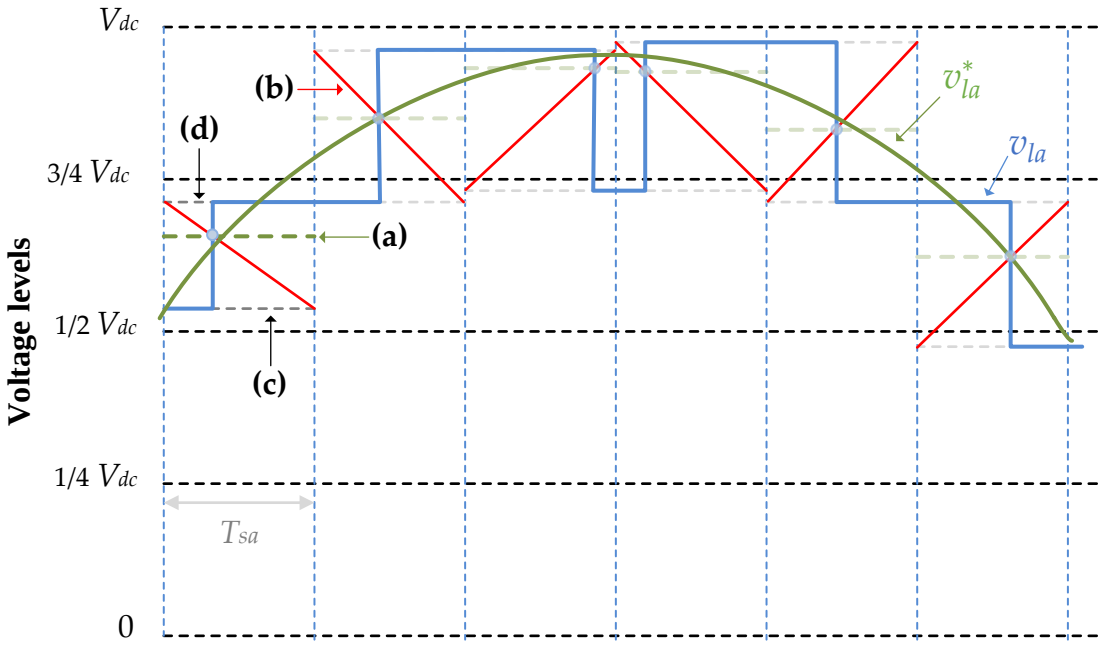

Figure 6.6: LC-PWM modulation generates, a more accurate output voltage for each arm, following a reference (a) generated at each sampling period T_{sa}, using a local carrier (b) computed using the known converter voltages at the beginning (c) and at the end (d) of that period. This figure referred to as the lower arm of phase 'a'.

In these equations, previous voltages are known from the previous sampling period, and target voltages at the end of the sampling period can be estimated after a decision is made on which cell must be inserted or bypassed at each arm and this voltage value should never equal zero.

$$v_{la}(t) = \sum_{j=1}^{N_{sm}} Vcl_j(t) \cdot Sl_j(t) \tag{6.9}$$

$$v_{ua}(t) = \sum_{j=1}^{N_{sm}} Vcu_j(t) \cdot Su_j(t) \tag{6.10}$$

$$v_{la}(t + T_{sa}) \cong \sum_{j=1}^{N_{sm}} Vcl_j(t) \cdot Sl_j(t + T_{sa}) \tag{6.11}$$

$$v_{ua}(t+T_{sa}) \cong \sum_{j=1}^{N_{sm}} Vcu_j(t) \cdot Su_j(t+T_{sa}) \tag{6.12}$$

In these equations, Vcu_j and Vcl_j represent the SM voltages for the upper and lower arms, whereas Su_j and Sl_j are the switch statuses on the upper and lower SMs at the beginning and end of the switching period.

Figure 6.7 shows in detail how the LC-PWM strategy generates the local carrier for each sampling period T_{sa} for the upper and lower arms of phase 'a'.

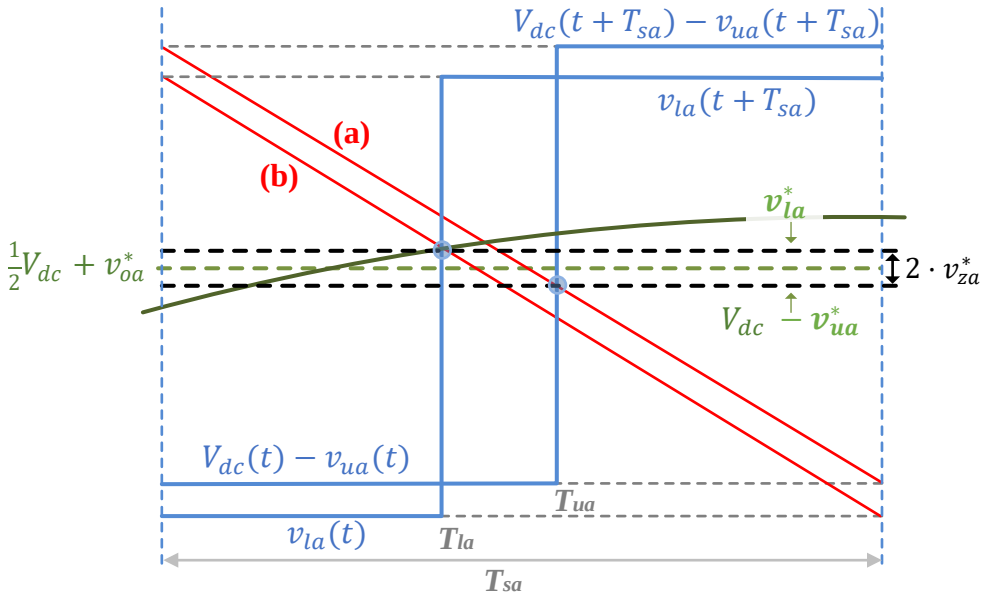

Figure 6.7: Upper and lower arms voltage generation using local carriers (a) Upper local carrier (b) Lower local carrier.

The intersection of two separate carriers with the two output references, v^*_{la} and ($V_{dc} - v^*_{ua}$), generate an upper arm voltage and a lower arm voltage that exactly match the desired voltage for each arm during that period. Even with no circulating current controller, that is mean $v^*_{zx} = 0$, the upper and lower voltage references generate different voltages due to the separation of the upper local carrier and the lower local carrier, as shown in Figures 6.7(a) and (b), respectively.

Therefore, the desired duty cycles, d_{ua} for the upper arm and d_{la} for the lower arm, are computed using Equations (6.13) and (6.14) for each sampling period:

$$d_{ua} = \frac{T_{ua}}{T_{sa}} = \left| \frac{v^*_{ua}(t) - v_{ua}(t + T_{sa})}{v_{ua}(t) - v_{ua}(t + T_{sa})} \right| \tag{6.13}$$

$$d_{la} = \frac{T_{la}}{T_{sa}} = \left| \frac{v^*_{la}(t) - v_{la}(t + T_{sa})}{v_{la}(t) - v_{la}(t + T_{sa})} \right| \tag{6.14}$$

where T_{ua} and T_{la} are the exact timing when an SM must be inserted or bypassed, and v^*_{ua} and v^*_{la} are the reference voltages for the upper and lower arms, as described in Equations (6.3) and (6.4), respectively. Furthermore, the absolute value is added to get the integer number, as the duty cycle represents a ratio of the time to switch on over the sampling time.

In fact, an important contribution of the proposed method is that the LC-PWM accurately finds the precise times to change from one state level to the next, allowing full control of the generated voltages. In fact, the more precise the duty cycle computation is, the smaller the circulating current produced will be. This modulation improves the generating switching sequence to the point where the circulating current is no longer out of control.

6.3.2 Level Crossing Synchronization

As can be seen below in Figure 6.15, in the simulation results, when using capacitor voltage information on duty cycle computation, the switching sequences generated by the LC-PWM greatly reduce the root mean square (RMS) value of the circulating currents by removing the 100 Hz component. However, an important source of noise remains on those internal currents due to the lack of any level crossing synchronization. In several situations, when the converter changes the number of cells used to modulate the output, for example when it alternates between using one or two cells and two or three cells, it is possible that the voltage given as reference cannot be reached in those switching periods just by inserting or bypassing one cell; and then an important transient alters the circulating current, seriously affecting its RMS value. Thus, the LC-PWM must anticipate all those events, adapting the duration of a few sampling periods just before each crossing point, in such a way that it guarantees the converter will have the appropriate number of active cells when arriving at all crossing points. In the given example, the converter must have exactly two active cells at every sampling period when the converter changes from one or two active cells to two or three. So, the following steps must be applied for better level crossing:

1. The first step for this task is to anticipate the voltage for the following crossing level, as shown in Figure 6.8. Depending on the selected cells regarding the voltage level, the upper and lower arms have many different options to generate a voltage near the targeted crossing voltage, and these options increase by increasing the number of SM in the MMC, as shown in Table 6.1. This is true for any of the three phases, where the available options of the SMs for generating upper and lower arm voltages based on MMC with four SMs and five levels of conversion are detailed.

Table 6.1. Upper and lower arm options to generate a voltage near the targeted crossing voltage level.

Voltage level	Options for selected SMs for generating Lower arm voltages	Options for selected SMs for generating Upper arm voltages
0	0	$[V_{dc} - V_{SM1} - V_{SM2} - V_{SM3} - V_{SM4}]$
1	$[V_{SM1}]$ or $[V_{SM2}]$ or $[V_{SM3}]$ or $[V_{SM4}]$	$[V_{dc} - V_{SM1} - V_{SM2} - V_{SM3}]$ or $[V_{dc} - V_{SM1} - V_{SM2} - V_{SM4}]$ or $[V_{dc} - V_{SM1} - V_{SM3} - V_{SM4}]$ or $[V_{dc} - V_{SM2} - V_{SM3} - V_{SM4}]$
2	$[V_{SM1} + V_{SM2}]$ or $[V_{SM1} + V_{SM3}]$ or $[V_{SM1} + V_{SM4}]$ or $[V_{SM2} + V_{SM3}]$ or $[V_{SM2} + V_{SM4}]$ or $[V_{SM3} + V_{SM4}]$	$[V_{dc} - V_{SM1} - V_{SM2}]$ or $[V_{dc} - V_{SM1} - V_{SM3}]$ or $[V_{dc} - V_{SM1} - V_{SM4}]$ or $[V_{dc} - V_{SM2} - V_{SM3}]$ or $[V_{dc} - V_{SM2} - V_{SM4}]$ or $[V_{dc} - V_{SM3} - V_{SM4}]$
3	$[V_{SM1} + V_{SM2} + V_{SM3}]$ or $[V_{SM1} + V_{SM2} + V_{SM4}]$ or $[V_{SM1} + V_{SM3} + V_{SM4}]$ or $[V_{SM2} + V_{SM3} + V_{SM4}]$	$[V_{dc} - V_{SM1}]$ or $[V_{dc} - V_{SM2}]$ or $[V_{dc} - V_{SM3}]$ or $[V_{dc} - V_{SM4}]$
4	$[V_{SM1} + V_{SM2} + V_{SM3} + V_{SM4}]$	V_{dc}

As a compromise solution, valid for the upper and lower arms, the modulator will use the midpoint between the greatest and the lowest of all the options, for both the upper and lower arms, as an appropriate estimation for the following crossing voltage. To do so, the upper and lower cell voltages are always kept sorted, and a few cells in each sampling period are selected at the beginning and at the end. Their voltages are then added to compute four values, named $v_{max\_up\_a}$, $v_{min\_up\_a}$, $v_{max\_lw\_a}$, and $v_{min\_lw\_a}$. Then, the estimated voltage for the following crossing is computed for each phase by using Equation (6.17). Here, the average of the maximum voltage, v_{max_a}, computed in Equation (6.15) depends on the maximum voltage in the upper and lower arms, while the average of the minimum voltage, v_{min_a}, is computed in Equation (6.16) depends on the minimum voltage in the upper and lower arms. Briefly, Equation (6.17) attempts to find a value for the voltage levels based on the voltage change in each SM capacitor in the upper and lower arms, rather than the fixed levels specified previously as [0, ¼V_{dc}, ½V_{dc}, ¾V_{dc}, V_{dc}], when using four SM per arm.

$$v_{max\_a} = \max\left(v_{max\_up\_a}, v_{max\_lw\_a}\right) \tag{6.15}$$

$$v_{min\_a} = \min\left(v_{min\_up\_a}, v_{min\_lw\_a}\right) \tag{6.16}$$

$$\hat{v}_{level\_a} = \frac{v_{max\_a} + v_{min\_a}}{2} \tag{6.17}$$

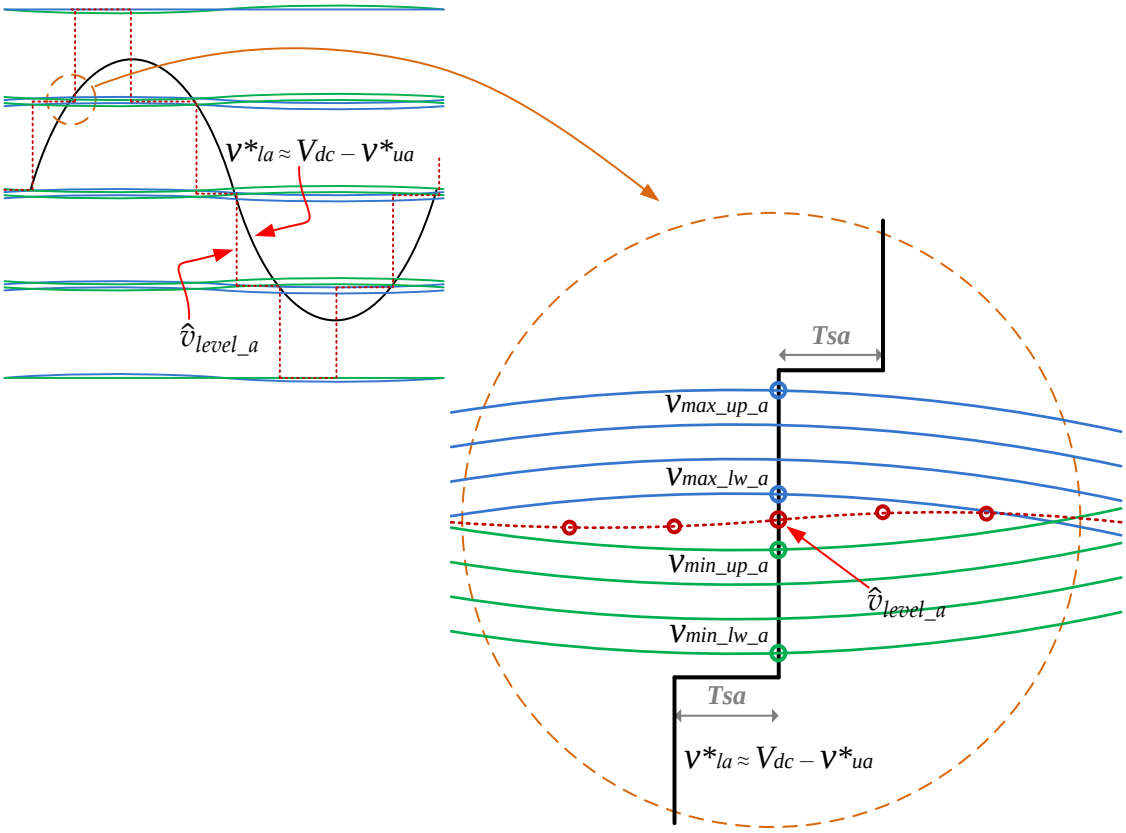

Figure 6.8: Depending on the selected cells, the upper and lower arms may generate different voltages near each level. At each sampling period, an intermediate value is computed using the maximum and minimum values over all available options.

2. The second step applied to achieve clean crossings, defines the modulator state as 'even' or 'odd'. The 'even' state means that the oscillations are at the same voltage level, so the transition number required to move from one voltage level to the next and back is an even number of transitions. The 'odd' state means that, when switching from one voltage level to another, the number of transitions required is an odd number, thus allowing for a clear crossing. When an arm voltage is near to the next crossing voltage, the value previously computed as $\hat{v}_{level\_a}$ for the first phase, then the arm is said to be at an 'even' state, because

the next crossing will be cleaner if the modulator executes an even number of switches before the transition. The opposite situation is found when the arm voltage is far from the crossing level, where an 'odd' number of sampling periods is then desired.

3. The third step, described in Equations (6.18), (6.19), and (6.20), computes the length for the following PWM period using the remembered time for the next crossing point $t_{next\_cross\_a}$ and the registered time $t_{current}$ during the grid cycle. In this case, a central value of the sampling time, T_S / 2, is used for a nominal switching frequency (*Fs*) to generate a local carrier to define the required time to switch on, and another T_S / 2 would be needed to generate another local carrier to switch off for a full duty cycle. In fact, this sampling time is changed by adding or subtracting about 10% of T_S / 2 to consistently reach the following crossing point at an 'even' state, which guarantees the correct switching decision and removes undesired transients from the circulating current at each phase. In the case of 2 kHz, the sampling period T_{sa} would be 250µs when the modulation is aligned to the following crossing point, but would be changed to 225µs, or 275µs, when acceleration or deceleration is required to guarantee the correct switching decision; while also removing undesired transients from the circulating current at each phase. Equation (6.18) shows the crossing time calculation.

$$t_{cross\_a} = t_{next\_cross\_a} - t_{current} \tag{6.18}$$

When the modulator is in the 'even' state, near the estimated $\hat{v}_{level\_x}$, Equation (6.19) is used to calculate the next sampling time; when it is in the 'odd' state, far from $\hat{v}_{level\_x}$, Equation (6.20) is used:

$$T_{sa} = \frac{T_S}{2} + \left(\frac{T_S}{2} \cdot 10\%\right) \cdot sign\left(t_{cross\_a} - T_S \cdot \left(\left\lfloor t_{cross\_a}/T_S + 0.5 \right\rfloor\right)\right) \tag{6.19}$$

$$T_{sa} = \frac{T_S}{2} + \left(\frac{T_S}{2} \cdot 10\%\right) \cdot sign\left(t_{cross\_a} - T_S \cdot \left(\left\lfloor t_{cross\_a}/T_S + 0.5 \right\rfloor\right)\right) \tag{6.20}$$

where all times including the sampling period 'T_{sa}' for phase 'a', are measured in microseconds and $\lfloor x \rfloor$ represents the lower bounded integer of 'x'.

4. The final step for this task detects the exact time when the MMC converter crosses from one level to the next in order to remember that point for the next cycle. It is not difficult to detect each crossing by comparing the reference voltage and the estimated voltage $\hat{v}_{level\_x}$ for the next crossing. At each crossing, the current and previous voltage differences computed in Equations (6.21) and (6.22) have different signs. At those sampling periods, assuming a smooth evolution on the capacitor voltages, the time deviation of the crossing

point from the middle of the sampling period is estimated using Equation (6.23). Figure 6.9 shows the schematic diagram calculating the time deviation of the crossing point, where the equivalent triangle approach is used to calculate the Δt_{cross_a} in Equation (6.23).

$$\Delta v_a(t) = \hat{v}_{level_a} - v^*_{la}(t) \tag{6.21}$$

$$\Delta v_a(t - T_{sa}) = \hat{v}_{level_a} - v^*_{la}(t - T_{sa}) \tag{6.22}$$

$$\Delta t_{cross\_a} = \frac{T_{sa}}{2} \cdot \frac{|\Delta v_a(t)| - |\Delta v_a(t - T_{sa})|}{|\Delta v_a(t)| + |\Delta v_a(t - T_{sa})|} \tag{6.23}$$

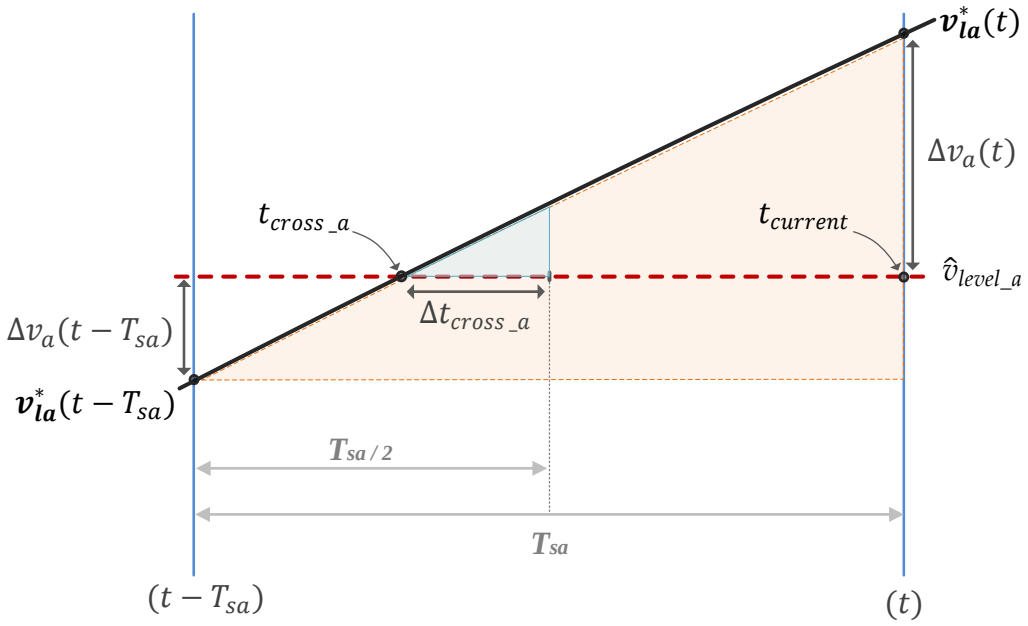

Figure 6.9: The time deviation of the crossing point is computed using the equivalent triangle approach.

Afterward, this information is used in Equation (6.24) and stored to give a better estimation of the current crossing point for the following crossing of the same kind, and Equation (6.26) is used to retrieve the position of the incoming crossing point from the same suitable store:

$$crossings\_\ phaseA[i_a] = t_{current} - \Delta t_{cross_a} \tag{6.24}$$

$$i_a = (i_a + 1) \bmod 6 \tag{6.25}$$

$$t_{next\_cross\_a} = crossings\_ phaseA[i_a] \tag{6.26}$$

where i_a is an integer value that identifies each type of crossing point. Because the utilized MMC has four SMs per arm, this index is changed in Equation (6.25) to have a value ranging from 0 to5. This implies there might be up to six possible crossing places.

6.3.3 Sorting Method Development

Traditional MMC controllers search for the greatest or lowest capacitor voltages at each arm to select those cells for switching in order to keep all the cell capacitors balanced, so well-known sorting methods such as bubble sort are used [169]; these methods have a complexity from O($n \cdot log_2 n$) to O(n^2), where n is the number of sorting items, and can be used to sort all the SM voltages before choosing the most appropriate for each case. When using internal energy sources, however, the distance to each cell reference voltage must be used instead of the absolute value of the voltages. In any case, in order to use Equations (6.11) and (6.12), the required SMs to be inserted or bypassed during the current switching time must be chosen using a quick and simple sorting process.

Sorting all the cell voltages using bubble sort and choosing the cell with the greatest or lowest voltage to be inserted would cost O(n^2), as this algorithm needs (n-1) passes over n elements. As an improvement, the developed sorting is simply based on looking for one or two cells with the highest or lowest voltage to be inserted, only checking on bypassed cells when they must be inserted, or only checking on inserted cells that must be bypassed. This approach generally reduces the sorting task to O(n), as well as reducing the switching in the MMC.

However, the LC-PWM actually needs to know the greatest and lowest sum of the voltages of the available cells that would be inserted, as described in section 6.3.2; however, adding up all the possibilities is an overwhelming task. It is much better to sort all the voltages and compute the sum of one of the cells that needs to be inserted, which is located at the beginning or the end of the sorted list. Then, a full sorting of all the voltages is required, and bubble sort is an O(n^2) task, as said above. As long as the capacitor voltages evolve slowly, this task can be executed in several sampling periods, running only one bubble sort step at each sampling period, and keeping the location of all the cells in a linked list that stores their relative positions will reduce the sorting cost to O(n).

6.4 Simulation Results

In order to validate the proposed local carrier modulation, different simulation scenarios were conducted using a MATLAB/Simulink model for three-phase MMC converter-based PV applications. The model was conducted twice, once with external PV cells linked directly to the MMC DC-link side, and another with distributed PV panels attached to each SM at the MMC, as shown in Figure 6.1. The proposed LC-PWM has been validated first with a grid connection in scenario 1, then a comparison between the PS-PWM and LC-PWM connected to an isolated load to rule out any possible effect of the grid or controller interaction applied in scenarios 2 and 3, respectively. In the simulations, a discrete 0.25-microsecond sampling period was used for the plant and the converter, with Tustin integration. Switching signals were generated with a resolution of 1 microsecond. For the controller, a 25-microsecond period was used for LC-PWM to switch one SM in each phase every 225, 250, or 275 microseconds; a constant 250-microsecond period was used with PS-PWM.

6.4.1 PV Panel Module

The PV system implemented by simulation uses the Suntech STP320-24/Ve PV cell parameters described in Table 6.2. Figure 6.10 shows the *I-V* and *P-V* curve characteristics of the Suntech STP320-24/Ve PV cells for different irradiances at a temperature of 25°C, using a test bench module with MATLAB/Simulink and the module datasheet in [170].

Table 6.2. Parameters of the Suntech STP320-24/Ve PV panels.

Parameters	Value
Maximum power (P_{max})	320 W
Maximum power voltage (V_{max})	36.7 V
Maximum power current (I_{max})	8.72 A
Open circuit voltage (V_{oc})	45.6 V
Short circuit current (I_{sc})	9.07 A
Shunt resistance (R_{sh})	4.24 Ω
Series resistance (R_s)	0.03 Ω
Ideally factor of diode (m)	1.1238

The different irradiance impacts, caused by clouds or shadows, on the PV panel can be seen in Figure 6.10, where Figure 6.10(a) shows how the current produced by the PV panel decreases as the irradiance declines; while Figure 6.10(b) shows how the power produced by the PV panel depends on the current and voltage produced in each irradiance situation, where the power curve reaches its maximum point at the maximum current and voltage produced by the PV panel for each irradiance.

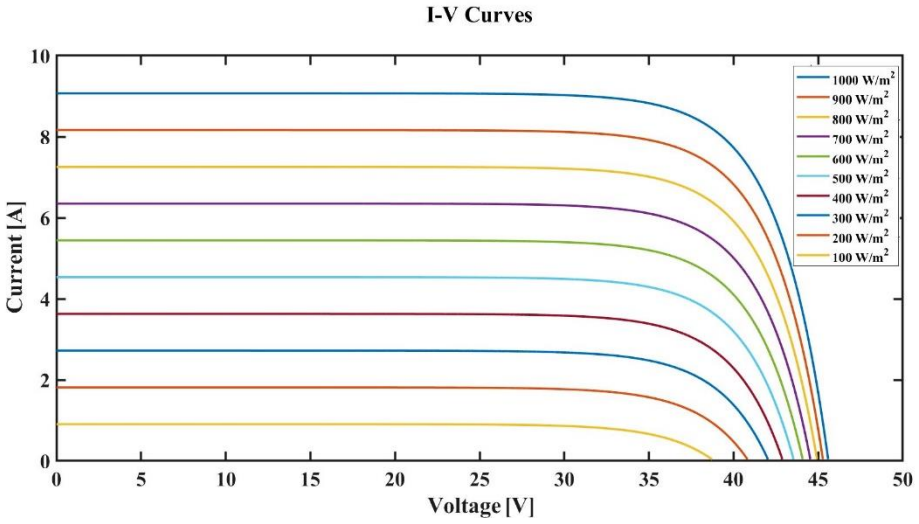

(a)

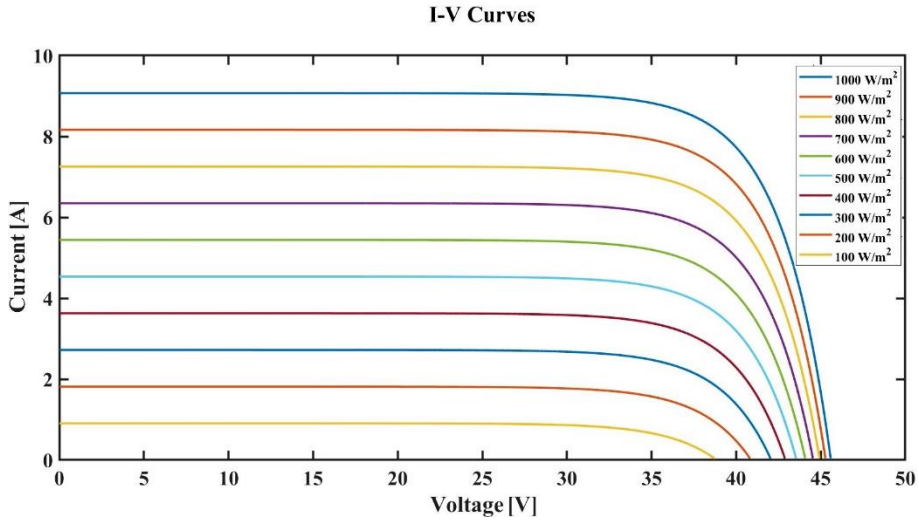

(b)

Figure 6.10: Characteristics of the Suntech STP320-24/Ve PV panel for different irradiances at T = 25°C (a) *I-V* curves (b) *P-V* curves.

6.4.2 Approximated Behavior of PV Panel Model

The behavior of the PV panel module was approximated in the simulation instead of using a PV panel module included in MATLAB. This was due to unexpected errors related to the sampling time, which led to stopping the processing of the simulation. In fact, the MATLAB model is very precise, but it uses a closed-loop model which introduces problems when using a fixed sampling period. In order to provide a more realistic behavior of the PV panel characteristics, especially in terms of the MPPT computation, the developed PV panels are also used in the simulations instead of a fixed voltage source or current source at the external or internal connections.

The behavior of the PV panel was modeled as a voltage-controlled current source, using a fifth-order polynomial approximation that guarantees the correct power and slope at the maximum power point and other relevant points, such as open circuit and short circuit. A full set of polynomials was developed for different irradiance values, ranging from 100 W/m^2 to 1000 W/ m^2, with steps of 25 W/m^2.

Figure 6.11 shows the PV characteristics of the panel model, which is developed using a fifth-order polynomial based on the datasheet of the STP320-24-Ve polycrystalline PV module manufactured by Suntech at standard test conditions (irradiance G = 1000 W/m^2 and temperature T = 25ºC) [170]. The characteristic *P-V* curve of the developed PV module was then scaled to follow different irradiance values ranging from 100 W/m^2 to 1000 W/ m^2, with steps of 25 W/m^2. The scaling considered the variations in the maximum power point voltage and the open-circuit voltage for each irradiance change.

The fifth-order polynomial in Equation (6.27) is used to represent the curved part of the *P-V* curve, whereas Equation (6.28) is used to compute the straight-line part, as depicted in Figure 6.11(a). Here we assume that the current at the short circuit is nearly constant and equal to *k* until 31.8 V, as described in Figure 6.11(b).

$$P_{pv}(V_{pv}) = a \cdot V_{pv}^5 + b \cdot V_{pv}^4 + c \cdot V_{pv}^3 + d \cdot V_{pv}^2 + e \cdot V_{pv} + f \tag{6.27}$$

$$P_{pv}(V_{pv}) = k \cdot V_{pv} \tag{6.28}$$

To obtain the values of the polynomial coefficients *a*, *b*, *c*, *d*, *e*, and *f*, six equations must be constructed, given the following constraints:

1. At the maximum power point voltage, $V_{pv} = V_{mpp}$, the given maximum power point is as in Equation (6.29).

$$P_{mpp}(V_{mpp}) = a \cdot V_{mpp}^5 + b \cdot V_{mpp}^4 + c \cdot V_{mpp}^3 + d \cdot V_{mpp}^2 + e \cdot V_{mpp} + f$$

$$320 = a \cdot 36.7^5 + b \cdot 36.7^4 + c \cdot 36.7^3 + d \cdot 36.7^2 + e \cdot 36.7 + f \quad (6.29)$$

where V_{mpp} is equal to 36.7 V and P_{mpp} is equal to 320 W, as obtained from the PV model datasheet.

2. At the open circuit voltage, $V_{pv} = V_{oc}$, the output power, P_{pv}, is zero.

$$P_{pv}(V_{oc}) = a \cdot V_{oc}^5 + b \cdot V_{oc}^4 + c \cdot V_{oc}^3 + d \cdot V_{oc}^2 + e \cdot V_{oc} + f$$

$$0 = a \cdot 45.6^5 + b \cdot 45.6^4 + c \cdot 45.6^3 + d \cdot 45.6^2 + e \cdot 45.6 + f \quad (6.30)$$

where V_{oc} is 45.6 V, as obtained from the PV model datasheet.

3. At a point beyond peak power point, an output power P_{pv} of 291.2 W is measured through the Matlab module for a voltage V_{pv} of 41 V.

$$P_{pv}(V_{pv}) = a \cdot V_{pv}^5 + b \cdot V_{pv}^4 + c \cdot V_{pv}^3 + d \cdot V_{pv}^2 + e \cdot V_{pv} + f$$

$$291.2 = a \cdot 41^5 + b \cdot 41^4 + c \cdot 41^3 + d \cdot 41^2 + e \cdot 41 + f \quad (6.31)$$

4. At the peak power point, the power slope is equal to zero, where the V_{mpp} is equal to 36.7 V and the derivative of the power P_{pv} is equal to zero, as applies in Equation (6.32).

$$\frac{dP_{pv}}{dV_{pv}}(V_{mpp}) = a \cdot 5V_{mpp}^4 + b \cdot 4V_{mpp}^3 + c \cdot 3V_{mpp}^2 + d \cdot 2V_{mpp} + e$$

$$0 = a \cdot 5 \cdot 41^4 + b \cdot 4 \cdot 41^3 + c \cdot 341^2 + d \cdot 2 \cdot 41 + e \quad (6.32)$$

5. The meeting point of the straight line with the curved portion is represented by the power before the peak power point, where V_{pv} is equal to 31.8 V and the measured P_{pv} is equal to

286 W, making k equal to 8.99 A, as the short circuit current value to match the left and the right parts.

$$P_{pv}(V_{pv}) = a \cdot V_{pv}^5 + b \cdot V_{pv}^4 + c \cdot V_{pv}^3 + d \cdot V_{pv}^2 + e \cdot V_{pv} + f$$
$$286 = a \cdot 31.8^5 + b \cdot 31.8^4 + c \cdot 31.8^3 + d \cdot 31.8^2 + e \cdot 31.8 + f \quad (6.33)$$

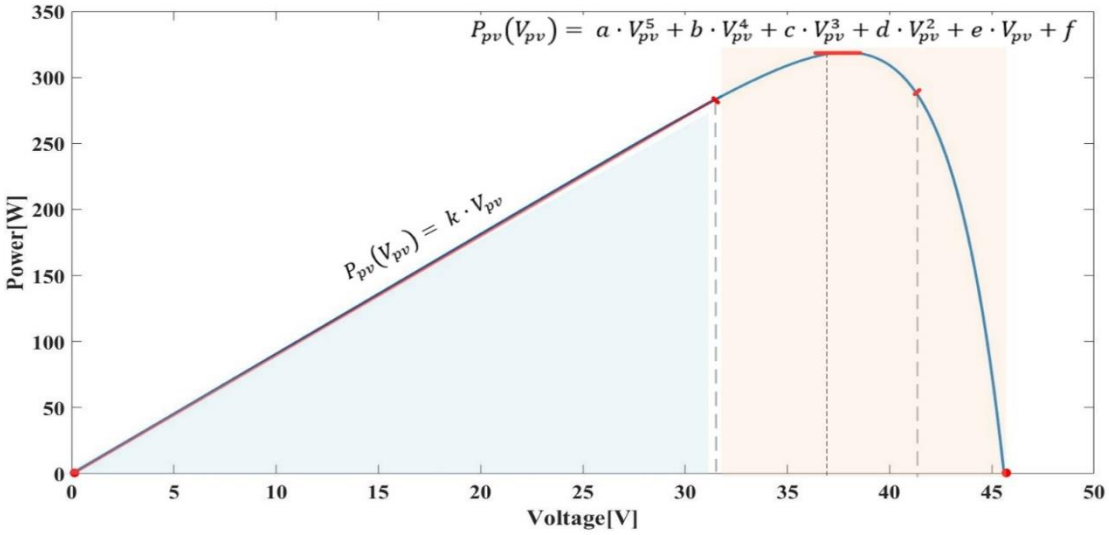

(a)

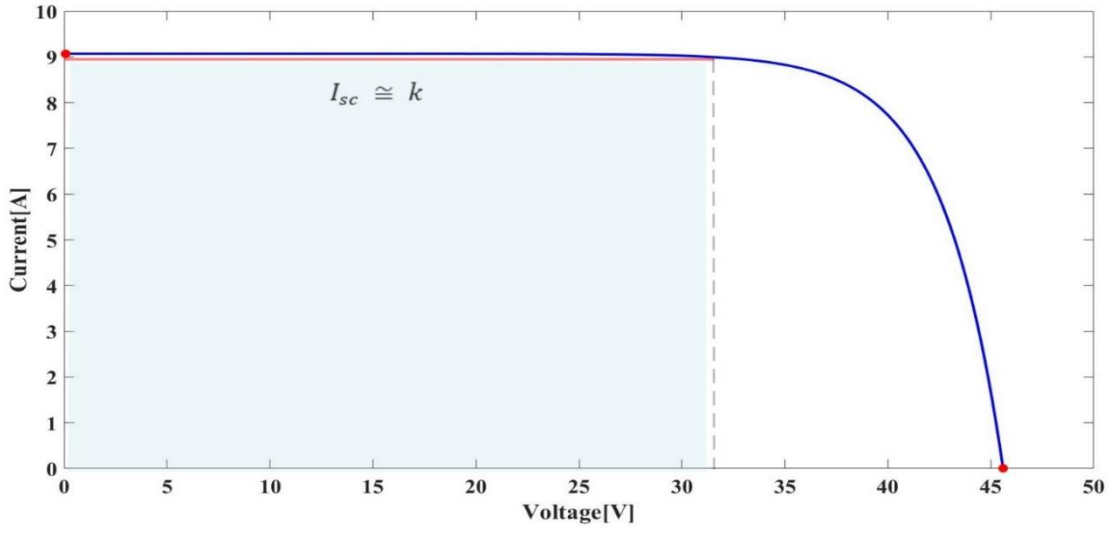

(b)

Figure 6.11: Characteristics of the Suntech STP320-24/Ve PV panel for different irradiances at T = 25°C (a) *I-V* curve (b) *P-V* curve.

6. At the short circuit point, where the V_{pv} is equal to zero, the output power P_{pv} is set to zero in order to give the coefficient f the value of zero in order to simplify the polynomial computation.

Solving the above equations constructed at each point by the matrix described in Equation (6.34), we get the value of the coefficients for the fifth-order polynomial to describe the curved part in the *P-V* curve characteristic of the PV panel model.

$$\begin{bmatrix} 320 \\ 0 \\ 291.2 \\ 0 \\ 286 \\ 0 \end{bmatrix} = \begin{bmatrix} (36.7)^5 & (36.7)^4 & (36.7)^3 & (36.7)^2 & (36.7)^1 & 1 \\ (45.6)^5 & (45.6)^4 & (45.6)^3 & (45.6)^2 & (45.6)^1 & 1 \\ (41\ \ )^5 & (41\ \ )^4 & (41\ \ )^3 & (41\ \ )^2 & (41\ \ )^1 & 1 \\ 5(36.7)^4 & 4(36.7)^3 & 3(36.7)^2 & 2(36.7)^1 & 1 & 0 \\ 5(31.8)^4 & 4(31.8)^3 & 3(31.8)^2 & 2(31.8)^1 & 1 & 0 \\ 0 & 0 & 0 & 0 & 0 & 1 \end{bmatrix} \begin{bmatrix} a \\ b \\ c \\ d \\ e \\ f \end{bmatrix} \quad (6.34)$$

Figure 6.12 compares the calculated *P-V* curve, using a fifth-order polynomial approximation, Equation (6.27) and the line equation, Equation (6.28), to the modeled *P-V* curve of the identical Suntech STP320-24/Ve PV panel module. The calculation of the approximated module shows a similar behavior so it can be applied within the simulation as a PV application.

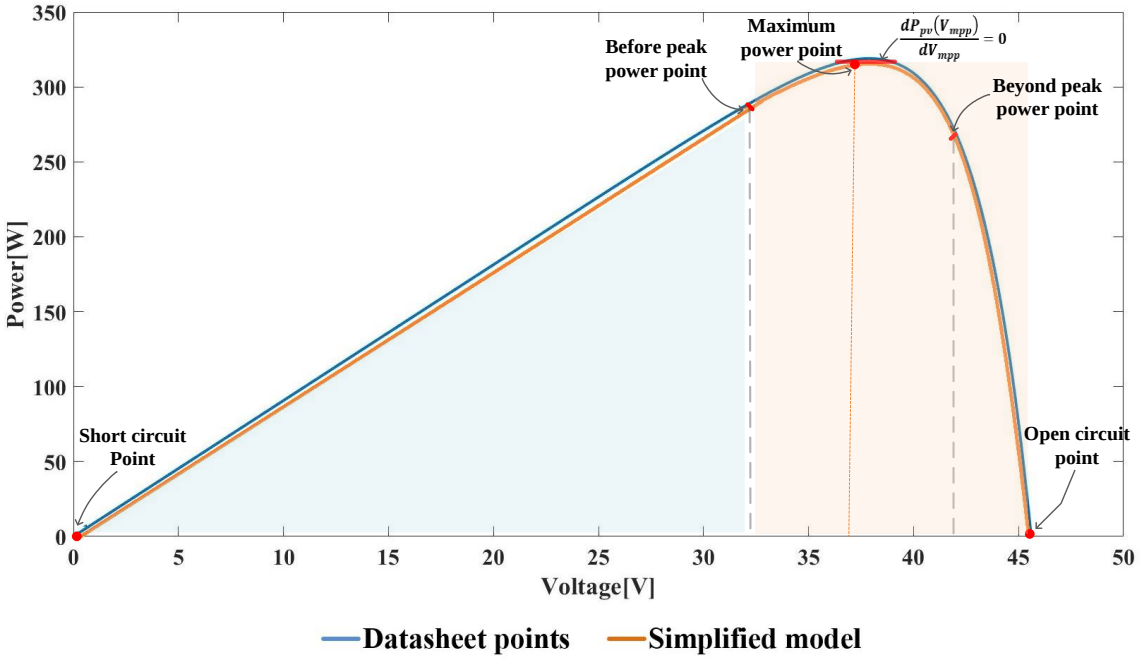

Figure 6.12: The behavior of the PV panel module is modeled using a fifth-order polynomial approximation and the line equation for the modeled P-V curve of the same Suntech STP320-24/Ve PV panel module.

6.4.3 Total Harmonic Distortion and Low Order Harmonic Distortion Computation

The THD and LHD measurements for the voltage and current signals out of the converter in the various scenarios are included in the simulation analysis. These measurements are important to validate the output quality and to reflect the PWM implementation controlling the MMC. In fact, unlike high order harmonic distortion, LHD measurements show the distortion of the output signal at low frequencies that are difficult to eliminate using a filter. Higher and lower order harmonics both cause distortion or noise at the output signals, so the LHD must be very low and within acceptable limits to keep the distortion under control. High-frequency distortion can be removed more easily at the output by using a filter without affecting the current or voltage signal.

Indeed, the THD and LHD of the output voltage and current represent the quality of the converted signal and how near they are to the pure sinusoidal signal used with an AC grid or AC load [171]. The distortion of a signal caused by the presence of several harmonics in the same signal is known as harmonic distortion, where harmonic frequencies are frequency components in a periodic voltage or current signal that are integer multiples of the main signal frequency [171]. In the electric system, a voltage or current signal that is not perfectly sinusoidal will have higher frequency components in it, adding to the signal harmonic distortion. In general, the less a periodic signal resembles a sine wave, the stronger the harmonic components and the greater the harmonic distortion. This is the basic outcome that the Fourier analysis of a periodic signal shows. Equation 6.35 explains the major component of the signal using Fourier analysis [172].

$$x(t) = a_0 + \sum_{k=1}^{\infty} (a_k cos(k \cdot \omega t)) + (b_k sin(k \cdot \omega t)) \tag{6.35}$$

After performing the Fourier analysis expansion, $x(t)$ represents the voltage or current signal as a function in the time domain. The average value of the DC component is a_0, the cosine component is a_k, and the sine component is b_k in the waveform, where k is the harmonic number. These components must be calculated to find the harmonics magnitude in each component, as indicated in Equations (6.36), (6.37), and (6.38).

$$a_0 = \frac{1}{T} \int_0^T x(t)\, dt \tag{6.36}$$

$$a_k = \frac{2}{T} \int_0^T x(t) \cdot cos(k \cdot \omega t)\, dt \tag{6.37}$$

$$b_k = \frac{2}{T} \int_0^T x(t) \cdot sin(k \cdot \omega t)\, dt \tag{6.38}$$

where the harmonic magnitude, H_k, can be calculated as follows:

$$H_k = \sqrt{{a_k}^2 + {b_k}^2} \tag{6.39}$$

In practice, LHD and THD must be calculated by obtaining the harmonic magnitude value of the fundamental frequency and all the harmonics, where THD is defined as the ratio of all the harmonic frequencies (from the 2nd harmonic on) over the fundamental frequency harmonics. The fundamental frequency is the main frequency of the signal, i.e., the frequency that would be identified when examining the signal with an oscilloscope.

In the simulated scenarios, LHD was calculated using Equation (6.40), which considers the impact of low harmonics from the 2nd to the 19th harmonic; while the THD computation obtained by applying Equation (6.41).

$$LHD = \frac{\sqrt{\sum_{k=2}^{19} {H_k}^2}}{H_1} \cdot 100\% \tag{6.40}$$

$$THD = \frac{\sqrt{\sum_{k=2}^{\infty} {H_k}^2}}{H_1} \cdot 100\% \tag{6.41}$$

where H_1 represents the first harmonic magnitude. So, the proportion of harmonic distortion is calculated using Equations (6.40) and (6.41) to obtain the percentage of LHD and THD, respectively.

6.4.4 Power Losses, Accuracy, Efficiency and Performance Computation

The analysis of power losses is important for demonstrating the impact of the modulation controller on the MMC-based PV applications. The power loss measurements indicate the efficiency of the converter and attempt to demonstrate the improvement gained by the proposed LC-PWM for both external and internal PV panel connections over conventional modulation, as detailed in each scenario in the following sections. Switching losses have not been considered in the power loss calculations, as the switching loss calculations depend on the switch device type and the switching frequency, where all the scenarios use the same IGBT in the SMs and the switching frequency for all cases is fixed at about 2 kHz. This gives no advantage to any modulation used with MMC, where the switching losses, by definition, occur when a switch is switched from off to on or vice versa. This interval is characterized by a significant voltage across the switch terminals and a significant current flow through it, and the energy dissipated in each transition needs to be multiplied by the frequency to obtain the switching losses [127].

The total converter power losses (P_{losses}) have been estimated using a simplified model that includes three main components, as shown in Equation (6.42): first, the power losses when each semiconductor is ON (P_{losses_on}), where a 30 mΩ series resistance (R_{on}) has been considered for each IGBT and FWD when they are active; second, the power losses when each semiconductor is OFF (P_{losses_off}), where a 100 KΩ resistance (R_{off}) has been considered for each IGBT and FWD when they are bypassed; third the power losses at the phase output (P_{losses_out}), where a 30 mΩ resistance (R_{on}) has been considered for each output reactor.

$$P_{losses} = P_{losses\_on} + P_{losses\_off} + P_{losses\_out} \tag{6.42}$$

The P_{losses_on}, P_{losses_off} and P_{losses_out} have been estimated using Equations (6.43), (6.44), and (6.45), respectively, throughout a period (T) of 20 milliseconds for a 50 Hz system.

$$P_{losses\_on} = \frac{1}{T}\int_0^T N_{sm} \cdot R_{on} \cdot (i_{ua}^2 + i_{ub}^2 + i_{uc}^2 + i_{la}^2 + i_{lb}^2 + i_{lc}^2)\, dt \tag{6.43}$$

where N_{sm} is the number of SM in each arm, this means that N_{sm} semiconductors are always active at each MMC arm in the applied simulation. i_{ux} and i_{lx} represent the upper and lower arm currents, respectively, where x refers to phase 'a', 'b', or 'c'.

$$P_{losses\_off} = \frac{1}{T}\int_0^T \frac{1}{R_{off}} \sum_{j=1}^{N_{sm}} \left(V_{c\_ua}^2(j) + V_{c\_la}^2(j) + V_{c\_ub}^2(j) + V_{c\_lb}^2(j) + V_{c\_uc}^2(j) + V_{c\_lc}^2(j)\right) dt \tag{6.44}$$

$V_{c\_ux(j)}$ and $V_{c\_lx(j)}$ represent the voltage in the upper and lower arms at each MMC cell, respectively.

$$P_{losses\_out} = \frac{1}{T}\int_0^T R_o \cdot (i_{oa}^2 + i_{ob}^2 + i_{oc}^2)dt \tag{6.45}$$

where R_o is a small series resistance due to the windings of the output inductor L_o, which is included with the MMC component. This is due to the converter output current flow through it.

Then, the accuracy of the MMC regulators, the efficiency of the MMC converter, and the performance of the application can all be computed using Equations (6.46) to (6.48).

$$\text{Accuracy} = \frac{P_{MMC\_IN}}{P_{mpp}} \cdot 100\% \tag{6.46}$$

$$\text{Efficiency} = \frac{P_{MMC\_OUT}}{P_{MMC\_IN}} \cdot 100\% \tag{6.47}$$

$$\text{Performance} = \frac{P_{MMC\_OUT}}{P_{mpp}} \cdot 100\% \tag{6.48}$$

where P_{mpp} represents the maximum power that can be extracted from the PV panels at their maximum power point under different situations of irradiance, P_{MMC_IN} represents the measured power at the input of the MMC, and P_{MMC_OUT} represents the power delivered by the MMC to an AC grid or load. In ideal circumstances, by removing any type of noise and power loss, these powers would be equal to attaining 100% accuracy, efficiency, and performance.

The calculation of the P_{MMC_IN} is described by Equation (6.49) for the external and internal PV panel connection.

$$P_{MMC\_IN} = V_{dc} \cdot I_{pv\_ex} + \sum_{j=1}^{N_{sm}} \begin{pmatrix} \left[V_{c\_ua}(j) \cdot i_{pv\_ua}(j)\right] + \left[V_{c\_la}(j) \cdot i_{pv\_la}(j)\right] \\ + \left[V_{c\_ub}(j) \cdot i_{pv\_ub}(j)\right] + \left[V_{c\_lb}(j) \cdot i_{pv\_lb}(j)\right] \\ + \left[V_{c\_uc}(j) \cdot i_{pv\_uc}(j)\right] + \left[V_{c\_lc}(j) \cdot i_{pv\_lc}(j)\right] \end{pmatrix} \tag{6.49}$$

where, for the external PV connection, the power would simply be equal to the multiplication of the V_{dc} by the current generated by all the connected PV panels, I_{pv_ex}, which is the same as the

current described previously as I_{dc}. The currents i_{pv_ux} and i_{pv_lx} would be zero in this situation, as they represent the current produced by the internal PV panels connected to each SM and vice versa, while the I_{pv_ex} would be zero in the internal connection and the P_{MMC_IN} would be the sum of the power produced in each SM.

The P_{mpp} has been calculated using Equation (6.50) for the external PV panel connection and Equation (6.51) for the distributed PV panel connection.

$$P_{mpp} = V_{mpp} \cdot I_{mpp} \tag{6.50}$$

where V_{mpp} and I_{mpp} represent the voltage and current at the maximum power point, respectively.

$$P_{mpp} = \sum_{j=1}^{N_{sm}} \begin{matrix} \left(\left[V_{mpp\_ua}(j) \cdot I_{mpp\_ua}(j)\right] + \left[V_{mpp\_la}(j) \cdot I_{mpp\_la}(j)\right]\right. \\ +\left[V_{mpp\_ub}(j) \cdot I_{mpp\_ub}(j)\right] + \left[V_{mpp\_lb}(j) \cdot I_{mpp\_lb}(j)\right] \\ \left. + \left[V_{mpp\_uc}(j) \cdot I_{mpp\_uc}(j)\right] + \left[V_{mpp\_lc}(j) \cdot I_{mpp\_lc}(j)\right]\right) \end{matrix} \tag{6.51}$$

where $V_{mpp\_ux(j)}$ and $I_{mpp\_ux(j)}$ represent the voltage and current at the maximum power point in the upper arm at each MMC cell, respectively. Also, $V_{mpp\_lx(j)}$ and $I_{mpp\_lx(j)}$ indicate the voltage and current at the maximum power point in the lower arm at each MMC cell.

Equation (6.52) is used to calculate the P_{MMC_OUT}, which represents the power provided to a grid or to an AC load in the off-grid connection.

$$P_{MMC\_OUT} = v_{ac\_a} \cdot i_{oa} + v_{ac\_b} \cdot i_{ob} + v_{ac\_c} \cdot i_{oc} \tag{6.52}$$

where v_{ac_x} is the voltage at the grid, that is the voltage after the MMC output reactors, which performs better than the voltage out of the MMC before the LC filter and which allows for a more accurate measurement of the output power. In fact, v_{ox} contains a high-frequency noise produced in the SM at each arm, which affects the converter power out value.

Furthermore, the approximation of the so-called power measure errors has been described for a more accurate calculation of the losses. This attempts to depict the unexplained power losses and to express a percentage of the differences between the input power and the unexplained power losses. The percentage of the power measure errors has been calculated using Equation (6.53).

$$Measure\_Error = \left|\frac{P_{measure\_error}}{P_{mpp}}\right| \cdot 100\% \tag{6.53}$$

where $P_{measure\_error}$ has been computed in Equation (6.54) to reflect the difference between the power in and power out of the MMC after subtracting the power loss, and the stored power in the MMC instantaneously, in order to validate the accuracy, efficiency, and performance measurements.

$$P_{measure\_error} = P_{MMC\_IN} - P_{MMC\_OUT} - P_{store\_MMC} - P_{losses} \tag{6.54}$$

where P_{store_MMC} indicates the power stored in the MMC since the MMC contains N_{sm} of SMs in each arm and each SM includes a floating capacitor as well as an arm inductor that can store energy also output inductor for each phase that can store energy during converter operation. The power store computation is depicted in Equation (6.55) in a simplified form.

$$P_{store\_MMC} = P_{store\_C_{SM}} + P_{store\_L_{arm}} + P_{store\_L_o} \tag{6.55}$$

where P_{store_Csm} represents the power stored in the SM capacitor, P_{store_Larm} shows the power stored in the arm inductor, and P_{store_Lo} shows the power stored in the phase-out inductor, where Equation (6.55) adds up all the potential components inside the MMC that store energy throughout the conversion. These stored powers in capacitors and inductors were estimated by differentiating the energy over time, since the energy is power integrated over time. Equations (6.56) and (6.57) indicate the power and energy stored in the SM capacitors.

$$P_{store\_C_{SM}} = \frac{dE_{store\_C_{SM}}}{dt} \cong \frac{E_{store\_C_{SM}}(t) - E_{store\_C_{SM}}(t-T)}{T_s} \tag{6.56}$$

where $E_{store\_C_{SM}}$ refers to the energy stored in the three phase MMC SM capacitors.

$$E_{store\_C_{SM}} = \frac{1}{2} \cdot C_{SM} \sum_{j=1}^{N_{sm}} \left(V_{c\_ua}^2(j) + V_{c\_la}^2(j) + V_{c\_ub}^2(j) + V_{c\_lb}^2(j) + V_{c\_uc}^2(j) + V_{c\_lc}^2(j) \right) \tag{6.57}$$

Equations (6.58) and (6.59) indicate the power and energy stored in the arm inductor, respectively.

$$P_{store\_L_{arm}} = \frac{dE_{store\_L_{arm}}}{dt} \cong \frac{E_{store\_L_{arm}}(t) - E_{store\_L_{arm}}(t-T)}{T_s} \tag{6.58}$$

where E_{store_Larm} refers to the energy stored in the three phase MMC arms inductors.

$$E_{store\_L_{arm}} = \frac{1}{2} \cdot L_{arm} \cdot [i_{ua}^2 + i_{ub}^2 + i_{uc}^2 + i_{la}^2 + i_{lb}^2 + i_{lc}^2] \tag{6.59}$$

while the power and energy stored in the output phase inductor are shown in Equations (6.60) and (6.61), respectively.

$$P_{store\_L_o} = \frac{dE_{store\_L_o}}{dt} \cong \frac{E_{store\_L_o}(t) - E_{store\_L_o}(t-T)}{T_s} \tag{6.60}$$

where E_{store_Lo} refers to the energy stored in the three phase MMC phase out inductors.

$$E_{store\_L_o} = \frac{1}{2} \cdot L_o \cdot [i_{oa}^2 + i_{ob}^2 + i_{oc}^2] \tag{6.61}$$

In fact, the power stored in the capacitors and the inductors will be zero in the steady state. These stored power computations were included to acquire exact calculations instantaneously from the simulation model execution, so that the influence of those elements on the power delivered through the MMC to the grid connection could be seen.

6.4.5 Scenario 1: LC-PWM Controlled MMC Connected to Grid

In this scenario, the proposed LC-PWM modulation is simulated by connecting the MMC to an AC grid. An MMC with four SMs per arm is used to analyze the converter behavior in two cases: first, connecting the PV panels externally to the MMC; in the second case, PV panels are integrated directly in the MMC cells, and the converter is then connected to the grid system. The simulation used the parameters described in Table 6.2 for the PV panels, while the MMC parameters are described in Table 6.3. A uniform averaged irradiance is used on the external PV array, and different irradiances are used for different MMC cells when using distributed PV panels, in such a way that the MMC arms receive approximately the same PV power.

In fact, the distributed PV panels may be arranged in clusters to keep the energy balanced between phases on the one hand, and between the upper and lower arms on the other. The idea is based on putting the SM of each arm from each phase in the same place. This is referred to as a cluster, and it keeps the arms and legs of the converter as balanced as possible. This distribution ensures that the connected PV panels in each SM receive the same irradiance and temperature. The cluster greatly reduces the unbalanced energy, particularly in this situation, when the PV string is

integrated directly into the SM, resulting in energy sources in the converter, which increases the control requirements because the energy imbalances typically generate more power losses due to circulating currents. All six arms of the MMC converter will therefore receive the same average irradiance, so there will be a very small energy transfer from phase to phase, or from arm to arm, needed to keep them in a balanced situation.

Table 6.3. Parameters of the three-phase MMC connected to the grid.

Parameters	Value
Active power (P)	169 kW
DC link voltage (V_{dc})	3200 V
DC link Capacitor (C_{dc})	20000 µF
Grid voltage at converter side (V_{grid})	1200 V
Grid voltage at grid side	400 V
Transformer ratio (star/delta connection)	√3:1
Fundamental frequency (f_{fund})	50 Hz
Switching frequency (F_s)	2000 Hz
SM capacitance (C_{SM})	6000 µF
SM capacitor voltage (V_{SM})	807.4 V
Number of SM in each arm (N_{sm})	4
Arm inductor (L_{arm})	3000 µH
Output inductor (L_o)	6000 µH
Output capacitor (C_o)	83 µF
Grid inductor (L_{grid})	500 µH

Modeled PV panels were then distributed as an array of cells when arranging the PV panels field externally to the MMC, giving a nominal DC voltage of 3200 V, or as 24 strings of 22 panels serially attached to each one of the 24 SMs of a five-level three-phase MMC, giving 807.4 V at each cell at their maximum power point. After that, the MMC was connected to the AC grid. Table 6.3 shows the grid connection parameters, as illustrated in Figure 6.1.

The MMC-based grid connection topology includes different inductors and capacitors on both MMC and grid connection sides. These values were determined for the reasons of filtering, resonant frequency effect, reactive power minimization, and power losses, as well as take into consideration of the robust grid connection.

As previously stated in Chapter 5, the C_{SM} size was estimated using Equation (5.19) to limit the amount of capacitor voltage ripple. The chosen value leads to a voltage ripple of about ±1.8% of the SM capacitor voltage.

Meanwhile, the capacitor at the output, C_o, must produce a tolerable reactive power at the output capacitor, Q_c, which is typically less than 40% of the nominal transmitted power, where the power factor must be above 0.9 to be acceptable. In this case, the MMC reactive power reference has been set to a value that reduces the grid reactive power to near zero. Based on the specified C_o value, Equation (6.62) would be used to calculate Q_c at the three-phase output capacitor.

$$Q_c = 3 \cdot 2\pi \cdot f_{fund} \cdot C_o \left(\frac{V_{grid}}{\sqrt{3}}\right)^2 \tag{6.62}$$

where f_{fund} represents the fundamental frequency 50 Hz, C_o is the output star connected capacitor, and V_{grid} is the RMS phase to phase voltage.

As a result, the C_o has been chosen to achieve about 22% of reactive power Q_c. In addition, the size of the C_o with the equivalent inductor L_{eq} at the converter output has a significant impact on the output filter, which must be determined to eliminate any resonant frequency with the switching frequency or fundamental frequency of the output current. The resonant frequency should be around 10 times less than the switching frequency, F_s, on the LC filter bode plot diagram to achieve -40dB at switching frequency. Thus, L_{eq} can be calculated using Equation (6.63) to match the above requirement.

$$\omega_n = \frac{1}{\sqrt{L_{eq} \cdot C_o}} < \frac{1}{10} \cdot 2\pi \cdot F_s \tag{6.63}$$

In Chapter 4 Equation (4.12), L_{eq} decided the sizes of both the arm inductor L_{arm} and the output inductor L_o.

The arm inductor, L_{arm}, role is important in limiting the circulating current and the DC fault current within the phase-leg of the MMC. It also enables the control of the converter's internal circulating current [168]. The presence of floating capacitors, C_{SM}, in each SM may induce resonant frequency distortion with the L_{arm} in the MMC output current and voltage. Then, the resonant frequency, ω_n, may produce between the connected capacitors on the arm and the arm inductor, where, in fact, an average of serial connected capacitors in each arm was used in the calculation to check the chosen size of the L_{arm}. This is based on the resonant frequency effect,

using Equation (6.64), giving an average resonant frequency of approximately 53 Hz. In fact, the resonant frequency in this situation will change frequently, depending on the number of SMs in the status *ON*.

L_o can then be estimated, depending on the L_{eq} and L_{arm} to be at the right size to achieve the above requirements of the reactive power and resonant frequency effect.

$$\omega_n = \frac{1}{\sqrt{L_{arm} \cdot \left(\frac{C_{SM}}{N_{sm}/2}\right)}} \tag{6.64}$$

In addition, L_{eq} must be less than the grid inductor, L_{grid}, because the PV application system is generally linked to a strong grid with a power greater than the power generated by the connected PV panels. Furthermore, the resonant frequency between L_{grid} and C_o should be considered, where the resonant frequency is determined to be about 780 Hz and may have a resonant effect in harmonic 15 or 16, which is distant from the fundamental frequency and does not exhibit a real influence on the grid side.

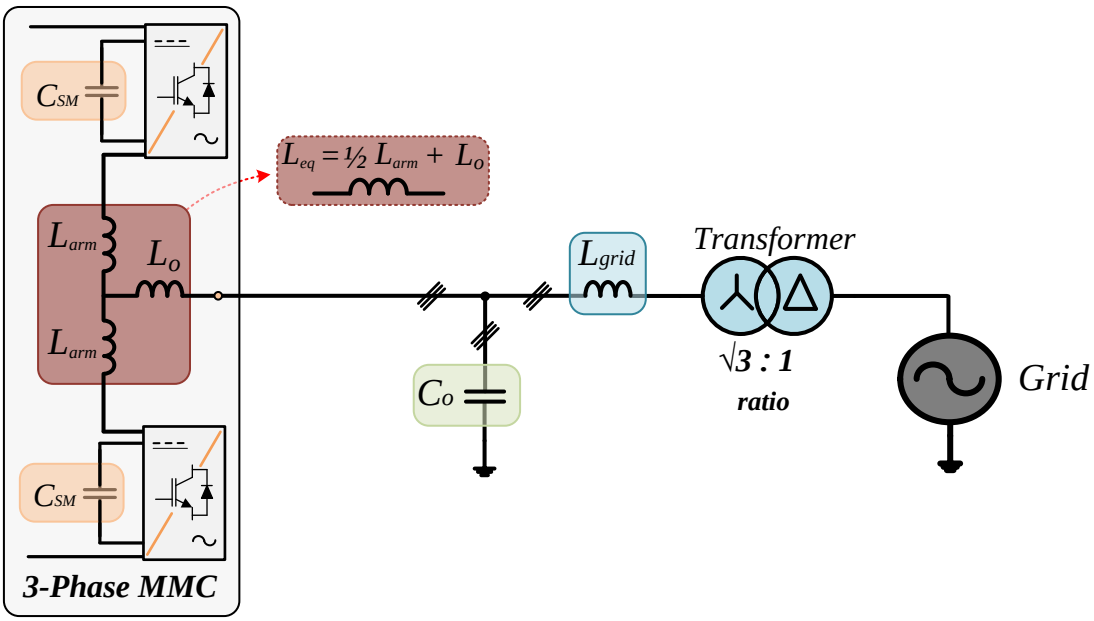

Figure 6.13: The main inductors and capacitors used in the MMC-based grid connection.

The output capacitors *(C_o)* in Figure 6.13 are star-connected, although they could be physically linked after the transformer on the grid side with a delta connection. In this case, the equivalent size will be equal to 250 µF instead of 83 µF, by considering the transformer connection

type and transform ratio. In addition, if the grid inductor (L_{grid}) were connected after the transformer the equivalent L_{grid} would be 55 µH instead of the 500 µH given in Table 6.3.

In fact, the capacitor and inductor values in Figure 6.13 reflect the most essential aspects required to achieve high performance from the MMC side, while still maintaining a reliable connection to the AC grid.

Furthermore, connecting the MMC to an AC grid requires the use of several regulators to control the active power, reactive power, output current control, and circulating current, as previously explained, and those controllers must be fine-tuned to achieve the expected value. The coefficients of various PI controller tunings applied in the simulation have been specified and described. However, as previously stated, a PI regulator contains tuning components that are independent of other regulators, indicated by K_p for the proportional gain and K_i for the integral gain, as can be seen in Figure 6.3, where K_i represents the ratio of the proportional gain with the time response T_i. If the value of T_i is small, the PI response will be faster, and vice versa. These coefficients would be used to tweak the regulator to achieve the desired response over the controller. Various methods for providing a proposed value for better tuning were introduced in [173], which in the end may not be enough and must be continually modified through the trial-and-error approach to be able to apply the regulator.

In practice, a trial-and-error technique was used to tune all the regulators by locked controllers at their expected values. Four controllers were applied in sequence in the simulation as follows:

1. The output current controller.
2. The active power controller in Figure 6.3.
3. The AC component of the circulating current in Figure 6.5(b).
4. The DC component of the circulating current in Figure 6.5(a).

Since this PV application used in the simulation connection knew the expected active power to share with the grid or consume at the load side and specified an initial value for the DC-link side, those values contributed to locking controllers 3 and 4 at their expected values. In addition, controller 2 was locked by applying an external balancer to keep the upper and lower arms in a balanced position throughout all the phases. Then, for the first controller, the trial-and-error approach was used to get the system on the proper path and provide an accepted behavior. After the system obeys correctly, the external balancer is removed, and the second PI controller for the AC component of the circulating current is calibrated to stabilize the system. Then, the circulating current's DC component is fine-tuned to maintain the MMC legs balanced. Eventually, the active power controller is set to correct the load power consumption, or the load power must be shared or requested from the grid side. The PI controller coefficients used in each controller are listed in Table 6.4.

Table 6.4. The proportional and integral PI controller coefficients.

PI coefficients	T_i	K_P	K_i
Output current control	0.0027	8	3000
Active power control	0.8	1.2	1.5
Circulating current control (AC component)	1.4	0.06	0.043
Circulating current control (DC component)	2	0.025	0.0125

Table 6.4 indicates that the T_i coefficient value for the first controller was the smallest, increased for the second, and then increased again for the others. This provides a logical explanation for why the controllers should be applied in that order, from faster to slower.

6.4.5.1 Case 1: PV Panels Located Externally to the MMC

In this case, the PV panels are connected as a central converter, using a 6X88 PV array connected at the DC side of a five-level MMC converter-based grid connection. The newly proposed LC-PWM modulation is applied to control the MMC in the simulation module.

Table 6.5 illustrates the results of these simulations including a measure of the total harmonic distortion at the converter output for the voltage and current (THD_{CV} and THD_{CI}), the LHD from the 2nd to the 19th harmonic for both voltage and current (LHD_{CV} and LHD_{CI}), and most importantly, a measure of the total harmonic distortion of the current at the AC grid (THD_{GI}), as it must be smooth enough and have a sufficiently high quality to move the power to the grid.

The distortion results shown in Table 6.5 are consistent in a wide operation range (irradiance from 100% to 10%). Here, the THD_{CV} and THD_{CI} measurements are important for validating the output quality and to reflect the LC-PWM implementation that controls the MMC. In particular, the results show a steady result at different situations of irradiances over the connected PV panels, which may be caused by clouds or shadows. The LHD_{CV} and LHD_{CI} measurements, however, show that the distribution of the low frequency components at the output is low and under control, which gives a good intention of the proposed modulation. This is carried out by pushing the distortion to the high-frequency areas, which can then be easily filtered at the output. On the other hand, THD_{GI} shows the quality of the current provided to the AC grid.

Table 6.5. Simulation results of the MMC modulated using LC-PWM with external PV panels.

Situation	Irradiance [W/m^2]	THD_{CV} [%]	LHD_{CV} [%]	THD_{CI} [%]	LHD_{CI} [%]	THD_{GI} [%]
1	1000	22.8	0.42	1.4	0.22	0.44
2	850	27.2	0.50	2.1	0.20	0.56
3	700	27.8	0.50	2.3	0.21	0.58
4	550	30.2	0.57	2.5	0.25	0.62
5	400	29.9	0.64	2.4	0.33	0.70
6	250	29.9	0.64	2.1	0.24	0.71
7	100	23.3	0.44	0.60	0.10	0.47

Figure 6.14 displays the three-phase voltage and current output measurements for situation 1 of the irradiance, demonstrating the high quality of the current and voltage out of the MMC before applying the filter, as well as the smooth sinusoidal wave of the current and voltage at the point connected to the grid, which reflects the low distortion measurements in Table 6.5.

Furthermore, Table 6.6 shows the results analysis of the DC and RMS components of the circulating current, and the RMS value of the circulating current when its DC component is removed. Here, the DC value of the circulating current represents the power transferred between the phases to keep them in a balanced situation and to transfer power from the DC side to the MMC phases. The RMS value represents the 50 Hz component needed to maintain the arms balanced along with the noise of the unwanted components in the circulating current plus the DC component. Therefore, the last value in Table 6.6 shows the RMS value of the circulating current when its DC component is removed, in order to clearly display the noise and the ripple in the circulating current. The findings indicate a very low noise value, which will have an impact on the converter efficiency as well as the consistency of the noise in various situations, which makes a good impact on the action of the LC-PWM. This is due to the suppression of the noise to the minimum with different voltages.

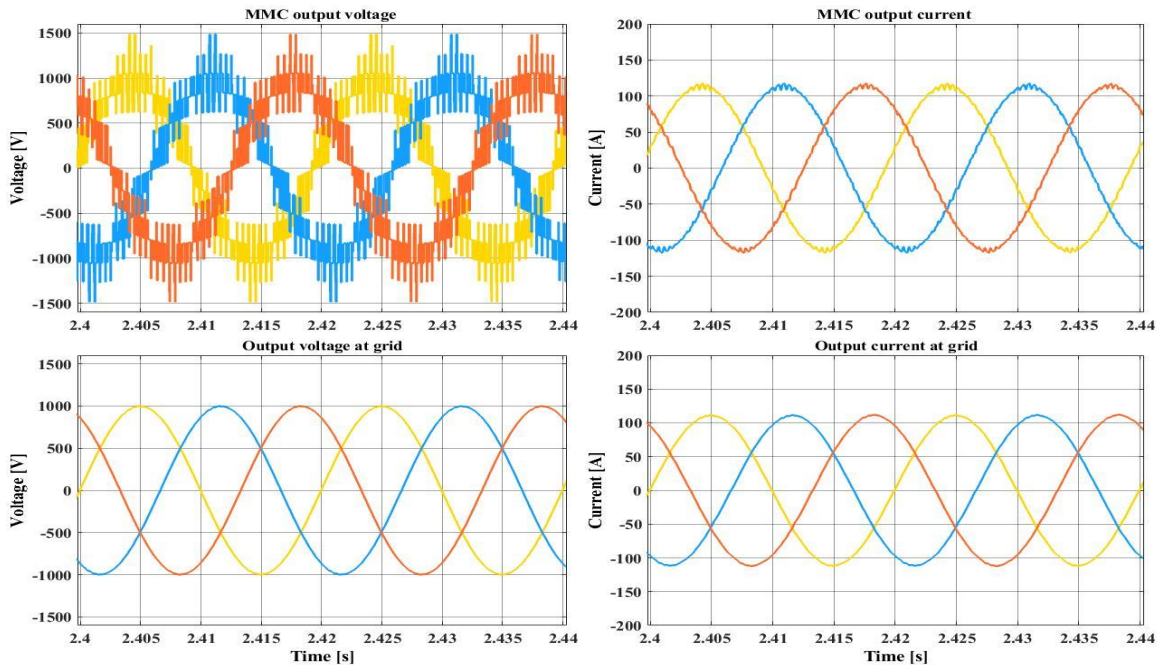

(a) (b)

Figure 6.14: Measurements of three-phase voltage and current output signals for irradiance in situation 1. (a) In the first row, the voltage at the MMC output; in the second row, the voltage at the grid connection. (b) In the first row, the current at the MMC output; in the second row, the current at the grid connection.

Table 6.6. Simulation results of the circulating currents of the MMC modulated using LC-PWM with external PV panels.

Situation	Irradiance [W/m^2]	DC (i_z) [A]	RMS (i_z) [A]	RMS [i_z – DC (i_z)] [A]
1	1000	17.37	17.38	0.58
2	850	14.80	14.81	0.54
3	700	12.21	12.22	0.49
4	550	9.61	9.62	0.43
5	400	7.01	7.02	0.37
6	250	4.42	4.43	0.29
7	100	1.84	1.85	0.19

Figure 6.15 clearly shows the relatively low circulating current in each phase of the MMC, as well as the noise ripple at a very high frequency. These values correspond to the measurement in the first Irradiance situation in Table 6.6.

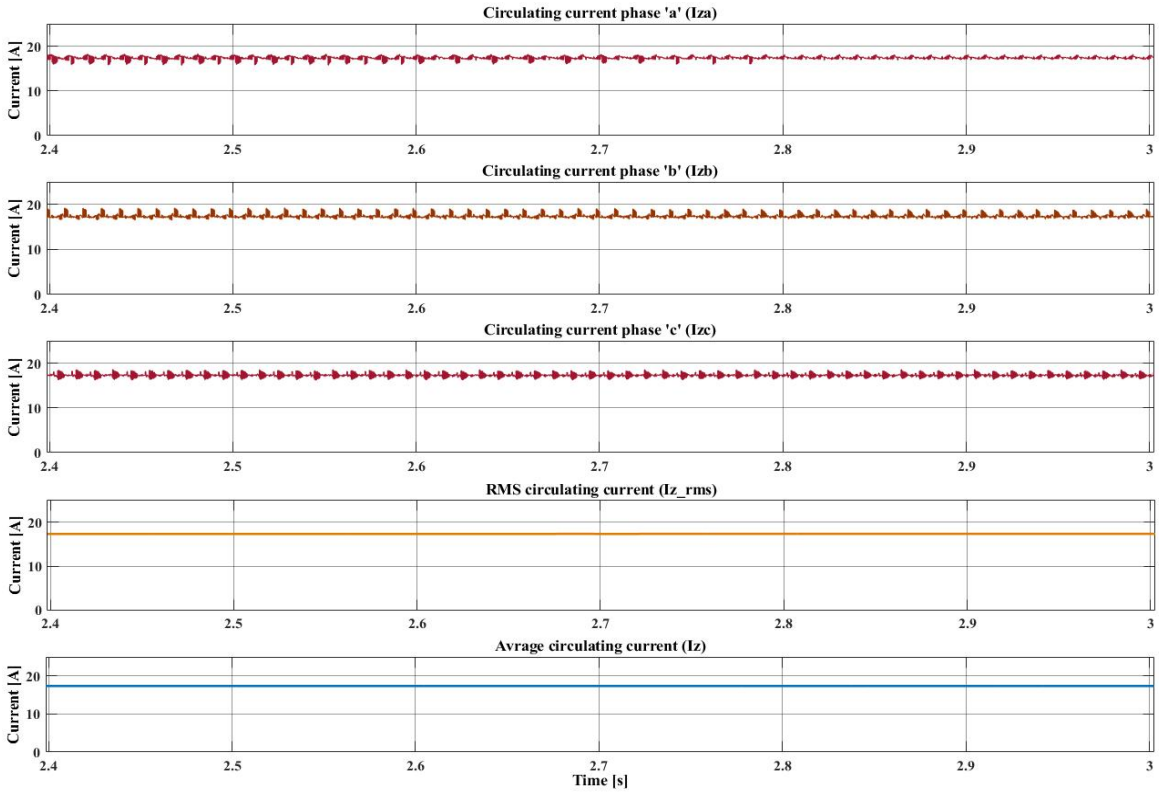

Figure 6.15: Displays the circulating current in phases 'a', 'b', and 'c', as well as the RMS and average values of the circulating current.

6.4.5.2 Case 2: PV Panels Distributed Throughout the MMC

In this case, strings with 22 PV panels in series were integrated directly on each SM of the MMC, as shown in Figure 6.1. Identical solar panels are used in all SM, but the irradiance changes with different SMs, as described in Table 6.7 and shown in Figure 6.16, which illustrates the irradiance situations applied in each PV string in SM1, SM2, SM3, and SM4. It also shows the voltage capacitor at each SM in the upper arm for irradiance situations (1, 3, 4, 6, and 7), respectively.

Table 6.7. Irradiance received at the PV string located at SMs in the simulated situations.

Situation	SM1 Irradiance [%]	SM2 Irradiance [%]	SM3 Irradiance [%]	SM4 Irradiance [%]	Average Irradiance [%]
1	100	100	100	100	100
2	100	90	80	70	85
3	100	80	60	40	70
4	100	70	40	10	55
5	70	50	30	10	40
6	40	30	20	10	25
7	10	10	10	10	10

In situation 1 (100%), the integrated PV panel string in each SM has the same irradiance level and all the SM have the same target voltage. In situation 3, shown in the second row in Figure 6.16, the irradiance variations increased more than in the previous situations, and then the voltage level differences at each SM start to be clear. In situations 4 to 6, the third and fourth rows in Figure 6.16, the irradiance differences at each SM farther increased, representing the hardest situation for the traditional modulations that work with a fixed frame of voltage levels, underestimating the differences of voltage levels in those situations. The last situation, the last row in Figure 6.16, represents situation 7, which aims to show the efficiency of the converter under a very low irradiance situation (10%). Figure 6.16 has no display for situation 2 because it is similar to situation 3, while situation 5 is not included as it is very similar to situation 6. It must be noted that, at different irradiance situations, all SM voltages move together, because the selection method of the cells to be inserted or bypassed depends on the sorting of all the SM voltages.

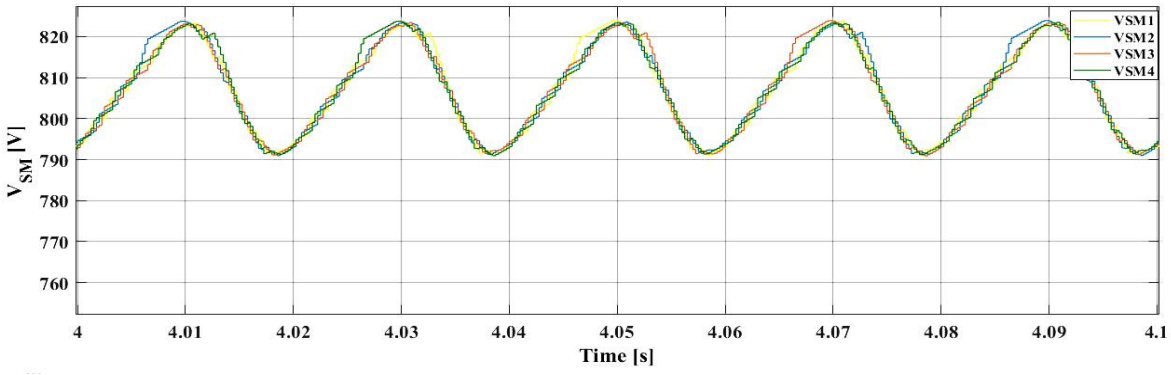

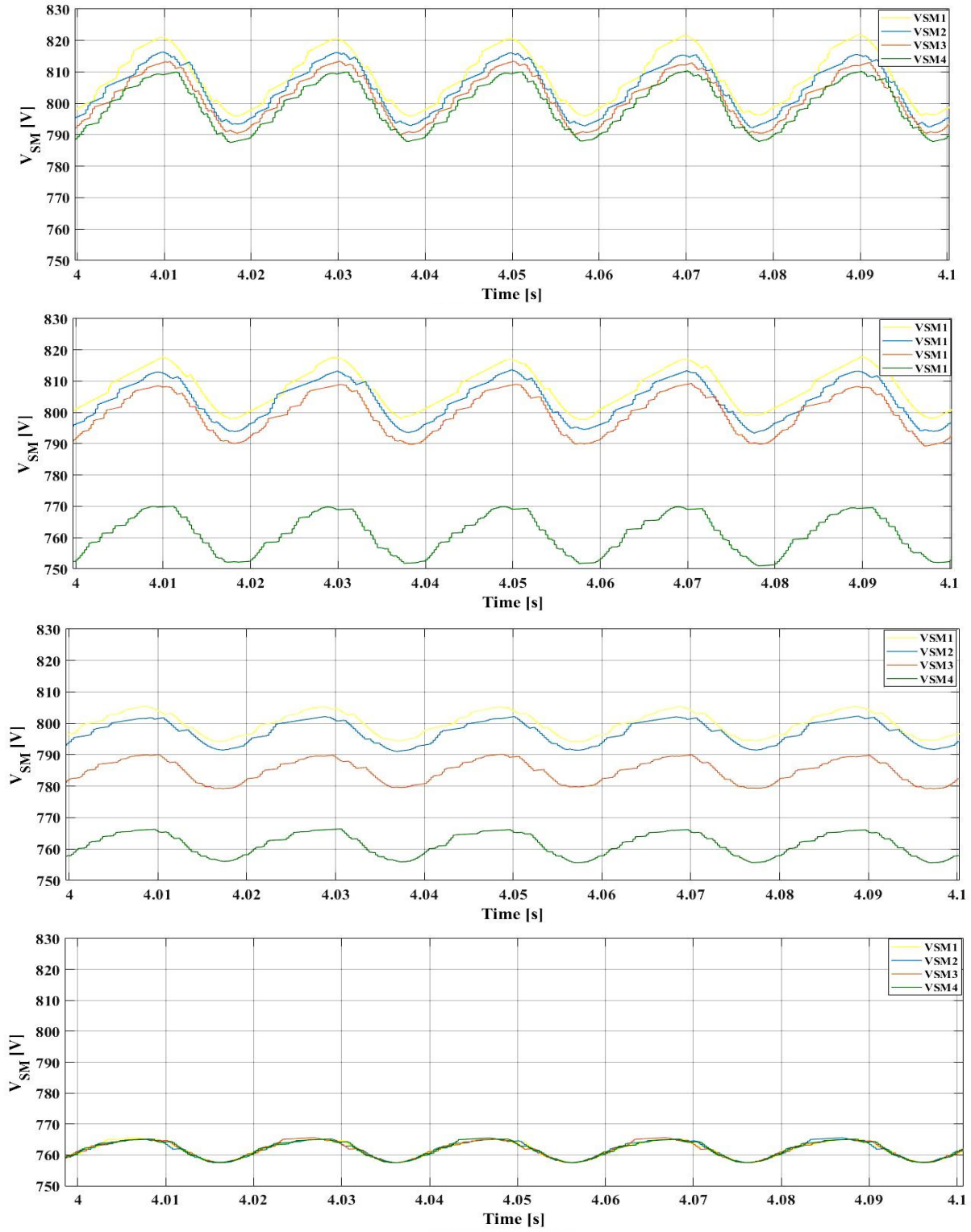

Figure 6.16: Capacitor voltages at each SM in the upper arm for irradiance situations [1, 3, 4, 6, and 7].

Table 6.8 displays the simulation results obtained by using the various irradiance circumstances listed in Table 6.7. The measurements also include a measure for THD_{CV} and THD_{CI}, the LHD from the 2nd to the 19th harmonic for LHD_{CV} and LHD_{CI}; and the most importantly, a measure of THD_{GI}, where the simulation is performed repeatedly in each situation to illustrate the influence of the change in irradiance in terms of shadows or clouds. Now, the voltage differences between the different cells are compensated by the LC-PWM and, as a result, the output distortion is under control in the whole operation range for this application, from 100% to 10% irradiance, even with variable irradiance for different MMC cells.

Table 6.8. Simulation results of the MMC modulated using LC-PWM with internal PV panels.

Situation	THD_{CV} [%]	LHD_{CV} [%]	THD_{CI} [%]	LHD_{CI} [%]	THD_{GI} [%]
1	22.8	0.44	1.43	0.23	0.45
2	24.8	0.40	2.10	0.20	0.60
3	26.8	0.47	2.31	0.20	0.61
4	28.9	0.61	2.42	0.40	0.72
5	28.2	0.58	2.40	0.33	0.74
6	28.3	0.51	1.90	0.24	0.72
7	23.2	0.41	0.55	0.10	0.48

Figure 6.17 shows the three-phase voltage and current output measurements for irradiance situation 1, indicating the good quality of the current and voltage out of the MMC prior to applying the filter, as well as the smooth sinusoidal wave of the current and voltage at the point connected to the grid, which represents the low distortion measurement in Table 6.8.

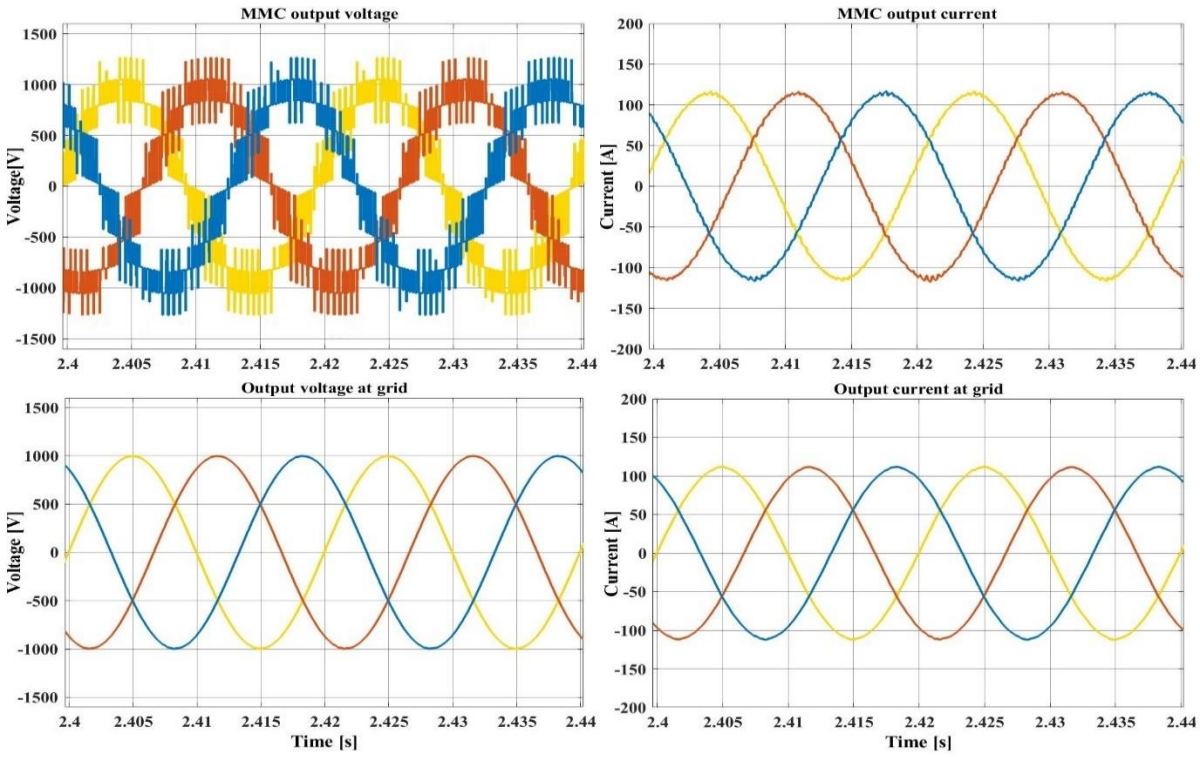

(a) (b)

Figure 6.17: Measurements of three-phase voltage and current output signals for irradiance in situation 1. (a) In the first row, the voltage at the MMC output; in the second row, the voltage at the grid connection. (b) In the first row, the current at the MMC output; in the second row, the current at the grid connection.

Furthermore, Table 6.9 shows the results analysis including the DC and RMS components of the circulating current, and the RMS value of the circulating current when its DC component is removed. Here, the DC component of the circulating current has been eliminated as the PV panels supply energy directly to the MMC capacitors, while the RMS value of the circulating current represents the 50 Hz component in order to maintain the arms balanced with a few undesired components due to the switching. Thus, the RMS value, which represents the noise and the ripple of unwanted components in the circulating current, is almost the same value as the RMS value of the circulating current when its DC component is removed due to the DC component already being zero.

The results show that the circuiting current produces relatively low noise, which will have an impact on converter efficiency. The RMS value demonstrates the consistency of the behavior of the LC-PWM in various irradiance situations, even when the SM voltages change instantaneously due to the PV string being directly integrated into each SM. This is because the proposed LC-PWM modulation generates a local carrier based on the voltage measurements at each SM instantaneously and precisely calculates the duty cycle to switch those SMs that greatly suppress the noise and ripple in the circulating current.

Table 6.9. Simulation results of the circulating currents of the MMC modulated using LC-PWM with internal PV panels.

Situation	DC (i_z) [A]	RMS (i_z) [A]	RMS [i_z – DC (i_z)] [A]
1	-0.002	0.38	0.38
2	-0.011	0.32	0.32
3	0.002	0.28	0.28
4	0.001	0.57	0.57
5	-0.001	0.48	0.48
6	-0.002	0.39	0.39
7	0.000	0.12	0.12

The circulating current in each phase of the MMC is extremely low, as shown in Figure 6.18, and the noise ripple occurs at a very high frequency, their impact being easily removed with a filter at the output. These values are based on the data in Table 6.9 for the first irradiance situation.

Figure 6.19 clearly shows that the LC-PWM can keep distortion within acceptable levels for any irradiance situation when using external or internal PV panels in a consistent manner. In addition, the behavior is better in the internal PV connection, because the DC component of the circulating current has been removed which, produces smaller ripples in the capacitor cells compared to the external PV connection and this is reflected in the LHD and THD of the current out.

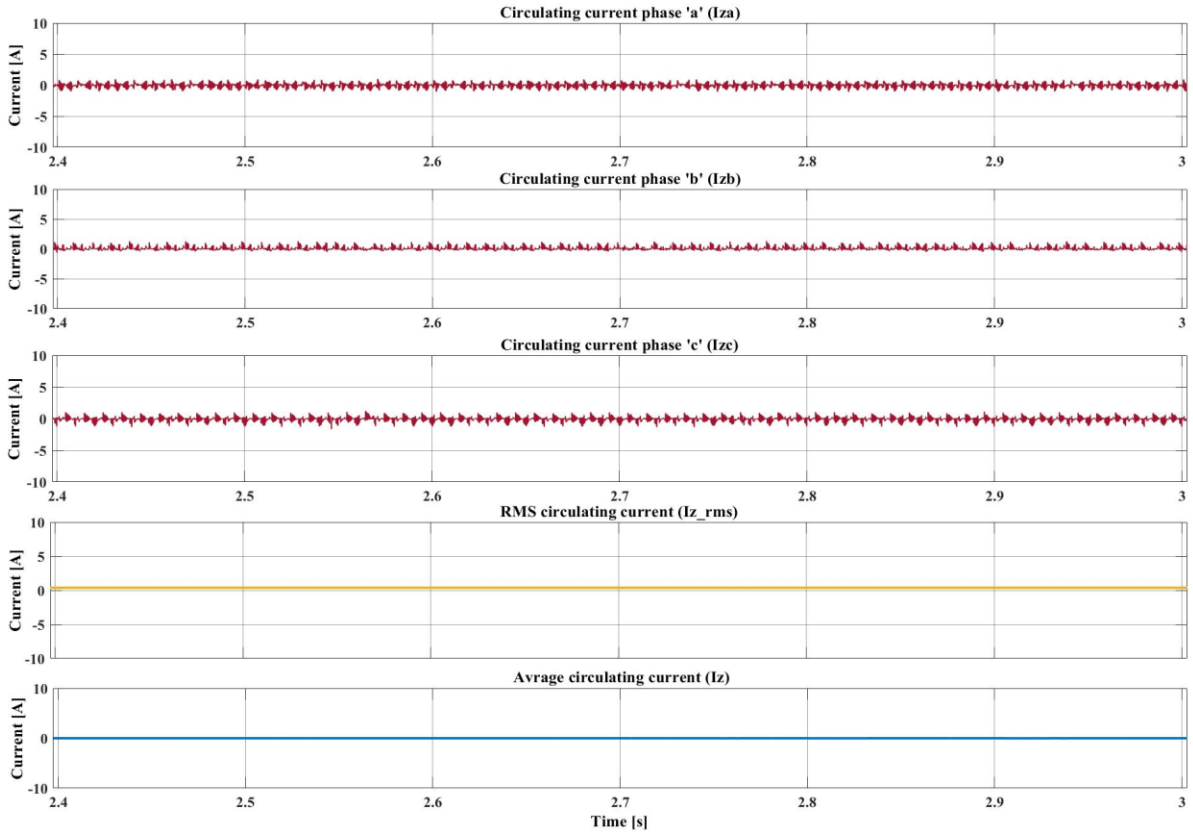

Figure 6.18: Measurements of the circulating current in phases 'a', 'b', and 'c', as well as the RMS and average values of the circulating current for irradiance in situation 1.

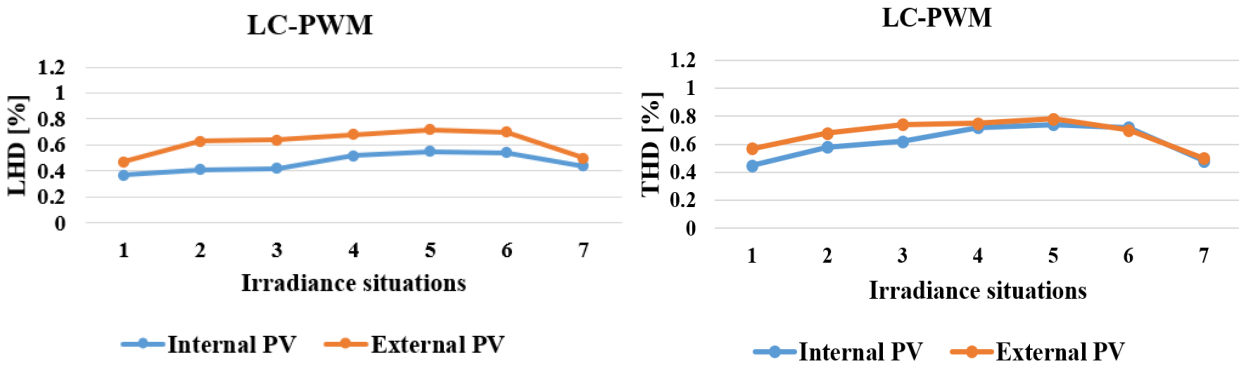

(a) (b)

Figure 6.19: Comparison of the output current harmonic distortion in external and internal PV panel connections using LC-PWM. (a) Reflects low order harmonic distortion (LHD) (b) Reflects absolute harmonic distortion in terms of total harmonic distortion (THD).

The power loss analysis, registered in Table 6.10, confirms the improvement achieved by the LC-PWM for both external and internal PV panel connections. An optimized modulation takes into account the measured voltages of the MMC cells and synchronizes each level-to-level transition in order to remove all transients in the circulating current.

Table 6.10. The converter power loss based on measurements of a switch on power loss, switch off power loss, phase output power loss, and total power losses using LC-PWM.

PV panels connection	Situation	P_{losses_on} [W]	P_{losses_off} [W]	P_{losses_out} [W]	P_{losses} [W]
External PV	1	1395	157	589	2140
	2	1032	156	437	1625
	3	724	156	308	1188
	4	473	155	203	831
	5	280	154	123	557
	6	147	151	67	364
	7	73	140	35	248
Internal PV	1	1177	156	588	1922
	2	874	156	437	1467
	3	617	155	308	1081
	4	407	151	203	762
	5	245	150	123	518
	6	133	148	66	348
	7	71	140	35	245

As can be seen in Table 6.10, the power losses are a bit better, being reduced by 16%, when using the internal PV panel rather than the external PV panel connection. This is because the effect of the DC component of the circulating current has been removed by integrating the PV string directly with the MMC cell, which reduces the RMS value of the uncontrolled circulating current a little, as displayed previously in Tables 6.6 and 6.9, respectively. This effect appears clearly in the P_{losses_on}, as the circulating current has a direct effect on the cell capacitor when the SM is in status *ON*, while the P_{losses_off}, and P_{losses_out}, are mostly equal in both the internal and external PV panels. In other words, the results in Table 6.10 are consistent, whereas, P_{losses_on} has more varied values between each two-irradiance condition. This is because those values are proportional to the current in each SM, which is proportional to the arm current, as indicated in Equation (6.40). Furthermore, due to the proportional relationship with the output current, as indicated in Equation (6.42), P_{losses_out} has quite a large difference between the irradiance situations, while the P_{losses_off} values are proportional to the voltage at the SM in each irradiance circumstance, as indicated in Equation (6.41), so they have less variation across all the irradiance situations.

Table 6.11 displays the accuracy of the input power, the efficiency of the MMC converter, and the performance of the application under different situations of irradiance for the external and internal PV panel connection. The results in Table 6.11 show the internal PV connection has the same accuracy and application performance as the external connection compared to the best situation that can be obtained from the external connection. This is because the MPPT is applied globally over the PV panels and can achieve better a MPPT computation than the internal connection.

In fact, MPPT controllers are less accurate when using internal panels: each SM has its own MPPT, but the active power controller can only regulate the total of all the MMC voltage cells. When using external PV panels, the accuracy is higher because the whole PV array voltage, the DC-link voltage, is directly measured and regulated. Furthermore, the irradiance situations are applied differently throughout the internal PV string as opposed to the external PV, which uses the average change in the irradiances. Moving the PV panels into the MMC provides more advantages, taking into account the fact that different irradiance situations could be applied over the external PV panels instead of the average situation change, which reduces the computation accuracy of the MPPT in different situations and effectively reduces their performance and accuracy.

As a result, the variations in accuracy and performance between the external and internal PV panel connections, as illustrated in Figure 6.20(a) and (c), are very small. However, the proposed LC-PWM provides a very consistent behavior in different situations.

On the other hand, the internal PV connection improves the converter efficiency somewhat more than the external PV connection, as shown in Figure 6.20(b). This is because the PV panel string is connected directly to the MMC SMs, which brings the energy sources within the converter and removes the effect of the circulating current DC component losses.

Table 6.11. Converter input power accuracy, converter efficiency, application performance, and the percentage of the uncalculated error measurements using LC-PWM.

PV panels connection	Situation	Accuracy [%]	Efficiency [%]	Performance [%]	Measure Errors [%]
External PV	1	99.99	98.76	98.72	0.0225
	2	99.99	98.87	98.85	0.0230
	3	99.98	99.00	98.98	0.0346
	4	99.98	99.10	99.10	0.0323
	5	99.97	99.20	99.16	0.0493
	6	99.96	99.20	99.10	0.0814
	7	99.81	98.70	98.40	0.1748
Internal PV	1	99.94	98.90	98.78	0.0180
	2	99.94	99.10	98.90	0.0250
	3	99.94	99.20	99.00	0.0301
	4	99.93	99.40	99.10	0.0430
	5	99.94	99.50	99.20	0.0560
	6	99.95	99.60	99.20	0.0640
	7	99.92	99.30	98.70	0.1330

Table 6.11 also indicates the percentage of the uncalculated power loss measurement as a measurement error, which is consistently very low in all situations and even lower in the internal PV connection compared to the external PV connection due to the higher efficiency. In fact, as unexplained or uncalculated power losses, there were roughly 36 W in the external PV panel connection and about 30 W in the internal PV panel connection at 100 percent irradiance. In both circumstances, when the total power delivered by the PV panels declined with decreasing irradiation, those numbers decreased.

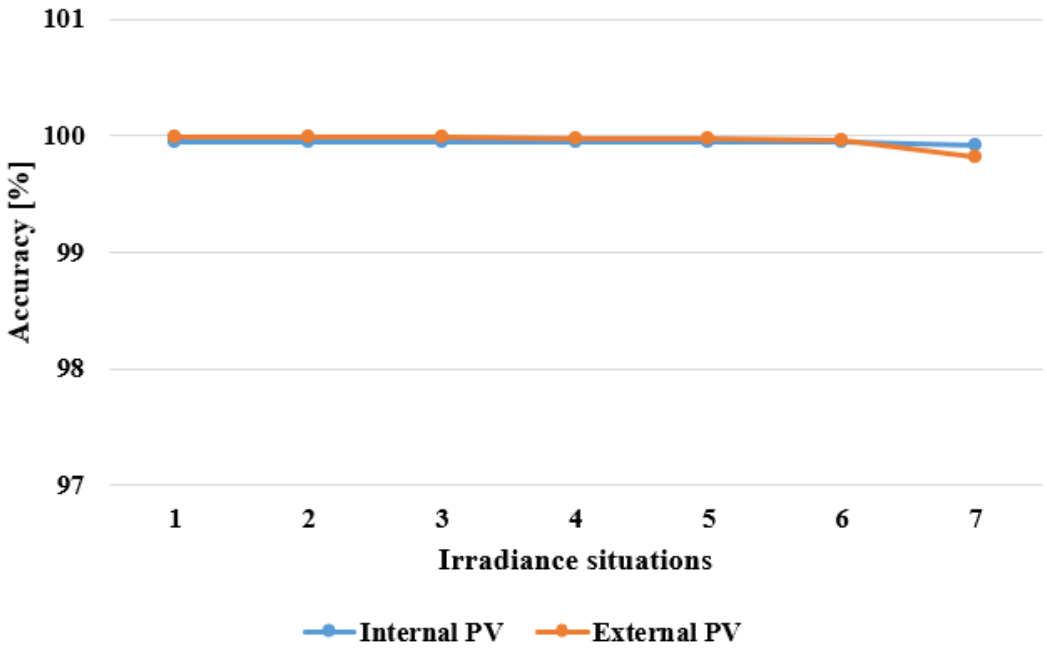
101
100
99
98
97
Accuracy [%]
1
2
3
4
5
6
7
Irradiance situations
Internal PV
External PV

(a)

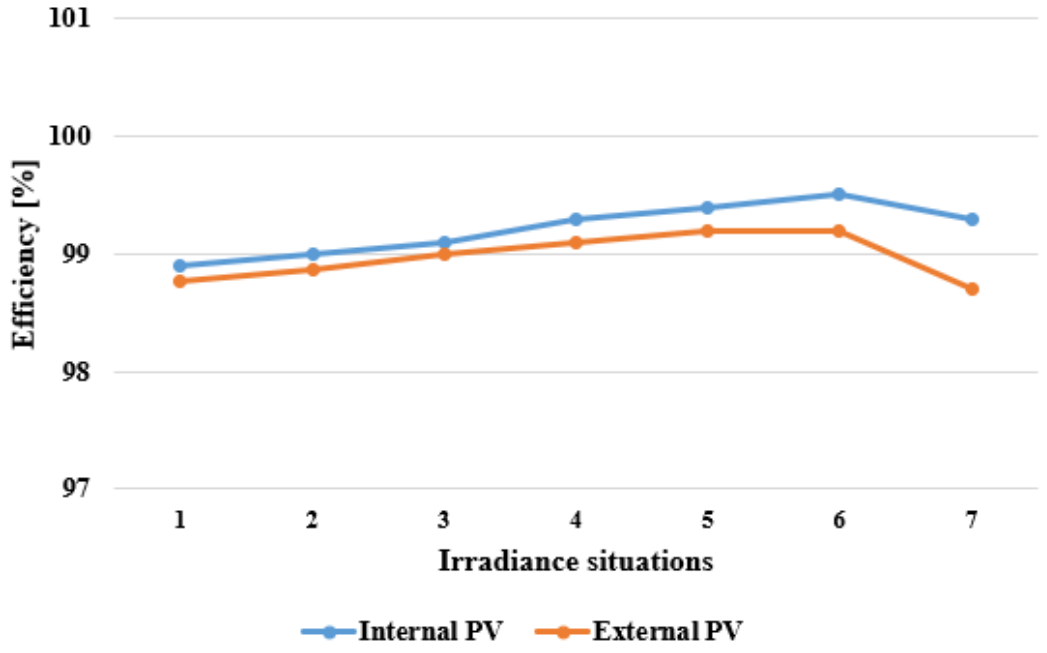
101
100
99
98
97
Efficiency [%]
1
2
3
4
5
6
7
Irradiance situations
Internal PV
External PV

(b)

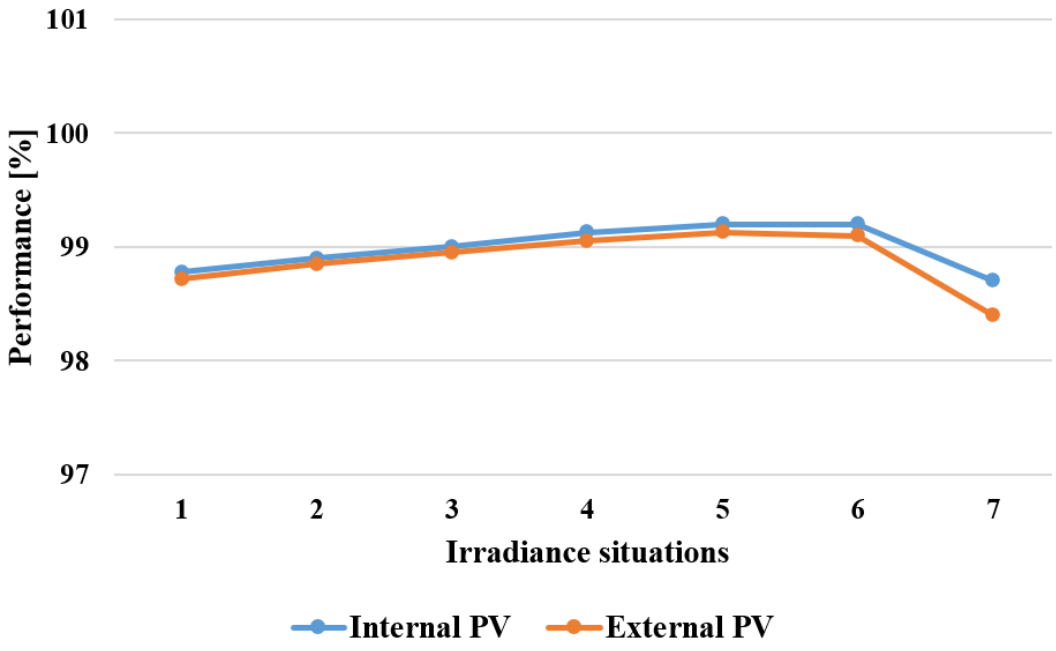

(c)

Figure 6.20: MMC comparison using LC-PWM for internal and external PV panel connections (a) Converter input power accuracy (b) Converter efficiency (c) Application performance.

6.4.5.3 The Effects of Different Capacitor Cell Sizes on the Performance of PV Applications in MMC

The impact of the capacitor cell size on the performance of the PV application has been considered, particularly because connecting the PV string directly to the MMC SMs would make it very sensitive to the capacitor voltage ripple while computing the MPPT. The external PV panel connection, on the other hand, is not directly connected to the SM capacitor and is more dependent on the ripple of the DC-link capacitor. Figure 6.21 shows how changing the SM capacitor size between 3, 6, and 9 mF affects the accuracy of the input power, the efficiency of the MMC converter, and the application's performance for both internal and external PV panels. Thus, a C_{SM} with size 3 mF introduces roughly ±3.9% voltage ripple from the V_{SM}, while the 6 mF and 9 mF introduce a voltage ripple of less than ±1.8% and ±1.3%, respectively.

In fact, as the voltage ripple decreases by more than 50% in the 6 mF and even more with 9 mF, this boosts the performance of the application in the event of internal PV connections and increases the accuracy of the input power. Reduced voltage ripple at the SM, on the other hand, lowers the circulating current and the power losses, but at the cost of increasing the capacitor size.

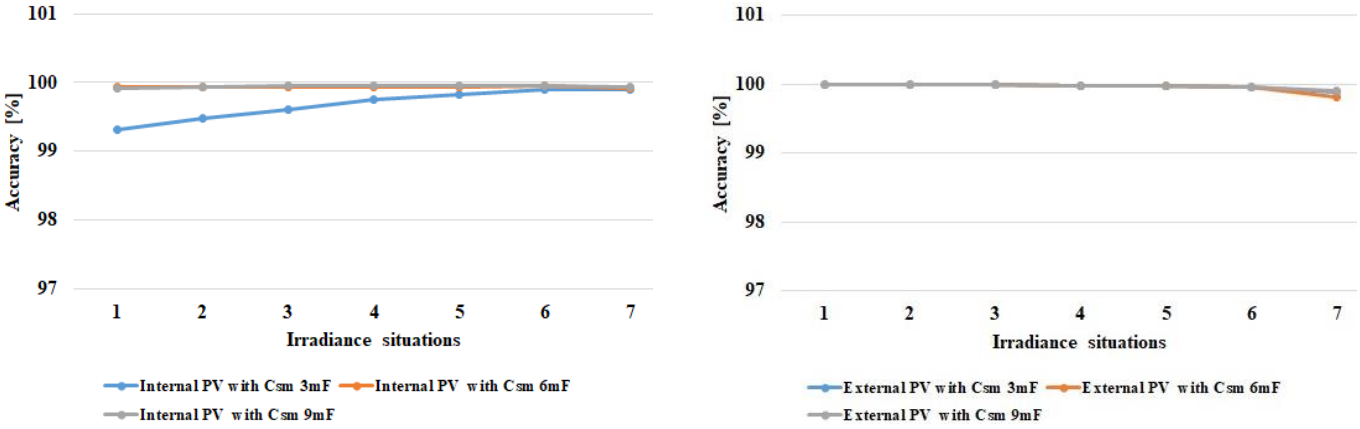

(a)

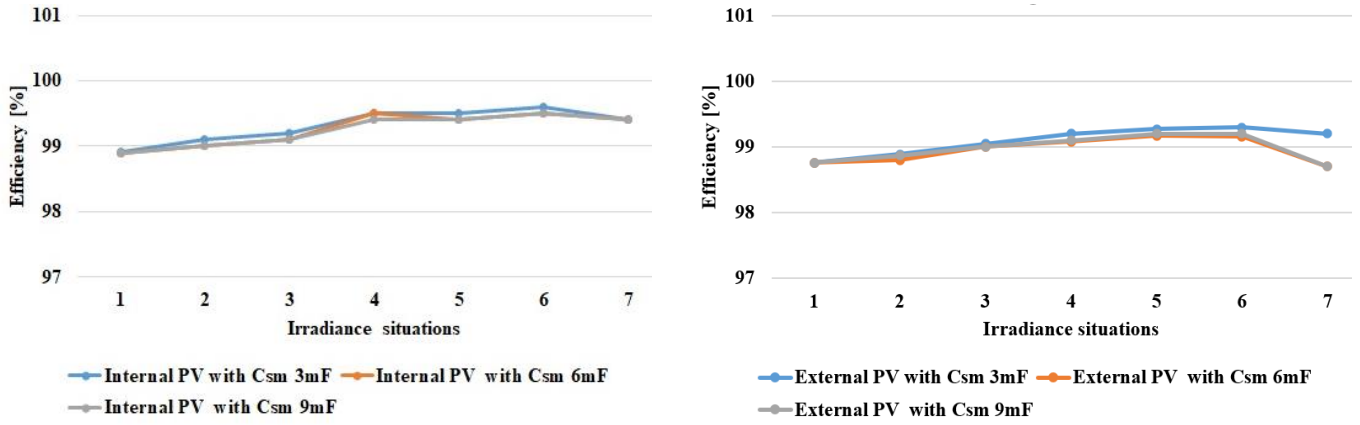

(b)

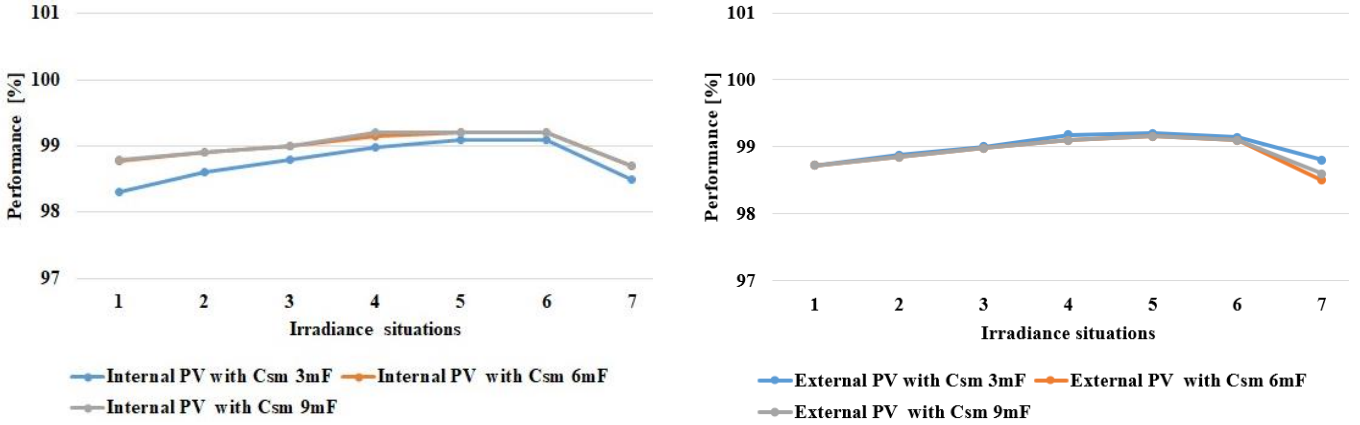

(c)

Figure 6.21: MMC comparison using the LC-PWM for internal and external PV connections for an SM capacitor size of 3, 6, and 9 mF (a) Converter input power accuracy (b) Converter efficiency (c) Application performance.

6.4.6 Scenario 2: PS-PWM Controlled MMC Connected to an Isolated Load

PS-PWM modulation controlling the MMC has been simulated in this scenario, where an MMC with four SMs per arm is used to analyze the converter behavior in two cases: first, by connecting the PV panels externally to the MMC; while, in the second case, the PV panels are integrated directly with the MMC cell. Then, the converter is connected to a three-phase resistive load, with 13 Ω per phase when the irradiance is 100%, but 130 Ω when the irradiance decreases to 10%. The target phase voltage on the outputs is required to achieve steady conditions, and it is almost constant in all irradiance situations in order to replicate the behavior of a grid connection.

Table 6.12 displays the parameters of a three-phase MMC connected to an isolated load, and they are virtually identical to those used to connect the MMC to the grid, as shown previously in Table 6.3.

Table 6.12. Parameters of the three-phase MMC connected to the isolated load.

Parameters	Value
Active power (P)	169 kW
DC link voltage (V_{dc})	3200 V
DC link Capacitor (C_{dc})	9000 µF
Switching frequency (F_s)	2000 Hz
SM capacitance (C_{SM})	6000 µF
SM capacitor voltage (V_{SM})	807.4 V
Number of SM in each arm (N_{sm})	4
Arm inductor (L_{arm})	340 µH
Output inductor (L_o)	680 µH
Output capacitor (C_o)	187 µF
Nominal load resistor (R)	13 Ω

Meanwhile, the arm inductors, output inductors, and output capacitors have all been decreased in size to clearly demonstrate the impact of the circulating current by clearly displaying the circulating current ripples and components on the one hand, while the output filter has been lowered in order to clearly view the output voltage distortion on the other hand. Thus, in scenarios two and three, the contrast between the behavior of the PS-PWM and that of the proposed LC-PWM would be clearly displayed.

6.4.6.1 Case 1: PV Panels Located Externally to the MMC

In this case, the PV panels are connected as a central converter using an array of 88 panels in series and six strings in parallel; all receiving the same irradiance. The performance of the MMC converter has been measured under different irradiance levels, evolving from 100% (situation 1) to 10% (situation 7), increasing the load resistors accordingly in order to keep the output voltage constant.

Table 6.13 illustrates the results of these simulations, including a measure of the low harmonic distortion (LHD) from the 2nd to the 19th harmonic, the total harmonic distortion at the converter output voltage (THD_C), the total harmonic distortion at the load voltage (THD_O), the DC and RMS components of the circulating current, and the RMS value of the circulating current when its DC component is removed.

Table 6.13. Simulation results of the MMC modulated using PS-PWM with external PV panels.

Situation	Irradiance [W/m^2]	LHD [%]	THD_C [%]	THD_O [%]	DC (i_z) [A]	RMS (i_z) [A]	RMS [i_z – DC (i_z)] [A]
1	1000	0.22	23.7	0.98	17.4	58.5	55.8
2	850	0.20	23.8	0.97	14.8	53.6	51.5
3	700	0.24	23.8	1.10	12.3	49.1	47.5
4	550	0.24	23.8	1.06	9.7	45.3	44.2
5	400	0.21	23.7	0.98	7.1	42.1	41.5
6	250	0.20	24.7	1.20	4.5	39.5	39.2
7	100	0.23	24.6	1.10	1.8	37.3	37.2

6.4.6.2 Case 2: PV Panels Distributed Throughout the MMC

In this case, strings with 22 PV panels in series were integrated directly into each SM of the MMC, as shown in Figure 6.1. Identical solar panels are used in all the SM, but the irradiance changes at different SMs, as with the irradiance situations described in Table 6.7. However, all six arms of the MMC converter receive the same average irradiance; so there will be very little energy transferred from phase to phase or from arm to arm to keep them in a balanced situation. Therefore, situations 1 to 7 of this case are mostly equivalent to those situations described in the previous case.

The PV panels can be placed in clusters, as previously indicated in section 6.4.5, to keep the energy balanced across phases on the one hand, and between the upper and lower arms on the other.

Table 6.14 displays the simulation results obtained by using the various irradiance circumstances listed in Table 6.7, where the simulation is performed repeatedly in each situation to illustrate the influence of the changes in irradiance in terms of shadow or clouds.

Table 6.14. Simulation results of the MMC modulated using PS-PWM with distributed PV panels.

Situation	LHD [%]	THD_C [%]	THD_O [%]	DC (i_z) [A]	RMS (i_z) [A]	RMS [i_z – DC (i_z)] [A]
1	0.23	23.8	1.2	0	63.1	63.1
2	0.26	23.7	1.3	0	57.3	57.3
3	0.28	23.6	1.2	-0.01	52.5	52.5
4	0.88	23.4	2.7	-0.07	53.1	53.1
5	0.82	23.5	3.7	-0.03	48.9	48.9
6	0.84	23.6	4.3	0.04	43.7	43.7
7	0.26	23.6	1.4	0	63.1	63.1

These results, also included in Figure 6.22, clearly show the ability of PS-PWM to manage an external array of PV panels even with different irradiances, as they clearly show a steady distortion while the irradiances change, but they also demonstrate the problems that arise when trying to deal with different irradiance levels for different PV cells when they are distributed throughout the MMC cells. In such a case, the target voltages are different due to the MPPT, while

fixed PWM carriers do not adapt to the said changes. Thus, the LHD and THD_O of the voltage distortion increase beyond tolerable levels. This issue is more evident in situations 4 to 6 due to the irradiance differences in those situation ranges being much higher than in other situations.

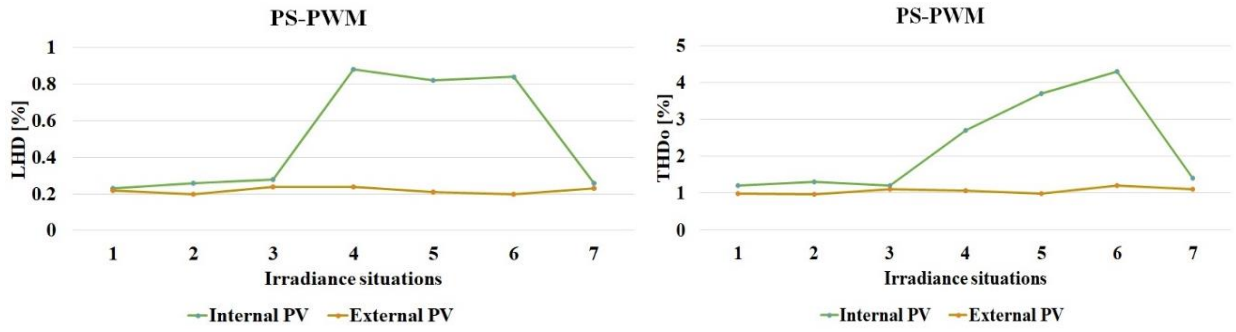

(a) (b)

Figure 6.22: Comparison of the voltage harmonic distortion in external and internal PV panel connections using PS-PWM. (a) Reflect LHD (b) Reflect harmonic distortion in terms of THD_O.

External PV panels are a better option when using PS-PWM, not only because of a wider operation range, as demonstrated above, but also because the achieved performance is greater. Table 6.13 clearly shows that the DC component of the circulating current is proportional to the power supplied by the external PV panels, and Table 6.14 registers that this DC component is completely removed when moving PV panels into the MMC converter. However, the RMS value of the circulating current remains mostly constant when moving the PV panels into the MMC converter, and an increase of about 10% is observed when removing the DC component from the circulating current.

This issue reflects the lack of control on circulating currents when using PS-PWM, and it must influence the conduction power losses of the MMC converter. Table 6.15 shows the results of these simulations where the conduction power losses, the power losses when each semiconductor is *ON* (P_{losses_on}), have been estimated using Equation (6.43). Then, the efficiency of the MMC converter and the performance of the application can be computed to describe the behavior of the MMC under the PS-PWM controller.

As can be seen in Table 6.15, the power losses and converter efficiency are mostly equal when using internal or external PV panels, because the RMS value of the uncontrolled circulating currents remains constant. Moreover, the application performance when using internal PV panels is even smaller than the corresponding value seen with external panels. This is because the MPPT controllers are less accurate: when using internal panels, each SM has its own MPPT, but only the sum of all the MMC voltage cells can be regulated by the active power controller; while the whole PV array voltage, the DC-link voltage, is directly measured and regulated when using external PV panels. In this case, moving PV panels into the MMC converters gives no advantage.

Table 6.15. Converter power losses, converter efficiency, and application performance using PS-PWM.

PV panels connection	Situation	Power losses [W]	Efficiency [%]	Performance [%]
External PV	1	3712	97.7	97.5
	2	3117	97.7	97.5
	3	2615	97.6	97.4
	4	2212	97.4	97.2
	5	1905	96.9	96.7
	6	1671	95.7	95.5
	7	1480	90.3	90.2
Internal PV	1	4110	97.4	97.1
	2	3405	97.4	97.1
	3	3056	97.4	97.1
	4	2668	96.8	96.6
	5	2310	96.1	96.0
	6	1968	94.9	94.7
	7	1486	90.0	90.1

However, from another perspective, the external PV panels connection is actually a central connection, as this type of connection normally requires an intermediated booster converter to regulate the voltage of the PV panels, which adds extra cost and installation work. Furthermore, the performance defect of the booster converter will add to this situation, giving the internal PV connection an advantage.

6.4.7 Scenario 3: LC-PWM Controlled MMC Connected to an Isolated Load

The proposed LC-PWM modulation has been simulated in this scenario in the same situations as the second scenario for PS-PWM, using the same parameters of the PV panels as described in Table 6.2, as well as the same parameters of the MMC as described in Table 6.12. In case 1 of this scenario, a uniform averaged irradiance is once more used on the external PV array; while different irradiances are used at different MMC cells when using internal PV panels in case 2, following the same situations as those described previously in Table 6.7.

6.4.7.1 Case 1: PV Panels Located Externally to the MMC

Again, a 6x88 PV array is connected at the DC side of a five level MMC converter that feeds a resistive load, but in this case, the newly proposed LC-PWM modulation is applied. The distortion results shown in Table 6.16 are consistent in a wide operation range (irradiance from 100% to 10%) and moderate when compared to those results registered for the PS-PWM in Table 6.13.

Table 6.16. Simulation results of the MMC modulated using LC-PWM with external PV panels

Situation	Irradiance [W/m^2]	LHD [%]	THD_C [%]	THD_O [%]	DC (i_z) [A]	RMS (i_z) [A]	RMS [i_z – DC (i_z)] [A]
1	1000	0.43	26.7	1.37	17.3	18.4	6.2
2	850	0.45	26.8	1.35	14.8	15.7	5.2
3	700	0.45	26.9	1.37	12.2	12.9	4.2
4	550	0.47	27.1	1.38	9.6	10.3	3.7
5	400	0.46	27.3	1.37	7.1	7.5	2.4
6	250	0.45	27.4	1.39	4.4	4.8	1.9
7	100	0.47	26.4	1.39	1.9	2.6	1.7

The main difference is that circulating current is mostly limited to the function of moving energy from the external PV panels to the internal capacitors. In comparison to the PS-PWM, the proposed modulation LC-PWM keeps the arms of the converter balanced and suppresses the 50 Hz component of the circulating current to the minimum under the same circumstances. This is due to the method based on measuring the instantaneous voltages of the MMC SMs, which precisely synchronizes the transition from one level to another, and this effectively removes all the unwanted glitches from the circulating currents.

6.4.7.2 Case 2: PV Panels Distributed Throughout the MMC

In this case, PV panels are once more distributed throughout the MMC cells, placing a string of 22 serially connected PV panels at each SM. As above, all the panels at each SM receive the same irradiance, but different cells receive different irradiances, as described in Table 6.7.

Table 6.17 shows the results generated in these simulations. Now, the voltage differences between different cells are compensated by the LC-PWM and as a result, the output distortion is under control in the whole operation range for this application, from 100% irradiance to 10%, even with variable irradiance at different MMC cells.

Table 6.17. Simulation results of the MMC modulated using LC-PWM with distributed PV panels.

Situation	LHD [%]	THD_C [%]	THD_O [%]	DC (i_z) [A]	RMS (i_z) [A]	RMS [i_z – DC (i_z)] [A]
1	0.37	26.1	1.38	-0.02	3.35	3.35
2	0.39	26.2	1.38	-0.03	2.85	2.85
3	0.39	26.2	1.38	0	2.44	2.44
4	0.42	26.3	1.38	-0.01	3.68	3.68
5	0.41	26.1	1.40	0	3.48	3.48
6	0.38	26.2	1.42	-0.02	3.12	3.12
7	0.36	26.1	1.41	0	2.33	2.33

In addition, Figure 6.23 clearly shows that the LC-PWM can keep distortion within acceptable levels for any irradiance situation when using external and also internal PV panels in a consistent manner.

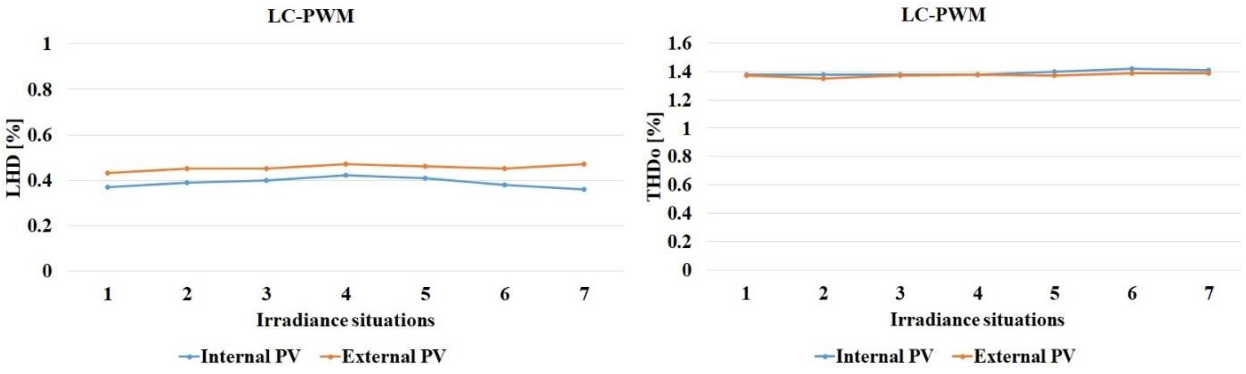

(a) (b)

Figure 6.23: Comparison of the voltage harmonic distortion in external and internal PV panel connections using LC-PWM. (a) Reflect LHD (b) Reflect absolute harmonic distortion in terms of THD_O.

Table 6.17 further illustrates that the DC component of the circulating current has been eliminated, since the PV panels supply energy directly to the MMC capacitors, and the RMS value of the circulating current represents just the 50 Hz component needed to maintain the arms balanced with undesired components due to switching. This is lower than in the previous case, indicating that the proposed modulation works more accurately with distributed PV panels than with external PV panels.

The power loss analysis, registered in Table 6.18, confirms the improvement achieved with the LC-PWM, an optimized modulation that takes into account the measured voltages of the MMC cells and synchronizes each level-to-level transition to remove all transients in the circulating current.

Table 6.18. Converter power losses, converter efficiency, and application performance using LC-PWM.

PV panels connection	Situation	Power losses [W]	Efficiency [%]	Performance [%]
External PV	1	1588	99.1	99.1
	2	1304	99.1	99.1
	3	1065	99.1	99.1
	4	872	99.1	99.1
	5	723	98.9	98.9
	6	621	98.6	98.5
	7	554	96.7	96.6
Internal PV	1	1329	99.2	99.1
	2	1116	99.2	99.1
	3	937	99.2	99.1
	4	794	99.2	99.1
	5	679	99.1	99.0
	6	610	98.7	98.6
	7	536	96.9	96.8

Figure 6.24 clearly shows that the proposed LC-PWM modulation may decrease the conduction losses of the MMC converter by more than 60% when comparing it to the traditional PS-PWM modulation, and this feature is immediately translated to the converter efficiency. Moreover, using the proposed modulation reduces power losses further, by up to 17%, when moving the PV panels into the MMC converter, as seen in Table 6.18.

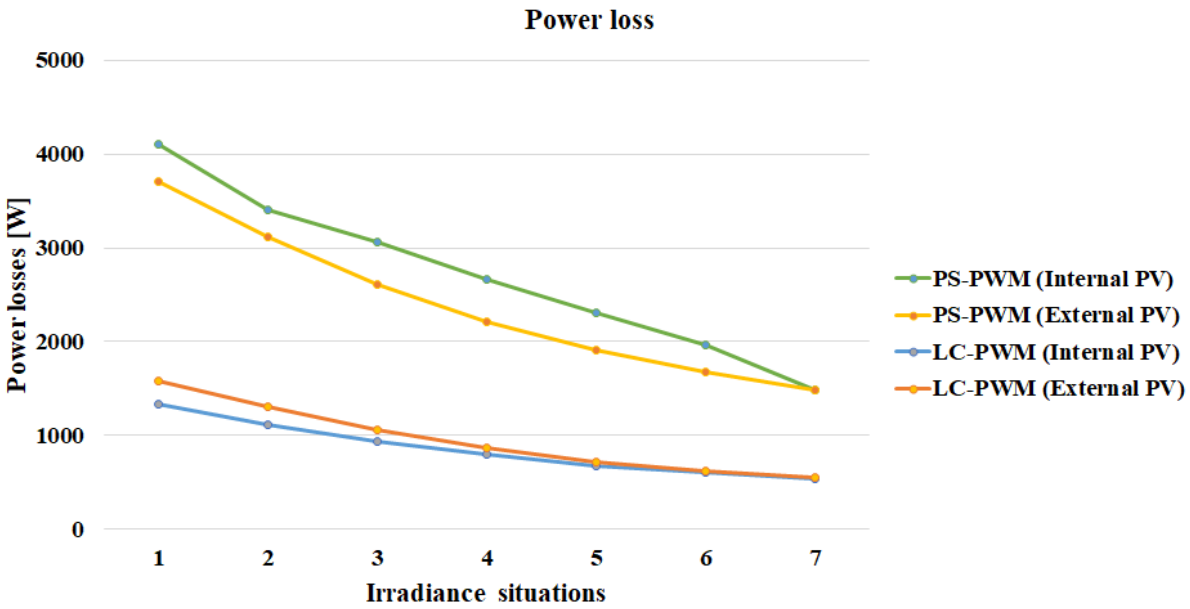

Figure 6.24: Comparison of MMC power losses using LC-PWM and PS-PWM.

The performance analysis for this application is shown in Figure 6.25. Both, the LC-PWM and PS-PWM modulations are applied first to a set up with external PV panels and uniform irradiance, and then to a second set up with internal PV panels and variable irradiance. A third setup, represented using dashed lines, shows the application performance when the PV panels are connected outside the MMC converters, and 99% efficient boosters are used on each PV string to deal with variable irradiances.

The best performance results were achieved when using the LC-PWM and internal panels, with no boosters, offer two reasons: first, integrating the PV panel string directly into the SM removes the DC component of the circulating current effect; second, the proposed modulation keeps the arms of the converter balanced and suppresses the 50 Hz component of the circulating current to the minimum under the same circumstances; this is due to the method being based on measuring the instantaneous voltages of the MMC SMs and precisely synchronizing the transition from one level to another, which effectively removes all unwanted glitches from the circulating currents. This also means the external PV connection has almost the same performance as the internal connection using the LC-PWM.

Furthermore, in this situation, the internal PV connection compared to the best situation that can be obtained for the external PV connection. This is due to the external PV panel having a global and direct MPPT, where the MPPT is applied over the entirety of the connected PV panels to get the V_{mpp}. However, this setup can only be used when uniform irradiance is expected in the application and a global MPPT can be applied. For applications where variable irradiance throughout the PV field is an important issue or frequent situations of partial shadowing are expected; then the best performance results were obtained using LC-PWM and PV panels spread

throughout the MMC converter, a topology that uses the switches of the MMC cells to apply an MPPT at each PV string.

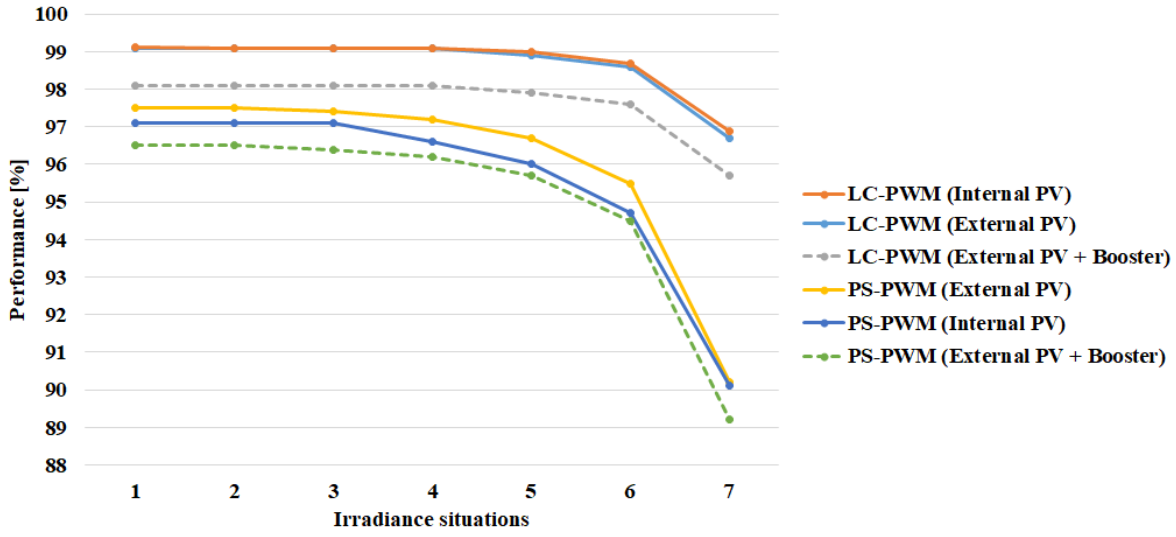

Figure 6.25: MMC performance comparison using LC-PWM and PS-PWM.

On the other hand, the PV application performance in the external and internal PV panel connections with the PS-PWM is worse than those with the proposed LC-PWM. This is because the PS-PWM is working with the fixed frame of voltage, which increases the RMS value of the uncontrolled circulating currents. Furthermore, when the internal PV panel is used, the performance is worse than the corresponding value seen with the external panel using the PS-PWM. This is because, as mentioned before, the MPPT controllers are less accurate when using internal panels, where each SM has its own MPPT. The sum of all the MMC voltage cells can only be regulated by using the active power controller; while the whole PV array voltage, the DC-link voltage, is directly measured and regulated when using the external PV panels.

In addition, Figure 6.26 shows the behavioral differences between LC-PWM and PS-PWM in distributed PV panels on irradiance simulations for situation 4, which is the most difficult situation since the irradiance variation among the MMC cells is around 30%. One of the MMC phase voltages, phase 'a', shown in the upper row, describes the smooth transition between each two-level, reflecting the low THD described in the above tables; the second row displays the voltages of the upper and lower capacitors, where it can be seen that the capacitor ripples, while using the proposed modulation, fluctuate less during the charge and discharge which eventually means a better performance; while the last row shows the circulating current in one phase, demonstrating a clean and controlled behavior when using LC-PWM.

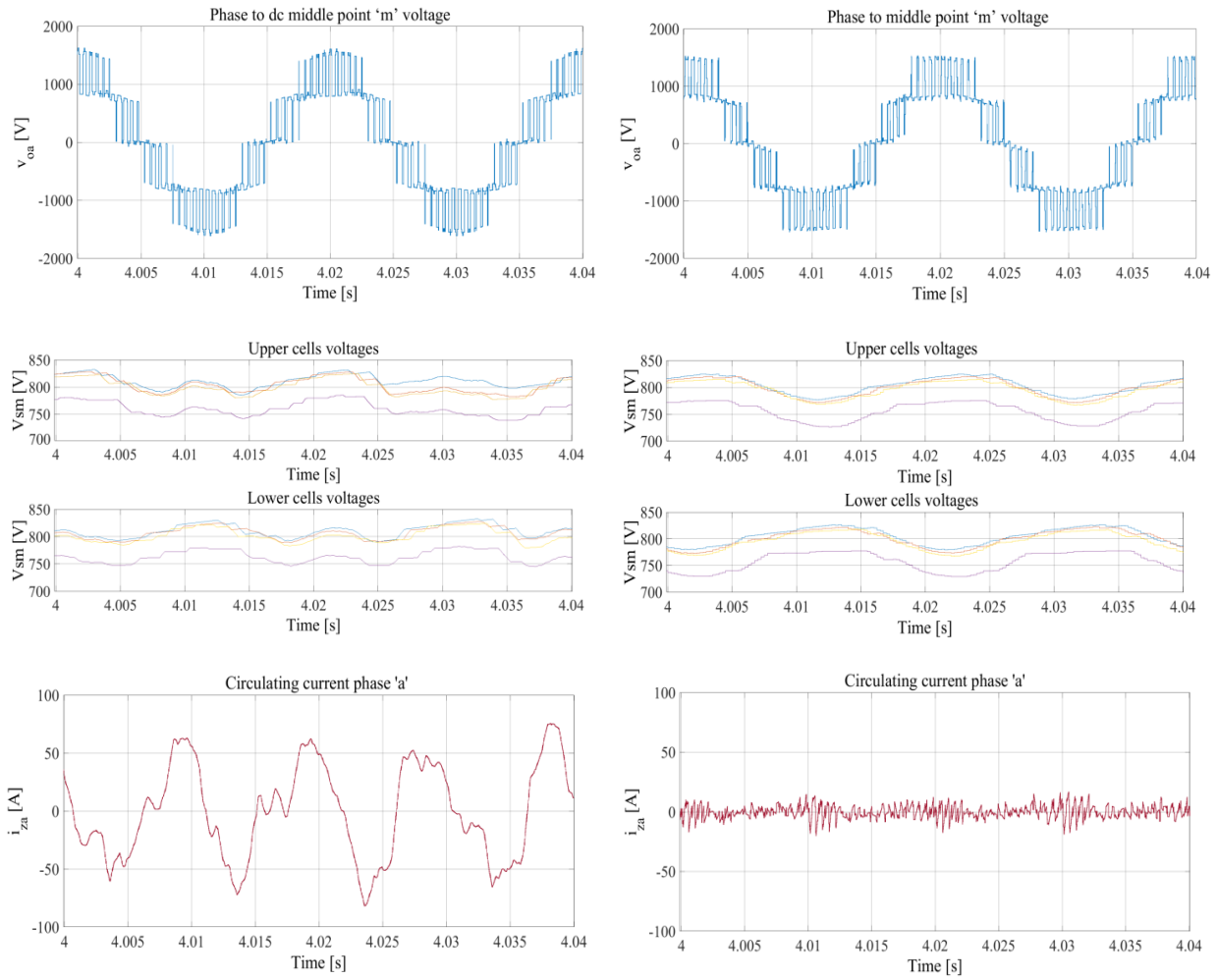

Figure 6.26: PS-PWM modulation (a) is compared to LC-PWM modulation (b) using distributed PV panels on simulations referred to the irradiance in situation 4. The first row displays a phase to DC midpoint voltage at the output of the MMC converter; the second row shows the capacitor voltages; and the third row registers the internal circulating current in one phase when using these two modulations.

Figure 6.26 clearly shows that the circulating current produced while using LC-PWM is very small and has no 100 Hz component, unlike the circulating current on the PS-PWM, where it can clearly be seen that the 100 Hz component appears and a regulator has to be applied to remove it on the one hand, and to suppress the other components on the other hand.

7

Conclusions and Future Work

Contents of This Chapter

- **Section 7.1** summarizes the most important findings of this research work.
- **Section 7.2** outlines the proposals for further research made in the individual chapters.

7.1 Conclusions

Grid-connected PV power systems have grown increasingly significant, popular, and widely used across the world, particularly as many countries seek to enhance their usage of clean and renewable energy sources. This popularity grew even further as the price of PV modules fell by an average of 10% per year over the previous three decades across the entire world. PV cells use the photovoltaic effect to convert solar energy into electric energy; therefore, their efficiency and dependability are critical for capturing as much solar energy as is feasible. The power converters that condition the power and provide it to the grid or load, on the other hand, are vital. As the power conversion system is so important and has very effective results over the power used by these applications, the design of the power conversion stage inside the PV inverter system is continuously evolving to increase the accuracy, efficiency, and longevity of the power converters. More recently, the dependability and safety of the complete PV system in operation has received more attention.

This research project, which was conducted from March 2018 to December 2021 at the Department of Electronic Technology at the University of Valladolid in Spain, identified a new modulation method named “local carrier PWM” (LC-PWM) as a result of the study and evaluation of electronic power converters distributed in photovoltaic generation applications. This new proposed modulation has been found to control MMCs with PV panel strings distributed throughout their cells. In this application, each SM is connected to a PV string, and it applies an MPPT that targets a voltage not related to other cells. These variable voltages at MMC cells generate an unacceptable distortion at the output voltage when using traditional modulations, as seen in a few simulations; they also increase the internal circulating currents with an undesirable effect on the semiconductor ratings and converter power losses.

The proposed LC-PWM uses the available cell voltage information to generate more accurate voltages at the MMC arms, which reduce the internal circulating currents to a great extent and maintain the output distortion in moderate values for a wide operating range. Furthermore, the modulator sampling period is slightly lengthened or shortened to reach each level-to-level transition with the correct number of inserted cells, removing undesired fast transients from the circulating currents.

A few simulations of different irradiance situations were used to validate this development. They demonstrate the behavior and consistency of the proposed LC-PWM that greatly reduces the circulating currents; they also demonstrate that the power losses of PV applications can be reduced by 16% when using MMCs with distributed PV panels rather than external PV panel connections on applications connected to the AC grid, while a 17% reduction has also been measured when connecting to an AC load. Furthermore, the proposed LC-PWM modulation decreases conduction power losses of the MMC converter by more than 60% when compared to the traditional PS-PWM modulation, and this feature is immediately translated to the converter efficiency.

In addition, the circulating current produced when controlling the MMC using the proposed LC-PWM is not only small, but the results show no 100 Hz component; this is due to the method being based on measuring the instantaneous voltages of the MMC SMs that result in lower losses. Furthermore, the proposed modulation method includes a precisely synchronized transition from one level to another, which further reduces losses by effectively removing any undesirable glitches from the circulating currents.

Finally, since traditional PWM methods contribute to balancing the energy stored at the MMC arms in the situation of small imbalances while LC-PWM does not, a separate PI controller to control the AC and DC components has been implemented to react to any unbalanced energy, taking into account the phase to phase and arm to arm power imbalances.

Besides that, it has also been proposed that PV panels should be arranged in clusters of six, one for each MMC arm, so that the power generation of all the arms is mostly the same for any situation of irradiance and temperature, and thus circulating currents and losses will be minimized.

7.2 Future Development

The modular characterization of the MMC, represented by modularity, scalability, and high conversion efficiency, can be used as a perfect converter candidate to work with the PV application systems by efficiently extracting and converting energy from PV panels. Storage energy can thus be increased, allowing the PV system to supply more power to consumers at night. This flexible capability is also beneficial for battery energy system grid integration.

Over the last few years, there has been a broad range of research developments in the MMC in terms of analyzing and improving different topologies, output current control methods, circulating current control techniques, modulation techniques, and applications. Still, there are a few research thoughts that need to be addressed in order to broaden the compatibility of converter applications. This research project has uncovered important areas of further research which could not be addressed during its limited timeframe:

- The PV panels distributed throughout the MMC topology must be further analyzed and modified due to the need to gain more power and minimize losses further in order to compete with typical high voltage converters. Basically, research and analyses of various power semiconductors are required to construct the MMC SM, and the studies must also contain topologies and connection improvements. It is also necessary to analyze the connections between the MMCs elements.

- One of the disadvantages of the MMC is that it needs the use of expensive and bigger floating capacitors in converter cells to avoid voltage ripple during low-frequency operation, thereby reducing converter imbalances. To address this problem, a high-

performance control strategy must be developed and implemented. The MMC application range might be extended by overcoming this issue, and application voltages could be increased to medium/high levels.

- The design and implementation of capacitor voltage control systems, which reduce system imbalances and losses by employing various capacitor types and sizes. Two further, very interesting research subjects for consideration are the cost of the converter and its stability.

- Another important consideration when employing the MMC in high-voltage systems is its DC-side fault-blocking capabilities. The majority of high-voltage application-based MMCs employ HBSM, which is unable to stop DC fault current. As a result, DC fault concerns can be solved with FBSM and/or clamp-double SM; although these SMs are rarely employed in commercial devices due to the increases in converter cost and complexity. It is also possible that the converter efficiency may decline as the semiconductors increases. This issue has given rise to the possibility of new ideas and studies centered on the use of circuit breakers to regulate the DC fault current.

- Finally, the development of a fully functional MMC-based distributed PV application appropriate for the experimental verification and validation of all the principles covered in this thesis is required. It would also be required if the existing control techniques were to be extended to include MMC behavior under an imbalanced grid connection.

Bibliography

[1] Y. Yang, K. A. Kim, F. Blaabjerg, and A. Sangwongwanich. *Advances in grid-connected photovoltaic power conversion systems.* Woodhead Publishing Series in Energy, 2018.

[2] IRENA (2017), Renewable Energy Statistics 2017, The International Renewable Energy Agency, Abu Dhabi.

[3] S. Philipps, and W. Warmuth, "Fraunhofer ISE: photovoltaics report updated: 23 june," 2021. [Online]. Available: https://www.ise.fraunhofer.de/content/dam/ise/de/documents/publications/studies/Photovoltaics-Report.pdf. (accessed Nov. 11, 2021).

[4] J. D. Farmer and F. Lafond, "How predictable is technological progress?," *Res. Policy*, vol. 45, no. 3, pp. 647–665, 2016, doi: 10.1016/j.respol.2015.11.001.

[5] L. Yuanyuan, "China's solar PV module exports reached 37.9 GW in 2017, renewable energy world," 2019. [Online]. Available: https://www.renewableenergyworld.com/solar/china-s-pv-module-exports-reached-37-9-gw-in-2017/. (accessed Dec. 10, 2021).

[6] IHS Markit, "New global solar PV installations to increase 27% to record 181 GW this year," *Reuters*. https://www.reuters.com/business/energy/new-global-solar-pv-installations-increase-27-record-181-gw-this-year-ihs-markit-2021-03-29/. (accessed Dec. 03, 2021).

[7] REN21, "Renewables 2017 global status report," 2017. [Online]. Available: https://www.ren21.net/wp-content/uploads/2019/05/GSR2017_Full-Report_English.pdf. (accessed Nov. 22, 2021).

[8] Y. Yang and F. Blaabjerg, "Overview of single-phase grid-connected photovoltaic systems," *Electr. Power Components Syst.*, vol. 43, no. 12, pp. 1352–1363, 2015, doi: 10.1080/ 15325008.2015.1031296.

[9] L. Hassaine, E. Olias, J. Quintero, and V. Salas, "Overview of power inverter topologies and control structures for grid connected photovoltaic systems," *Renew. Sustain. Energy Rev.*, vol. 30, pp. 796–807, 2014, doi: 10.1016/j.rser.2013.11.005.

[10] E. Romero-Cadaval, G. Spagnuolo, and L. G. Franquelo, "Grid-connected photovoltaic generation plants: components and operation," *IEEE Ind. Electron. Mag.*, vol. 7, no. 3, pp. 6–20, 2013, doi: 10.1109/MIE.2013.2264540.

[11] S. B. Kjaer, J. K. Pedersen, and F. Blaabjerg, “A review of single-phase grid-connected inverters for photovoltaic modules,” *IEEE Trans. Ind. Appl.*, vol. 41, no. 5, pp. 1292–1306, 2005, doi: 10.1109/TIA.2005.853371.

[12] F. Rong, X. Gong, and S. Huang, “A novel grid-connected PV system based on MMC to get the maximum power under partial shading conditions,” *IEEE Trans. Power Electron.*, vol. 32, no. 6, pp. 4320–4333, 2017, doi: 10.1109/TPEL.2016.2594078.

[13] S. Barcellona, M. Barresi, and L. Piegari, “MMC-based PV single-phase system with distributed MPPT,” *Energies*, vol. 13, no. 15, pp. 125–134, 2020, doi: 10.3390/en13153964.

[14] A. Lesnicar and R. Marquardt, “An innovative modular multilevel converter topology suitable for a wide power range,” *2003 IEEE Bol. PowerTech - Conf. Proc.*, vol. 3, pp. 272–277, 2003, doi: 10.1109/PTC.2003.1304403.

[15] S. Debnath and M. Saeedifard, “Optimal control of modular multilevel converters for low-speed operation of motor drives,” *Conf. Proc. - IEEE Appl. Power Electron. Conf. Expo. - APEC*, pp. 247–254, 2014, doi: 10.1109/APEC.2014.6803317.

[16] R. Marquardt, “Modular multilevel converter: an universal concept for HVDC-networks and extended DC-bus-applications,” *2010 Int. Power Electron. Conf. - ECCE Asia -*, pp. 502–507, 2010, doi: 10.1109/IPEC.2010.5544594.

[17] R. Marquardt, “Modular multilevel converter topologies with DC-Short circuit current limitation,” *8th Int. Conf. Power Electron. - ECCE Asia*, pp. 1425–1431, 2011, doi: 10.1109/ICPE.2011.5944451.

[18] J. Mei, B. Xiao, K. Shen, L. M. Tolbert, and J. Y. Zheng, “Modular multilevel inverter with new modulation method and its application to photovoltaic grid-connected generator,” *IEEE Trans. Power Electron.*, vol. 28, no. 11, pp. 5063–5073, 2013, doi: 10.1109/TPEL.2013. 2243758.

[19] S. P. Swetha and B. V. Sumangala, “Solar photovoltaic power conversion using modular multilevel inverter,” *2015 Int. Conf. Emerg. Res. Electron. Comput. Sci. Technol. (ICERECT)*, pp. 387–391, 2016, doi: 10.1109/ERECT.2015.7499046.

[20] A. B. Acharya, M. Ricco, D. Sera, R. Teodorescu, and L. E. Norum, “Arm power control of the modular multilevel converter in photovoltaic applications,” *Energies*, vol. 12, no. 9, pp. 1–23, 2019, doi: 10.3390/en12091620.

[21] D. Tiku, “Modular multilevel MMI (HB) topology for single-stage grid connected PV plant,” *11th IET Int. Conf. AC and DC Power Transm.*, pp.1-8, 2015, doi: 10.1049/cp.2015. 0086.

[22] M. Saeedifard and R. Iravani, “Dynamic performance of a modular multilevel back-to-back HVDC system,” *IEEE Trans. Power Deliv.*, vol. 25, no. 4, pp. 2903–2912, 2010, doi: 10. 1109/TPWRD.2010.2050787.

[23] H. Kim, S. Kim, Y. H. Chung, D. W. Yoo, C. K. Kim, and K. Hur, “Operating region of modular multilevel converter for HVDC with controlled second-order harmonic circulating current: elaborating P-Q capability,” *IEEE Trans. Power Deliv.*, vol. 31, no. 2, pp. 493–502, 2016, doi: 10.1109/TPWRD.2015.2458038.

[24] S. Norrga, L. Ängquist, and K. Ilves, "Operating region extension for multilevel converters in HVDC applications by optimisation methods," *10th IET International Conference on AC and DC Power Transmission (ACDC 2012)*, 2012, pp. 1-6, doi: 10.1049/cp.2012.1987.

[25] R. Picas, J. Pou, S. Ceballos, J. Zaragoza, G. Konstantinou, and V. G. Agelidis, "Optimal injection of harmonics in circulating currents of modular multilevel converters for capacitor voltage ripple minimization," *2013 IEEE ECCE Asia Downunder*, pp. 318–324, 2013, doi: 10.1109/ECCE-Asia.2013.6579115.

[26] Q. Tu, Z. Xu, Y. Chang, and L. Guan, "Suppressing DC voltage ripples of MMC-HVDC under unbalanced grid conditions," *IEEE Trans. Power Deliv.*, vol. 27, no. 3, pp. 1332–1338, 2012, doi: 10.1109/TPWRD.2012.2196804.

[27] J. Li, G. Konstantinou, H. R. Wickramasinghe, J. Pou, X. Wu, and X. Jin, "Investigation of MMC-HVDC operating region by circulating current control under grid imbalances," *Electr. Power Syst. Res.*, vol. 152, pp. 211–222, 2017, doi: 10.1016/j.epsr.2017.07.003.

[28] I. A. López. *Design and simulation of a grid-connected PV system for self-consumption.* Master's Thesis, Universitat Politècnica de Catalunya, 2020.

[29] D. Sica, O. Malandrino, S. Supino, M. Testa, and M. Claudia, "Management of end-of-life photovoltaic panels as a step towards a circular economy," *Renew. Sustain. Energy Rev.*, vol. 82, no. 3, pp. 2934–2945, 2018, doi: 10.1016/j.rser.2017.10.039.

[30] G. M. Wilson *et al.*, "The 2020 photovoltaic technologies roadmap," *J. Phys. D. Appl. Phys.*, vol. 53, no. 49, pp. 1–47, 2020, doi: 10.1088/1361-6463/ab9c6a.

[31] A. Jäger-Waldau, "PV Status Report 2019," *EUR 29938 EN, Publ. Off. Eur. Union, Luxemb.*, p. 85, 2019, doi: 10.2760/326629.

[32] Danish Government, "The danish climate policy plan," 2013. [Online]. Available: https://ens.dk/sites/ens.dk/files/Analyser/danishclimatepolicyplan_uk.pdf. (accessed Jul. 20, 2020).

[33] N. Jantharamin and L. Zhang, "Model-based maximum power point tracking," *The 2010 ECTI International Confernce on Electrical Engineering/Electronics, Computer, Telecommunications and Information Technology*, 2010, pp. 83-87.

[34] R. K. Akikur, R. Saidur, H. W. Ping, and K. R. Ullah, "Comparative study of stand-alone and hybrid solar energy systems suitable for off-grid rural electrification: a review," *Renew. Sustain. Energy Rev.*, vol. 27, pp. 738–752, 2013, doi: 10.1016/j.rser.2013.06.043.

[35] X. Sun, "Solar technology got cheaper and better in the 2010s. Now what?," *Wood Mackenzie*, 2019. https://www.woodmac.com/news/opinion/solar-technology-got-cheaper-and-better-in-the-2010s.-now-what/. (accessed Nov. 07, 2021).

[36] M. G. Villalva, J. R. Gazoli, and E. R. Filho, "Comprehensive approach to modeling and simulation of photovoltaic arrays," *IEEE Trans. Power Electron.*, vol. 24, no. 5, pp. 1198–1208, 2009, doi: 10.1109/TPEL.2009.2013862.

[37] S. Vijayalekshmy, S. RamaIyer, and B. Beevi, “Evaluation of power losses in a short string of series-connected and parallel-connected photovoltaic modules for low power application,” *2013 Int. Conf. Control Commun. Comput.*, pp. 125–130, 2013, doi: 10.1109/ICCC.2013.6731636.

[38] A. Maki and S. Valkealahti, “Power losses in long string and parallel-connected short strings of series-connected silicon-based photovoltaic modules due to partial shading conditions,” *IEEE Trans. Energy Convers.*, vol. 27, no. 1, pp. 173–183, 2012, doi: 10.1109/TEC.2011.2175928.

[39] M. Killi and S. Samanta, “Modified perturb and observe MPPT algorithm for drift avoidance in photovoltaic systems,” *IEEE Trans. Ind. Electron.*, vol. 62, no. 9, 2015, doi: 10.1109/TIE.2015.2407854.

[40] V. Jack, Z. Salam, and K. Ishaque, “Cell modelling and model parameters estimation techniques for photovoltaic simulator application : a review,” *Appl. Energy*, vol. 154, pp. 500–519, 2015, doi: 10.1016/j.apenergy.2015.05.035.

[41] Texas Instruments, “Power topologies quick reference guide,” 2016. [Online]. Available: https://www.ti.com/lit/ug/slyu032/slyu032.pdf?ts=1644240840073. (accessed Jul. 21, 2021)

[42] Z. A. Aljawary, S. de Pablo, L. C. Herrero-de Lucas, and F. Martinez-Rodrigo, “Local carrier PWM for modular multilevel converters with distributed PV cells and circulating current reduction,” *Energies*, vol. 13, no. 21, 2020, doi: 10.3390/en13215585.

[43] P. Sudheer and C. Chengaiah “Maximum power point tracking algorithms for solar power system-review,” *Int. Res. J. Eng. Technol.*, vol. 4, no. 1, pp. 1507–1514, 2017.

[44] M. A. Mamun, M. M. Islam, M. Hasanuzzaman, and J. Selvaraj, “Effect of tilt angle on the performance and electrical parameters of a PV module: comparative indoor and outdoor experimental investigation,” *Energy and Built Environment*, 2021, doi: 10.1016/j.enbenv.2021.02.001.

[45] T. Esram and P. L. Chapman, “Comparison of photovoltaic array maximum power point tracking techniques,” *IEEE Trans. Energy Convers.*, vol. 22, no. 2, pp. 439–449, 2007, doi: 10.1109/TEC.2006.874230.

[46] I. Houssamo, F. Locment, and M. Sechilariu, “Maximum power tracking for photovoltaic power system: development and experimental comparison of two algorithms,” *Renew. Energy*, vol. 35, no. 10, pp. 2381–2387, 2010, doi: 10.1016/j.renene.2010.04.006.

[47] H. J. El-Khozondar, R. J. El-Khozondar, K. Matter, and T. Suntio, “A review study of photovoltaic array maximum power tracking algorithms,” *Renewables Wind. Water, Sol.*, vol. 3, no. 1, 2016, doi: 10.1186/s40807-016-0022-8.

[48] V. Mahendran and R. Ramabadran, “Impact of modified perturb and observe control on MPPT of PV/battery fed three-port DC-DC converter,” *Acta Sci. - Technol.*, vol. 39, no. 3, pp. 313–323, 2017, doi: 10.4025/actascitechnol.v39i3.29502.

[49] D. Sera, L. Mathe, T. Kerekes, S. V. Spataru, and R. Teodorescu, "On the perturb-and-observe and incremental conductance MPPT methods for PV systems," *IEEE J. Photovoltaics*, vol. 3, no. 3, pp. 1070–1078, 2013, doi: 10.1109/JPHOTOV.2013.2261118.

[50] A. A. Elbaset, S. A. Abdelwahab, H. A. Ibrahim, and M. A. Eid. *Performance analysis of photovoltaic systems with energy storage systems*. Springer International Publishing, 2019.

[51] D. Sera, T. Kerekes, R. Teodorescu, and F. Blaabjerg, "Improved MPPT algorithms for rapidly changing environmental conditions," *2006 12th Int. Power Electron. Motion Control Conf. IEEE*, pp. 1614–1619, 2006, doi: 10.1109/EPEPEMC.2006.4778635.

[52] N. Femia, G. Petrone, G. Spagnuolo, and M. Vitelli, "Optimization of perturb and observe maximum power point tracking method," *IEEE Trans. Power Electron.*, vol. 20, no. 4, pp. 963–973, 2005, doi: 10.1109/TPEL.2005.850975.

[53] C. Zhang, D. Zhao, J. Wang, and G. Chen, "A modified MPPT method with variable perturbation step for photovoltaic system," *2009 IEEE 6th Int. Power Electron. Motion Control Conf. IPEMC 2009*, pp. 2096–2099, 2009, doi: 10.1109/IPEMC.2009. 5157744.

[54] D. Verma, S. Nema, A. M. Shandilya, and S. K. Dash, "Maximum power point tracking (MPPT) techniques: recapitulation in solar photovoltaic systems," *Renew. Sustain. Energy Rev.*, vol. 54, pp. 1018–1034, 2016, doi: 10.1016/j.rser.2015.10.068.

[55] S. Agarwal and M. Jamil, "A comparison of photovoltaic maximum power point techniques," *12th IEEE Int. Conf. Electron. Energy, Environ. Commun. Comput. Control (INDICON)*, pp. 1–6, 2015, doi: 10.1109/INDICON.2015.7443435.

[56] J. S. Kumari, C. S. Babu, and J. Yugandhar, "Design and analysis of open circuit voltage based maximum power point tracking for photovoltaic system," *Int. J. Adv. Sci. Technol.*, vol. 2, no. 2, pp. 51–60, 2011.

[57] A. R. Reisi, M. H. Moradi, and S. Jamasb, "Classification and comparison of maximum power point tracking techniques for photovoltaic system: a review," *Renew. Sustain. Energy Rev.*, vol. 19, pp. 433–443, 2013, doi: 10.1016/j.rser.2012.11.052.

[58] P. Bhatnagar and R. K. Nema, "Maximum power point tracking control techniques: state-of-the-art in photovoltaic applications," *Renew. Sustain. Energy Rev.*, vol. 23, pp. 224–241, 2013, doi: 10.1016/j.rser.2013.02.011.

[59] H. A. Sher, A. F. Murtaza, A. Noman, K. E. Addoweesh, and M. Chiaberge, "An intelligent control strategy of fractional short circuit current maximum power point tracking technique for photovoltaic applications," *J. Renew. Sustain. Energy*, vol. 7, no. 1, pp. 1–15, 2015, doi: 10.1063/1.4906982.

[60] D. Baimel, S. Tapuchi, Y. Levron, and J. Belikov, "Improved fractional open circuit voltage MPPT methods for PV systems," *Electron.*, vol. 8, no. 3, pp. 1–20, 2019, doi: 10.3390/ electronics8030321.

[61] M. A. Abo-Sennah, M. A. El-Dabah, and A. E. Mansour, "Maximum power point tracking techniques for photovoltaic systems: a comparative study," *Int. J. Electr. Comput. Eng.*, vol. 11, no. 1, pp. 57–73, 2013, doi: 10.11591/ijece.v11i1.pp57-73.

[62] M. A. Eltawil and Z. Zhao, "MPPT techniques for photovoltaic applications," *Renew. Sustain. Energy Rev.*, vol. 25, pp. 793–813, 2013, doi: 10.1016/j.rser.2013.05.022.

[63] J. S. Kumari and C. S. Babu, "Comparison of maximum power point tracking algorithms for photovoltaic system," *Int. J. Adv. Eng. Technol.*, vol. 1, no. 5, pp. 133–148, 2011.

[64] Q. M. Abdulmajeed *et al.*, "Photovoltaic maximum tracking power point system: review and research challenges," *Int. J. Adv. Trends Comput. Sci. Eng.*, vol. 2, no. 5, pp. 16–21, 2013.

[65] M. A. de Brito, L. Galotto, L. P. Sampaio, G. de Azevedo e Melo, and C. A. Canesin, "Evaluation of the main MPPT techniques for photovoltaic applications," *IEEE Trans. Ind. Electron.*, vol. 60, no. 3, pp. 1156–1167, 2013, doi: 10.1109/TIE.2012.2198036.

[66] H. A. Attia and F. D. Gonzalo, "Stand-alone PV system with MPPT function based on fuzzy logic control for remote building applications," *Int. J. Parallel, Emergent Distrib. Syst.*, vol. 10, no. 2, pp. 842–851, 2019, doi: 10.11591/ijpeds.v10.i2.pp842-851.

[67] F. Bouchafaa, D. Beriber, and M. S. Boucherit, "Modeling and simulation of a gird connected PV generation system with MPPT fuzzy logic control," *2010 7th Int. Multi-Conference Syst. Signals Devices*, 2010, doi: 10.1109/SSD.2010.5585530.

[68] M. Kumar, S. R. Kapoor, R. Nagar, and A. Verma, "Comparison between IC and fuzzy logic MPPT algorithm based solar PV system using boost converter," *Int. J. Adv. Res. Electr. Electron. Instrum. Eng.*, vol. 04, no. 06, pp. 4927–4939, 2015, doi: 10.15662/ijareeie.2015.0406007.

[69] S. Qazi. *Standalone photovoltaic (PV) systems for disaster relief and remote areas.* Elsevier, 2016.

[70] P. Thamke, "Applications of photovoltaic systems," *Satheesh Krishnamurthy OPEN Univ. UK*, 2018. Available: https://www.scribd.com/document/394172035/PV-cells. (accessed May. 11, 2021)

[71] Inverter.com, "Solar water pump DC controller user manual inverter," 2019. [Online]. Available: https://www.inverter.com/doc/Solar-water-pump-external-dc-controller-user-manual.pdf. (accessed Jul. 30, 2021).

[72] *ESSENSE*, "Solar water pumping," 2021. [Online]. Available: https://www.essense.com.pk /SolarWaterPumping.html. (accessed Jul. 29, 2021).

[73] Neeraj Enterprises, "Electric vehicle solar charging stations," *IndiaMART*, 2020. [Online]. Available: https://www.indiamart.com/proddetail/electric-vehicle-solar-charging-stations-20773113633.html. (accessed Jul. 29, 2021).

[74] B. Liu, S. Duan, and T. Cai, "Photovoltaic DC-building-module-based BIPV system — concept and design considerations," *IEEE Trans. Power Electron.*, vol. 26, no. 5, pp. 1418–1429, 2011, doi: 10.1109/TPEL.2010.2085087.

[75] "Onyx Solar - Photovoltaic glass for buildings," 2018. [Online]. Available: https://www.onyxsolar.com/ (accessed Jul. 29, 2021).

[76] Y. Zhang and Y. Li. *Current source converters and their control*. Elsevier Inc., 2018.

[77] R. E. Torres-Olguin, A. Garces, M. Molinas, and T. Undeland, "Integration of offshore wind farm using a hybrid HVDC transmission composed by the PWM current-source converter and line-commutated converter," *IEEE Trans. Energy Convers.*, vol. 28, no. 1, pp. 125–134, 2013, doi: 10.1109/TEC.2012.2230535.

[78] K. Sharifabadi, L. Harnefors, H. P. Nee, S. Norrga, and R. Teodorescu. *Design, control and application of modular multilevel converters for HVDC transmission systems*. John Wiley & Sons, 2016.

[79] E. N. Abildgaard and M. Molinas, "Modelling and control of the modular multilevel converter (MMC)," *Energy Procedia*, vol. 20, pp. 227–236, 2012, doi: 10.1016/j.egypro. 2012.03.023.

[80] K. Friedrich, "Modern HVDC PLUS application of VSC in modular multilevel converter topology," *IEEE Int. Symp. Ind. Electron.*, pp. 3807–3810, 2010, doi: 10.1109/ISIE.2010. 5637505.

[81] B. Jacobson, P. Karlsson, G. Asplund, L. Harnefors, and T. Jonsson, "VSC-HVDC transmission with cascaded two-level converters," *Cigré session*, pp. B4–B110, 2010.

[82] M. Barnes and A. Beddard, "Voltage source converter HVDC links - The state of the art and issues going forward," *Energy Procedia*, vol. 24, pp. 108–122, 2012, doi: 10.1016/j. egypro.2012.06.092.

[83] J. Rodríguez, J. S. Lai, and F. Z. Peng, "Multilevel inverters: a survey of topologies, controls, and applications," *IEEE Trans. Ind. Electron.*, vol. 49, no. 4, pp. 724–738, 2002, doi: 10.1109/TIE.2002.801052.

[84] G. P. Adam, O. Anaya-Lara, G. Burt, and J. R. McDonald, "Comparison between flying capacitor and modular multilevel inverters," *IECON Proc. Ind. Electron. Conf.*, pp. 271–276, 2009, doi: 10.1109/IECON.2009.5414934.

[85] S. Khomfoi and L. M. Tolbert. *Multilevel power converters*. Third Edit. Elsevier Inc., 2011.

[86] O. Peake, "The history of high voltage direct current transmission," *Aust. J. Multi-Disciplinary Eng.*, vol. 8, no. 1, pp. 47–55, 2010, doi: 10.1080/14488388.2010.11464824.

[87] A. Dekka, B. Wu, R. L. Fuentes, M. Perez, and N. R. Zargari, "Evolution of topologies, modeling, control schemes, and applications of modular multilevel converters," *IEEE J. Emerg. Sel. Top. Power Electron.*, vol. 5, no. 4, pp. 1631–1656, 2017, doi: 10.1109/ JESTPE.2017.2742938.

[88] L. Weimers, "HVDC light: a new technology for a better environment," *IEEE Power Eng. Rev.*, vol. 18, no. 8, pp. 19–20, 1998, doi: 10.1109/MPER.1998.691411.

[89] Y. H. Liu, J. Arrillaga, and N. R. Watson, "Addition of four-quadrant power controllability to multi-level VSC HVDC transmission," *IET Gener. Transm. Distrib.*, vol. 1, no. 6, pp. 872–878, 2007, doi: 10.1049/iet-gtd:20070097.

[90] C. C. Davidson and D. R. Trainer, “Innovative concepts for hybrid multi-level converters for HVDC power transmission,” *9th IET Int. Conf. AC and DC Power Transm.*, 2010, doi: 10.1049/cp.2010.0982.

[91] S. Kouro *et al.*, “Recent advances and industrial applications of multilevel converters,” *IEEE Trans. Ind. Electron.*, vol. 57, no. 8, pp. 2553–2580, 2010, doi: 10.1109/TIE.2010.2049719.

[92] C. Osawa, Y. Matsumoto, T. Mizukami, and S. Ozaki, “A state-space modeling and a neutral point voltage control for an NPC power converter,” *Proc. Power Convers. Conf. IEEE*, vol. 1, pp. 225–230, 1997, doi: 10.1109/PCCON.1997.645616.

[93] J. Rodriguez, S. Bernet, P. K. Steimer, and I. E. Lizama, “A Survey on neutral-point-clamped inverters,” *IEEE Trans. Ind. Electron.*, vol. 57, no. 7, pp. 2219–2230, 2010, doi: 10.1109/TIE.2009.2032430.

[94] P. Barbosa, P. Steimer, J. Steinke, M. Winkelnkemper, and N. Celanovic, “Active-neutral-point-clamped (ANPC) multilevel converter technology,” *2005 Eur. Conf. Power Electron. Appl.*, pp. 10-pp, 2005, doi: 10.1109/epe.2005.219713.

[95] I. Mattsson, A. Ericsson, B. D. Railing, J. J. Miller, B. Williams, G. Moreau, and C. D. Clarke, “Murraylink, the longest underground HVDC cable in the world,” *Pap. B4-103 Present. Cigré Conf. Paris, Fr.*, 2004.

[96] T. A. Meynard and H. Foch, “Multi-level conversion: high voltage choppers and voltage-source inverters,” *PESC Rec. - IEEE Annu. Power Electron. Spec. Conf.*, pp. 397–403, 1992, doi: 10.1109/PESC.1992.254717.

[97] S. Dieckerhoff, S. Bernet, and D. Krug, “Power loss-oriented evaluation of high voltage IGBTs and multilevel converters in transformerless traction applications,” *IEEE Trans. Power Electron.*, vol. 20, no. 6, pp. 1328–1336, 2005, doi: 10.1109/TPEL.2005.857534.

[98] A. Ruderman, B. Reznikov, and M. Margaliot, “Analysis of a flying capacitor converter : a switched systems approach,” *13th EPE-PECM Conf.*, p. 20, 2008.

[99] V. T. Tran, M. K. Nguyen, C. C. Ngo, and Y. O. Choi, “Three-phase five-level cascade quasi-switched boost inverter,” *Electron.*, vol. 8, no. 3, 2019, doi: 10.3390/electronics 8030296.

[100] B. Xiao, K. Shen, J. Mei, F. Filho, and L. M. Tolbert, “Control of cascaded H-bridge multilevel inverter with individual MPPT for grid-connected photovoltaic generators,” *2012 IEEE Energy Convers. Congr. Expo. ECCE 2012*, pp. 3715–3721, 2012, doi: 10.1109/ ECCE.2012.6342474.

[101] E. Kontos, G. Tsolaridis, R. Teodorescu, and P. Bauer, “Full-bridge MMC DC fault ride-through and STATCOM operation in multi-terminal HVDC grids,” *Bull. Polish Acad. Sci. Tech. Sci.*, vol. 65, no. 5, pp. 653–662, 2017, doi: 10.1515/bpasts-2017-0070.

[102] M. H. Nguyen and S. Kwak, “Improved indirect model predictive control for enhancing dynamic performance of modular multilevel converter,” *Electron.*, vol. 9, no. 9, pp. 1–19, 2020, doi: 10.3390/electronics9091405.

[103] U. N. Gnanarathna, A. M. Gole, and R. P. Jayasinghe, "Efficient modeling of modular multilevel HVDC converters (MMC) on electromagnetic transient simulation programs," *IEEE Trans. Power Deliv.*, vol. 26, no. 1, pp. 316–324, 2011, doi: 10.1109/TPWRD.2010. 2060737.

[104] M. A. Perez, S. Bernet, J. Rodriguez, S. Kouro, and R. Lizana, "Circuit topologies, modeling, control schemes, and applications of modular multilevel converters," *IEEE Trans. Power Electron.*, vol. 30, no. 1, pp. 4–17, 2015, doi: 10.1109/TPEL.2014.2310127.

[105] S. Rivera, S. Kouro, B. Wu, J. I. Leon, J. Rodríguez, and L. G. Franquelo, "Cascaded H-bridge multilevel converter multistring topology for large scale photovoltaic systems," *2011 IEEE Int. Symp. Ind. Electron.*, pp. 1837–1844, 2011, doi: 10.1109/ISIE.2011.5984437.

[106] N. Celanovic, and D. Boroyevich, "A comprehensive study of neutral-point voltage balancing problem in three-level neutral-point-clamped voltage source PWM inverters," *IEEE Trans. Power Electron.*, vol. 15, no. 2, pp. 242–251, 2000, doi: 10.1109/63.838096.

[107] M. Schweizer and J. W. Kolar, "Design and implementation of a highly efficient three-level T-type converter for low-voltage applications," *IEEE Trans. Power Electron.*, vol. 28, no. 2, pp. 899–907, 2013, doi: 10.1109/TPEL.2012.2203151.

[108] R. Oliveira and A. Yazdani, "A modular multilevel converter with DC fault handling capability and enhanced efficiency for HVDC system applications," *IEEE Trans. Power Electron.*, vol. 32, no. 1, pp. 11–22, 2017, doi: 10.1109/TPEL.2016.2523338.

[109] R. Zeng, L. Xu, L. Yao, and D. J. Morrow, "Precharging and DC fault ride-through of hybrid MMC-based HVDC systems," *IEEE Trans. Power Deliv.*, vol. 30, no. 3, pp. 1298–1306, 2015, doi: 10.1109/TPWRD.2014.2360042.

[110] K. Sharifabadi, L. Harnefors, H. P. Nee, S. Norrga, and R. Teodorescu. *Design, control, and application of modular multilevel converters for HVDC transmission systems*. John Wiley & Sons, 2016.

[111] S. P. Teeuwsen, "Modeling the trans bay cable project as voltage-sourced converter with modular multilevel converter design," *IEEE Power Energy Soc. Gen. Meet.*, pp. 1–8, 2011, doi: 10.1109/PES.2011.6038903.

[112] M. Pereira, D. Retzmann, J. Lottes, M. Wiesinger, and G. Wong, "SVC PLUS: an MMC STATCOM for network and grid access applications," *2011 IEEE Trondheim PowerTech 2011*, pp. 1–5, 2011, doi: 10. 1109/PTC.2011.6019245.

[113] S. Fan, K. Zhang, J. Xiong, and Y. Xue, "An improved control system for modular multilevel converters with new modulation strategy and voltage balancing control," *IEEE Trans. Power Electron.*, vol. 30, no. 1, pp. 358–371, 2015, doi: 10.1109/TPEL.2014. 2304969.

[114] Z. Li, P. Wang, H. Zhu, Z. Chu, and Y. Li, "An improved pulse width modulation method for chopper-cell-based modular multilevel converters," *IEEE Trans. Power Electron.*, vol. 27, no. 8, pp. 3472–3481, 2012, doi: 10.1109/TPEL.2012.2187800.

[115] R. Adapa, "High-wire act: HVDC technology: the state of the art," *IEEE power energy Mag.*, vol. 10, no. 6, pp. 18–29, 2012, doi: 10.1109/MPE.2012.2213011.

[116] N. Flourentzou, V. G. Agelidis, and G. D. Demetriades, "VSC-based HVDC power transmission systems: an overview," *IEEE Trans. Power Electron.*, vol. 24, no. 3, pp. 592–602, 2009, doi: 10.1109/TPEL.2008.2008441.

[117] N. R. Watson and J. D. Watson, "An overview of HVDC technology," *Energies*, vol. 13, no. 17, 2020, doi: 10.3390/en13174342.

[118] H. J. Knaak, "Modular multilevel converters and HVDC / FACTS : a success story," *Proc. 14th Eur. Conf. Power Electron. Appl. (EPE 2011).IEEE*, pp. 1–6, 2011.

[119] E. Solas, G. Abad, J. A. Barrena, A. Cárcar, and S. Aurtenetxea, "Modulation of modular multilevel converter for HVDC application," *Proc. EPE-PEMC 2010 - 14th Int. Power Electron. Motion Control Conf.*, pp. 84–89, 2010, doi: 10.1109/EPEPEMC.2010.5606876.

[120] J. I. Leon, S. Kouro, L. G. Franquelo, J. Rodriguez, and B. Wu, "The essential role and the continuous evolution of modulation techniques for voltage-source inverters in the past, present, and future power electronics," *IEEE Trans. Ind. Electron.*, vol. 63, no. 5, pp. 2688–2701, 2016, doi: 10.1109/TIE.2016.2519321.

[121] J. C. Colque, E. Ruppert, R. Z. Vargas, and J. L. Azcue, "Comparative analysis based on the switching frequency of modulation techniques for MMC applications," *2019 IEEE 15th Brazilian Power Electron. Conf. 5th IEEE South. Power Electron. Conf. COBEP/SPEC*, 2019, doi: 10.1109/COBEP/SPEC44138.2019.9065389.

[122] Y. Deng and R. G. Harley, "Space-vector versus nearest-level pulse width modulation for multilevel converters," *IEEE Trans. Power Electron.*, vol. 30, no. 6, pp. 2962–2974, 2015, doi: 10.1109/TPEL.2014.2331687.

[123] F. Martinez-Rodrigo, L. C. Herrero-de Lucas, S. de Pablo, A. B. Rey-Boué, and D. Ramirez, "Calculation of the number of modules and the switching frequency of a modular multilevel converter using near level control," *Electr. Power Syst. Res.*, vol. 165, pp. 68–83, 2018, doi: 10.1016/j.epsr.2018.08.019.

[124] F. Blaabjerg. *Control of power electronic converters and systems: Volume 2*. Academic Press, 2018.

[125] A. Hassanpoor, S. Norrga, H. P. Nee, and L. Angquist, "Evaluation of different carrier-based PWM methods for modular multilevel converters for HVDC application," *IECON Proc. Industrial Electron. Conf.*, pp. 388–393, 2012, doi: 10.1109/IECON.2012.6388789.

[126] L. G. Franquelo, J. Rodriguez, J. I. Leon, S. Kouro, R. Portillo, and M. A. Prats, "The age of multilevel converters arrives," *IEEE Ind. Electron. Mag.*, vol. 2, no. 2, pp. 28–39, 2008, doi: 10.1109/MIE.2008.923519.

[127] Q. Tu, Z. Xu, and L. Xu, "Reduced switching-frequency modulation and circulating current suppression for modular multilevel converters," *IEEE Trans. Power Deliv.*, vol. 26, no. 3, pp. 2009–2017, 2011, doi: 10.1109/TPWRD.2011.2115258.

[128] A. Ferreira, C. Collados, and O. Gomis-Bellmunt, "Modulation techniques applied to medium voltage modular multilevel converters for renewable energy integration: a review," *Electr. Power Syst. Res.*, vol. 155, pp. 21–39, 2018, doi: 10.1016/j. epsr.2017.08.015.

[129] S. Du, A. Dekka, B. Wu, and N. Zargari. *Modular multilevel converters: analysis, control, and applications.* John Wiley & Sons, 2017.

[130] G. S. Konstantinou and V. G. Agelidis, "Performance evaluation of half-bridge cascaded multilevel converters operated with multicarrier sinusoidal PWM techniques," *2009 4th IEEE Conf. Ind. Electron. Appl. ICIEA 2009*, pp. 3399–3404, 2009, doi: 10.1109/ICIEA.2009.5138833.

[131] B. P. McGrath, C. A. Teixeira, and D. G. Holmes, "Optimized phase disposition (PD) modulation of a modular multilevel converter," *IEEE Trans. Ind. Appl.*, vol. 53, no. 5, pp. 4624–4633, 2017, doi: 10.1109/TIA.2017.2697953.

[132] P. M. Meshram and V. B. Borghate, "A simplified nearest level control (NLC) voltage balancing method for modular multilevel converter (MMC)," *IEEE Trans. Power Electron.*, vol. 30, no. 1, pp. 450–462, 2015, doi: 10.1109/TPEL.2014.2317705.

[133] A. Perez-Basante, S. Ceballos, G. Konstantinou, M. Liserre, J. Pou, and I. M. de Alegria, "Circulating current control for modular multilevel converter based on selective harmonic elimination with ultra-low switching frequency," *2016 18th Eur. Conf. Power Electron. Appl. EPE 2016 ECCE Eur.*, 2016, doi: 10.1109/EPE.2016.7695372.

[134] A. Darvish Falehi, "Analysis and application of inventive selective harmonic elimination strategy to eliminate high order harmonic from asymmetrical multi-level inverter," *Multidimens. Syst. Signal Process.*, vol. 31, no. 2, pp. 411–429, 2020, doi: 10.1007/s11045-019-00669-0.

[135] G. T. Son *et al.*, "Design and control of a modular multilevel HVDC converter with redundant power modules for noninterruptible energy transfer," *IEEE Trans. Power Deliv.*, vol. 27, no. 3, pp. 1611–1619, 2012, doi: 10.1109/TPWRD.2012.2190530.

[136] A. Moeini, H. Iman-Eini, and M. Bakhshizadeh, "Selective harmonic mitigation-pulse-width modulation technique with variable DC-link voltages in single and three-phase cascaded H-bridge inverters," *IET Power Electron.*, vol. 7, no. 4, pp. 924–932, 2014, doi: 10.1049/iet-pel.2013.0315.

[137] G. Konstantinou, M. Ciobotaru, and V. Agelidis, "Selective harmonic elimination pulse-width modulation of modular multilevel converters," *IET Power Electron.*, vol. 6, no. 1, pp. 96–107, 2013, doi: 10.1049/iet-pel.2012.0228.

[138] H. Robles-Campos and F. Mancilla-David, "Selective harmonic elimination for the modular multilevel converter," *2016 North Am. Power Symp. Proc.(NAPS)*, pp. 1–6, 2016, doi: 10.1109/NAPS.2016.7747996.

[139] G. Konstantinou, J. Pou, S. Ceballos, R. Darus, and V. G. Agelidis, "Switching frequency analysis of staircase-modulated modular multilevel converters and equivalent PWM techniques," *IEEE Trans. Power Deliv.*, vol. 31, no. 1, pp. 28–36, 2016, doi: 10.1109/TPWRD.2015.2416759.

[140] R. Darus, J. Pou, G. Konstantinou, S. Ceballos, R. Picas, and V. G. Agelidis, “A modified voltage balancing algorithm for the modular multilevel converter: evaluation for staircase and phase-disposition PWM,” *IEEE Trans. Power Electron.*, vol. 30, no. 8, pp. 4119–4127, 2015, doi: 10.1109/TPEL.2014.2359005.

[141] J. Peralta, H. Saad, S. Dennetière, J. Mahseredjian, and S. Nguefeu, “Detailed and averaged models for a 401-level MMC-HVDC system,” *IEEE Trans. Power Deliv.*, vol. 27, no. 3, pp. 1501–1508, 2012, doi: 10.1109/TPWRD.2012.2188911.

[142] Q. Tu and Z. Xu, “Impact of sampling frequency on harmonic distortion for modular multilevel converter,” *IEEE Trans. Power Deliv.*, vol. 26, no. 1, pp. 298–306, 2011, doi: 10.1109/TPWRD.2010.2078837.

[143] K. Ilves, A. Antonopoulos, S. Norrga, and H. P. Nee, “A new modulation method for the modular multilevel converter allowing fundamental switching frequency,” *IEEE Trans. Power Electron.*, vol. 27, no. 8, pp. 3482–3494, 2012, doi: 10.1109/TPEL.2012.2185832.

[144] Y. Deng, K. H. Teo, C. Duan, T. G. Habetler, and R. G. Harley, “A fast and generalized space vector modulation scheme for multilevel inverters,” *IEEE Trans. Power Electron.*, vol. 29, no. 10, pp. 5204–5217, 2014, doi: 10.1109/TPEL.2013.2293734.

[145] Y. Deng, Y. Wang, K. H. Teo, and R. G. Harley, “Space vector modulation method for modular multilevel converters,” *IECON Proc. Ind. Electron. Conf.*, pp. 4715–4721, 2014, doi: 10.1109/IECON.2014.7049213.

[146] S. de Pablo, A. B. Rey-Boué, L. C. Herrero, and F. Martínez, “Hexagon based algorithm for space vector modulation on multilevel voltage source inverters,” *2010 IEEE Int. Symp. Ind. Electron.*, pp. 3218–3223, 2010, doi: 10.1109/ISIE.2010.5637592.

[147] B. P. McGrath, D. G. Holmes, and T. Lipo, “Optimized space vector switching sequences for multilevel inverters,” *IEEE Trans. Power Electron.*, vol. 18, no. 6, pp. 1293–1301, 2003, doi: 10.1109/TPEL.2003.818827.

[148] L. M. Tolbert and X. Shi. *Multilevel Power Converters*. 4th ed. Elsevier Inc., 2018.

[149] J. Rodríguez, J. Pontt, P. Correa, P. Cortés, and C. Silva, “A new modulation method to reduce common-mode voltages in multilevel inverters,” *IEEE Trans. Ind. Electron.*, vol. 51, no. 4, pp. 834–839, 2004, doi: 10.1109/TIE.2004.831735.

[150] H. Mohammadi and M. T. Bina, “A transformerless medium-voltage STATCOM topology based on extended modular multilevel converters,” *IEEE Trans. Power Electron.*, vol. 26, no. 5, pp. 1534–1545, 2011, doi: 10.1109/TPEL.2010.2085088.

[151] M. N. Raju, J. Sreedevi, R. P. Mandi, and K. S. Meera, “Modular multilevel converters technology: a comprehensive study on its topologies, modelling, control and applications,” *IET Power Electron.*, vol. 12, no. 2, pp. 149–169, 2019, doi: 10.1049/iet-pel.2018.5734.

[152] S. Du and J. Liu, “A study on DC voltage control for chopper-cell-based modular multilevel converters in D-STATCOM application,” *IEEE Trans. Power Deliv.*, vol. 28, no. 4, pp. 2030–2038, 2013, doi: 10.1109/TPWRD.2013.2246195.

[153] R. Darus, G. Konstantinou, J. Pou, S. Ceballos, and V. G. Agelidis, “Comparison of phase-shifted and level-shifted PWM in the modular multilevel converter,” *2014 Int. Power Electron. Conf. IPEC-Hiroshima 2014- ECCE Asia*, pp. 3764–3770, 2014, doi: 10.1109/IPEC.2014.6870039.

[154] M. Rejas *et al.*, “Performance comparison of phase shifted PWM and sorting method for modular multilevel converters,” *2015 17th Eur. Conf. Power Electron. Appl. EPE-ECCE Eur. 2015*, pp. 1–10, 2015, doi: 10.1109/EPE.2015.7311700.

[155] A. Dekka, B. Wu, N. R. Zargari, and R. L. Fuentes, “A space-vector PWM-based voltage-balancing approach with reduced current sensors for modular multilevel converter,” *IEEE Trans. Ind. Electron.*, vol. 63, no. 5, pp. 2734–2745, 2016, doi: 10.1109/TIE.2016.2514346.

[156] A. Dekka, B. Wu, and N. R. Zargari, “A novel modulation scheme and voltage balancing algorithm for modular multilevel converter,” *IEEE Trans. Ind. Appl.*, vol. 52, no. 1, pp. 432–443, 2016, doi: 10.1109/TIA.2015.2477481.

[157] Y. Okazaki, H. Matsui, M. Hagiwara, and H. Akagi, “Design considerations on the DC capacitor of each chopper cell in a modular multilevel cascade inverters (MMCI-DSCC) for medium-voltage motor drives,” *2014 IEEE Energy Convers. Congr. Expo. ECCE 2014*, pp. 3393–3400, 2014, doi: 10.1109/ECCE.2014.6953861.

[158] A. J. Korn, M. Winkelnkemper, and P. Steimer, “Low output frequency operation of the modular multi-level converter,” *2010 IEEE Energy Convers. Congr. Expo. ECCE 2010 - Proc.*, pp. 3993–3997, 2010, doi: 10.1109/ECCE.2010.5617802.

[159] Y. Zhong, N. Roscoe, D. Holliday, T. C. Lim, and S. J. Finney, “High-efficiency MOSFET-based MMC design for LVDC distribution systems,” *IEEE Trans. Ind. Appl.*, vol. 54, no. 1, pp. 321–334, 2018, doi: 10.1109/TIA.2017.2754481.

[160] S. Debnath, J. Qin, B. Bahrani, M. Saeedifard, and P. Barbosa, “Operation, control, and applications of the modular multilevel converter: a review,” *IEEE Trans. Power Electron.*, vol. 30, no. 1, pp. 37–53, 2015, doi: 10.1109/TPEL.2014.2309937.

[161] M. Hagiwara and H. Akagi, “Control and experiment of pulsewidth-modulated modular multilevel converters,” *IEEE Trans. Power Electron.*, vol. 24, no. 7, pp. 1737–1746, 2009, doi: 10.1109/TPEL.2009.2014236.

[162] M. A. Perez, J. Rodriguez, E. J. Fuentes, and F. Kammerer, “Predictive control of AC-AC modular multilevel converters,” *IEEE Trans. Ind. Electron.*, vol. 59, no. 7, pp. 2832–2839, 2012, doi: 10.1109/TIE.2011.2159349.

[163] M. Zhang, L. Huang, W. Yao, and Z. Lu, “Circulating harmonic current elimination of a CPS-PWM-based modular multilevel converter with a plug-in repetitive controller,” *IEEE Trans. Power Electron.*, vol. 29, no. 4, pp. 2083–2097, 2014, doi: 10.1109/TPEL.2013.2269140.

[164] Z. Li, P. Wang, Z. Chu, H. Zhu, Y. Luo, and Y. Li, “An inner current suppressing method for modular multilevel converters,” *IEEE Trans. Power Electron.*, vol. 28, no. 11, pp. 4873–4879, 2013, doi: 10.1109/TPEL.2013.2242204.

[165] R. Darus, J. Pou, G. Konstantinou, S. Ceballos, and V. G. Agelidis, “Circulating current control and evaluation of carrier dispositions in modular multilevel converters,” *2013 IEEE ECCE Asia Downunder*, pp. 332–338, 2013, doi: 10.1109/ECCE-Asia.2013.6579117.

[166] A. Marzoughi, R. Burgos, D. Boroyevich, and Y. Xue, “Steady-state analysis of voltages and currents in modular multilevel converter based on average model,” *2015 IEEE Energy Convers. Congr. Expo. (ECCE). IEEE*, pp. 3522–3528, 2015, doi: 10.1109/ECCE.2015. 7310158.

[167] S. Li, X. Wang, Z. Yao, T. Li, and Z. Peng, “Circulating current suppressing strategy for MMC-HVDC based on nonideal proportional resonant controllers under unbalanced grid conditions,” *IEEE Trans. Power Electron.*, vol. 30, no. 1, pp. 387–397, 2015, doi: 10.1109/ TPEL.2014.2329059.

[168] B. Bahrani, S. Debnath, and M. Saeedifard, “Circulating current suppression of the modular multilevel converter in a double-frequency rotating reference frame,” *IEEE Trans. Power Electron.*, vol. 31, no. 1, pp. 783–792, 2016, doi: 10.1109/TPEL.2015.2405062.

[169] A. K. Karunanithi. *A survey, discussion, and comparison of sorting algorithms*. Master's Thesis, Umea University, 2014.

[170] Suntech Power, “320 Watt polycrystalline solar module features,” 2016. [Online]. Available: http://www.taipo-tech.com/wp-content/uploads/2017/02/STP310-320-24Vem.pdf. (accessed Dec. 10, 2021).

[171] R. Sinvula, K. M. Abo-Al-Ez, and M. T. Kahn, “Total harmonics distortion (THD) with PV system integration in smart grids: case study,” *Proc. 27th Int. Conf. Domest. Use Energy, DUE 2019*, pp. 102–108, 2019.

[172] A. Sufyanu, “Power quality and harmonic analysis in three phase systems,” *J. Electr. Electron. Syst.*, vol. 07, no. 04, 2018, doi: 10.4172/2332-0796.1000291.

[173] O. Ibrahim, N. Z. Yahaya, and N. Saad, “Comparative studies of PID controller tuning methods on a DC-DC boost converter,” *2016 6th Int. Conf. Intell. Adv. Syst. (ICIAS)*, pp.1-5, 2016, doi: 10.1109/ICIAS.2016.7824044.

Appendix A

The MATLAB/Simulink simulation models for the MMC controlled by the proposed LC-PWM for this thesis work investigation are presented below.

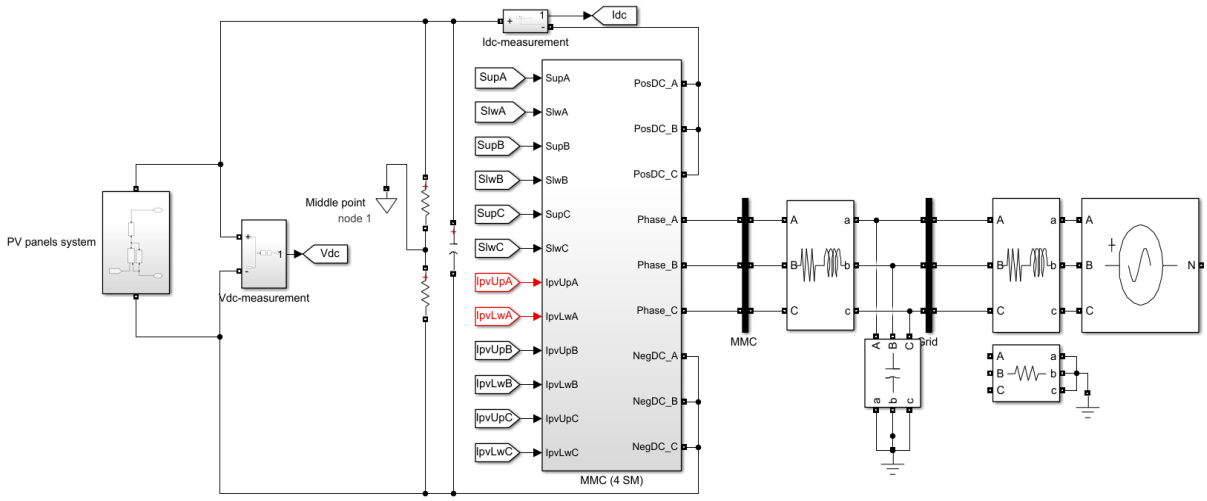

(a)

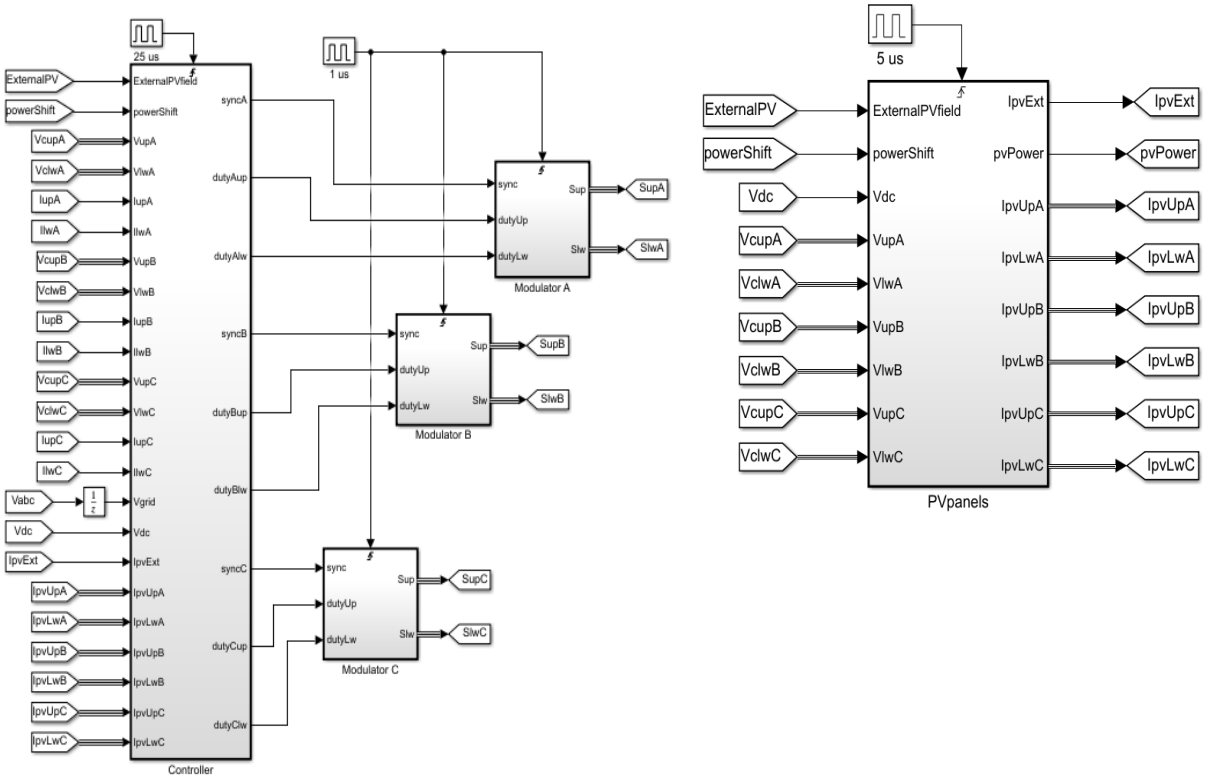

(b) (c)

Figure A.1: LC-PWM controlling MMC simulation module for Chapter 6 (a) Simulation overview-based grid /load connected PV MMC (b) LC-PWM switching signal to control the MMC after applying selection method (c) PV panels string for integrating to each MMC SMs.

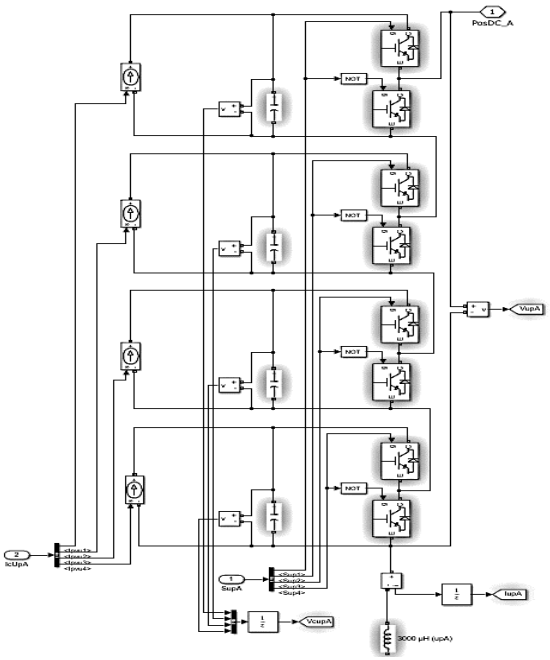

(a)

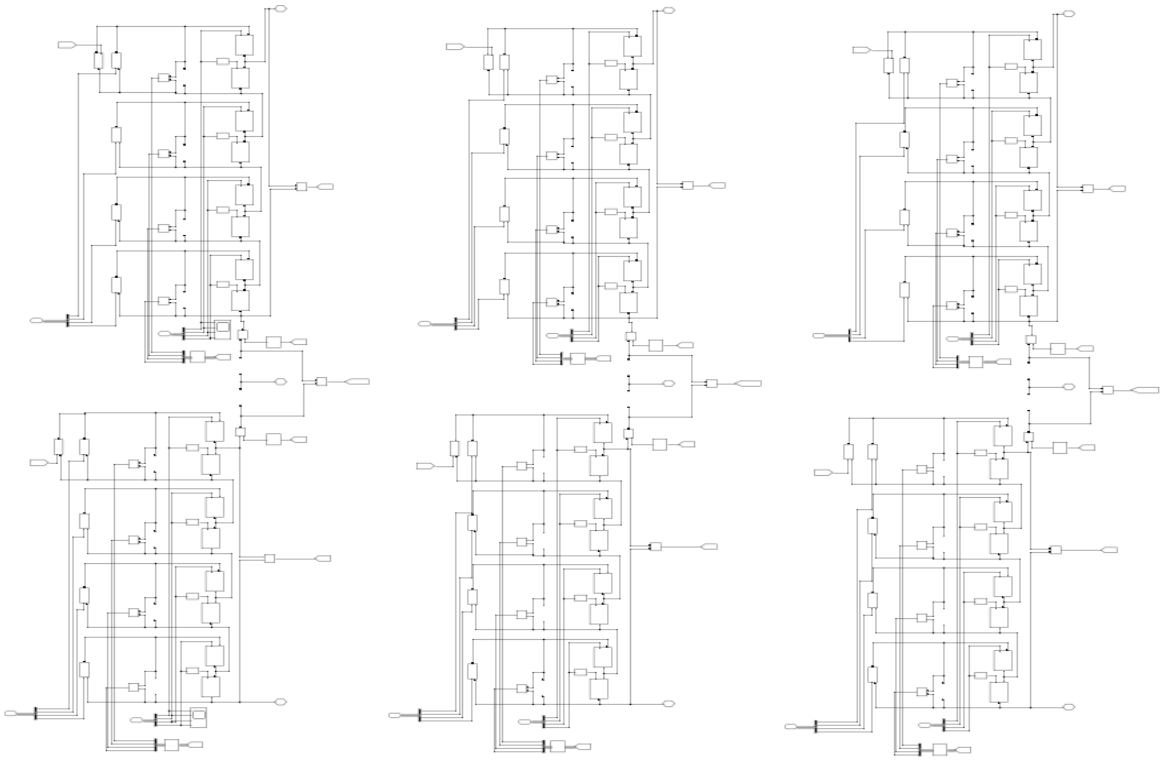

(b)

Figure A.2: (a) Upper arm connects parts in phase 'a'. (b) Legs and arms of the MMC simulation module for Chapter 6

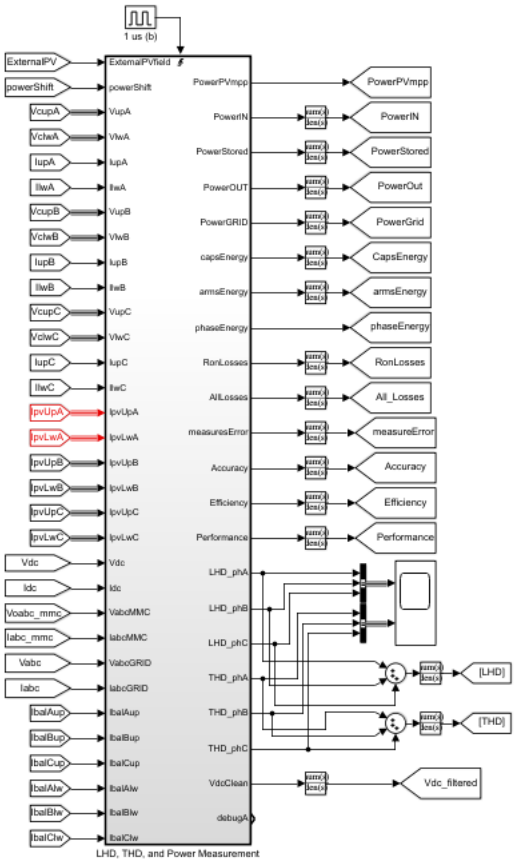

Figure A.3: The MMC simulation module for calculating LHD, THD, Accuracy, Efficiency, Performance, and unexpected errors by calculating the energy stored in the MMC element capacitors and inductors for Chapter 6.

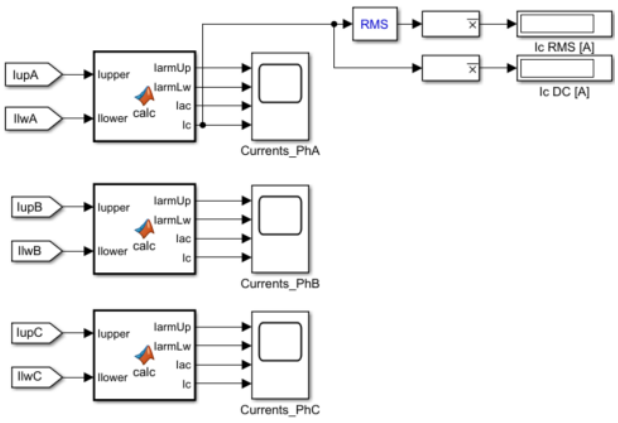

Figure A.4: Measurements of circulating currents in MMC phases 'a', 'b', and 'c', as well as the RMS value of the circulating current in phase 'a' and the DC value of the circulating current in phase 'a'.

Appendix B

The MATLAB/Simulink simulation models for the MMC controlled by the traditional PS-PWM for this thesis work investigation are presented below

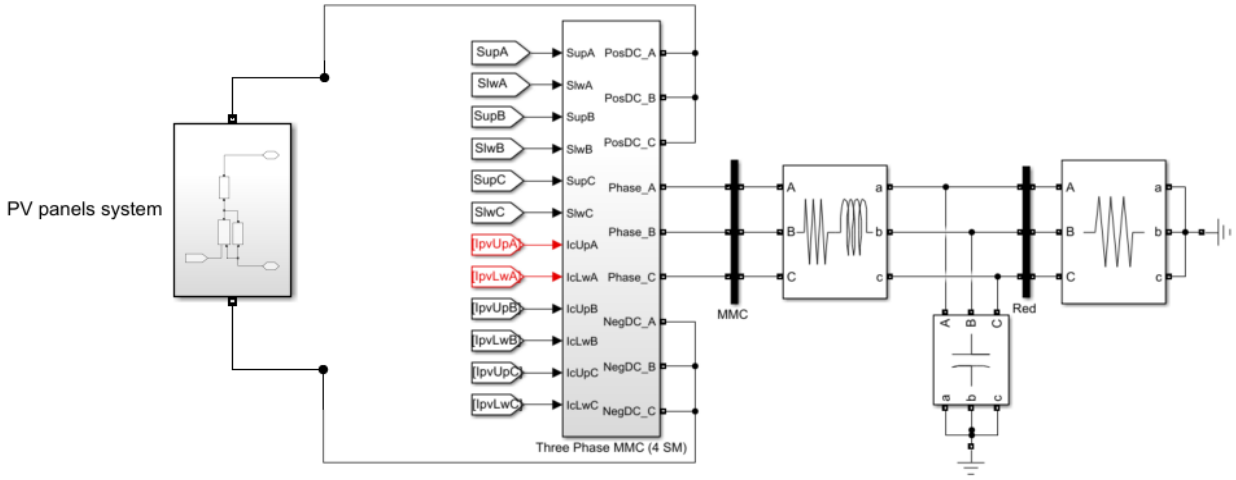

(a)

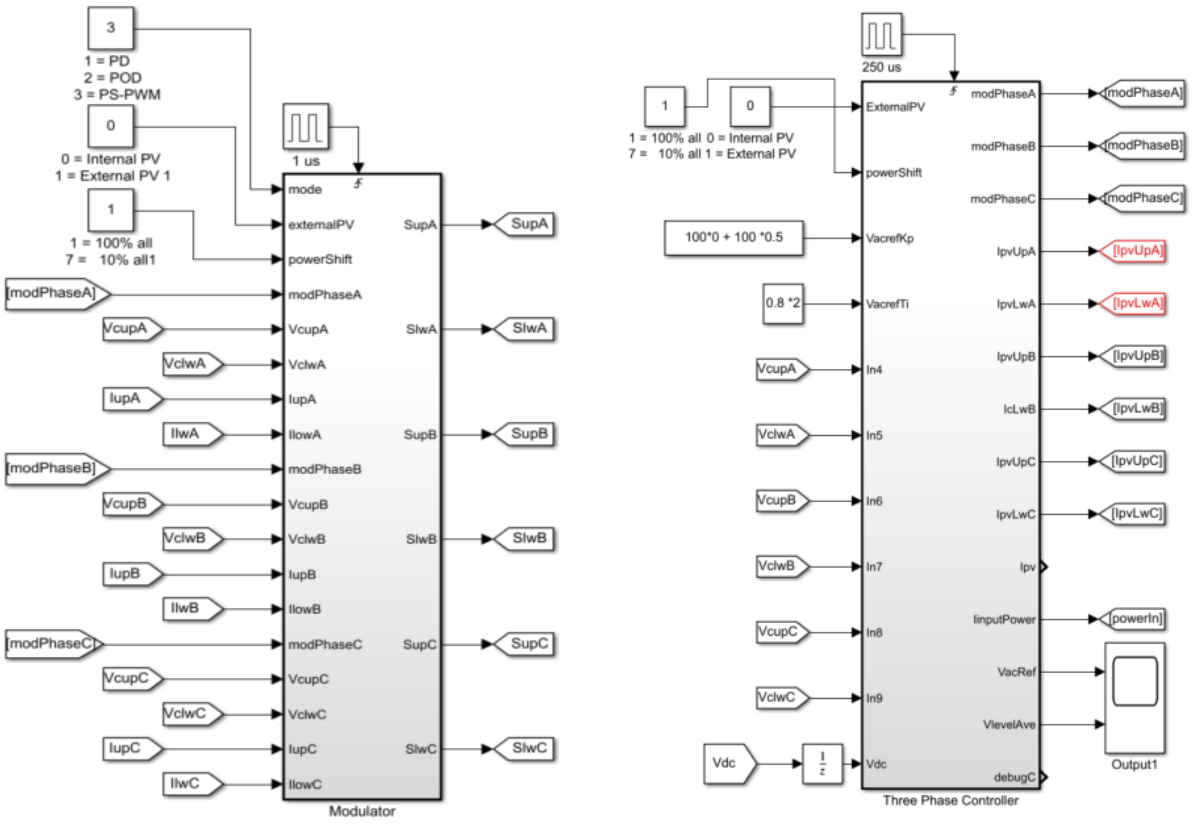

(b) (c)

Figure B.1: PS-PWM controlling MMC simulation module for Chapter 6 (a) Simulation overview-based load connected PV MMC (b) PS -PWM switching signal to control the MMC after applying selection method (c) PV panels string for integrating to each MMC SMs.

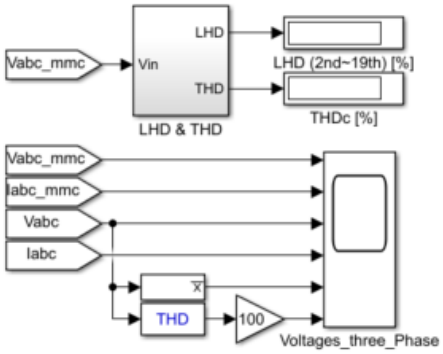

Figure B.2: The MMC simulation module for calculating LHD, and THD of the voltage out from the MMC and THD for the voltage at the load.

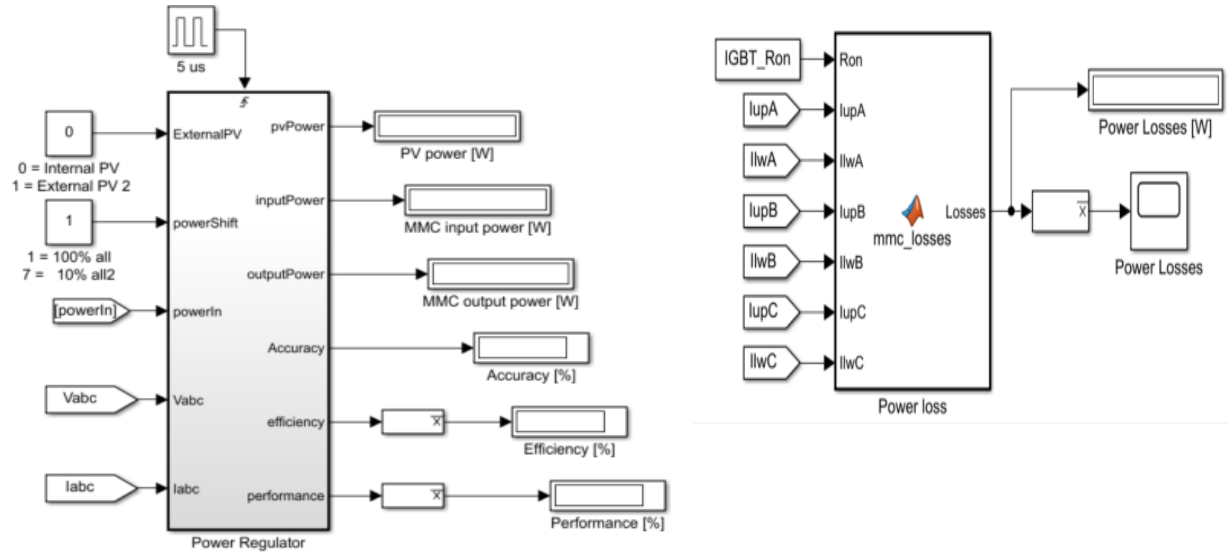

(a) (b)

Figure B.3: The MMC simulation module for calculating and measuring: (a) Accuracy, Efficiency, Performance; (b) Power loss.

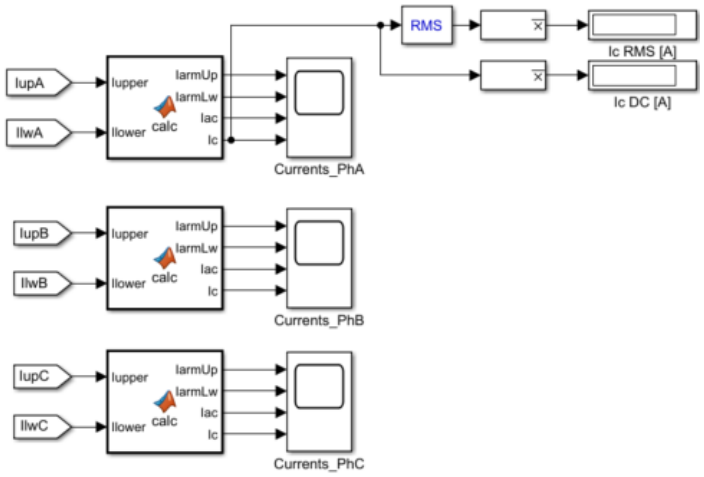

Figure B.4: Circulating current measurements at each MMC phase, RMS value of the circulating current in phase 'a', and the DC value of the circulating current in phase 'a'.